# ABSTRACT


Title of dissertation: MODELING MAGNETIC STRUCTURE IN 2D VAN DER WAALS MATERIALS WITH NEUTRON DIFFRACTION

Mario Lopez, Doctor of Philosophy, 2025

Dissertation directed by: Dr. Efrain E. Rodriguez
University of Maryland, College Park



In this thesis the magnetic structure was determined using neutron diffraction for three relatively novel van der Waals (vdW) crystals, $Fe_3GaTe_2$, $NiP(S_{1-x}Se_x)_3$, and $FeP(S_{1-x}Se_x)_3$. $Fe_3GaTe_2$ was found to be a self-intercalated ferrimagnet with interstitial iron sites between the vdW gaps. The magnetic space group was determined to be $P6_3/mm'c'$, which implies that a collinear antiferromagnetic arrangement exists among the interstitial iron site and iron sites in the telluride layers. Mixed anion $NiP(S_{1-x}Se_x)_3$ was observed to be an antiferromagnetic compound with a magnetic space group of $P1$ with the moment oriented in the *ab*-plane. The addition of Se to $NiPS_3$ results in a reduction in the total magnetic moment with it hovering between 1.0 - 1.5 $\mu_B$. Mixed anion substitution was found to have a greater affect on $FePS_3$ and $FePSe_3$. One additional antiferromagnetic magnetic phase besides the antiferromagnetic parent phase was observed for mixed anion $FePS_3$ and for mixed anion $FePSe_3$. Interestingly, the total magnetic moment for the new observed phases imply that the octahedral-coordinated Fe atoms form a low-spin configuration for a $d^6$ metal.

# MODELING MAGNETIC STRUCTURE IN 2D VAN DER WAALS MATERIALS WITH NEUTRON DIFFRACTION

by

Mario Lopez

Dissertation submitted to the Faculty of the Graduate School of the
University of Maryland, College Park in partial fulfillment
of the requirements for the degree of
Doctor of Philosophy
2025

Advisory Committee:
Dr. Efrain E. Rodriguez, Chair/Advisor
Dr. John T. Fourkas
Dr. Janice Ruett-Robey
Dr. Zhiwei Li
Dr. Ichiro Takeuchi

© Copyright by
Mario Lopez
2025

# Table of Contents


1 Introduction 1
- 1.1 What are Van der Waals Materials? . . . 1
- 1.2 Diffraction and its role in understanding vdW materials . . . 10
- 1.3 Summary of Thesis Chapters . . . 14

2 Experimental Methods 20
- 2.1 Synthesis of van der Waals Materials . . . 20
  - 2.1.1 Conventional Solid State Synthesis . . . 20
  - 2.1.2 Chemical Vapor transport . . . 21
  - 2.1.3 Flux Synthesis . . . 21
- 2.2 Diffraction . . . 22
  - 2.2.1 X-ray Diffraction . . . 24
  - 2.2.2 Neutron Diffraction . . . 26
  - 2.2.3 Constant Wavelength and Time-of-flight . . . 28
- 2.3 Solving Crystal Structures with Intensity Extraction . . . 28
- 2.4 Refining Crystal Structures with Rietveld Refinement . . . 29
  - 2.4.1 Measures of Fit . . . 30
  - 2.4.2 Energy Dispersive X-Ray Spectroscopy . . . 31
- 2.5 Magnetism . . . 31
  - 2.5.1 Types of Ordered Magnetism . . . 32
  - 2.5.2 Magnetic Susceptibility . . . 33
  - 2.5.3 Magnetization Vs. Applied Field Saturation Analysis . . . 34
- 2.6 Density Functional Theory . . . 35

3 Ferrimagnetism in $Fe_3GaTe_2$ 39
- 3.1 Introduction . . . 39
- 3.2 Experimental Methods . . . 42
  - 3.2.1 Synthesis . . . 42
  - 3.2.2 X-ray Diffraction . . . 43
  - 3.2.3 Neutron Diffraction . . . 44

3.2.4 Structural Refinements . . . 44
3.2.5 Measurement of Bulk Magnetic Properties . . . 45
3.2.6 Energy Dispersive Spectroscopy . . . 45
3.2.7 DFT Calculations . . . 45
3.3 Results and Discussion . . . 46
3.3.1 Structural and Elemental Characterization . . . 46
3.3.2 Bulk Magnetic Property Measurements . . . 51
3.3.3 Magnetic Structure Determination and Evidence of Ferrimagnetic Behavior in $Fe_3GaTe_2$ . . . 56
3.4 Conclusion . . . 78

4 Magnetic Structure Determination of Mixed Anion $NiP(S_{1-x}Se_x)_3$ 79
4.1 Introduction . . . 79
4.2 Experimental Methods . . . 82
4.2.1 Synthesis . . . 82
4.2.2 X-ray Diffraction . . . 83
4.2.3 Neutron Diffraction . . . 84
4.2.4 Magnetic Susceptibility . . . 85
4.2.5 Energy Dispersive Spectroscopy . . . 85
4.3 Results and Discussion . . . 86
4.3.1 Structural and Elemental Characterization . . . 86
4.3.2 Bulk Magnetic Property Measurements . . . 103
4.3.3 Magnetic Structure Analysis of Se-Subsituted $NiPS_3$ . . . 107
4.4 Conclusion . . . 129

5 Magnetic Structure Analysis of Mixed Anion $FeP(S_{1-x}Se_x)_3$ 130
5.1 Introduction . . . 130
5.2 Experimental Methods . . . 135
5.2.1 Synthesis . . . 135
5.2.2 Neutron Diffraction . . . 136
5.2.3 Structural Refinement . . . 136
5.2.4 Magnetic Susceptibility . . . 137
5.3 Results and Discussion . . . 137
5.3.1 Structural Characterization from Neutron Powder Diffraction . . . 137
5.3.2 Magnetic Structural Determination of Iron Chalcophosphates . . . 151
5.4 Conclusions . . . 169

6 Conclusions and Future Work 171

Bibliography 175

# Chapter 1: Introduction

## 1.1 What are Van der Waals Materials?

There are many properties that bulk materials exhibit that are said to be valuable. Some properties, like superconductivity offer resistance-free conductivity and magnetic repulsion.[1–7] Others, such as ferromagnetism can be used to store memory through the spins of an electron.[8–12] However, when it comes to scaling these properties down to the nanometer level, bulk materials have some difficulty in accomplishing this task. But, by using a certain class of bulk materials with certain layered structure motifs, an opportunity exists to scale these bulk properties down to the two-dimensional (2D) level. This special class of materials are colloquially known as van der Waals (vdW) materials. (**Figure 1.1**).

A vdW material is a crystal structure that is comprised of a series of two-dimensional layers that are stacked on top of each other. A crystal is a solid that is comprised of a repetitive arrangement of atoms in contrast to a random arrangement found in solids, such as plastics. In a vdW crystal, the atoms covalently bond just like any other 3D crystal. However, after a certain length, covalent bonding terminates in one direction, such as the $z$-axis, and remains for the other axes. As a consequence of this directional bonding sequence, vdW crystals have a stack of lattice layers that are separated by gaps of empty space.[13–17] The height of each of these layers ranges anywhere from 3-7 Å. Meanwhile, the intermediate gaps of empty space range between 3-5 Å.

This gap from the bonding perspective indicates that vdW crystals exhibit covalent

bonding in two directions to form these lattice planes, but very little bonding occurs in the direction normal to these lattice layers. Instead, coulombic interactions that form temporary dipoles known as van der Waals forces comprise the majority of these interactions in the gaps between the lattice layers. These dispersion forces are much weaker than typical bond enthalpies. For example, from experimental and theoretical calculations, we find that the van der Waal forces in $MoS_2$ have an energy near 3 kJ/mol.[18–24] This value is much smaller than the Mo-S bond energy, which is measured to be near 380 kJ/mol. Thus, the weak interactions in the direction normal to lattice planes are easily overcome by the application of a small mechanical force such as tape adhesion. In contrast, a crystal such as $BaTiO_3$ has no gaps and has bonds in *a*, *b* and *c* directions. For this material, the interactions between the atoms are too strong for them to be removed by simple mechanical exfoliation.

Since these 2D lattice layers stack using vdW forces, each layer can be removed by exfoliation until only single lattice layer, known as a monolayer, is left. From this state, monolayers of different vdW compounds can be forced to stack on top of each other to form heterostructures ( **Figure 1.2**). These heterostructures are structurally stable because the vdW forces hold the layers together. As a result, vdW crystals are able to perform a bottom-up approach to synthesize new materials with enhanced or new properties at the 2D level.[25–38]

Although vdW materials share the same dispersion forces that hold their lattice layers together, the composition of the layers themselves in terms of elemental composition and molecular geometry, can vary dramatically from system to system. For instance, there are vdW crystals comprised of just one element such as graphite or black phosphorus. However, despite both carbon and phosphorus exhibiting a coordination number of three, the geometry of their lattices are starkly different. For instance, in graphite the carbon atoms arrange themselves in a hexagonal-honeycomb lattice with each carbon atom exhibiting trigonal planar geometry. Phosphorus also has coordination number of three but one of

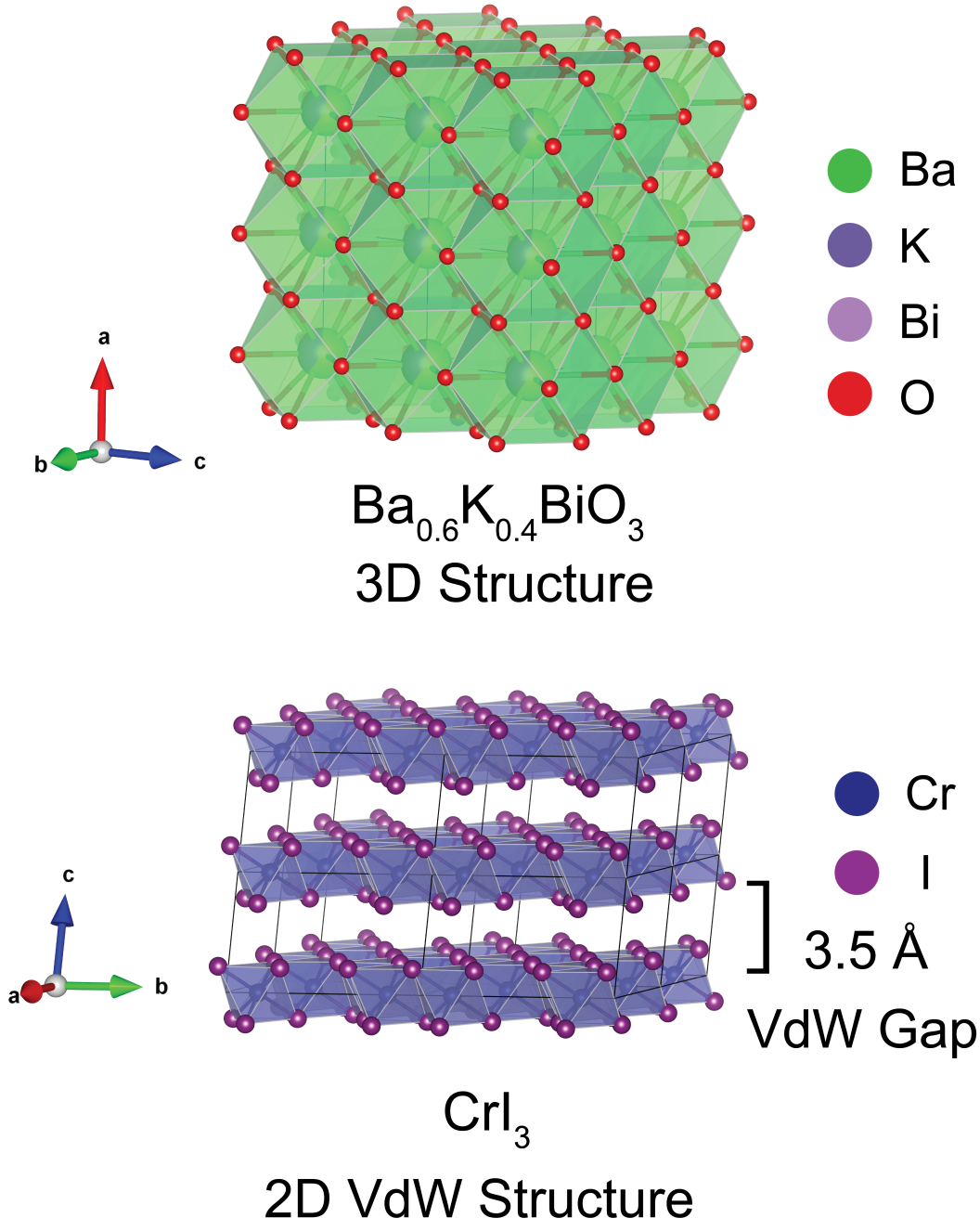



Figure 1.1: (Top) $2 \times 2 \times 2$ unit cell of $Ba_{0.6}K_{0.4}BiO_3$. (Bottom) $2 \times 2 \times 2$ unit cell of $CrI_3$.The defining feature of a vdW material is the existence of 2D lattice layers with a empty gap separating the layers.

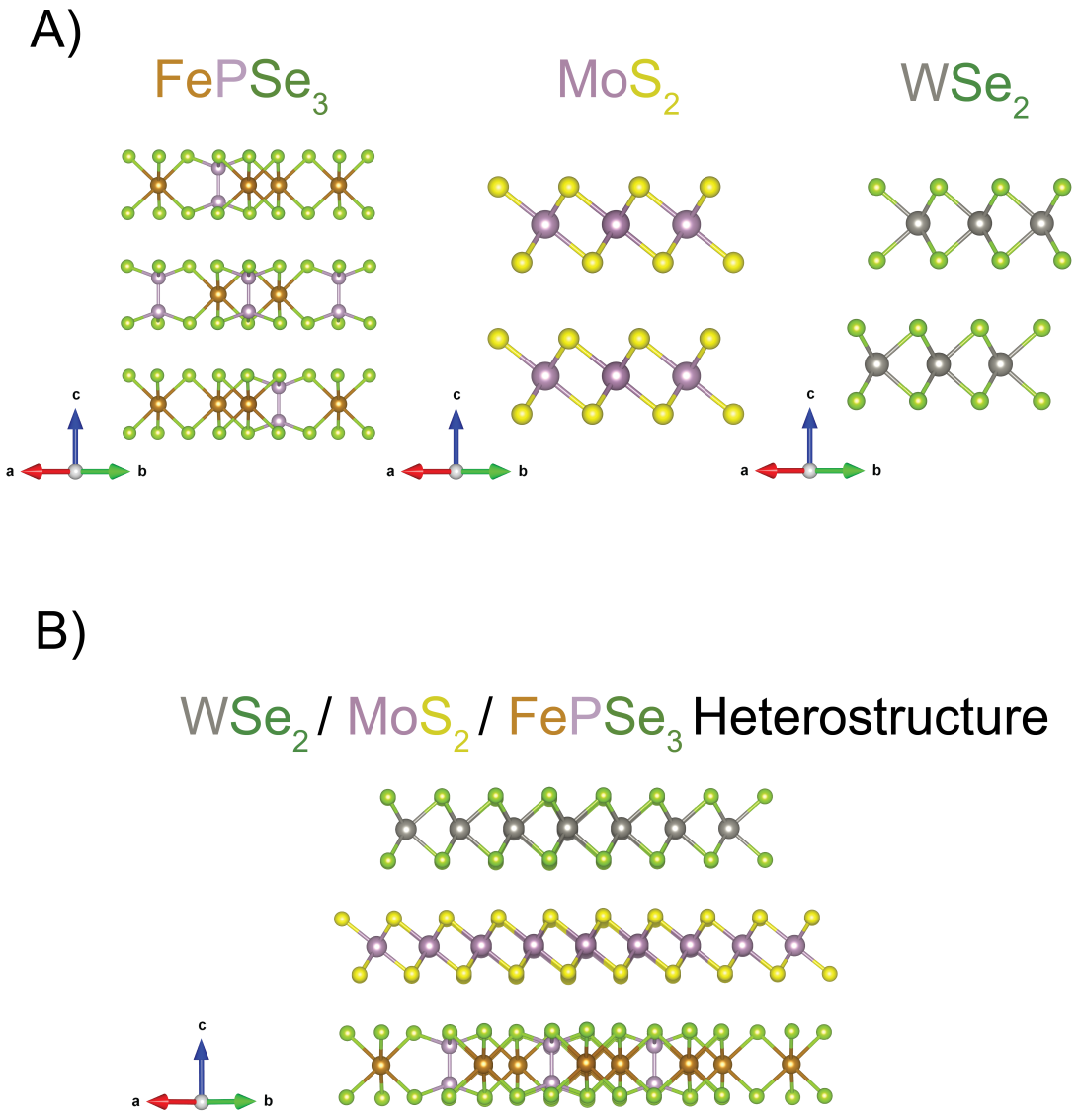



Figure 1.2: (A) Crystal structure of $FePSe_3$, $MoS_2$, and $WSe_2$. (B) Heterostructures comprised of monolayers of (A). Monolayers of vdW materials can be used to create heterostructures. These mixed structures provide a unique way to mix and match different properties.

the bonds is directionally out-of-plane leading to a distorted network of atoms. Thus, even a simple change in elemental composition is sufficient to change the structure of a vdW crystal.

If we take a look at the more complex vdW materials, we find that there are a sub-

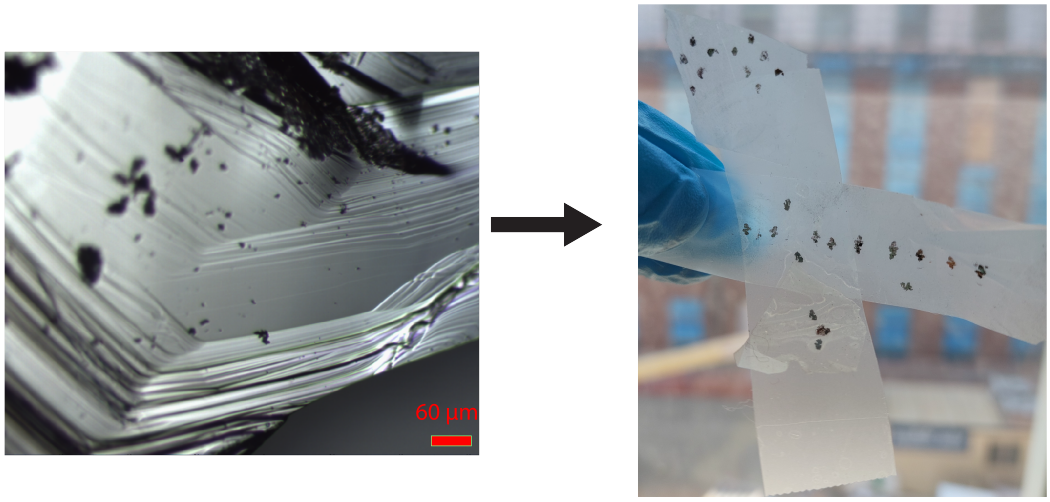



Figure 1.3: (Left) Image of $FePS_3$ single crystal from an optical microscope. $FePS_3$ forms thin plates that stack on top of each other. (Right) Imagne of exfoliated $FePS_3$ via the scotch-tape method.

class of vdW crystals called transition metal dichalcogenides (TMD), which combine a transition-metal with two sulfur or two selenium atoms. These metals typically coordinate using trigonal anti-prismatic geometry.[13,39–42] Then, there are transition metal chalcophosphates (TMC) that have transition-metals bond with $[P_2Q_6]^{4-}$, where Q is S or Se, ethane-like units to form a vdW crystal. In this crystal system the metals coordinate using an octahedral geometry.[43–56] (**Figure 1.5**).

These structural and elemental differences are important because often times they are responsible for the various properties that vdW materials exhibit. Depending on the identity of the element and its coordination environment different sub-classes of vdW crystals will determine what type of properties each vdW material will exhibit. These properties potentially include long-range magnetic ordering like ferromagnetism or antiferromagnetism; long-range electric dipole order, such as ferroelectricity; and various types of collective excitations such as excitons,[57–61] magnons,[62–65] and skyrmions.[66–68]

A good example of structure directly affecting the type of properties a vdW material

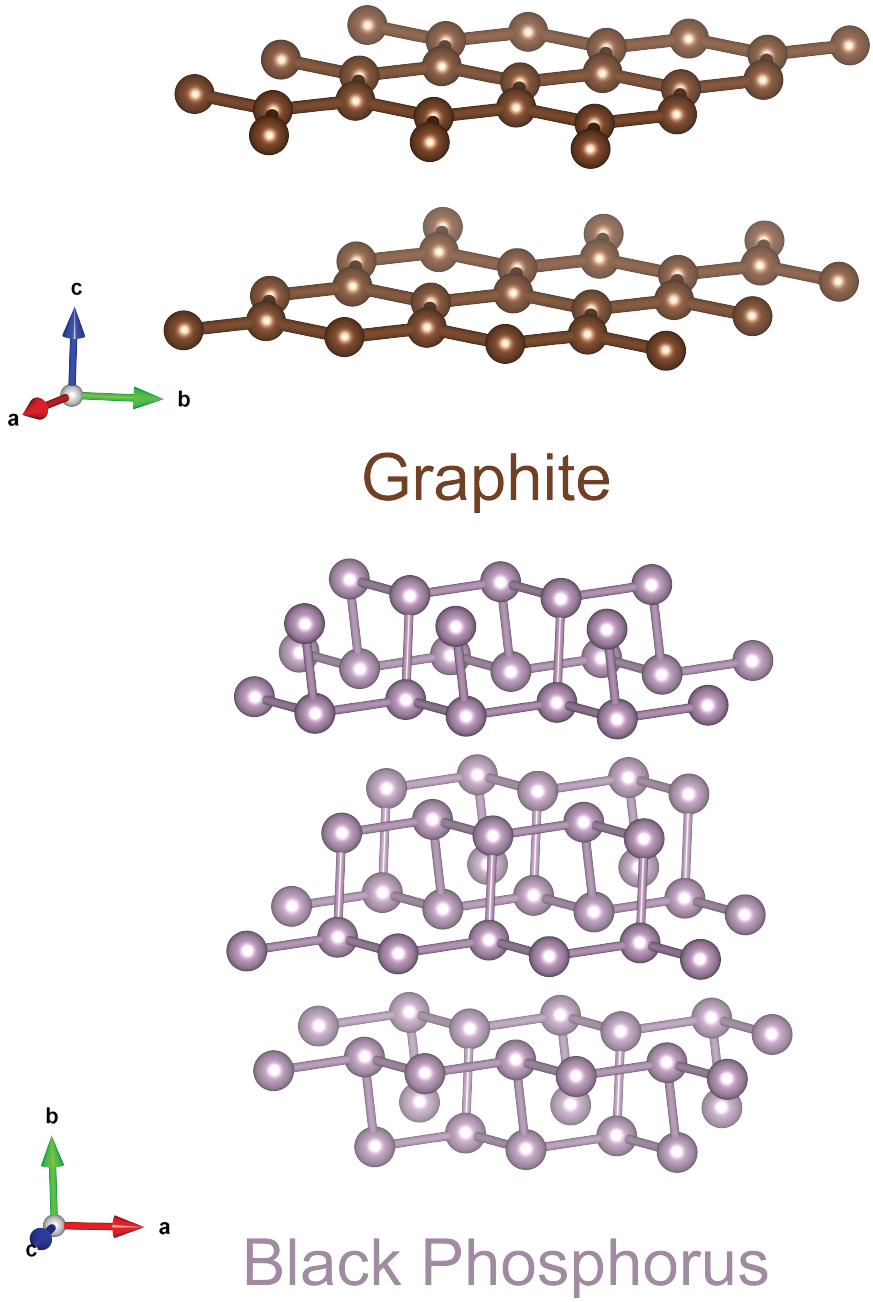



Figure 1.4: Even a change in element composition can affect the structure of a vdW material. For example, the carbon atoms in graphite form a honeycomb lattice, but with phosphorus the bond angles change to form puckered 6-member rings.

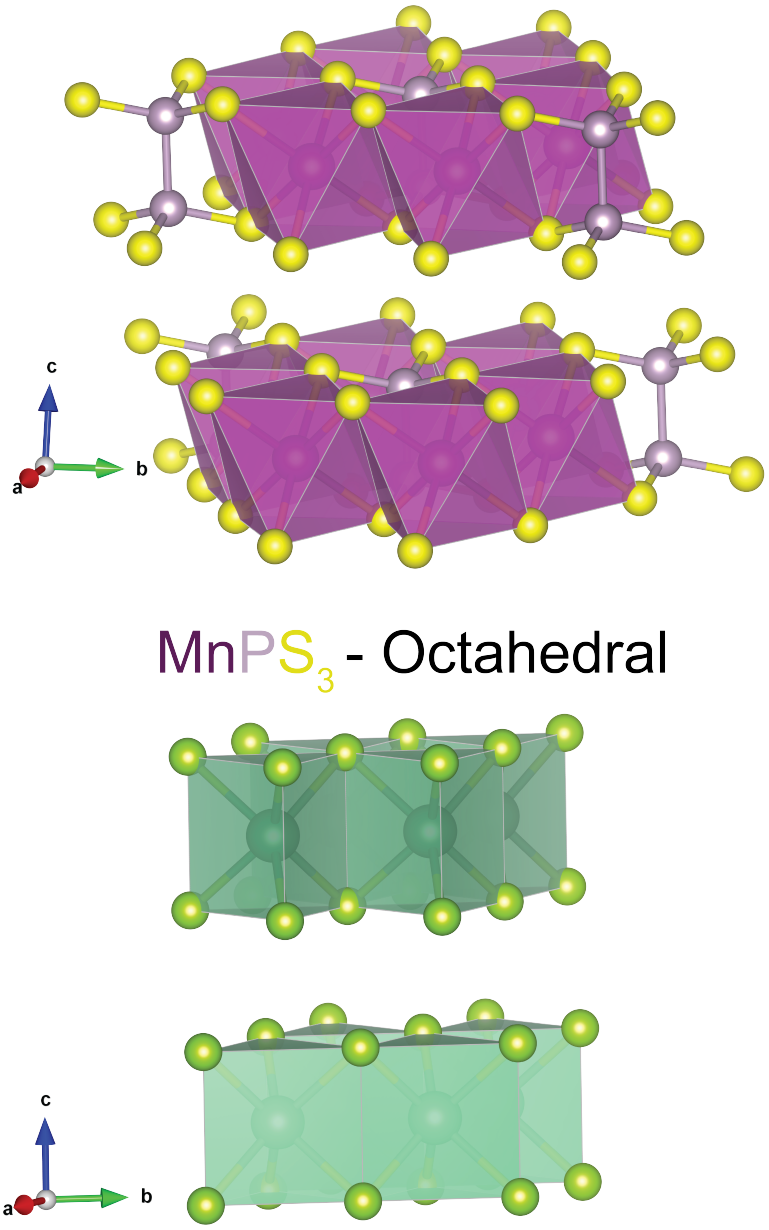



Figure 1.5: vdW crystals can be made through a variety of compositions. However, the coordination of metals generally varies from one sub-category to another. For example, in TMDs the metal atoms coordinate in a trigonal prismatic geometry, while in TMCs metals form an octahedral coordination.

can have is found in $MoS_2$. $MoS_2$ is observed to stack in three ways that are labeled 1T, 2H, and 3R. The numbers stand for the amount of layers that are need to stack before the layer configuration is the same as the 1st layer. T, H, and R stand for the trigonal, hexagonal, and rhombohedral unit cell. Since the 3R stacking sequence breaks inversion symmetry it is able to become a piezoelectric material while 2H $MoS_2$ cannot. Additionally, in the 1T stacking configuration, $MoS_2$ is observed to be several times more conductive than its 2H counterpart.

Chemical insertion of ions or molecules is another example of how structure and elemental changes can manipulate the properties of a vdW material. For instance, $CrGeTe_3$ (CGT), becomes ferromagnetic below 67 K. However, by intercalating tert-butylammonium, the Curie temperature ($T_c$) for CGT can increase to over 200 K. This change occurs because the intercalates are cations and in order for charge balance to be maintained in the system they must transfer an electron to CGT. The addition of extra electrons occupies different energy states that lead to the increase of the $T_c$.[69]

Lastly, comparing $MnPSe_3$ and $CrGeTe_3$ demonstrates the role that elemental composition has in determining properties. Both $MnPSe_3$[44,70] and $CrGeTe_3$[71,72] crystallize in the same space group $R\bar{3}$. The bonding arrangement is also identical with metal ions forming octahedral coordination with the anions, and the P and Ge atoms forming the ethane-like units with the anions. Yet, $MnPSe_3$ is an antiferromagnetic with a Neél temperature of 76 K while $CrGeTe_3$ is a ferromagnetic with a $T_c$ of 67 K (**Figure 1.6**). Furthermore, with a band gap value of over 2 eV, $MnPSe_3$ is an insulator while $CrGeTe_3$ is a semiconducting material with a band gap of 0.67 eV. This difference in properties is due to the identity of the elements. P and Se are more electronegative than Te. Additionally, P and Se also exhibit a smaller atomic radii than Ge and Te. Thus, the nature of the bond between the metal atom and the anion will be more covalent and longer for $CrGeTe_3$ versus more ionic and shorter for $MnPSe_3$.

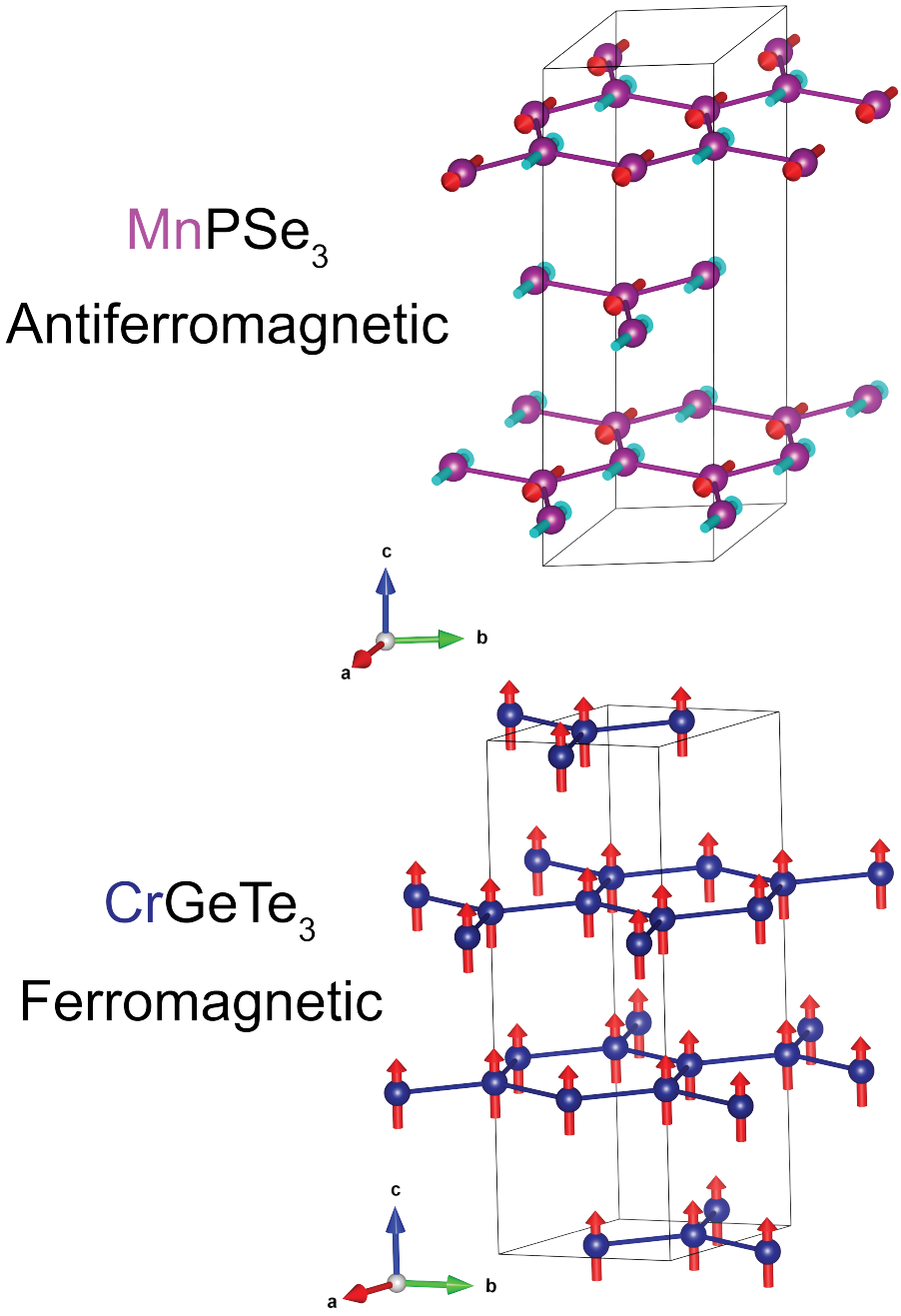



Figure 1.6: $MnPSe_3$ and $CrGeTe_3$ are examples of elemental composition dictating property behavior. Despite the same crystal symmetry, similar atomic positions, and same bonding coordination, replacing Mn with Cr and P with Ge results in a change in magnetic ordering.

Fundamental understanding of these properties are of great interest because vdW materials have great potential to be use in several applications such as storage/conversion,[28,73,74] catalysis,[75–78] and computation devices[79–83] to name a few examples. However, while vdW materials can exhibit bulk properties to the monolayer limit, often times these properties degrade because of the lack of additional layers. Thus, if vdW materials are to be used in the aforementioned applications then great emphasis is needed to find strategies to design functional vdW materials that overcome this degradation effect by either negating the effect or by raising the transition temperature of the property.

## 1.2 Diffraction and its role in understanding vdW materials

Thus, in order to accomplish this goal of creating functional vdW materials an experimental technique must be used to compare the properties of different vdW materials based on a unifying metric. This unifying metric can be the crystal structure of the vdW material since there are many examples that demonstrate a correlation between the structure of a vdW material and its properties. Successful structural analysis would result in established design principles that would link desirable properties as a function of elemental composition, bond lengths, crystal symmetry, coordination environment and other relevant structural metrics.

One of the best techniques for structural analysis on crystalline solids is diffraction.[84–87] Due to the repetitive arrangement of atoms in a crystalline solid, certain incident angles of radiation will scatter in a manner that will cause constructive interference (**Figure 1.7**). This scattering forms a diffraction pattern. Each reflection seen in the diffraction pattern represents specific aspects of crystal structure via a mathematical relationship. The intensity of the reflections are determined by how well the specific parts of the crystals scatter together. Generally more scattering results in higher counts or intensities for the

observed reflections. There are 230 space groups or ways to arrange in a crystalline manner.[88] The space group will determine the number of reflections seen as well as influence the intensities of each reflection. Through analysis of the diffraction data one can obtain a structure solution (also known as a crystallographic information file or CIF) that contains information on elemental composition, atomic positions, crystal symmetry, etc. With this information one can now begin to compare different vdW crystals and relate structure to property behavior. Additionally, further analysis can be achieved since CIFs can also enable theoretical calculations, such as band structure calculations.

Neutron diffraction, where the source of incident radiation comes from neutrons, is especially equipped to measure long-range magnetic ordering in crystalline solids[89–94] because the moment in a neutron interacts with the moments from the unpaired electrons. This interaction results in magnetic scattering similar to the scattering described in X-rays. However, the key insight in neutron diffraction is that if the unpaired electrons in the sample have no long-range order then they will scatter the neutrons randomly and no constructive interference occurs. But, if there is long-range magnetic ordering then there will be a certain parts of the crystalline sample that will scatter the neutrons constructively to give rise to new magnetic reflections or enhance the intensities of pre-existing reflections depending on the relationship between the magnetic unit cell and crystal unit cell otherwise known as the propagation vector, $\vec{k}$, (**Figure 1.8**).

By analyzing the magnetic reflections one can then derive the magnetic structure from the data and determine if the magnetic material is 1) ferromagnet where all the magnetic moments are aligned to one direction resulting in a net magnetization in the sample, 2) An antiferromagnet where the material experiences no net magnetization due to half the moments canceling out the other half, or 3) a ferrimagnet where the sample still exhibits a net magnetization but a minority of the moments are anti-aligned towards the direction of the magnetization.

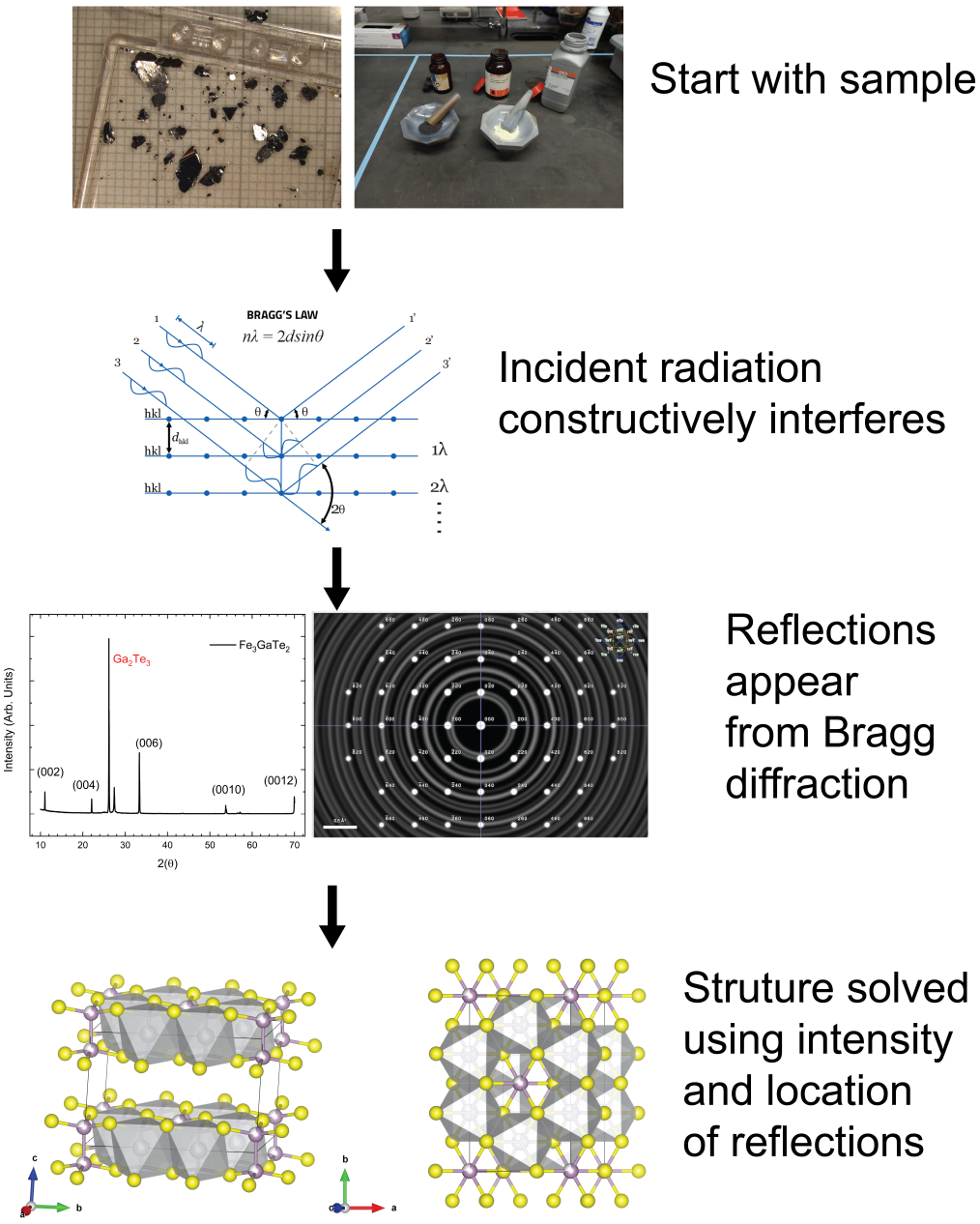



Figure 1.7: Regardless if the sample is a powder or a single crystal. If the sample is crystalline then it will diffract upon incident radiation. Once the data is collected the intensities and placement of the reflections can be used to solve the structure of the sample. The Bragg's law figure was acquired from www.veqter.co.uk. The simulated precession image was acquired from www.crystalmaker.com

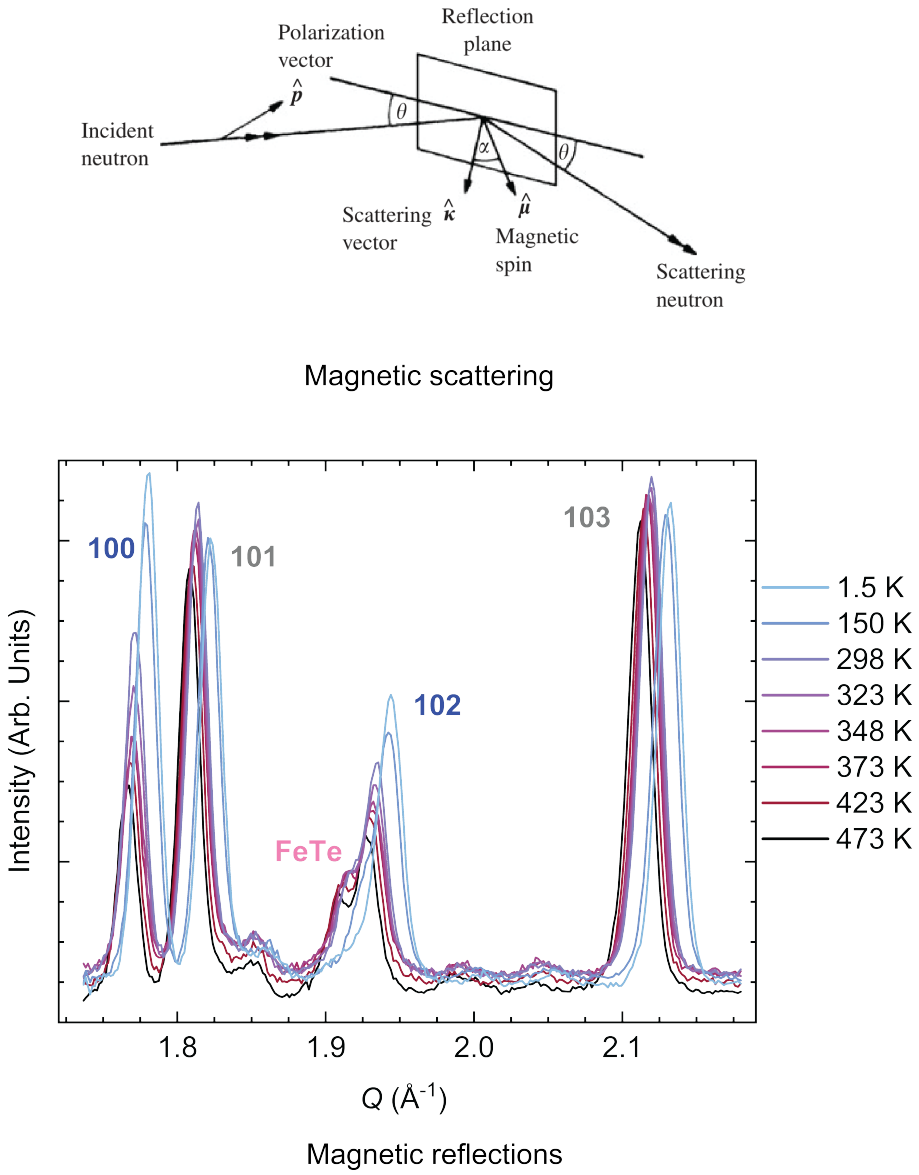



Figure 1.8: Because neutrons carry a magnetic moment they are able to interact with the magnetic moment of electrons. As a result, Bragg diffraction can occur from this magnetic scattering. This means that new reflections can arise or pre-existing reflections may exhibit an increase in intensity as demonstrated in the bottom image of this figure.

## 1.3 Summary of Thesis Chapters

Due to this causal link between property and structure, it is of great importance to investigate the structure of crystalline solids as it will not only confirm the successful synthesis of relatively unexplored vdW materials, but also provide insights on the origin and performance of these properties through from the perspective of structure. This is why this thesis focuses on using neutron diffraction as the primary means to determine the crystal and magnetic structures of three vdW crystals, $Fe_3GaTe_2$, $NiP(S_{1-x}Se_x)_3$, and $FeP(S_{1-x}Se_x)_3$. Each of these materials are relatively novel and have not been explored in detail in terms of their crystal structure. Additionally, these three vdW compounds exhibit magnetic properties such as 2D magnetism,[95–98] and plethora of collective excitations[99–104] that can be used for device applications. Neutron diffraction is an established and accurate experimental technique that can determine the magnetic structure of crystalline compounds .

In the first chapter, I discuss the observation of ferrimagnetism from neutron diffraction data in $Fe_3GaTe_2$. $Fe_3GaTe_2$ is a relatively unexplored material, that has great potential to be used in spintronic applications as it exhibits both above room temperature ferromagnetism and other exotic magnetic properties, such as skyrmions. By performing a combination of neutron and X-ray diffraction this thesis reports a detailed crystallographic structure of $Fe_3GaTe_2$. The structure derived from the diffraction data suggests the existence of an additional interstitial Fe site that is located in the middle of the van der Waals gap (**Figure 1.9**). This result is unexpected because it implies that the nuclear and magnetic structure of $Fe_3GaTe_2$ is not the same as $Fe_3GeTe_2$. Furthermore, these results imply that $Fe_3GaTe_2$ is ferrimagnetic because the interstitial sites are anti-parallel to Fe sites within the lattice layers.[105] Thus, these findings have profound implications for property engineering strategies, such as elemental substitution, because these interstitial sites affect the band structure differently than the other metal sites.

The second chapter investigates the magnetic structure of mixed anion nickel chalcophosphate compounds. A combination of powder and single-crystal neutron diffraction and magnetic susceptibility measurements reveals that an increase of selenium in $NiP(S_{1-x}Se_x)_3$ results in an increase in Neél temperature from 155 K to about 200 K. Neutron powder diffraction data suggests that the strength of the total magnetic moment is relatively constant with a value of 1.5 $\mu_B$ throughout the whole solid solution series. In contrast, a the moment was observed to decrease from 1.5 to 1.0 $\mu_B$ according to single-crystal neutron diffraction data. (**Figure 1.10**). Despite the change in selenium concentration, $NiP(S_{1-x}Se_x)_3$ was observed to exhibit antiferromagnetic ordering throughout the whole solid solution series. The magnetic structure for this antiferromagnetic phase was able to be modeled using a magnetic unit cell with $P1$ space group symmetry. This magnetic structure is very similar to the one observed in $NiPS_3$. Additionally, $NiP(S_{1-x}Se_x)_3$ exhibits significant structural distortion due to the shifting of the lattice layers affecting the stacking sequence in the direction of the $c$-axis. However, these distortions can be minimized if the thickness of the single crystal is minimized.

The next chapter describes the results of neutron powder diffraction experiments on mixed anion $FeP(S_{1-x}Se_x)_3$ compounds. When iron chalcophosphate is sulfur-rich, the crystal space group is $C2/m$. When the materials are selenium-rich, the space group is $R\overline{3}$. Neutron diffraction data suggest that the presence of both sulfur and selenium results in the appearance of new antiferromagnetic phases. In sulfur-rich $FeP(S_{1-x}Se_x)_3$ there are two magnetic phases. One phase has a propagation vector $\overrightarrow{k} = [01\frac{1}{2}]$, this means that the magnetic units cell is twice the size of the nuclear unit cell. The second phase has propagation vector $\overrightarrow{k} = [010]$. Both have magnetic structures that were modeled using a magnetic unit cell with $P1$ symmetry. Similarly, selenium-rich $FeP(S_{1-x}Se_x)_3$ also hosts two magnetic phases. One phase has $\overrightarrow{k} = [\frac{1}{2}0\frac{1}{2}]$, which is the same phase found in $FePSe_3$. The second phase has $\overrightarrow{k} = [0\frac{1}{2}0]$. Both of these phases were also modeled using a magnetic

unit cell with $P1$ symmetry. Interestingly, the relationship between the two phases is that the parent magnetic phase has a higher magnetic moment that the new magnetic phase. This difference was found to be near 2 $\mu_B$, which implies that new phase has a lower spin of about $S = 1$ compared to the other magnetic phase. We hypothesize that this complex magnetic structure is due to a combination of chemical pressure, structural disorders and changes in the crystal field that are sufficient to form a new magnetic phase. This work is a first step toward establishing successful engineering principles for manipulating magnetic behavior through elemental substitution.

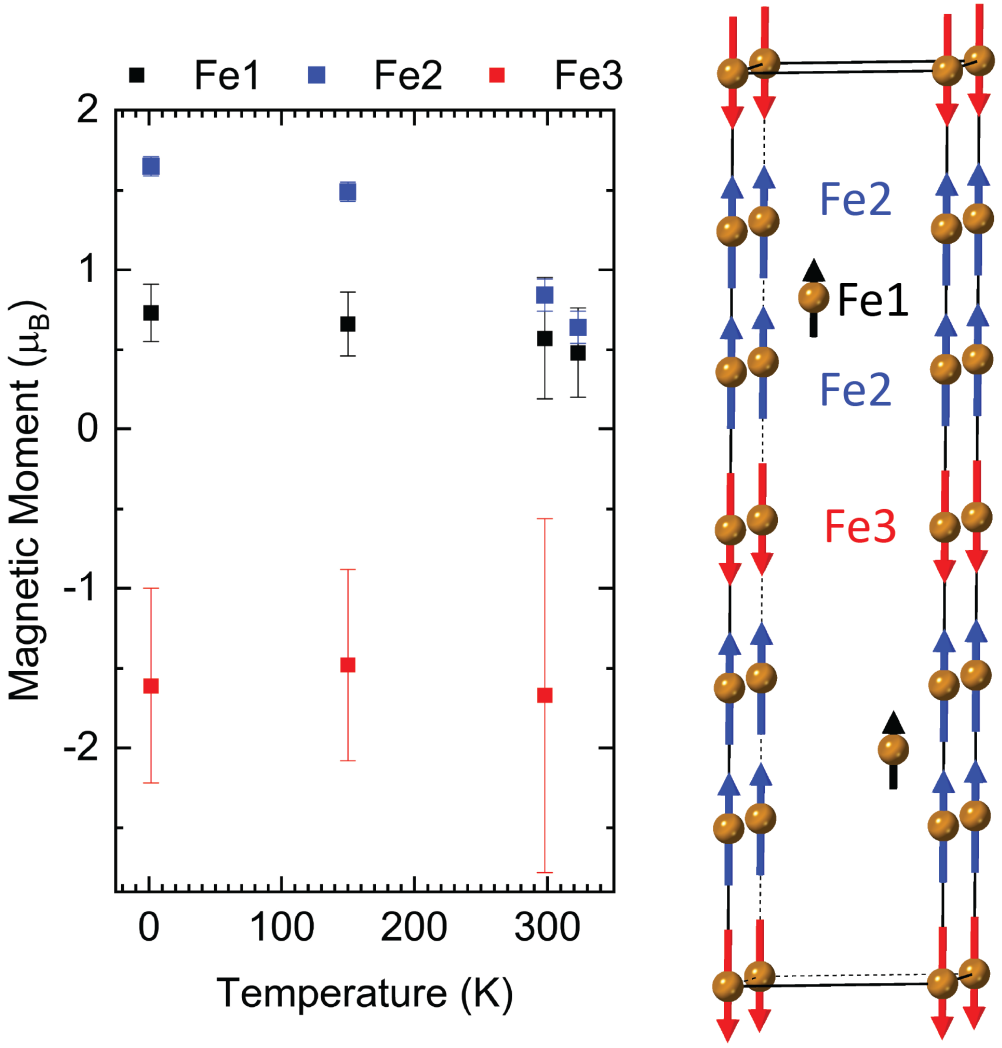



Figure 1.9: The magnetic structure of $Fe_3GaTe_2$ was found to be ferrimagnetic with the interstitial Fe3 sites hosting magnetic moments anti-aligned to the moments for Fe1 and Fe2. About 3-5% of the Fe atoms sits in the the van der Waals gap. We observed that FGaT is still magnetically order until 340 K.

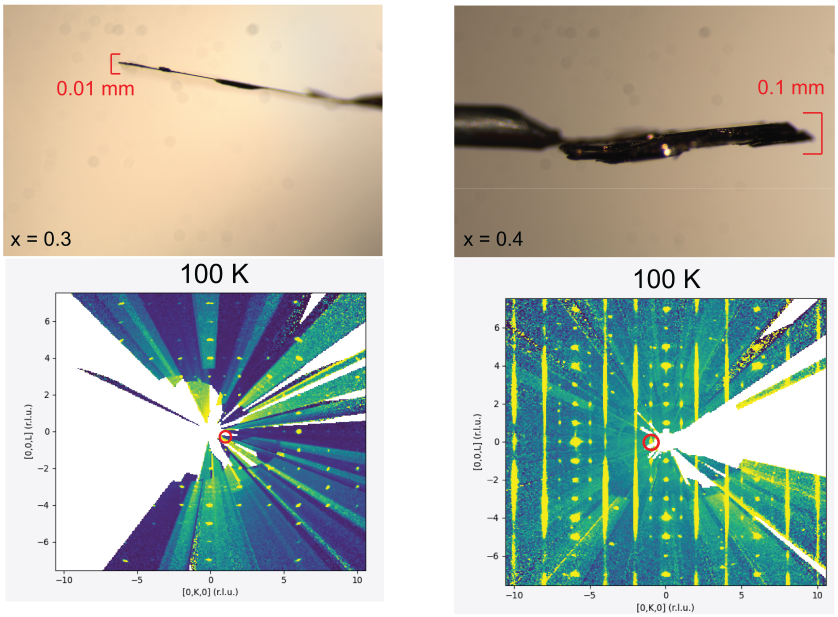



Figure 1.10: Diffuse features was observed to be correlated to crystal thickness. Mixed anion $NiP(S_{1-x}Se_x)_3$ was found to be antiferromagnetic crystal with a propagation vector $\vec{k}$ = [010]. The appearance of the (010) reflection suggests that its crystal symmetry is broken resulting in a $P1$ magnetic space group with the magnetic moments aligned normal to the stacking direction. Each spin has 2 FM neighbors and 1 AFM neighbor. Magnetic moments are found to vary a between 1.0 -1.5 $\mu_B$ upon the introduction of Se.

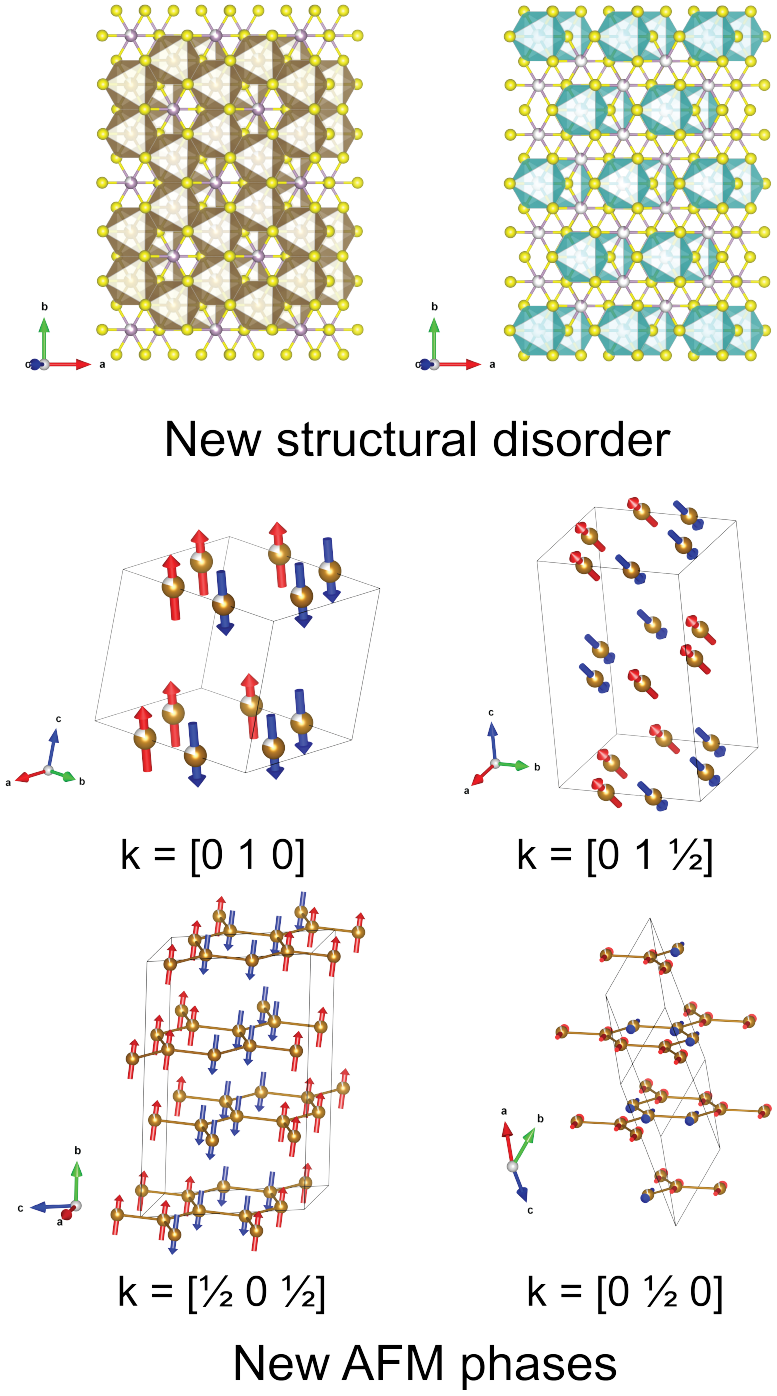



Figure 1.11: Creation of a mixed anion $FeP(S_{1-x}Se_x)_3$ results in the introduction of the same structural disorder found in $NiPQ_3$ compounds. The addition of Se to $FePS_3$ and S to $FePSe_3$ resulted in the observation of a new AFM phases. This new magnetic phase was observed to have a lower total magnetic moment equivalent to $S = 1$

# Chapter 2: Experimental Methods

## 2.1 Synthesis of van der Waals Materials

In this work, a combination of solid-state synthesis, chemical vapor transport, and flux synthesis were used to synthesize the materials investigated in this work. However, there are other synthesis techniques that can produce vdW materials such as liquid exfoliation, pulsed-laser deposition, chemical and physical vapor deposition.

### 2.1.1 Conventional Solid State Synthesis

The conventional approach can be considered as the most rudimentary technique for solid state synthesis. In this technique, different elements are mixed together and then subsequently heated to a target temperature. At the target temperature the reagents dwell for some time before they are cooled naturally through the furnace. The reagents can also be cooled rapidly by quenching in ice or water. Afterwards, the products are collected as a powder. However, occasionally a small crystal (less than $1 \times 1 \times 0.01$ mm$^3$) may be extracted from powder product.

For oxides, the reaction can take place inside $Al_2O_2$ crucibles. For non-oxide compounds, the reagents are generally mixed within an air-free environment, such as an argon or nitrogen-filled glove box, and placed inside a sealed quartz ampule.

Alumina crucibles are prevalent in this technique because aluminum oxide is generally a non-reactive surface area that can withstand temperatures as high as 2000 $^{\circ}$C. Likewise,

quartz tubing is another vessel of choice since it is inert, and a cheap way of isolating the reagents from ambient conditions. However, the limiting factor for silica tubing is its inability to withstand temperatures past 1200 $^{\circ}$C. For higher temperatures tantalum or tungsten tubing is used.

Generally the time scale for this synthesis technique can range from a few days, to weeks or even months.

### 2.1.2 Chemical Vapor transport

Chemical vapor transport or CVT is a synthesis technique that is typically performed for the growth of large single crystals. The approach takes advantage of the equilibrium reaction between the transport agent and a powdered sample by using a thermal gradient within a horizontal tube. Since the equilibrium constant changes as a function of temperature, one end of the ampule will promote the chemical reaction of the reagents with the transport agent to form a gaseous complex agent, and at the other end, the crystallization of the gaseous species.

### 2.1.3 Flux Synthesis

Another method that can grow single crystals is flux synthesis. This technique primary uses an inert low melting point element so that the flux agent can dissolve the reagents in its liquid state of matter and then later on induce the crystal growth process by lowering the temperature. From this perspective, flux synthesis is analogous to crystal growth from a supersaturated solution. A liquid solution is able to dissolve much more solute at an elevated temperature and once the temperature drops crystal growth begins upon further stirring of the solution. Typical candidates for flux agents are Ga, In, Sn, Pb, Te. These elements have relatively low melting points ($< 700$ $^{\circ}$C). A low melting point is desirable

because the flux agent can be separated from the crystal products through decantation.

## 2.2 Diffraction

Diffraction in the most general sense describes a certain interaction between a wave and matter. However, in this work, the type of diffraction that will be referenced most often is Bragg diffraction. Bragg diffraction refers to a type of scattering that is coherent, or unmodified in energy or phase, and results in constructive interference. In particular, there is mathematical relationship that predicts which incident angles will result in constructive interference as a function of the distance between a set of lattice points so long as the wavelength of the incident radiation is of a similar magnitude to the spacing between the lattice points (**Figure 2.1**). **Equation (2.1)** lists the mathematical relationship known as Bragg's Law.

$$n\lambda = 2d\sin\theta \tag{2.1}$$

The spacing between the lattice points that diffract constructively is known as the $d$-spacing which is typically in units of nanometers (nm) or angstroms (Å). For a 3D crystal lattice there are seven lattice systems that can be used. These lattice system are triclinic, monoclinic, orthorhombic, tetragonal, trigonal, hexagonal and cubic. Each lattice system has its own mathematical relationship that relates d-spacing with $hkl$-planes, such as **Equation (2.2)**. A $hkl$-plane refers to the plane that is formed among the points $a/h$, $b/k$, $c/l$, where $a$, $b$, $c$ are the unit cell lattice parameters and $h$, $k$, $l$ are integer values. For example, **Figure 2.2** displays the the family of $\{111\}$ planes in cubic face-centered cobalt. As we can see, each plane cuts each of the axis once and that this family of planes have the same d-spacing

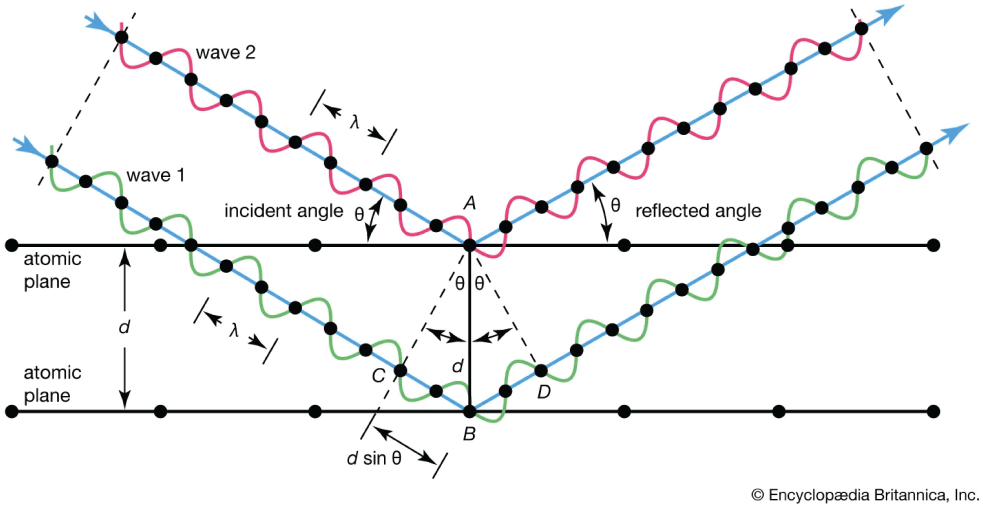



Figure 2.1: Because of the difference in path length, the only way for wave 1 and wave 2 to constructively interfere is if the CBD path of wave 1 is equal to an integer wavelength of wavelength. If this condition is fulfilled, then the amplitudes of both phase are in-phase regardless of the path difference. If not, then the waves destructively interfere an no reflection is observed.

distance.

$$\frac{1}{d^2} = \frac{h^2 + k^2 + l^2}{a^2} \tag{2.2}$$

Thus, if a certain incident angle is known to result in a Bragg reflection, then that d-spacing value can be used to calculate the set of hkl planes, also known as Miller indices, that contributes to Bragg diffraction. As a result, every reflection we observe describes parts of the crystal structure with the whole diffraction pattern alluding to the complete crystal structure.

Occasionally, the d-spacing units are described in units of Q which is calculated by $2\pi/d$. This expression implies that the units of Q is in inverse distance units. Similar to how frequency refers to an action per second, Q is unit of periodicity. With regards to diffraction, an observed Bragg reflection at some Q means that within the crystal structure

every $2\pi/d$ is constructively interfering to give rise to that reflection.

### 2.2.1 X-ray Diffraction

In a diffraction pattern each reflection can be described by two components the angle/d-spacing where it appears in the data and the intensity of the reflection. The previous section dealt with Bragg diffraction, which describes where in the crystal will reflections will arise. However, the intensity of those reflections is entirely dependent on how much the electrons in the atoms and their distribution within the unit cell scatter coherently. The technical name for the former is called the atomic scattering factor while the latter is referred to the structure factor.

X-ray diffraction refers to experiments where the source of the incident radiation comes from x-rays. These x-rays come from the emission of accelerating electrons colliding with an object. Due to x-rays being electromagnetic waves, when they can encounter atoms, they can interact with both the electrons and the nucleus of an atom. In fact, the Thomson equation, as seen in **Equation (2.3)**, describes the intensity of a beam of photons coherently scattered by a single electron.

$$I = I_o(\frac{\mu_o}{4\pi})(\frac{e^4}{m^2r^2})sin^2\theta \tag{2.3}$$

Where $I$ is equal to the final intensity in units of erg$\cdot$ sec cm$^{-2}$, $I_o$ equal to the initial intensity, $\mu_o$ is $4\pi \times 10^{-7}$ m $\cdot$ kg C$^{-2}$, $m$ is mass, r is meters from electrons, and $\theta$ is the angle between the scattering direction and the direction of the the accelerating electron. It is important to note that mass is inversely proportional to intensity scattered by an electron, which means that the nucleus with its significantly larger mass will not contribute to the scattering of the beam as much as atom's electrons.

Since atoms beyond hydrogen carry more than one electron, a new equation is needed

to describe how well many-electron atoms will scatter radiation as a function of direction. This new value is called the atomic scattering factor or $f$. This value is entirely dependent on the concentration of electrons and the scattering angle.

$$f = \int n(\rho) e^{i2\theta} dV \tag{2.4}$$

Where **Equation (2.4)** displays the equation for calculating atomic form factor where $n(\rho)$ as the function that describes an atom's electron distribution, $2\theta$ represents the angle between the scattering vector and the radial position of the electron integrated through all space.

$$f = \int n(\rho) e^{i2\theta} dV = Z \tag{2.5}$$

If the angle between these two vectors is equivalent then a special case occurs where the atomic form factor $f$ is equal to $Z$ or the number of electrons the atom has resulting in **Equation (2.5)**. A visual example of the special case can be seen in **Figure 2.3**. Although we know how each individual atom will scatter an x-ray, we run into a problem once we try to calculate how the x-rays will scatter in a crystal lattice. This problem occurs because there are many atoms with either different positions in the unit cell or the atoms each host a different amount of electrons. This predicament causes x-rays to scatter with different phases and carry different amplitudes relative to one another. Fortunately, the structure factor is the solution to this issue.

$$F_{hkl} = \sum^{N} f_n e^{2\pi i(hu_n + kv_n + lw_n)} \tag{2.6}$$

The structure factor, $F_{hkl}$, can be represented as the resultant wave scattered by all atoms within the unit cell that diffract. To calculate the structure factor for a reflection ($hkl$), three

components are needed, the (*hkl*) of the reflection of interest, each atom's atomic scattering factor, $f_n$, and each atom's fractional coordinates, $u_n, v_n, w_n$, with respect to the unit cell. The summation of these components, using **Equation (2.6)**, will equal the structure factor for reflection (*hkl*). Due to the structure factor carrying an imaginary component, it is $|F^2|$ that equals intensity, $I$.

### 2.2.2 Neutron Diffraction

The source of radiation for diffraction is just limited to x-rays, neutrons can also be used. Similar to x-ray diffraction, neutron diffraction can also be used to solve crystalline samples due to Bragg diffraction also occurring when the neutrons scatter off the sample. However, the scattering dynamics are different for neutrons. Neutrons are found to scatter isotopically unlike x-rays where the form factor decreases as a function of incident angle. Additionally, neutrons themselves carry a magnetic moment, which can interact with the magnetic moments of electrons from the sample. This extra interaction means that both scattering from the crystal lattice and the magnetic scattering need to be taken into account when calculating the intensity for an observed reflection.

Although the intensity is still calculated through the structure factor, the values needed to calculate the structure factor are different due to the inherent difference between x-rays and neutrons. For example, there is no atomic scattering factor in neutron diffraction. Instead, the value called the scattering length is used to gauge how well an atom affects the flux of scattered neutrons to incident neutrons. Thus the structure factor for neutron diffraction is **Equation (2.7)**.

$$F_{hkl} = \sum^{N} b_n e^{2\pi i(hu_n + kv_n + lw_n)} \tag{2.7}$$

Where $F_{hkl}$ is the structure factor, (*hkl*) is the reflection of interest, and $b_n$ is the scatter-

ing length and position of each atom in fractional coordinates, $u_n, v_n, w_n$ with respect to the unit cell. Additionally, neutrons are able to interact with the magnetic moments of a sample due to neutrons exhibiting a magnetic moment. This property means that magnetic scattering must be calculated in addition to neutron scattering. Thus, another term is needed to describe the contribution of magnetic scattering which is **Equation 2.8**

$$F_{hkl}^{mag} = \sum^{N} p_n q_n e^{2\pi i(hu_n + kv_n + lw_n)} \tag{2.8}$$

Where $u_n, v_n, w_n$ $q_n$ is the position of each atom in position of each atom in fractional coordinates with respect to the unit cell. $q_n$ represents the angle between the scattering vector and the direction of the magnetic moment of an atom. While, $p_n$ represents the magnetic scattering length, which is further defined as in **Equation (2.9)**

$$p = \left(\frac{e^2\gamma}{2m_e c^2}\right) g^J f \tag{2.9}$$

Where $e$ is the charge of the electron, $m_e$ is the mass of an electron, $\gamma$ magnetic moment of a neutron (1.913 $\mu_n$), c is the speed of light, $g^J$ is the Landé splitting factor. If there is no contribution from the orbital moments than the Landé splitting factor reduces to $2S$, where $S$ is the total spin of the system. Lastly, $f$ refers to magnetic form factor.

$$\mu_{tot} = 1.913\mu_n \cdot 2S \tag{2.10}$$

Assuming that the Landé factor is $2S$, the product of $g^J$ $\gamma$ can be used to find $\mu_B$ or the spin-only total magnetic moment (**Equation (2.10)**).

### 2.2.3 Constant Wavelength and Time-of-flight

If we recall Bragg's law, (**Equation (2.1)**, we find that a diffraction experiment can be set up to measure Bragg reflections as a function of either varying wavelength at a constant incident angle or constant wavelength at varying incident angles. These two types of instrumental set ups are referred as time-of-flight and constant wavelength.

Historically, time-of-flight experiments would allow more flux of the radiation source compared to constant wavelength. This result occurs because under constant wavelength conditions a monochromator needs to be used to filter out all other incident radiation at different wavelengths. This filtering reduces the amount of incident radiation that interacts with the sample, but raises the resolution due to the signal being produced by a single wavelength.

However, at the present moment the distinctions between TOF and constant wavelength instruments are narrowing due to next-generation facilities improving upon factors such as the neutron source and instrumental design[85]

## 2.3 Solving Crystal Structures with Intensity Extraction

One way of determining the diffraction pattern of a single crystal is by directly comparing the intensities of the observed reflections to the calculated intensities of crystal structure. Using a least squared approach, the best calculated structure factor fit can be found with the help of **Equation (2.11)**.

$$\overline{S} = \sum_{hkl} w_{hkl}(|F_{hkl}|^2_{obs} - S|F_{hkl}|^2_{calc})^2 \tag{2.11}$$

Where $S$ is the scale factor, $w_{hkl}$ is a constant that represents the weighing constant that corrects for values such as absorption, multiplicity, the Lorenz factor. The sum of squared

differences is minimized when $|F_{hkl}|^2_{calc}$ is similar to $|F_{hkl}|^2_{obs}$. A successful structure refinement would result in a linear curve when $F_{obs}$ is plotted with respect to $F_{calc}$ as seen in **Figure 4.24**

## 2.4 Refining Crystal Structures with Rietveld Refinement

Diffraction patterns from powder samples can also be solved. However, the technique used to solve the diffraction pattern is different than the intensity extraction approach used for single crystal samples. In principle, all the observed Bragg reflections from a crystalline sample can be found in the powder diffraction pattern. However, there is a problem in differentiating (*hkl*) reflections with similar d-spacing. This challenge arises due to the polycrystalline nature of a powder sample, which will produce diffraction rings instead of spots. With diffraction rings it becomes more difficult to isolate the individual intensities for a specific (*hkl*) reflection. While this issue may not be a problem for high symmetry crystal structures since many of their reflections are symmetrically equivalent, for lower symmetry structures this additional factor makes solving their structure very difficult since these low symmetry structures have many *hkl* reflections that are not symmetrically equivalent to other Bragg reflections and thus their contribution to the intensities cannot be assumed to be the same as is the case in higher symmetry crystal structures.

If the integrated-intensity approach can be thought as fitting observable diffraction patterns to an ideal crystal structure, then the Rietveld method can be summarized as fitting an ideal crystal structure to observed diffraction data. In fact, by utilizing a pre-existing crystal structure, the Rietveld method allows for the calculation of structure factors and hence bypassing the aforementioned problem of non-symmetric (*hkl*) reflections with sim-

ilar d-spacing. Under the Rietveld method, **Equation (2.11)** converts to **Equation (2.12)**.

$$\overline{S} = \sum_i w_i (y_i(obs) - y_i(calc))^2 \tag{2.12}$$

Where $y_i(obs)$ and $y_i(calc)$ represents the intensity of a data point from simulated diffraction pattern for the former and the observable data from the latter, lastly $w_i$ is a weighing constant.

Within the $y_i$ term are all the components that contribute to the intensity of a diffraction pattern, such as lattice parameters, atomic positions, and structure factors. Using the least squares method, these parameters are optimized to minimize the difference between the observable and calculated diffraction patterns. If the pre-existing structure is similar to the experimental crystal structure, then the difference between the experimental and calculated patterns should be small.

### 2.4.1 Measures of Fit

There are many types of fitting parameters used to describe how well the observable data fits to the calculated data. A combination of these residual metrics with a proper value is necessary for a fit to be considered good.

$$R_f = \sum \frac{|F_{obs}| - |F_{calc}|}{|F_{obs}|} \tag{2.13}$$

One measure of fit is the R-factor, listed as **Equation (2.13)**, which is a ratio of the difference between the observable and calculated structure factors over the observable structure factor. A low $R_f$ implies that an experimental crystal structure matches a simulated crystal structure. This is a metric typically used to compare Rietveld refinements to single crystal

structure solutions.

$$R_{wp} = \left( \frac{\sum_i w_i (y_i(obs) - y_i(calc))^2}{\sum_i w_i (y_i(obs)} \right)^{1/2} \tag{2.14}$$

Another residual of interest is the weighted profile R-factor or $R_{wp}$ (**Equation (2.14)**. This metric compares the intensity difference between the observed and calculated dataset multiplied by the aforementioned weighing constants, $w_i$. By normalizing with respect to the observed intensities, a fractional value that mirrors $\overline{S}$ can be obtained and be utilized to gauge the fitting quality of the calculated structure model to the observable data.

### 2.4.2 Energy Dispersive X-Ray Spectroscopy

Energy dispersive x-ray spectroscopy is a quantitative elemental analysis technique that can be performed in a scanning electron microscope (SEM). In an SEM, high energy electrons collide with a sample. This interaction removes electrons from an element's electron shell and forms a vacancy. Another electron from a different shell then fills this vacancy and releases a photon of energy that is similar to the difference in energy between the two shell levels. If these energy transitions from different elements are separated sufficiently from one another, then it is possible to link each excitation with an element and thus qualitatively determine how much of each elements is in a sample.

## 2.5 Magnetism

Magnetic behavior is primarily determined by unpaired electrons.[106–108] Electrons carry a spin, which results in each electron exhibiting a magnetic moment. However, an orbital can host two electrons with opposing spins. If this occurs, then the opposing spins result in opposing magnetic moments. Since there is no net magnetic moment, no form of long

range magnetic ordering occurs. Instead, the material is said to be a diamagnet, which repulses an applied magnetic field.

### 2.5.1 Types of Ordered Magnetism

If the electrons are not paired in the valance orbitals, then the material will interact with the magnetic field and other magnetic materials. There are few states that a magnetic material can follow. These states are referred as paramagnetic, ferromagnetic, antiferromagnetic, and ferrimagnetic (**Figure 2.4**).

A material is paramagnetic when its moments exhibit no long range magnetic ordering. Yet, with the application of a field, the magnetic moments of a paramagnetic material can align towards the direction of the applied field. However, once the field is removed the moments regress to random orientations. All materials with unpaired electrons given a high enough temperature begin as paramagnets. It is only when the temperature reaches a certain temperature where the long-range ordering occurs. For ferromagnets and ferrimagnets this temperature is called the Curie temperature or $T_c$. For antiferromagnets it is referred as Neél temperature or $T_n$.

A material is considered a ferromagnetic when all the moments in a material are all aligned in one direction. Because these moments are permanent, they end up creating a magnetic field, which allows ferromagnetic materials to exert a magnetic force on other materials.

Antiferromagnets are materials that also exhibit long-range ordering similar to ferromagnetic materials. Except that antiferromagnets exhibit no net magnetization. This property is due to half of the magnetic moments offsetting the other half in terms of magnitude and direction.

A ferrimagnet is a magnetic material that also has a net magnetization. However, unlike

its ferromagnetic counterpart there are a minority population of magnetic moments that align in the opposite direction of the net magnetization.

The key factor in determining whether a magnetic material will order as a ferromagnetic or antiferromagnetic is based on the exchange interactions between all of the unpaired electrons. In general, the exchange interaction can be described by the Heisenberg Hamiltonian, **Equation (2.15)**.

$$H = -2\sum_{i>j} J_{ij} S_i \cdot S_j \tag{2.15}$$

Where $J_{ij}$ represents the exchange constant between the unpaired electrons of atom $i$ and atom $j$. $S_i$ and $S_j$ represent the atomic spin for atom $i$ and $j$. If $J > 0$ then the moments in the crystal have a ferromagnetic interaction, while for $J < 0$ indicates an antiferromagnetic interaction.

### 2.5.2 Magnetic Susceptibility

Magnetic susceptibility is an experimental technique that measures the response of the magnetic moments of a material towards an applied magnetic field such that the relationship is defined by **Equation (2.16)**.

$$\frac{M}{H} = \chi \tag{2.16}$$

Where $M$ is magnetization of the material, $H$ is the applied field, $\chi$ is the susceptibility of the material. Generally paramagnetic, ferromagnetic, antiferromagnetic, and diamagnetic materials all have a distinct response to an applied field. As a result, the shape of a magnetic susceptibility curve can be used as a first approximation in determining the type of magnetic ordering a material exhibits.

One issue with this type of analysis is that magnetic susceptibility measurements cannot differentiate a ferromagnet from a ferrimagnet. Due to the overall net magnetization within the sample, a ferrimagnet will behave similarly to a ferromagnet in magnetic susceptibility.

From magnetic susceptibility experiments we can find the effective moment, which is an estimate of the magnetic moment of a material when it is in the paramagnetic state. The effective moment or $\mu_{eff}$ can be found by plotting inverse susceptibility versus temperature and extrapolating a liner fit to the x-intercept. The equation of this linear fit can then be related to the Curie-Weiss law (**Equation (2.17)**.

$$\chi^{-1} = \frac{T}{C} - \frac{\theta_{CW}}{C} \tag{2.17}$$

Where $C$ is the Curie constant, $\theta_{CW}$ is the Curie-Weiss temperature and $T$ is temperature. The spin-only effective moment can then be found using **Equation (2.18)**.

$$\mu_{eff} = 2.828C^{1/2} \tag{2.18}$$

### 2.5.3 Magnetization Vs. Applied Field Saturation Analysis

If the material has net magnetization, then the strength of its moments can be obtained by directly applying a varying field at constant temperature until the magnetization saturates. Since magnetization is traditionally measured in election-magnetic units, these values can be converted into Bohr magneton units for comparison to the total moment obtained from neutron diffraction demonstrated by **Equation (2.10)**.

## 2.6 Density Functional Theory

Due to the electron repulsion term, solving Schrodinger wavefunctions for many-electron atoms is computationally too expensive. Instead, density functional theory proposes that all of the properties described by Schrodinger's equations can be represented by functionals, or functions that describe other functions as numbers. Since these functionals model the electron density of the atoms, they bypass the need for an electron repulsion term and reduce the number of variables needed for calculations, which reduces the computational cost.

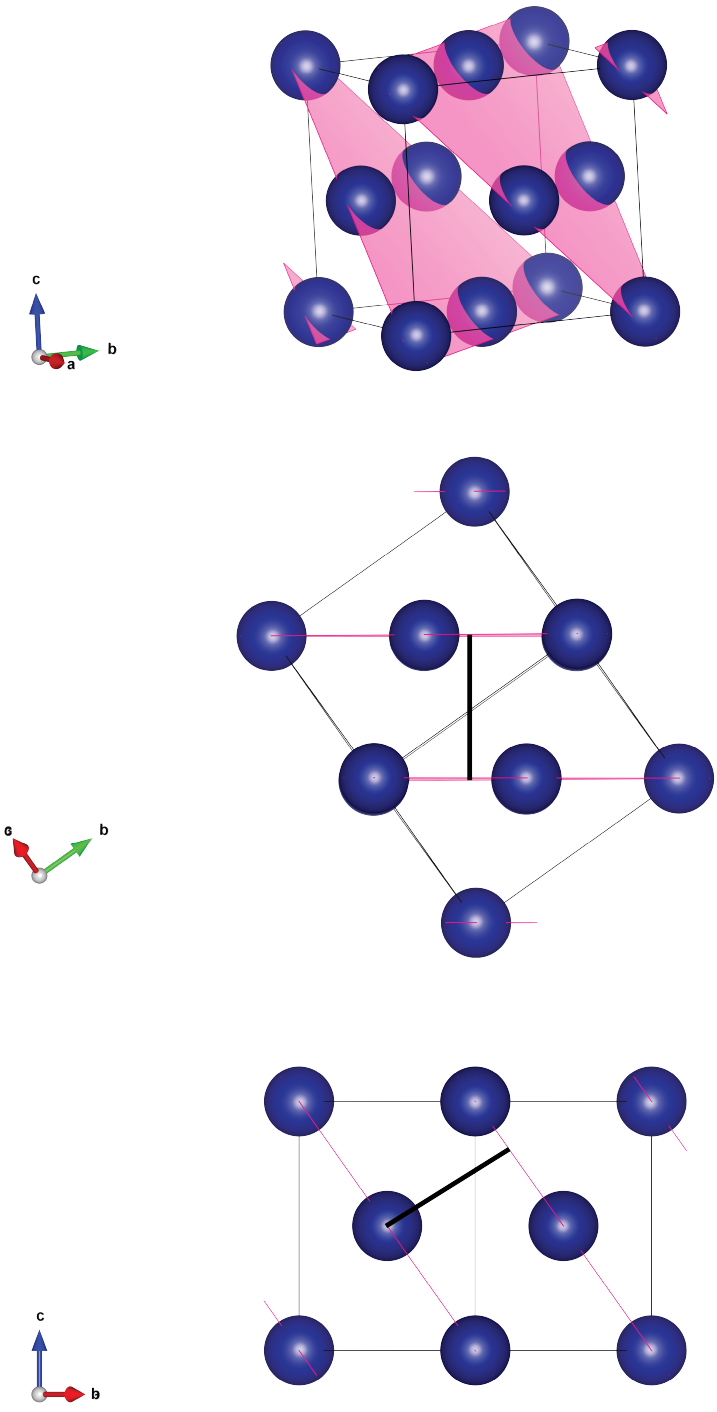



Figure 2.2: In pink, $\{111\}$ family planes shown in face-center-cubic Co crystal structure from various perspectives. Black bars represent the d-spacing between the $\{111\}$ planes.

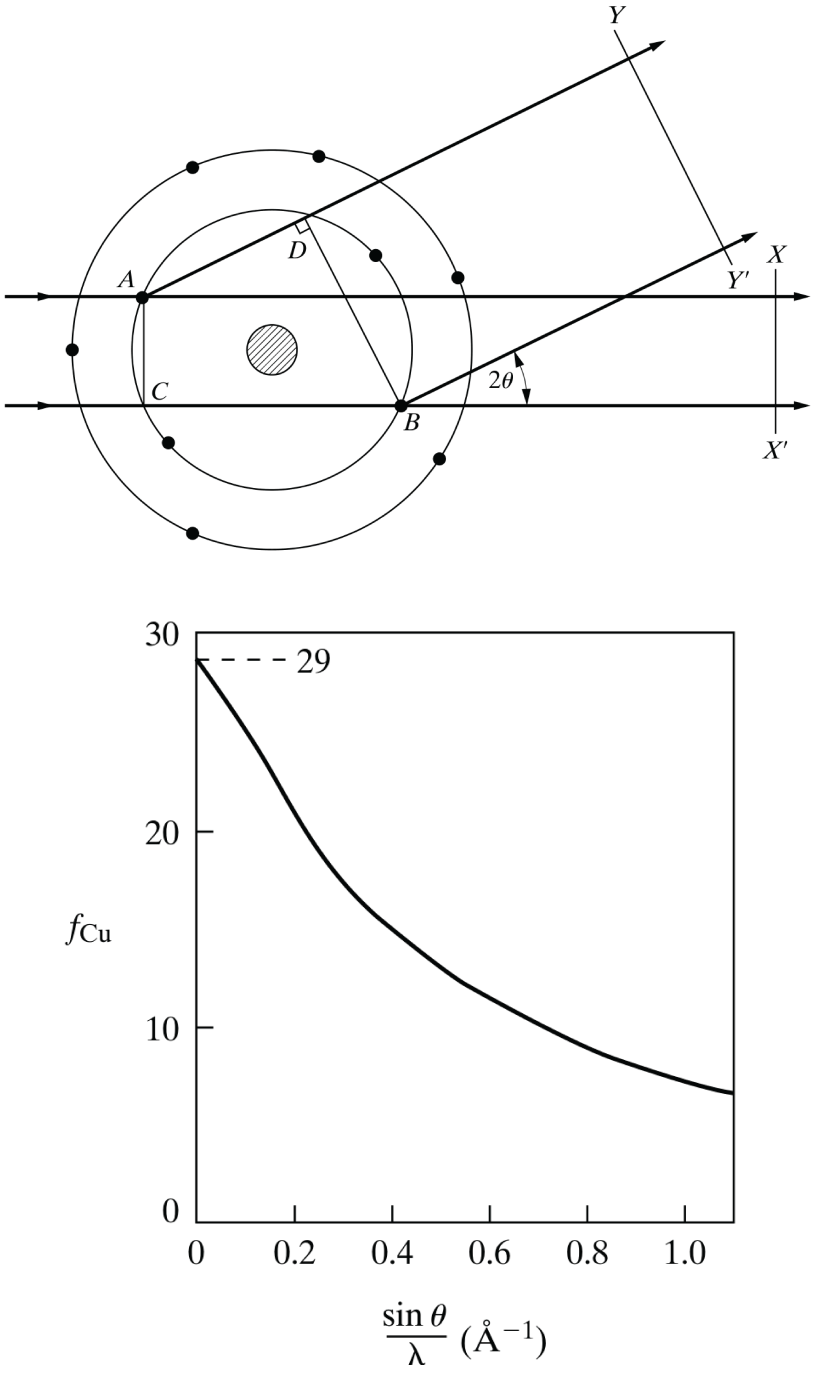



Figure 2.3: (Top) Example of x-ray scattering in different directions. Wave path $X'$ and $X$ represents scattering in the forward direction or special case where $f = Z$. Wavefront $Y$ and $Y'$ display x-rays scattered by some angle $2\theta$. (Bottom) The atomic scattering factor for copper. When the scattering angle is minimized $f$ is maximized.

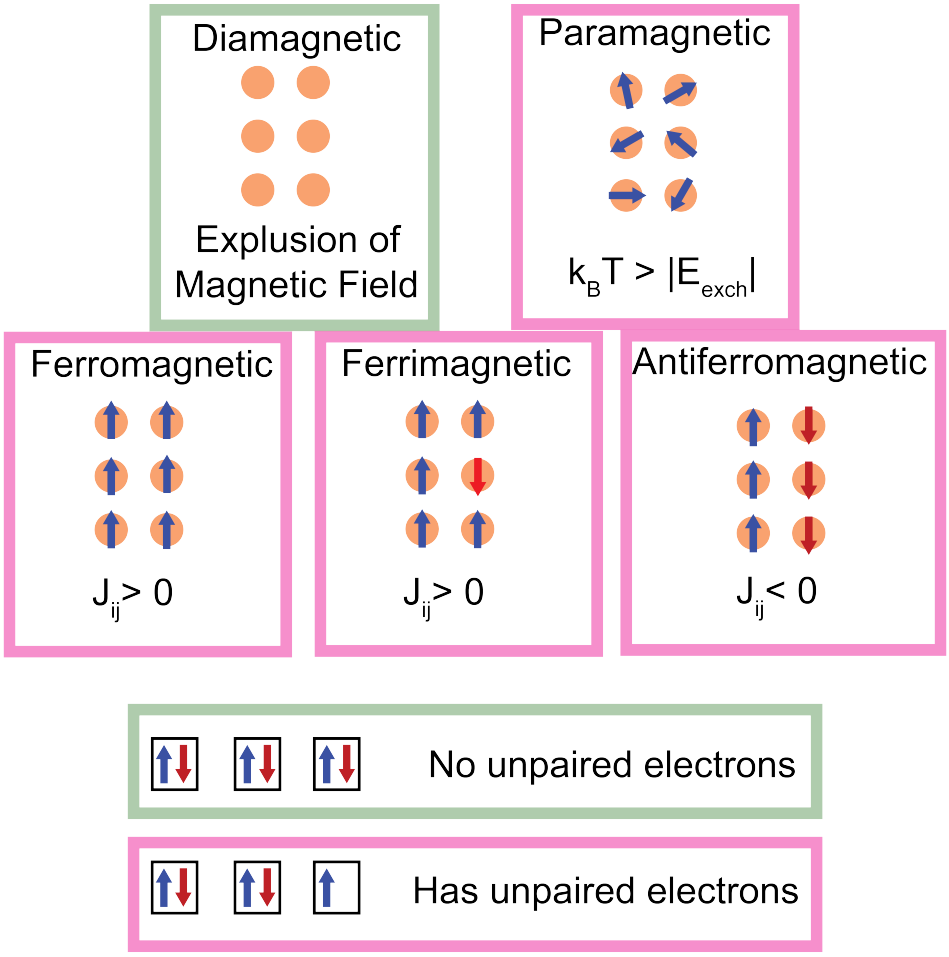



Figure 2.4: The type of magnetic order depends on if the material has elements with unpaired electrons in its configuration. If there unpaired electrons exist then for long range order to arise the the thermal energy of the system must be less than the magnitude of the exchange energy. Other wise paramagnetic behavior will be observed.

# Chapter 3: Ferrimagnetism in $Fe_3GaTe_2$

## 3.1 Introduction

The ability to increase computational power and to minimize energy consumption is of great importance. Spintronic devices made from 2D materials could possibly open a path to achieve these next-generation device requirements.[109]

Spintronics is a new design principle in electronic devices in which instead of using current, the spins of the electrons is what drives all the properties.[9,83,110,111] These devices typically involve heterostructures in which single layers of different compounds are stacked on top each other to generate properties, such as magnetoresistance.[112–116] The key requirement is that the magnetic material is able to be synthesized in two dimensions while simultaneously exhibiting ferromagnetic behavior above room temperature. If these devices are to be used in applications, then the magnetic properties need to exist at room temperature.

2D materials, or van der Waals, compounds are bulk materials that can be exfoliated into a single layer of atoms. If the bulk properties are preserved to the monolayer limit, then the vdW materials could potentially be a means to reduce the dimensions of every day applications such as catalytic reactions, wearable electronics, and memory devices.[9,109]

Historically, before FGaT there were very few, if any, above-room temperature vdW ferromagnets. In fact, the state-of-the-art 2D ferromagnet prior to FGaT was considered to be the $Fe_xGeTe_2$, where $x = 1 - 4.85$. Depending on the occupancy of the iron, the

Curie temperature, or $T_c$, ranges anywhere from 180 - 310 K.[117–122] Furthermore, at higher Fe occupancies $Fe_xGeTe_2$ exhibits complex magnetic behavior that could potentially make it difficult to exploit its room-temperature ferromagnetism.[123] In contrast, $Fe_3GaTe_2$ is known to have all its magnetic atoms co-aligned to the *c*-axis and exhibits a higher $T_c$ between 340 K - 380 K.[124] This transition temperature would make FGaT the highest temprature vdW ferromagnet currently reported to date.

Already many papers have reported using FGaT in various hetero-structure devices in the realm of magnetoresistance,[125,126] magnetic tunnel junctions,[127,128] spin-valve junctions,[129,130] which are necessary components to build spintronic devices for memory and computational applications. FGaT also exhibits skyrmions, which are vortex-like configurations that the magnetic moments organize themselves into. These configurations sometimes reach over hundreds of nanometers in length. Skyrmions represent some form of excitation. If these excitations can be controlled, then in principle skyrmions could be applied in computational devices.[68,99,131–133]

With all these exotic properties, it is no wonder that FGaT is considered a promising material for next-generation devices. As a result, fundamental investigation of FGaT is of great importance to elucidate the origin of these properties.

Ever since the discovery of FGaT in 2022, researchers have assumed that its crystal structure is identical to that of $Fe_3GeTe_2$ (FGeT).[124,134] The structure of FGeT is reported to be a hexagonal unit cell with a space group symmetry of $P6_3/mmc$ with two unique Fe sites.[135] Two-thirds of the Fe atoms have an oxidation state of $3^+$. $Fe^{3+}$ forms an octahedral comprised of three Te atoms and three Ge atoms. The rest of the Fe atoms have an oxidation state of $2^+$. $Fe^{2+}$ has a trigonal bipyramidal coordination geometry, where the three in-plane atoms are Ge and the two axial atoms are Te. Each lattice layer can be thought as 5-layer stack comprised of Te, $Fe^{3+}$, $Fe^{2+}$ and Ge, $Fe^{3+}$, and Te. Each of the atoms forms a hexagonal lattice.

If one makes a single crystal of FGeT and measures it on a conventional powder diffractometer, such as a Bruker D8, then sharp reflection are observed. These reflections are indexed as $(002l)$, specifically $(002), (004), (006)$ and $(0012)$. Ever since the first publication on FGaT by G. Zhang *et al.*[124] the standard for structure analysis was performing PXRD on single crystals of FGaT. They observed $(002l)$ reflections, particularly $(002), (004), (006)$ and $(0012)$. Considering that these reflections are the same as in $Fe_3GeTe_2$, it was assumed that $Fe_3GaTe_2$ has an identical structure to its germanium counterpart.

More recent work published by Li *et al.* and by Saha *et al.* report the observation of additional Fe sites and a space group symmetry of P3$m$1 instead of the previously reported P6$_3/mmc$.[99,131] Both authors' main argument for this new space group assignment depends on the observation of certain reflections such as odd $(00l)$ and $(h2hl)$ reflections where $l = 2n+1$, which should be systemically absent in $P6_3/mmc$ symmetry.

The implications of the aforementioned result are substantial, because a change in crystal symmetry can result in a change in magnetic space group symmetry. Furthermore, it is not clear whether $Fe_3GaTe_2$ is ferromagnet or a ferrimagnet because magnetic susceptibility cannot differentiate between the two types of magnetic ordering. These questions, among others, can be resolved through neutron diffraction, which is the primary purpose of this chapter.

We have grown single crystals of $Fe_3GaTe_2$ and report a crystal structure with P6$_3/mmc$ symmetry as we were not able to observe the symmetry breaking reflections in a statistically relevant way that Li *et al*. and Saha *et al*. reported. Furthermore, we observe a third iron site that is placed within the vdW gap. This new site has an occupancy near 7-10 %. We also synthesized polycrystalline $Fe_3GaTe_2$ and performed powder diffraction. We found that our crystal structure solution from single-crystal diffraction fits the PXRD diffraction data better compared to the 2-site $Fe_3GeTe_2$ crystal structure. Using the GEM instrument at the ISIS Neutron and Muon Source, we were able to observe a few magnetic reflections

using neutron diffraction. Our Rietveld refinements suggests that the magnetic space group is $P6_3/mm'c'$. This magnetic space group requires a magnetic moment on all Fe sites. The new magnetic moments on the new interstitial Fe site was found to be anti-parallel to the moments of the other two Fe sites. Thus, based on our result we claim that $Fe_3GaTe_2$ is a ferrimagnet. To further investigate the origins of the high Curie temperature, we performed DFT calculations with our $Fe_3GaTe_2$ crystal solution with and without the existence of the interstitial site. We found that the ferrimagnetic state is 66 meV lower than the ferromagnetic state. Additionally, the mixing of 3d orbitals from the interstitial Fe results in greater amount of DOS near the Fermi level, which result in more spin-polarization which raises the $T_c$.

## 3.2 Experimental Methods

### 3.2.1 Synthesis

**Synthesis of $Fe_3GaTe_2$ single crystals:** Single crystals were grown from a self-flux growth method reported in previous reports.[124] First, Ga pellets (Thermofisher, 99.99%) were placed inside the quartz tube. Next, Fe powder (Alfa Aesar, 99.5%) and Te powder (Sigma-Aldrich, 99.8%) were mixed and ground in a mortar and pestle in a 1:1:2 ratio inside a Ar-filled glove box and then placed inside the quartz ampule. The ampule was heated to 1000 $^\circ$C in 3 hours. Next, the ampoule dwelled at 1000 $^\circ$C for 24 hrs. Afterwards, the sample was quenched to 880 $^\circ$C within 1 hr followed by a slow cool to 780 $^\circ$C at a rate of 1 $^\circ$C/hr. Then, the sample was quenched. A large molten, metallic ingot was extracted from the ampule. This ingot was observed to be magnetic in ambient conditions, which is a sign that FGaT has grown within the rock sample. However, the FGaT was mixed in with the rest of rock, which is mostly comprised of $Ga_2Te_3$. To isolate $Fe_3GaTe_2$ from the ingot, a razor blade was carefully applied to scrape some flakes on the more metallic flat

surfaces on the ingot. Additionally, we found that tapping the ingot with a glass rod also can separate crystals from the ingot. The flakes collected exhibited a size less than $0.5 \times 0.5$ $mm^2$.

**Synthesis of polycrystalline $Fe_3GaTe_2$:** Powder $Fe_3GaTe_2$ was synthesized as follows: GaTe was synthesized in an ampule prepared in an Ar-filled glovebox at 900 $^\circ$C for 3 days. The ampule had one part Ga (Thermofisher, 99.99%) and one part Te (Sigma-Aldrich, 99.8%) with an additional 0.1-0.3% of Ga was added to ensure the production of GaTe instead of $Ga_2Te_3$ based on the binary phase diagram. Afterwards, inside an Ar filled glovebox, one part of GaTe, one part Te and three parts Fe (Alfa Aesar, 99.5%) was mixed a mortar and pestle and placed in an ampule. The reaction was heated to 700 $^\circ$C with 1-2 hours and welled at that temperature for 6 days. The ampule was then allowed to naturally cool in the furnace before extraction.

### 3.2.2 X-ray Diffraction

**Single crystal X-ray diffraction and structure refinement:** Single crystals of $Fe_3Ga_1Te_2$ were selected and measured on a Bruker D8 Venture with Photon III diffractometer with a Mo source. The crystal was kept at 250 K during data collection. The integral intensity was corrected for absorption using SADABS software. The resulting minimum and maximum transmission are 0.065 and 0.808 respectively. The structure was solved with the ShelXT program using least-square minimization. Zero constraints were used in the refinement.

**Powder X-ray diffraction and structure refinement:** X-ray diffraction was performed on a Bruker D8 Advance diffractometer with a Cu K$\alpha$ source at ambient conditions. For the Rietveld refinement, GSAS-II refinement software was used. The CIF file used for the $Fe_3GaTe_2$ phase was from our structure solution derived from the single crystal x-ray

diffraction (SCXRD) experiment. THe CIF file used for FeTe was obtained from the ICSD (Coll. Code: 180602). For the refinement only one constraint was used and it was forcing the thermal parameters between Fe1 and Fe3 to be equivalent to each other.

### 3.2.3 Neutron Diffraction

Neutron powder diffraction (NPD) was performed at the GEM Instrument at the ISIS Neutron and Muon Source. Data was collected through six banks ranging from 0.4 Å to 25 Å. Here two sample environments were used. In the cryo-environment setting, our samples were measured at 1.5 K, 50 K, 100 K, and 150 K. Each run was measured for 3 hours. For the ambient environment the low temperature furnace was used to measure FGaT from 298 K to 473 K in 25 K increments. Once again, each run lasted for 3 hours. The sample mass for this experiment was about 6 grams. Collected data was analyzed with GSAS-II refinement software. A combined refinement of Bank 2, 4, and 6 was used as the basis of our Rietveld refinement. For this refinement the only constraint applied was to make the the thermal parameters of both Fe1 and Fe3 equivalent.

### 3.2.4 Structural Refinements

For our Rietveld refinement this general approach was used. First, a Le Bail fit was performed to calculate the initial lattice parameters and background fit for each experiment. The Le Bail fit was then used to model any possible micro strain exhibited from the crystal domains. These initial values were then used in the subsequent Rietveld refinement. From this point the first parameter refined was the phase weight of the main FGaT and impure FeTe phases, followed by preferred orientation, then atomic positions, and later isotropic atomic displacement parameters. Fe 1 and Fe 3 were forced to have equivalent $U_{eq}$ or thermal parameters. Afterwards, occupancies were then refined followed by a refinement

involving all the variables until convergence was achieved. For the measurements at or under 323 K. Atomic positions and occupancies were fixed to values used at 348 K. For obtaining magnetic space groups the k-SUBGROUPMAG function from the Bilbao crystal server was used.

### 3.2.5 Measurement of Bulk Magnetic Properties

The magnetic properties of polycrystalline FGaT were studied with a Microsense© EZ 7 vibrating sample magnetometer. Magnetic susceptibility measurements were performed from 300 K to 450 K with a 1000 Oe field. Additional magnetic susceptibility measurements were performed utilizing a Quantum Design MPMS©3 SQUID from 2.5 K to 300K with ZFC and FC at 100 Oe. Magnetization measurements were performed on FGaT at 300, 330, 350, and 380 K with an applied magnetic field from -20 to 20 kOe with a Microsense© EZ 7 VSM.

### 3.2.6 Energy Dispersive Spectroscopy

The chemical composition of $Fe_3GaTe_2$ powders and single crystals were measured using a Hitachi SU-70 Schottky FEG-SEM equipped with the Bruker energy dispersive X-ray spectroscopy (EDS, XFlash(6/60).

### 3.2.7 DFT Calculations

First-principles calculations were performed using the open-source software package QUANTUM ESPRESSO,[136] based on periodic plane-wave density functional theory (DFT).[137–139] The Perdew–Burke–Ernzerhof (PBE) generalized gradient approximation (GGA) was adopted, along with the vdW interaction correction in Grimme's DFT-D2 method (with a global scaling factor $S_6 = 0.5$) for all calculations. GBRV ultrasoft pseudopotentials were used

to describe all atoms, with a plane-wave basis cutoff of 40 Ry for the primitive bulk structures. Lattice optimization calculations were performed using a $6 \times 6 \times 6$ Monkhorst–Pack k-point grid.[140] All self-consistent calculations were carried out with a convergence criterion of $1 \times 10^{-7}$ eV and a force tolerance of 1–5 meV/Å per atom. The optimized lattices were then used for band structure and projected density of states (PDOS) calculations, employing a $10 \times 10 \times 10$ Monkhorst–Pack k-point grid.

## 3.3 Results and Discussion

### 3.3.1 Structural and Elemental Characterization

We have performed powder X-ray diffraction (PXRD) on single crystals of $Fe_3GaTe_2$ (**Figure 3.1**). Just like previous reports, we observe several $(002l)$ reflections specifically, $(002), (004), (006)$. However, special care must be taken to extract a FGaT crystal from the $Ga_2Te_3$ because this impurity can easy attached it self to the FGaT crystals. If $Ga_2Te_3$ is found on a FGaT crystal, then a reflection at $26(2\theta)$ (**Figure 3.1**) will be seen. By tapping the flux rock into pieces with a glass rod and then taking a pair of tweezers to pluck the FGaT crystals from the self-flux rock, a few tiny $Fe_3GaTe_2$ crystals with very little $Ga_2Te_3$ can be obtained.

Additionally energy dispersive X-ray spectroscopy was performed on these crystals. As displayed by **Figure 3.2**, certain sections of the crystal were close to the ideal ratio of the 3:1:2 ratio of $Fe_3GaTe_2$, whereas other parts of the crystals contained $Ga_2Te_3$. This result highlights the importance of having good mechanical techniques to physically separate the flux residue from the main phase crystal.

**Table 3.1** displays the finalized crystal solution extracted from single crystal diffraction data. According to our data we observed that $Fe_3GaTe_2$ crystallizes with a space group symmetry of $P6_3/mmc$ with lattice parameters $a = b = 4.0723(3)$, and $c = 16.0928(15)$.

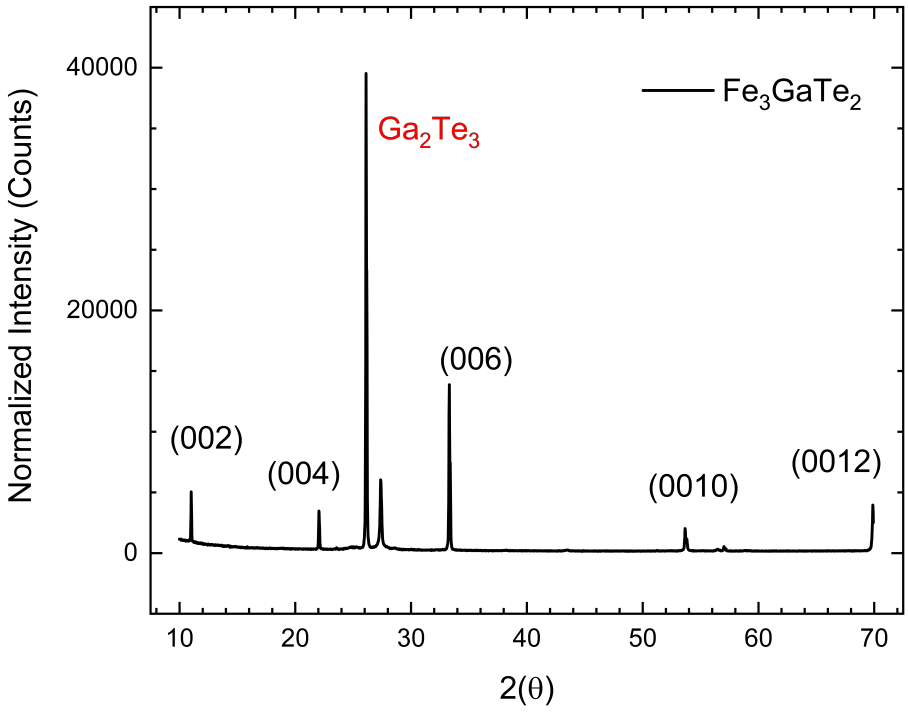



Figure 3.1: PXRD of single crystal $Fe_3GaTe_2$. $\lambda = 1.54$ Å. Without proper mechanical separation residual $Ga_2Te_3$ will always be found.

Compared to FGeT, the FGaTe the unit cell has contracted in the *c*-direction and elongated in the *ab* direction. There are five Wyckoff sites, three for Fe, one for Ga and one for Te. The specific coordinates and occupancies of these sites can be seen in **Table 3.2** along with a visual representation in **Figure 3.3**.

As one can see our structure model proposes that there three Iron sites. Two of the iron sites are analogous to the two Fe sites found in $Fe_3GeTe_2$. The third Fe site, however, is located between the vdW gaps formed between the tellurium atoms. According to our structure solution, this third site is about 7% occupied, which suggest that about 2-3% of all Fe atoms occupy this interstitial position. This Fe3 site also forms an octahydral

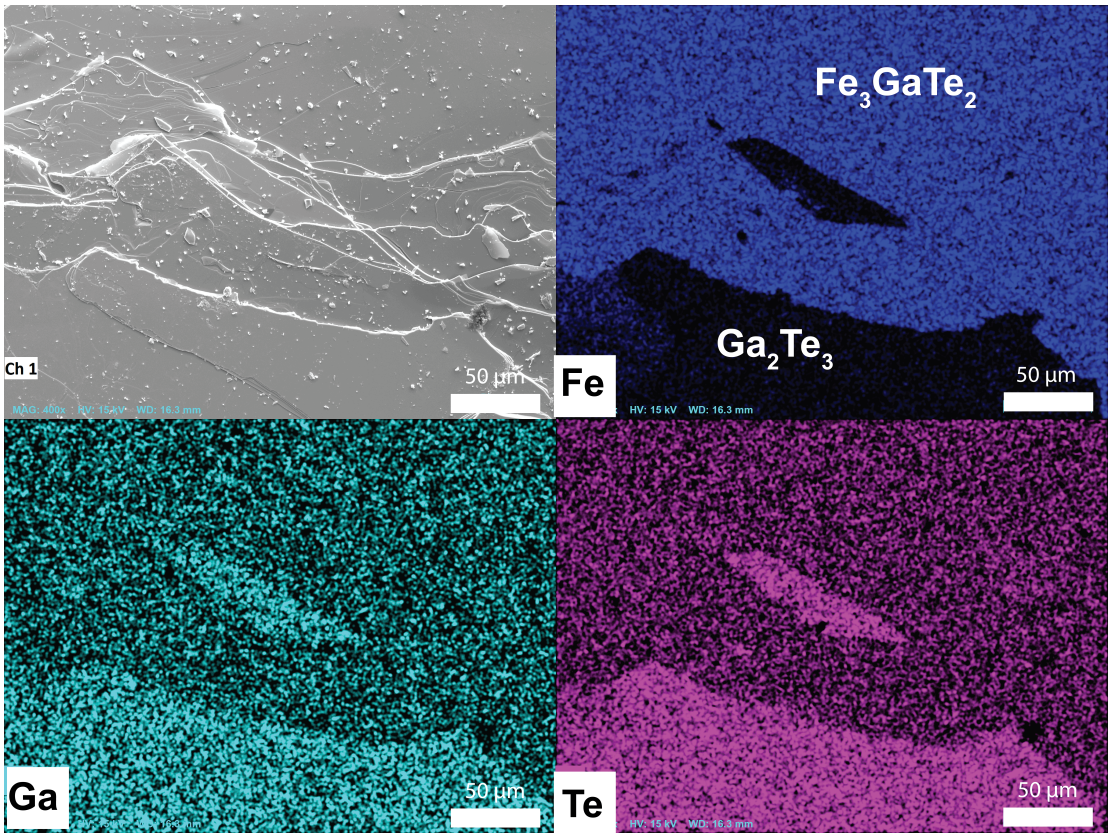



Figure 3.2: EDX demonstrates that single crystals have both $Fe_3GaTe_2$ and some $Ga_2Te_3$ residue.

coordination with its Te neighbors.

If we sum up the occupancies of each site we obtain a molecular formula of $Fe_{2.97}Ga_{0.93}Te_2$. Similar to what Li *et al.* and Saha *et al.* reported, a slight vacancy of Fe atoms was observed in our crystal solution. Moreover, we found that is that the Ga site is only 93% occupied. We speculate that these vacancies could indicate that there is some form of complex charge balance behavior within the FGaT system. From previous literature results, we know that $Fe_3GeTe_2$ has $Fe^{2+}$ and $Fe^{3+}$ oxidation states. In contrast, XPS from Zhang *et al.* suggest that the oxidation states is 0 for Fe1 and $3^+$ for Fe2.[124]

As previously mentioned, previous structure analysis done by Li *et al.* and Saha *et al.* propose that the actual crystal symmetry of $Fe_3GaTe_2$ is P3$m$1.[99,131] They cite that the ob-

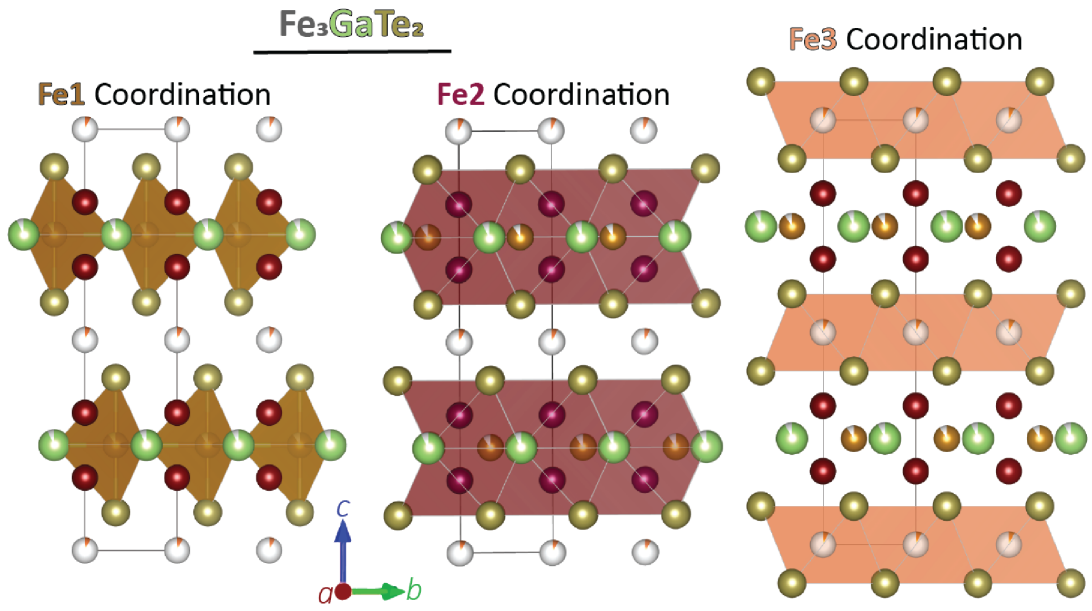



Figure 3.3: Crystal structure of $Fe_3GaTe_2$. There are three different coordination geometries among the three Fe sites. Fe1 and Fe2 are the interior sites while Fe3 is an interstitial site.

servation of systemically absent reflections such as odd $(00l)$ and $(h2hl)$ reflections where $l = 2n + 1$, warrant the change in space group symmetry. Our single crystal diffraction data suggests otherwise. According to our data, while we were technically able to observe reflections that ar systemically absent, the ratio between intensity and error of these symmetry-breaking reflections was not sufficient to decisively suggest that these reflections were distinct from background noise. **Table 3.3** displays a table of systemic absence exceptions. In this table, two columns are of interest, $6_3$ and - -$c$. These columns represent the amount of reflections that do not match a specific symmetry with the former representing the $(00l)$ reflection and the latter representing $(hhl)$ reflections. According to our data, the amount of reflections that have a sufficient intensity to error ratio is much smaller than the reflections that follow $P6_3/mmc$ symmetry. This result implies that $P6_3/mmc$ symmetry Fits our diffraction data than $P3m1$.

One of the potential reasons why our results are different that the literature's could be

Table 3.1: Selected parameters from single crystal X-ray diffraction of $Fe_3GaTe_2$.

| | |
|---|---|
| Empirical formula | $Fe_{2.97(2)}Ga_{0.93(1)}Te_2$ |
| Formula weight (g/mol) | 485.84 |
| Space group | $P6_3/mmc$ |
| $a$(Å) | 4.0724(3) |
| $b$(Å) | 4.0724(3) |
| $c$(Å) | 16.0928(15) |
| $\alpha$(°) | 90 |
| $\beta$(°) | 90 |
| $\gamma$(°) | 120 |
| Crystal system | Hexagonal |
| Volume (Å$^3$) | 231.13(4) |
| Calc. density (g/cm$^{-3}$) | 6.981 |
| Radiation | MoK$\alpha$ ($\lambda$=0.71073Å) |
| Crystal size (mm$^3$) | 0.21 × 0.18 × 0.01 |
| 2$\theta$ collection range (°) | 5.062 to 59.916 |
| Index ranges | -5 $\leq h \leq$ 5, -5 $\leq k \leq$, 4, -22 $\leq l \leq$, 22 |
| Reflections collected | 2096 |
| Independent reflections | 162 |
| $F$(000) | 420.0 |
| $R_1$ (all data) | 0.0319 |
| $wR_2$ (All Data) | 0.0694 |
| Goodness of fit | 1.2 |
| Temperature (K) | 250 |

Table 3.2: Wyckoff site labels with fractional atomic coordinates, equivalent isotropic displacement parameters, and occupancies (Å$^2\times10^3$) for single crystal FGaT. Ueq is defined as 1/3 of the trace of the orthogonalized $U_{IJ}$ tensor.

| **Atom** | $x$ | $y$ | $z$ | $U_{eq}$ | **Occ.** |
|---|---|---|---|---|---|
| **Fe1** (2$d$) | 0.333333 | 0.666667 | 0.75 | 10.1(8) | 0.90(1) |
| **Fe2** (4$e$) | 0 | 0 | 0.3270(1) | 10.7(4) | 1 |
| **Fe3** (2$a$) | 0 | 0 | 0.5 | 10.7(4) | 0.070(8) |
| **Ga1** (2$c$) | 0.333333 | 0.666667 | 0.25 | 18.7(8) | 0.93(1) |
| **Te1** (4$f$) | 0.333333 | 0.666667 | 0.5907(1) | 12.2(3) | 1 |

Table 3.3: Systemic absence exceptions. Column $6_3$ shows statistic for reflections that do not match $6_3$ screw axis, $(00l)$, $l \neq 2n$. Column –c shows statistic for reflections that do not match –c axis (HHL), L not-equal to 2n. N = number of reflections; I = Intensity; $\sigma$ = error

| | **61/65** | **62=31** | $6_3$ | **-c-** | **–c** |
|---|---|---|---|---|---|
| $N$ | 58 | 49 | 30 | 564 | 244 |
| $N\ I > 3\sigma$ | 34 | 30 | 8 | 434 | 38 |
| $< I >$ | 15.2 | 17.9 | 0.2 | 27.3 | 0.2 |
| $< I > / \sigma$ | 10.8 | 12.3 | 2.0 | 16.4 | 1.6 |

through sample preparation. As previously mentioned, the typical way to obtain $Fe_3GaTe_2$ single crystal involves using mechanical force to separate single crystals from the GaTe flux. The strain introduced by these techniques could potentially deform the extracted single crystals.

Furthermore, its possible that what we observe in place of the systemically absent reflections are actually satellite reflections. Satellite reflections typically have much lower intensity than their parent reflections. This drop intensity would mirror our result in **Table 3.3**. In our data the intensity to error ratio for those symmetry breaking reflections are much smaller than those for other reflections.

Finally, our structure has both Fe and Ga vacancies, whereas the other have reported only Fe vacancies in their experiments. A difference in Ga occupancies can affect the structure factors of some *hkl* reflections, hence why others may have reported more intense symmetry-breaking reflections.

### 3.3.2 Bulk Magnetic Property Measurements

Although magnetic susceptibility measurements have been performed on $Fe_3GaTe_2$ in detail several times,[95,96,124,141] we have performed the same measurements on our samples to provide evidence that our $Fe_3GaTe_2$ samples are similar to other reported $Fe_3GaTe_2$

experiments.

**Figure 3.4** displays the magnetic susceptibility of powder $Fe_3GaTe_2$ from a vibrating sample magnetometer. This sample was measured from 100 K to 450 K with an applied field of 1000 Oe. This experiment resulted in a sudden large increase in susceptibility near 340 K. This large increase is indicative of ferromagnetic behavior. Additionally, results from the SQUID magnetometer, (**Figure 3.5**), reveal splitting between zero-field cooling and field cooling measurements, which provides further evidence that $Fe_3GaTe_2$ has ferromagnetic-like behavior.

Additionally, **Figure 3.6** our magnetization measurements also reveal that $Fe_3GaTe_2$ is a ferromagnetic. We find that the field coercivity is near 100 Oe at 300 K which classify FGaT a as hard-type ferromagnet. We also note that the hysteretic behavior begins to appears below 340 K.

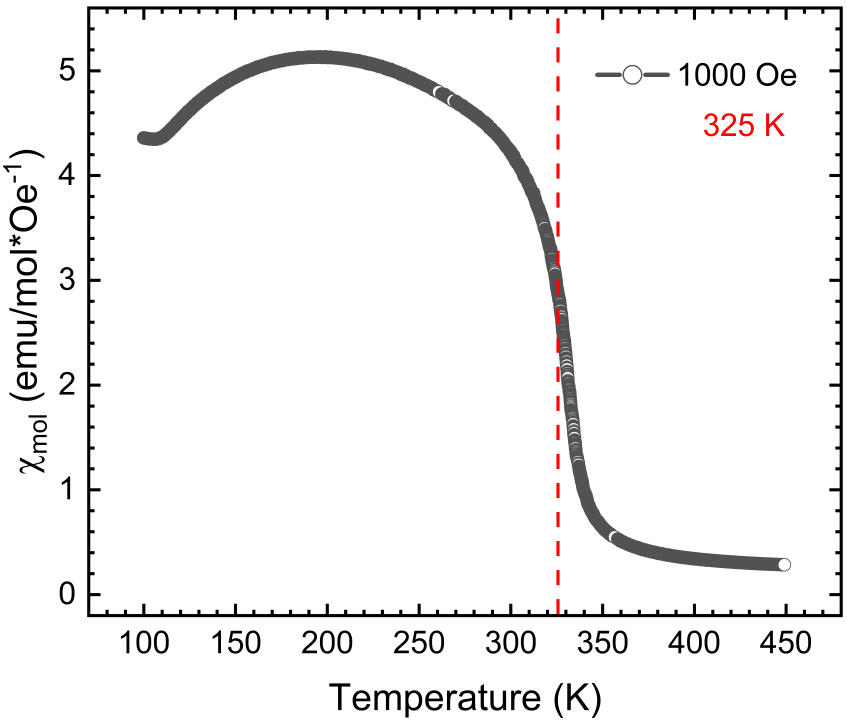



Figure 3.4: Magnetic susceptibility of polycrystalline FGaT. A vibrating sample magnetometer was used to perform this experiment. Ferromagnetic-like behavior was observed near 320 K - 330 K. 325 K is indicated with a dashed line for convenience.

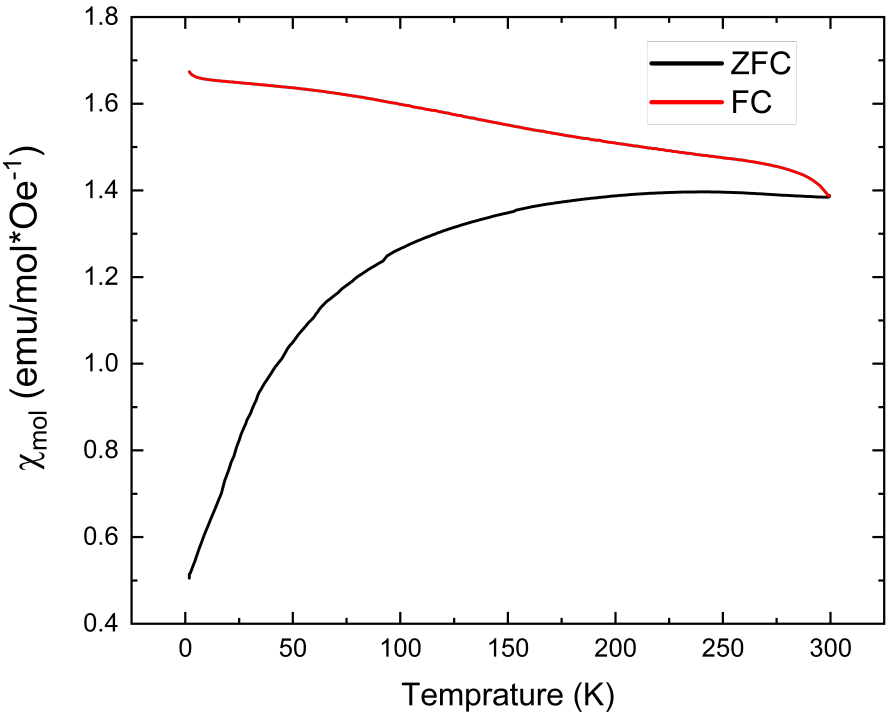



Figure 3.5: Magnetic susceptibility of polycrystalline FGaT using the SQUID instrument. ZFC and FC splitting at saturation was observed. These observations are indicative of ferromagnetic behavior.

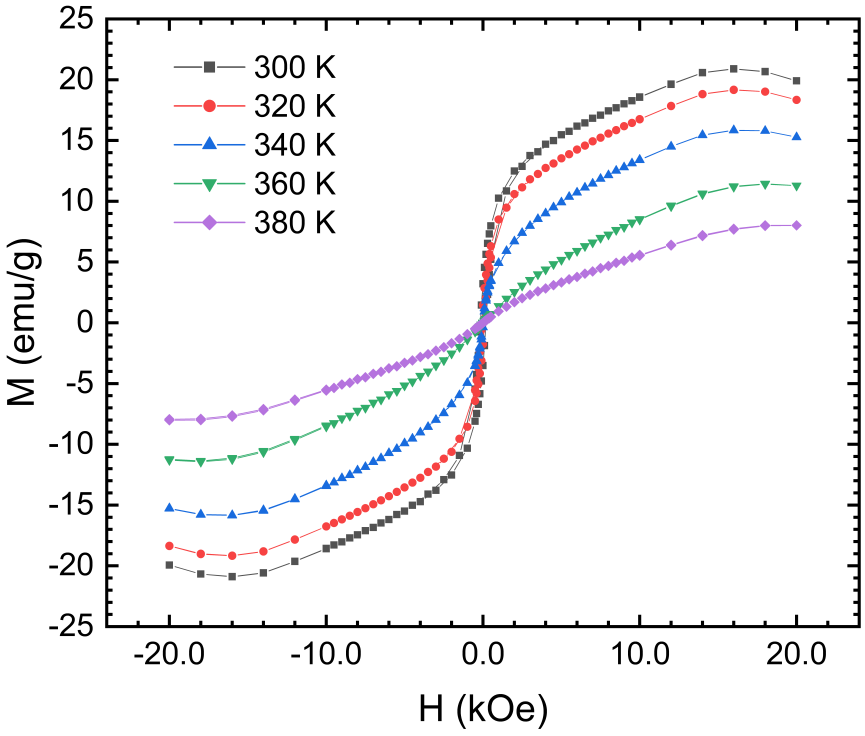



Figure 3.6: Magnetization vs. applied field curve of polycrystalline FGaT. Hysteresis was observed up until 340 K. The coercive field measured was near 100 Oe near 300 K

### 3.3.3 Magnetic Structure Determination and Evidence of Ferrimagnetic Behavior in $Fe_3GaTe_2$

**Table 3.4** and **Table 3.5** demonstrates the extracted structural parameters from our Rietveld refinement using the data measured at 348 K. Overall, our crystal solution from x-ray diffraction aligns with the neutron diffraction data. The biggest notable difference are the occupancies for each atomic position. Starting with the interstitial site, NPD states that the Fe3 site has an occupancy near 0.1 which is larger than the fractional occupancy found in our single crystal structure model. Meanwhile, the occupancy for Ga decreased to 0.91 from 0.93. Tellurium occupancy also experienced a drop to 0.97 compared to full occupancy in the single crystal data.

Regarding phase purity, our Rietveld refinement suggests that FeTe can be found with about an 8% by weight phase fraction in our sample. Although FeTe is antiferromagnetic below 75 K, its magnetic reflection is far from the magnetic reflections from $Fe_3GaTe_2$ and

Table 3.4: Selected parameters from neutron powder diffraction diffraction of $Fe_3GaTe_2$.

| | |
|---|---|
| Empirical Formula | $Fe_{2.89}Ga_{0.91}Te_{1.94}$ |
| Space Group | $P6_3/mmc$ |
| Crystal System | Hexagonal |
| $a$(Å) | 4.09986(3) |
| $b$(Å) | 4.09986(3) |
| $c$(Å) | 16.2141(2) |
| $\alpha(^\circ)$ | 90 |
| $\beta(^\circ)$ | 90 |
| $\gamma(^\circ)$ | 120 |
| Volume (Å$^3$) | 236.03(4) |
| Instrument | GEM |
| Sample mass (grams) | 6 |
| $wR_2$ (All Data) | 0.07145 |
| Temperature (K) | 348 |

Table 3.5: Wyckoff site labels with fractional atomic coordinates, equivalent isotropic displacement parameters ($Å^2 \times 10^3$), and occupancies for powder FGaT.

| **Atom** | $x$ | $y$ | $z$ | $\mathbf{U}_{eq}$ | **Occ.** |
|---|---|---|---|---|---|
| **Fe1** (2$d$) | 0.333333 | 0.666667 | 0.75 | 10.3(6) | 0.86(1) |
| **Fe2** (4$e$) | 0 | 0 | 0.3275(1) | 12.0(4) | 0.96(1) |
| **Fe3** (2$a$) | 0 | 0 | 0.5 | 10.3(6) | 0.11(1) |
| **Ga1** (2$c$) | 0.333333 | 0.666667 | 0.25 | 19.1(1) | 0.91(1) |
| **Te1** (4$f$) | 0.333333 | 0.666667 | 0.5908(2) | 11.4(7) | 0.97(1) |

should have a minimal impact in the analysis.[142–145]

Although we measured neutron data up to 473 K, we found that magnetic reflections began to appear below 348 K, specifically near the 1.7 $Å^{-1}$ – 2.2 $Å^{-1}$ region. There are two reflections of interest, $(100)$ and $(102)$. As demonstrated in (**Figure 3.7**) these two reflections have an increase in intensity as temperature decreases. This correlation suggest that $(100)$ and $(102)$ are magnetic reflections. Of the two magnetic reflections, $(100)$ has a sharper increase in intensity. At first glance, this observation suggests that the direction of the magnetic moments is parallel to the $c$-axis. Additionally, because no additional peaks where found, the $\overrightarrow{k}$-vector for this compound is $[000]$, which implies that the magnetic unit cell is identical to the nuclear unit cell.

The GEM instrument is designed to collect radiation scattering in six distinct banks. Each bank is specialized in collecting scattering events from different regions in a sample. What we found was that the data collected in bank 2 offered the best information regarding the dimensions of the unit cell. Meanwhile, bank 4 was the optimal perspective for observing the magnetic reflections. Lastly, bank 6 was the best for analyzing occupancy, atomic positions and their thermal parameters. Thus, a combined Rietveld refinement among the three data sets was performed for the subsequent temperatures, 348 K, 323 K, 298 K, 150 K, and 1.5 K. The data for these diffraction experiments is displayed in **Figures 3.8** - **3.22**.

Using the 1.5K data as the basis for the Rietveld refinement, we found through repre-

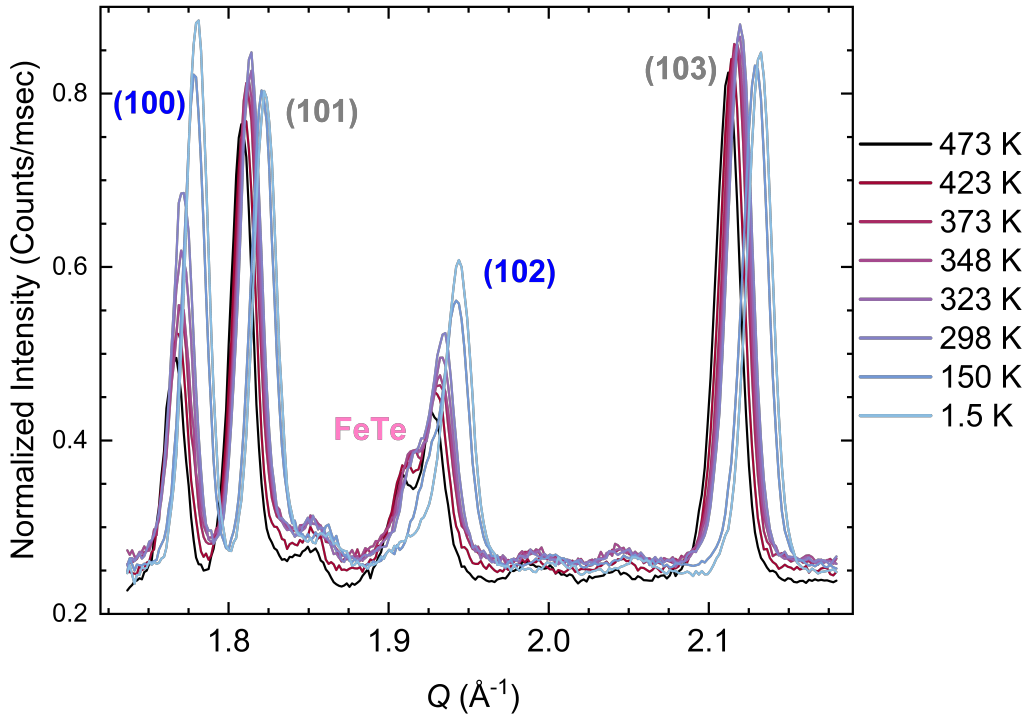



Figure 3.7: Select Q range of a temperature dependent NPD experiment. Key magnetic reflections are labeled in blue. Non magnetic reflections are labeled in grey. The reflection labeled by an asterisk is reflection from FeTe.

sentational analysis that $P6_3/mmc$ can exhibit eight possible magnetic space groups. However, if all three Fe sites have a magnetic moment then representational analysis predicts that only one magnetic space group can be chosen, which is $P6_3/mm'c'$. To test if all three Fe sites contained a moment we decided to run a Rietveld refinement for two magnetic structure models using our nuclear structure from the 348 K data. One model had only had magnetic moments on Fe1 and Fe2 atoms. The second model allowed magnetic moments to be hosted on all Fe sites. What we observed was that the model with no magnetic moment for the Fe3 interstitial site has great difficulty in contributing to the intensity of the $(100)$ and $(102)$ reflections. In contrast, the 3-site magnetic model fit was much closer to

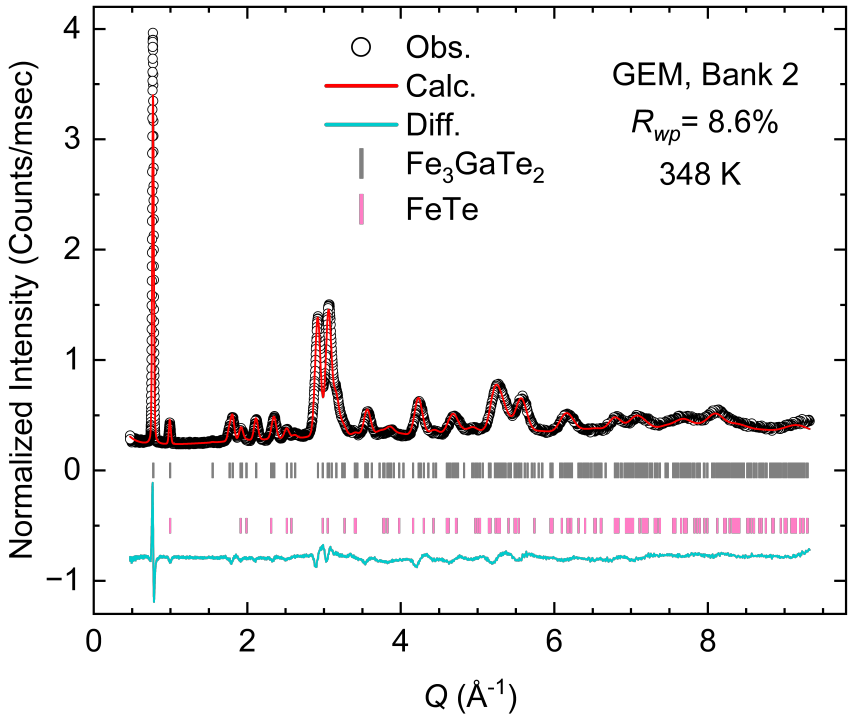



Figure 3.8: Rietveld refinement of $Fe_3GaTe_2$. Data were collected at 348 K utilizing bank 2 from the GEM instrument.

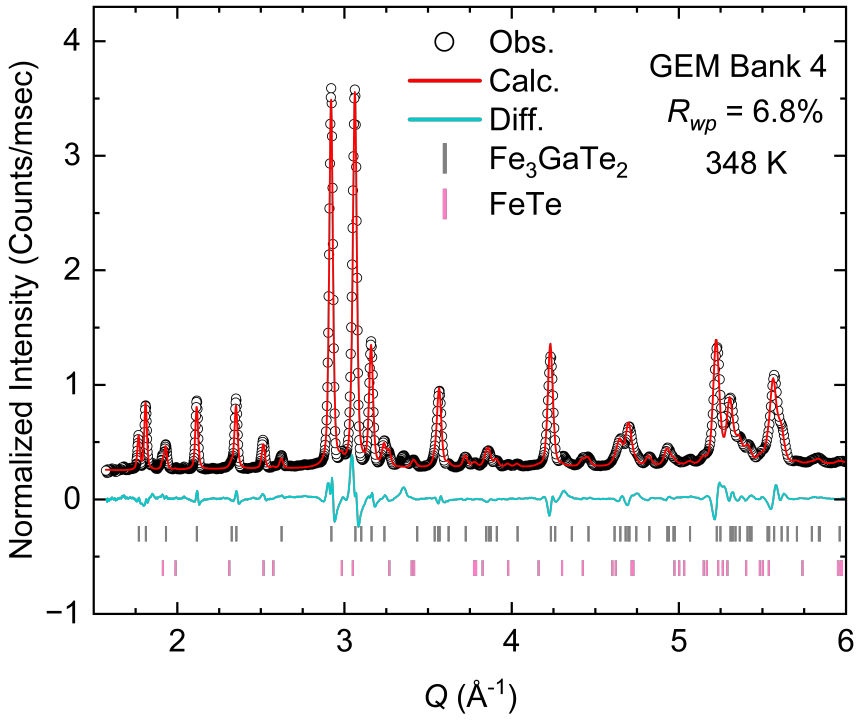



Figure 3.9: Rietveld refinement of $Fe_3GaTe_2$. Data were collected at 348 K utilizing bank 4 from the GEM instrument.

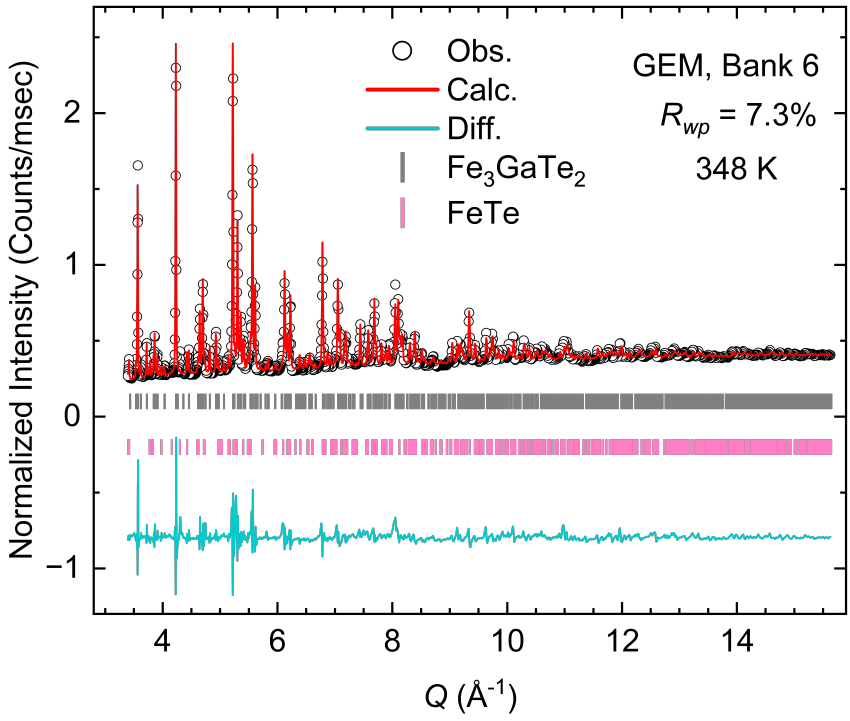



Figure 3.10: Rietveld refinement of $Fe_3GaTe_2$. Data were collected at 348 K utilizing bank 6 from the GEM instrument.

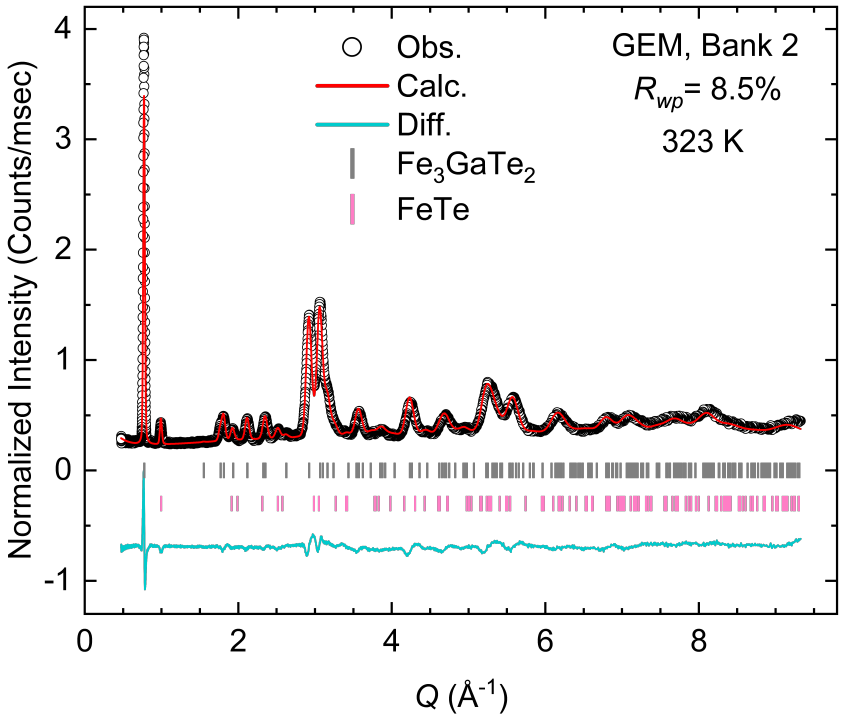



Figure 3.11: Rietveld refinement of $Fe_3GaTe_2$. Data were collected at 323 K utilizing bank 2 from the GEM instrument.

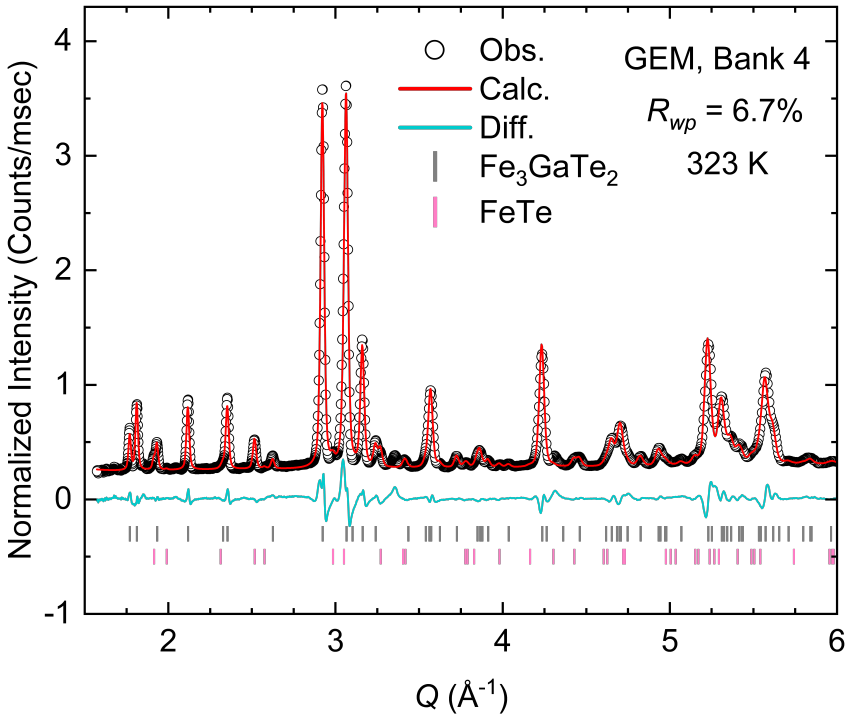



Figure 3.12: Rietveld refinement of $Fe_3GaTe_2$. Data were collected at 323 K utilizing bank 4 from the GEM instrument.

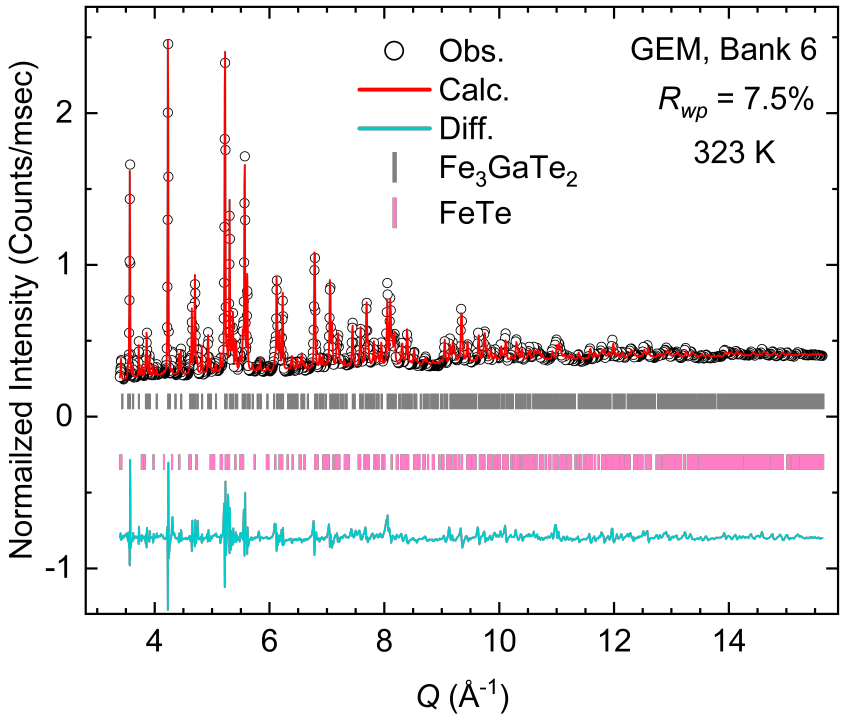



Figure 3.13: Rietveld refinement of $Fe_3GaTe_2$. Data were collected at 323 K utilizing bank 6 from the GEM instrument.

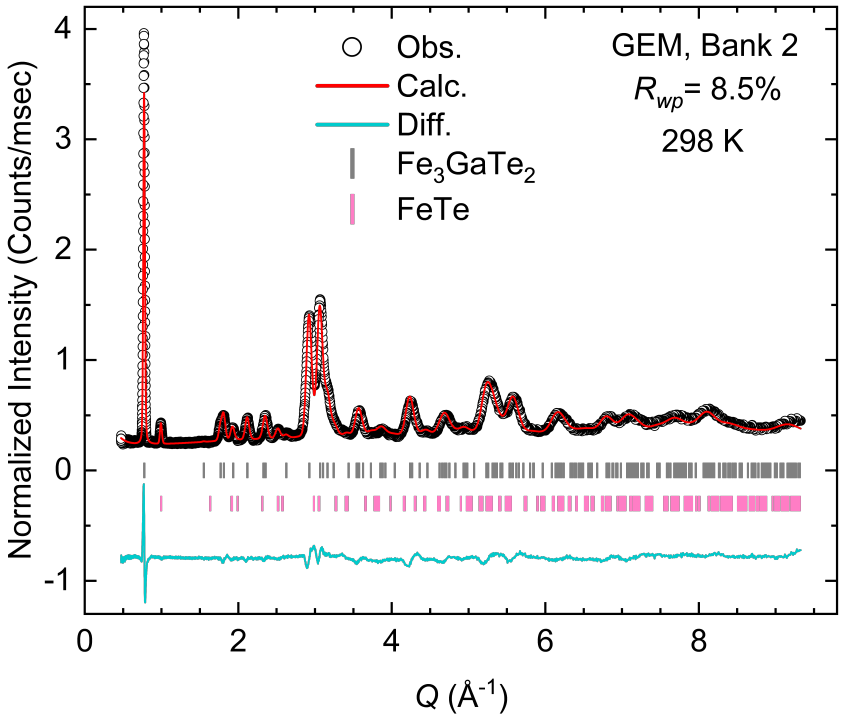



Figure 3.14: Rietveld refinement of $Fe_3GaTe_2$. Data were collected at 298 K utilizing bank 2 from the GEM instrument.

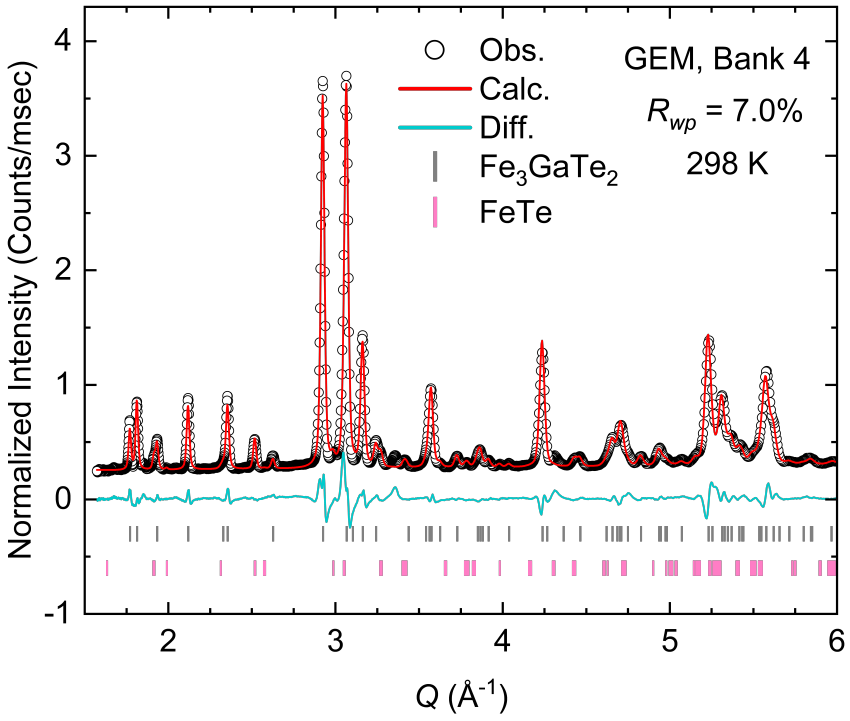



Figure 3.15: Rietveld refinement of $Fe_3GaTe_2$. Data were collected at 298 K utilizing bank 4 from the GEM instrument.

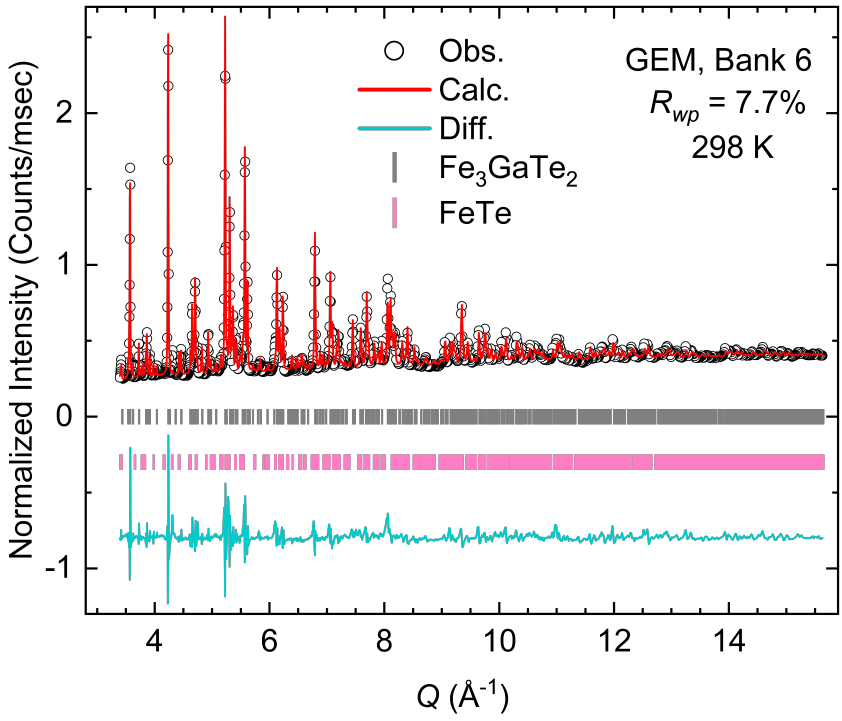



Figure 3.16: Rietveld refinement of $Fe_3GaTe_2$. Data were collected at 298 K utilizing bank 6 from the GEM instrument.

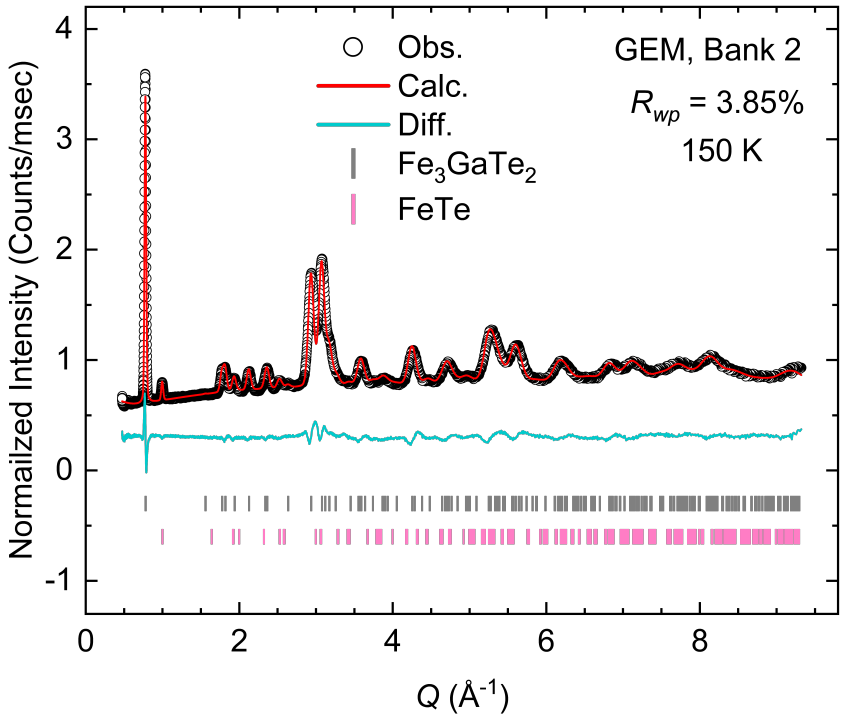



Figure 3.17: Rietveld refinement of $Fe_3GaTe_2$. Data were collected at 150 K utilizing bank 2 from the GEM instrument.

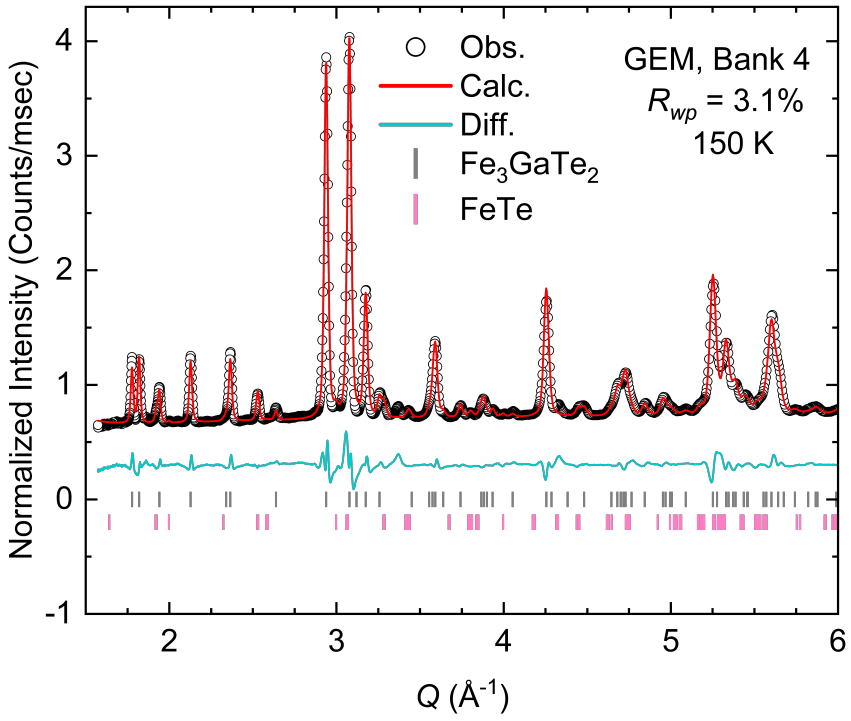



Figure 3.18: Rietveld refinement of $Fe_3GaTe_2$. Data were collected at 150 K utilizing bank 4 from the GEM instrument.

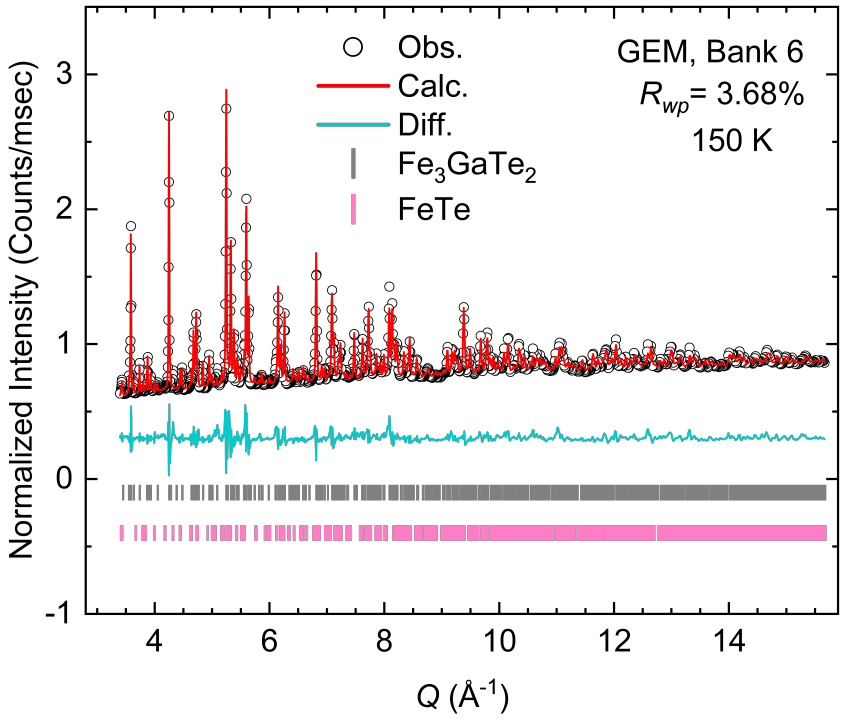



Figure 3.19: Rietveld refinement of $Fe_3GaTe_2$. Data were collected at 150 K utilizing bank 6 from the GEM instrument.

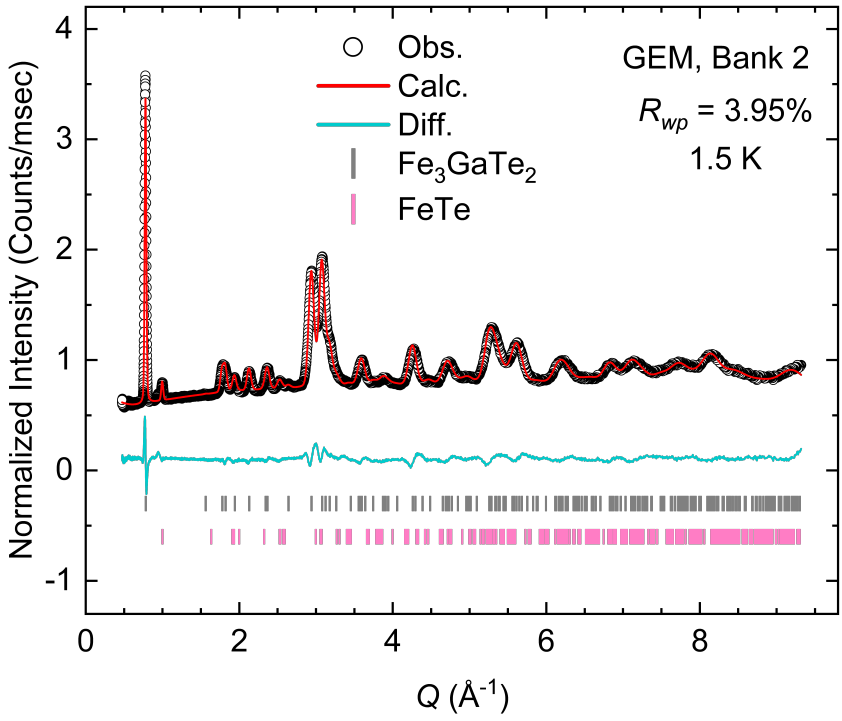



Figure 3.20: Rietveld refinement of $Fe_3GaTe_2$. Data were collected at 1.5 K utilizing bank 2 from the GEM instrument.

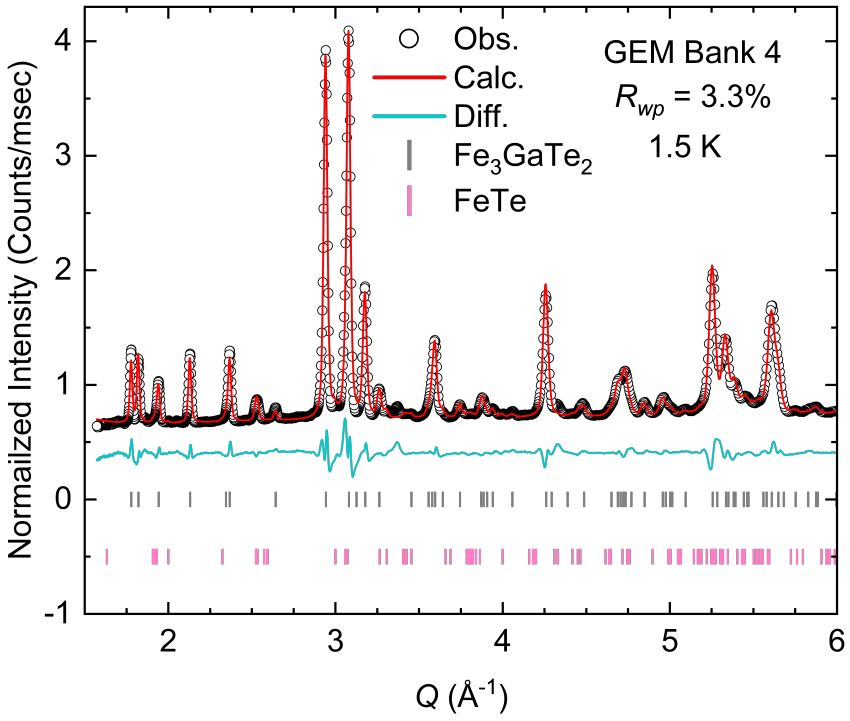



Figure 3.21: Rietveld refinement of $Fe_3GaTe_2$. Data were collected at 1.5 K utilizing bank 4 from the GEM instrument.

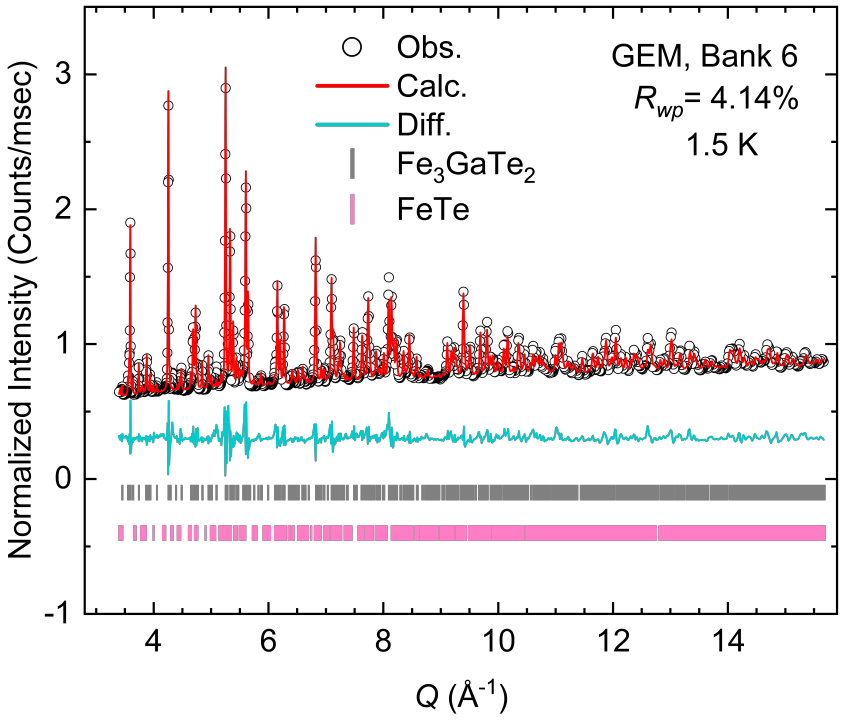



Figure 3.22: Rietveld refinement of $Fe_3GaTe_2$. Data were collected at 1.5 K utilizing bank 6 from the GEM instrument.

Table 3.6: Temperature Dependence of Magnetic Moments Results from Combined Bank 2,4, and 6 Rietveld Refinements.

| **Temperature (K)** | **Fe1($\mu_B$)** | **Fe2($\mu_B$)** | **Fe3($\mu_B$)** | **$R_{wp}$** |
|---|---|---|---|---|
| **1.5 K** | 0.7(2) | 1.65(6) | -1.6(6) | 3.2 |
| **150 K** | 0.7(2) | 1.4(1) | -1.5(6) | 3.4 |
| **298 K** | 0.6(4) | 0.8(1) | -1.7(1.0) | 7.4 |
| **323 K** | 0.5(3) | 0.6(1) | -3.2(1.4) | 7.1 |

the experimental data. This result implies that Fe3 contributes to the magnetic scattering for the the $(100)$ and $(102)$ reflections. Thus, all three Fe sites are magnetically active meaning that the magnetic space group is $P6_3/mm'c'$

As a consequence of this interstitial Fe, our Rietveld refinement suggest that FGaT is a ferrimagnet with the Fe3 magnetic moments anti-aligned to the moments from Fe1 and Fe2. If all three Fe sites are forced to be a ferromagnet then the residuals become worse.

**Figure 3.6** displays the changes in magnetic moments as a function of temperature. Starting with the 1.5 K data we see that our Rietveld model suggest that the magnetic moment of the interstitial site (Fe3) is -1.6(6) $\mu_B$ while Fe1 and Fe2 are 0.7(2) and 1.65(6) $\mu_B$. As temperature rises the magnitude of the moments decrease for Fe1 and Fe2. In contrast, the moments in Fe3 stay relatively constant however their error increases instead. Unexpectedly, at 323 K the Rietveld model states that moments in Fe3 are -3.2 $\mu_B$. Although this value is relatively high, the error for that data point is also high at 1.4 $\mu_B$. Overall, the total magnetic moment for Fe3 exhibits more error than the other sites due to its small fractional occupancy. Additionally, the majority of the moments carry a value of $1.6\mu_B$ which is different than what is expected for a spin-only total magnetic moment for $d^5$ Fe atom which is $3\mu_b$ for the high-spin configuration and $1\mu_B$ for the low-spin configuration.

In order to investigate the origins of $Fe_3GaTe_2$ magnetic structure we utilized DFT on our experimental crystal structure model and simulated different models such as $Fe_3GaTe_2$

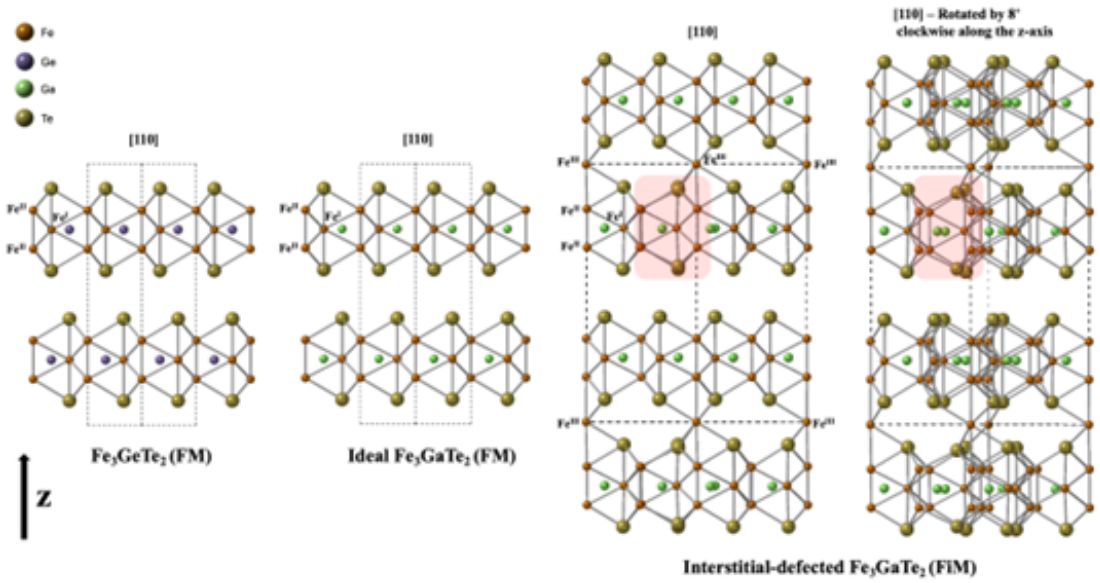



Figure 3.23: DFT-optimized crystal structures of $Fe_3GeTe_2$, ideal $Fe_3GaTe_2$ (the Ga-substituted version of $Fe_3GeTe_2$), and $Fe_3GaTe_2$ with interstitial defects (based on experimental data from XRD). For the interstitial-defected $Fe_3GaTe_2$, both the original [110] face and the rotated version (rotated by $8^{\circ}$ clockwise along the z-axis) are shown to clearly highlight the absence of Fe1 in the cage and the resulting distortion, highlighted by a pink rectangle.

with two active magnetic atoms against three active magnetic atoms, ferromagnetic FGaT versus ferrimagnetic FGaT, and comparing our $Fe_3GaTe_2$ results with $Fe_3GeTe_2$.

**Figure 3.23** displays a diagram of some of the structure models used in the DFT calculations. **Figure 3.24** displays a projected density of states that compares $Fe_3GaTe_2$ with only Fe1 and Fe2 to a $Fe_3GaTe_2$ crystal structure with Fe1, Fe2, and Fe3. **Table 3.7** lists the values of the magnetic moments for each Fe site according to the different types of structure models investigated.

Due to the computational cost we decided to only use a $2 \times 2 \times 2$ unit cell. In this model only one of the eight unit cells has 1 Fe atom in the interstitial position. This results in a occupancy of 12.5% which is comparable to the experimental result of 10%.

According to projected density of states calculations, the introduction of the interstitial site is substantial since the $3d$ orbitals of Fe3 lies within the Fermi level. Due to the addi-

tion of these 3*d* orbitals there are more states available that can be accessed by the system's electrons that can self-polarize. According to the Stoner model for an itinerant ferromagnet, each additional self polarized electron lowers the energy of the system. Although we did not calculate the spin-polarized density of states we suspect that introduction of new states from the interstitial Fe atoms are a major factor in the higher Curie temperature for $Fe_3GaTe_2$.[146,147]

Our DFT calculations also were able to somewhat match the experimental results with regards to the measurement of the magnetic moments. While the DFT calculations has overinflated the values of the magnetic moments these calculations mirror our experimental results that Fe1 has the smallest moments and that the magnitudes of the magnetic moments for Fe2 and Fe3 are similar. By comparing the energy state between a ferromagnetic structure versus a ferrimagnetic structure, our DFT calculation find that the ferrimagnetic structure is more energetically favorable by 66 meV.

Table 3.7: Comparison of the moment size for different magnetic orders from DFT calculations and neutron diffraction results. The models include ferromagnetic (FM) $Fe_3GeTe_2$ (FGT), ferromagnetic $Fe_3GaTe_2$ (FGaT) with only 2 sites and ferrimagnetic (FiM) with the interstitial site added (3-site). The experimental values from neutron diffraction are included for comparison.

| **Material** | **FGT** | **FGaT** | **FGaT** | **FGaT** |
|---|---|---|---|---|
| Model | DFT | 2-sites (DFT) | 3-sites (DFT) | (Exp) |
| Magnetic state | FM | FM | FiM | FiM |
| **Magnetic moment ($\mu_B$)** | | | | |
| - Fe1 (Avg.) | 1.54 | 1.54 | 1.68 | 0.73(18) |
| - Fe2 (Avg.) | 2.39 | 2.35 | 2.32 | 1.65(6) |
| - Fe3 (Avg.) | - | - | -2.82 | -1.6(6) |
| **Total magnetization ($\mu_B$/cell)** | 12.53 | 12.11 | 11.18 | - |
| **Absolute magnetization ($\mu_B$/cell)** | 14.10 | 13.99 | 14.30 | - |

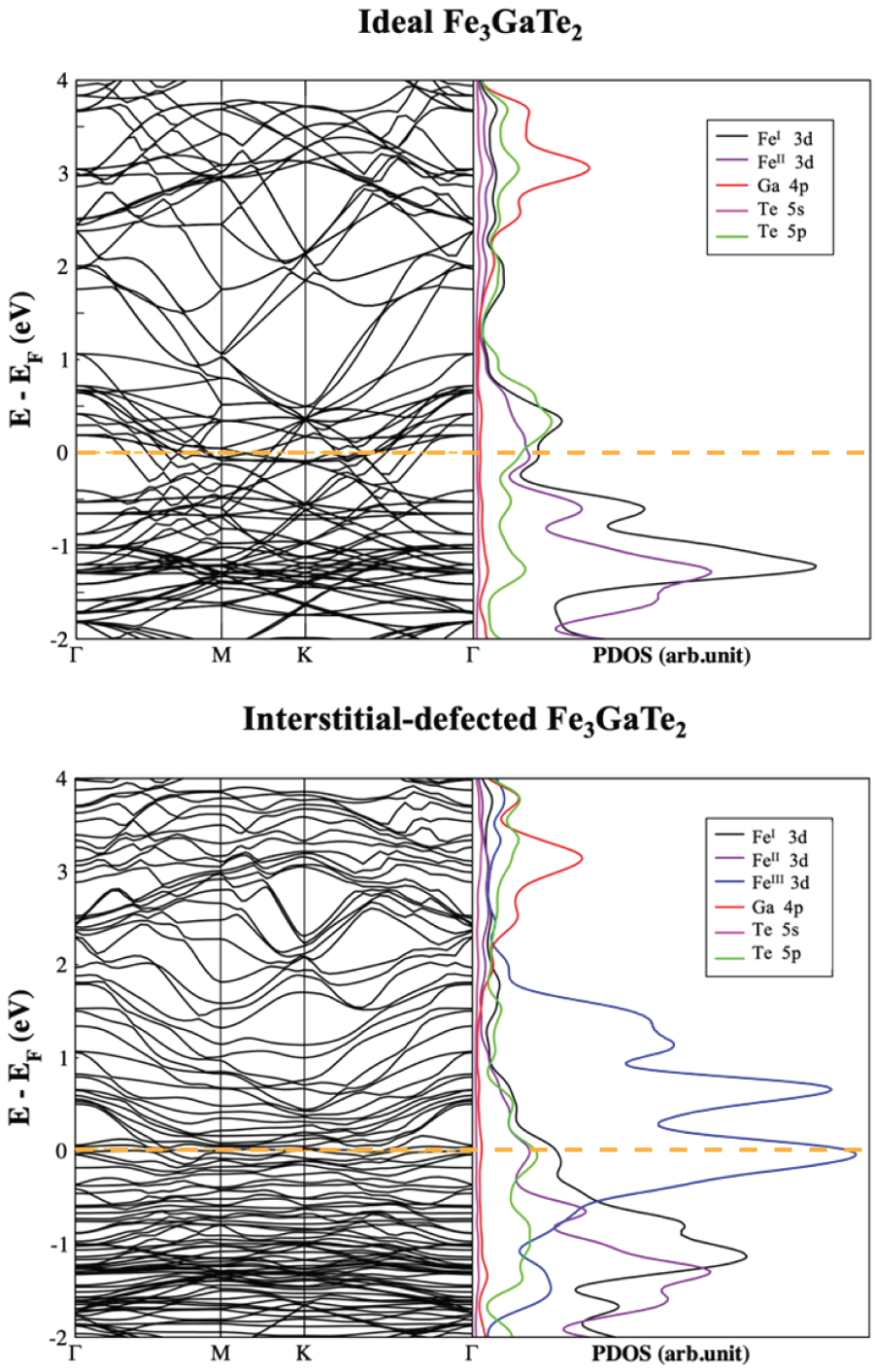



Figure 3.24: The band structure and projected density of states (left) of ideal $Fe_3GaTe_2$ (FGaT) and (right) $Fe_3GaTe_2$ (FGaT) with 12.5 % interstitial iron occupancy. The orange dash line on the left-hand side of each plot represents the Fermi level at 0 eV.

## 3.4 Conclusion

In conclusion, by using the flux method we synthesized single crystals of $Fe_3GaTe_2$. Single crystal X-ray diffraction revealed that the crystal structure for our samples is $P6_3/mmc$. In contrast, current literature suggest that the space group could be $P3m1$, however, according to our data we were not able to observe the symmetry breaking reflections in a statistically relevant way that Li *et al.* and Saha *et al.* reported. Our crystal structure has three unique Fe positions with two of the Fe position in the interior position while the third iron site is located within the van der Waals gap. The Fe3 position has an occupancy near 7-10 %. We find that our single crystal structure solution fits to powder diffraction data very well compared to a $Fe_3GeTe_2$ crystal structure. Using the GEM instrument at the ISIS Neutron and Muon Source, we were able to observe a few magnetic reflections using neutron diffraction. We found that the best fit required exhibits magnetic space group $P6_3/mm'c'$. We report that all three Fe sites are magnetically active. The magnetic structure can be described as Fe1 and Fe2 sites hosting a magnetic moment parallel to the $c$ axis while the Fe3 site is anti-parallel to the other moments. Thus, based on our data we state that $Fe_3GaTe_2$ is a ferrimagnet. To further investigate the origins of this ferrimagnetic behavior we performed DFT calculations and found that the ferrimagnetic state is 66 meV lower than the ferromagnetic state.

# Chapter 4: Magnetic Structure Determination of Mixed Anion $NiP(S_{1-x}Se_x)_3$

## 4.1 Introduction

Van der Waal materials are not just limited to ferromagnetic ordering, they can also exist as antiferromagnetic materials. Similarly to their ferromagnetic counterparts, these antiferromagnetic vdW materials are also capable of being used in a variety of applications by exploiting their ultra-fast dynamics[103,148,149] and quasiparticle excitations[64,150–152] for computational devices and applications in memory.[14,64,153,154] One prominent sub-group of 2D-vdW materials known to host these aforementioned properties are, transition metal chalcophosphates (TMCs).[103,155–158] Specifically, we are interested in nickel chalcophosphates due to its relatively larger Neél temperature compared to other TMCs.

Nickel chalcophosphates (NiPQ) have been reported to be synthesized in two compositions, $NiPS_3$ and $NiPSe_3$. In these materials the P atoms bond with the chalcogen atoms, S or Se, to form an ethane-like $[P_2Q_6]^{4-}$ units. This complex anion is then charge balanced by two $Ni^{2+}$ cations. Each lattice layer is then comprised of a honeycomb lattice formed by the metal cations and a hexagonal lattice formed by the $[P_2Q_6]^{4-}$ units. These atomic positions cause chalcogen atoms to form an octahedral coordination with the metal atoms and form slightly distorted bond angles and non-degenerate metal-chalcogen bond lengths.[44,159,160]

Compared to iron chalcophosphate (FePQ) and manganese chalcophosphate (MnPQ), NiPQ has unique structural properties compared to its peers. For instance, both the sulfur

and selenium variant of NiPQ have a monoclinic $C2/m$ space group crystal structure . Other TMCs, such as MnPQ and FePQ have their crystal structure shift from a monoclinic $C2/m$ to a trigonal $R\overline{3}$ space group upon substitution of sulfur with selenium.[47,161–168]

These structural differences are of interest because there is often a relationship between the magnetic structure and its nuclear structure. For example, the magnetic structure of $FePS_3$ has a propagation vector $\overrightarrow{k} = [01\frac{1}{2}]$ while the magnetic structure of $FePSe_3$ has a $\overrightarrow{k} = [\frac{1}{2}0\frac{1}{2}]$.[70] Here, the change in symmetry and chalcogen atoms results in a change in the propagation vector. Similarly, a change in chemical composition can influence the direction of the magnetic moments. For example, in MnPQ, the substitution of sulfur with selenium, shifts the direction of the moments from along the $c$-axis to perpendicular to the $c$-axis.[169–171] Curiously, there is no comprehensive study on the effects of selenium substitution on the magnetic structure of $NiPS_3$.

These differences between NiPQ and other antiferromagnetic TMCs continue to be seen in magnetic susceptibility data. Normally, for a susceptibility curve, a typical antiferromagnet has a cusp shape at the Neél temperature.[172] This shape is observed for FePQ and MnPQ, yet $NiPS_3$ and $NiPSe_3$ exhibit a broad susceptibility curve shape instead of a cusp shape.[173] The origin of this bowl-like shape is thought to derive from two-dimensional exchange interactions.[97,174] These directions are suspected to be in the $a$ and $b$ directions while very little exchange interactions occur in the $c$ direction. However, comparing the critical exponents between the antiferromagnetic TMCs provides a different perspective. The $\beta$ critical exponent is a metric that describes the magnetic ordering near the transition temperature. Different values correspond to different magnetic models and their dimensionality. In the case for $NiPS_3$ $\beta = 0.36$, $FePS_3$ $\beta = 0.125$, and $MnPS_3$ $\beta = 0.231$. With these $\beta$ values, the magnetism in $MnPS_3$ and $FePS_3$ can understood by the 2D Ising model for the former and the 2D-XY model for the latter. However, the $\beta$ value for $NiPS_3$ implies that the magnetization in $NiPS_3$ is three dimensional.

Until this work, neutron diffraction has only been performed on $NiPS_3$ and even those experiments have been a source of contention. Neutron diffraction experiments have been done on $NiPS_3$ on two separate occasions. With the first instance done by Ouvard *et al.*[47] and the second by Wildes *et al.*[160] Ouvard *et al.* argues that based on their neutron powder diffraction (NPD) data, the magnetic moments of $NiPS_3$ are aligned to be about 30° away from the c-axis. Additionally, each moment on a Ni atom has two antiferromagnetic neighbors and 1 ferromagnetic neighbor. Wildes *et al.* concluded that the neighbors of the magnetic Ni atoms also have 1 AFM and 2 FM neighbors. However, they state that the direction of the moments should be aligned parallel to the *ab*-plane when considering in-plane and out-of-plane magnetic susceptibility data and single crystal neutron diffraction results (SCND). Additionally, Wildes *et al.* notes that one reason for this discrepancy is that less magnetic reflections are seen in the NPD data than in the SCND, which ultimately be the reason why both authors report different magnetic structures. Further questions arise, when neutron inelastic scattering results are considered. From these experiments it was observed that some of the exchange constants are near zero,[175] which indicates that the magnetic behavior of $NiPS_3$ is unstable.

Considering the instability of the exchange interactions in $NiPS_3$, and the lack of a neutron diffraction experiments on $NiPSe_3$, and previous success in utilizing elemental substitution for physical property manipulation in vdW materials,[43,164,169,176–178] this work performed neutron diffraction on various compositions of Se-substituted $NiPS_3$ in order to observe if selenium's $4p$ orbitals will influence the magnetic Ni atoms' exchange interactions. If the type of neighbors changes from the initial 2 AFM and 1 FM orientation to some other orientation, then the magnetic scattering will change to reflect this new magnetic structure, which should be observable in neutron diffraction.

From our powder and single crystals neutron diffraction experiments we observe that $NiP(S_{1-x}Se_x)_3$ type compounds have a P1 magnetic space group symmetry. Each Ni atom

has 3 nearest neighbors, where 2 of the neighbors are FM aligned and 1 AFM aligned. This structural solution was found to be acceptable from both the powder and single crystal diffraction data sets. However, the main difference between the two data sets is in the number of magnetic reflections observed. The only reflection with meaningful intensity in the NPD data is the (010) reflection. The lack of multiple observable magnetic reflections makes it difficult to accurately pinpoint the direction of the magnetic moment. In contrast, the multiple magnetic reflections observed in the single crystal data set implies that the moments are mostly in the *a*- direction with a little contribution from the *b* and *c*-axis.

Interestingly, there is a slight discrepancy between the strength of the total magnetic moments depending if powder or single crystal diffraction is used. According to NPD, the total magnetic moment of $NiP(S_{1-x}Se_x)_3$ is measured to be near 1.5 $\mu_B$ and only drops to 1.4 $\mu_b$ when all the sulfur is replaced with selenium. In contrast, the data from SCND suggest that Se may have a greater influence on the strength of the moments. For x = 0.29, $M_T$ = 1.46(2) $\mu_B$. While for x = 0.43, $M_T$ = 1.01(4).

## 4.2 Experimental Methods

### 4.2.1 Synthesis

**Powder synthesis of $NiP(S_{1-x}Se_x)_3$:** $NiP(S_{1-x}Se_x)_3$ was synthesized using a direct combination of elemental nickel (Sigma-Aldrich, 99.7%), phosphorus (Alfa-Aesar, 98.9%), sulfur (ACROS Organics, 99.5%), and selenium (Sigma-Aldrich, 99.5%). The elements were mixed and ground by an agate mortar and pestle inside an argon-filled glove box. The reagents were mixed in a stoichiometric ratio according to the nominal composition desired. For example, if $NiPS_2Se$ is targeted, then the the ratio among Ni:P:S:Se is 1:1:2:1. The powder mixture was then placed in a quartz-glass ampule (Advalue Technologies) and sealed under a vacuum of 7.5 x 10-3 Torr. The ampule was then heated in a box furnace to

440 °C under a 2°C/min ramp and held at that temperature for a few hours to prevent the rupture of the ampule from sulfur's vapor pressure. Following this step, the furnace was then heated to 650°C with a 4°C/min ramp and dwelled at this temperature for 4 days.

**Single crystal Synthesis of NiP($S_{1-x}Se_x$)$_3$:** Single crystals of NiP($S_{1-x}Se_x$)$_3$, where x = 0.3 and 0.4, were synthesized using chemical vapor transport technique. Nickel (Sigma-Aldrich, 99.7%), phosphorus (Alfa-Aesar, 98.9%), sulfur (ACROS Organics, 99.5%), and selenium (Sigma-Aldrich, 99.5%) where mixed in stoichiometric amounts inside an Ar-filled glove box. Reagents were put in an ampule with an outer diameter of 1.4 cm and a length near 13 cm. Iodine was added to the ampule with a concentration of 3 mg/cm$^3$. The sealed ampule was then positioned in a tube furnace where the charge end would reach 650°C and the growth end would be 600°C. However, before the target temperatures were reached, the ampule was heated to 445°C at a ramp rate of 2°C/min dwelled at this temperature for 24 hrs and then ramped to the aforementioned temperatures at a rate of 4°C/min. At the target temperature the reaction vessel dwelled for 20 days. Afterwards, the reaction was allowed to furnace cool until room temperature. the crystals extracted from this CVT growth exhibited a size between 0.5 x 0.5 mm$^3$ to 3 x 3 mm$^2$ with a metallic like gray color.

### 4.2.2 X-ray Diffraction

**Polycrystalline X-ray diffraction and refinement:** X-ray diffraction was performed on a Bruker D8 Advance diffractometer with a Cu K$\alpha$ source at ambient conditions. For the Rietveld refinement, GSAS-II refinement software was used. A CIF file from the literature[160] was used as the structure model for the Rietveld refinement. For the $NiS_2$ and $NiSe_2$ impurities, CIF files from the ICSD were utilized. For the refinement $U_{iso}$ thermal

parameters between S and Se along with their atomic positions equivalent to each other.

**Single Crystal X-ray Diffraction and Refinement:** Suitable crystals of $NiP(S_{1-x}Se_x)_3$ were measured on a Bruker Smart Apex II CCD diffractometer. The crystal was kept at 296 K during data collection. The integral intensity was corrected for absorption using SAD-ABS software by using an integration method. The structure was solved with the ShelXT program and refined with the ShelXL program using least-square minimization. No constraints were used in the refinement.

### 4.2.3 Neutron Diffraction

**Neutron powder diffraction and refinement:** Time-of-flight unpolarized powder neutron diffraction (NPD) was performed at Oak Ridge National Lab's Spallation Neutron Source on the POWGEN instrument. For these experiments each sample weighed about 3 grams. An 8 mm length vanadium can was used to hold each sample. The frame 2 instrument setting, which has a d-spacing coverage between 0.5-12.5 Å, was used for this experiment. For good statistics, each experiment had an exposure time of approximately 2 hours. Each sample was measured at two temperatures, 300 K and 2 K.

Refinement program of choice in this case was GSAS-II. Constraints used included assigning the S and Se atoms the same atomic positions and the same thermal parameters. Ni and P both have majority and minority sites with the majority sites actually representing the crystal structure while the minority sites are a convenient proxy that represents the prevalence of layer shifting in the *ab*-plane. In this refinement the majority Ni sites and minority P sites were constrained such that the sum of the occupancies is one. The same constraints where applied towards the majority phosphorus sites and minority Ni sites. All Ni sites shared the same thermal parameters and all phosphorus sites had equivalent thermal

parameters. For the Rietveld refinement at 2 K, the magnetic moments were only calculated for the Ni majority sites.

**Single crystal neutron diffraction and Refinement:** Single crystal neutron diffraction (SCND) was performed at the TOPAZ instrument at Oak Ridge National Lab. In this experiment, the ambient goniometer was used. Two samples were measured at this instrument, a 2 x 1 x 0.15 $mm^3$ 3 mg sample of $Ni_{2.00(1)}P_{1.99(1)}S_{3.44(1)}Se_{2.56(1)}$ and a 1 x 1 x 0.01 $mm^3$ 1 mg sample of $Ni_2P_2S_{4.29(1)}Se_{1.71(1)}$. Each sample was measured at 100 K and 300 K. We measured enough frames to account for all possible $C2/m$ reflections for the room temperature measurements. For the 100 K experiments, the amount of frames collected were based on the observing all possible $P1$ reflections. Total collection time is estimated to be near 15 hrs and 36 hrs for the 300 K and 100 K measurements.

### 4.2.4 Magnetic Susceptibility

Powder magnetic susceptibility measurements were performed with a Quantum Design MPMS©3. $NiPS3 - xSe_x$ where x = 0.03, 0.11, 0.33, 0.5, 0.6 and 1.For both the field-cool and zero field-cool measurements the range of operation was between 2 K to 300 K at a scan rate of 2K/ min and a field of 100 Oe.

### 4.2.5 Energy Dispersive Spectroscopy

The chemical composition of $NiPS3 - xSe_x$ powders and single crystals were measured using a Hitachi SU-70 Schottky FEG-SEM equipped with the Bruker energy dispersive X-ray spectrometer (EDS, XFlash(6/60)).

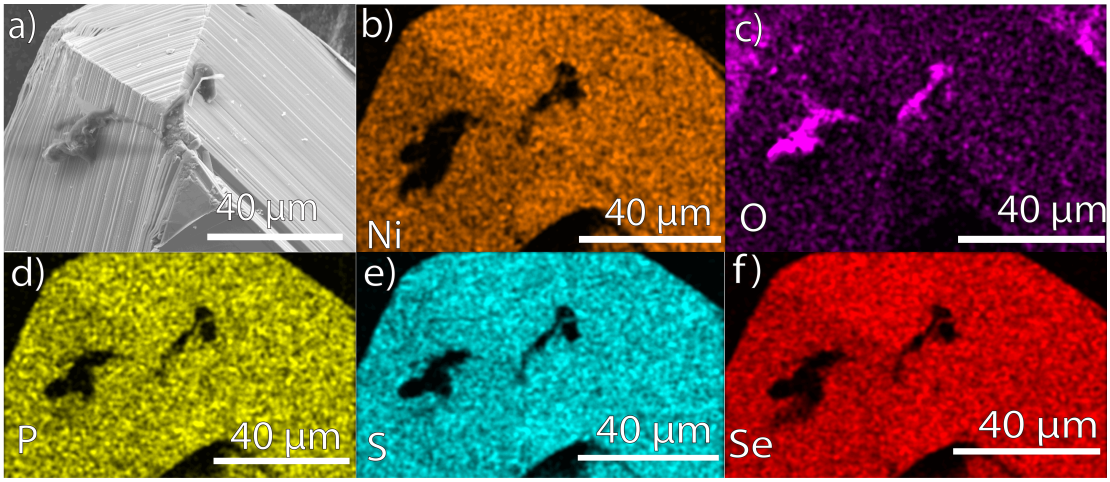



Figure 4.1: EDX of nominal $NiPS_2Se$. The actual composition is closer to $Ni_{0.94}PS_{2.1}Se_{0.9}$. Atomic % of each element is Ni: 15.6%; P: 17.2 %; S: 36.6%; Se 15.6 %; O: 14.5 %

## 4.3 Results and Discussion

### 4.3.1 Structural and Elemental Characterization

Mixed anion $NiP(S_{1-x}Se_x)_3$ samples were synthesized in both powder and single crystal forms. Visually, across all compositions the $NiPQ_3$ powders are dark in color. These powders also carry a slightly pungent odor that can easily overwhelm a person after prolong exposure, thus it is recommended to work with these materials in a fume hood or a glove box. As for the single crystals, they exhibit a metallic gray color and form thin plate that are no more thicker than 0.1 mm (**Figure 4.6 and 4.7**).

From the EDX measurements it can be seen that when selenium is added to the $NiPS_3$ synthesis, Se is found to be incorporated into the $NiPS_3$ structure. **Figure 4.1** demonstrates that the nominal composition is not achieved and that some of the selenium either does not insert into the $NiPS_3$ compound or forms an impurity. Interestingly, there is also a deficiency in Ni also observed. This deficiency can perhaps be traced to the formation of $NiSe_2$, which was identified from the diffraction data.

A combination of powder and single-crystal diffraction utilizing both x-rays and neutron sources was used to characterize the structure of $NiPQ_3$. Using a CIF from the literature,[160] a Rietveld refinement on powder diffraction data was able to model a crystal structure with a space group symmetry of *C2/m* on to the observed intensities. Regardless of the amount of selenium introduced to the reaction, no new symmetry breaking reflections were observed. This result suggests that the space group across all $NiPQ_3$ solid solutions is $C2/m$. However, despite the series exhibiting the same space group, the introduction of selenium does change the intensities of certain reflections such as (001), (131), $(20\overline{2})$ to name a few. Additionally, one new reflection appears that is able to be indexed as $(20\overline{2})$ and appears to be exclusive to $NiPSe_3$.

Only one impurity was observed, $NiSe_2$. $NiSe_2$ was found across all compositions with a weight percent ranging from 5 to 10%. Regarding the ion-exchange synthesis of $NiPSe_3$, $NiSe_2$ has a weight percent near 11%. Because $NiSe_2$ is paramagnetic its appearance does not greatly affect the analysis of the magnetic properties of $NiPQ_3$ compounds.[179–181]

The crystal structure of $NiPQ_3$ compounds can be described as a series of 2D lattices stacked on top of each other that are separated by empty gaps. Each lattice layer is comprised of a combination of a honeycomb lattice of Ni atoms and a hexagonal lattice of $[P_2Q_6]^{4-}$ units. **Figure 4.2** visually demonstrates these attributes.

The chalcogen atoms, be it S or Se are bonded to the P-P dimers to form an ethane-like structure. Although, the Ni atoms appear to form an octahedral with the chalcogen atoms, the bond lengths among the six ligands are not equal. Additionally the bond angles are not observed to have the ideal angles for an octahedral site. This structural arrangement has certain implications for the contribution of indirect exchange because exchange rules such as the Goodenough–Kanamori rules,[182,183] are not as applicable to the $NiPQ_3$ compounds due to the misalignment of the orbitals from the non-metal atoms.

According to literature, due to the layered crystal structure, $NiPQ_3$ samples tend to

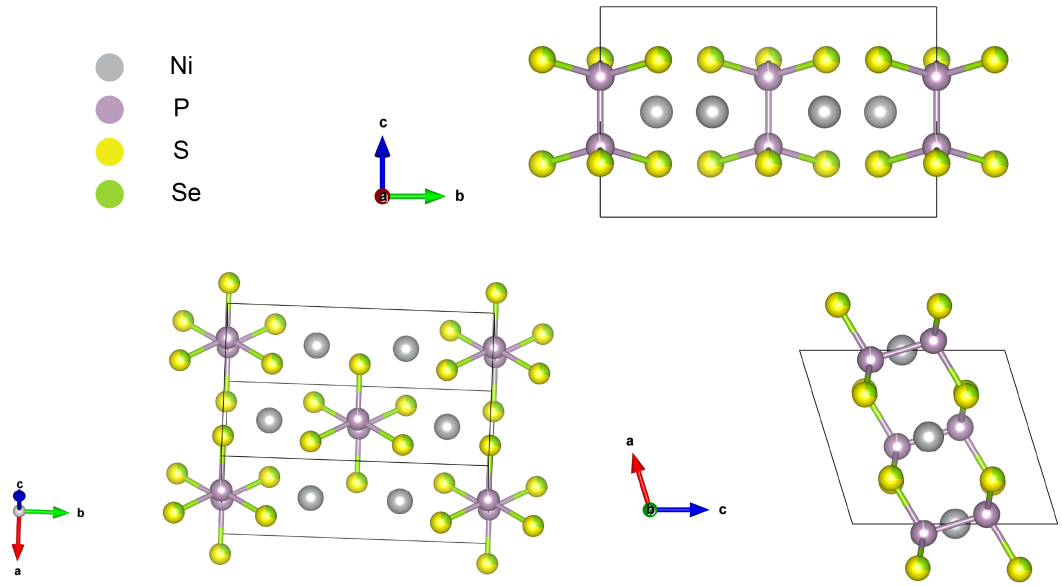



Figure 4.2: Crystal structure of $NiPQ_3$ compounds from different perspectives. Despite substituting Se for S the crystal space group remains $C2/m$.

exhibit significant amounts of layer shifting in the $c$-axis that tend to transform the shape of reflections from a spot to a line or streak in the diffraction pattern.[160,184] This layer shifting can be partially accounted for by adding two new additional Wyckoff sites in the CIF file. One site is used for nickel atoms and the other site is used for phosphorus atoms. Interestingly, these new sites swap the lattices between Ni and P atoms. If we look at **Figure 4.3** we see that these new Wyckoff positions for Ni form a hexagonal lattice, while the new P sites form a honeycomb lattice. According to our Rietveld refinements, regardless of the composition of the mixed anion $NiPQ_3$, Ni occupies the $2a$ Wyckoff site 30-40% of the time while P occupies the $8j$ site 20-25% of the time (**Figure 4.4**). This result implies that these structural defects are not correlated with increased Se concentration.

Without the use of these minority sites, the residual parameters are much worse for the Rietveld refinement. **Figure 4.5** compares one Rietveld refinement with and without additional Wyckoff sites. From this analysis we note that the Rietveld refinement without

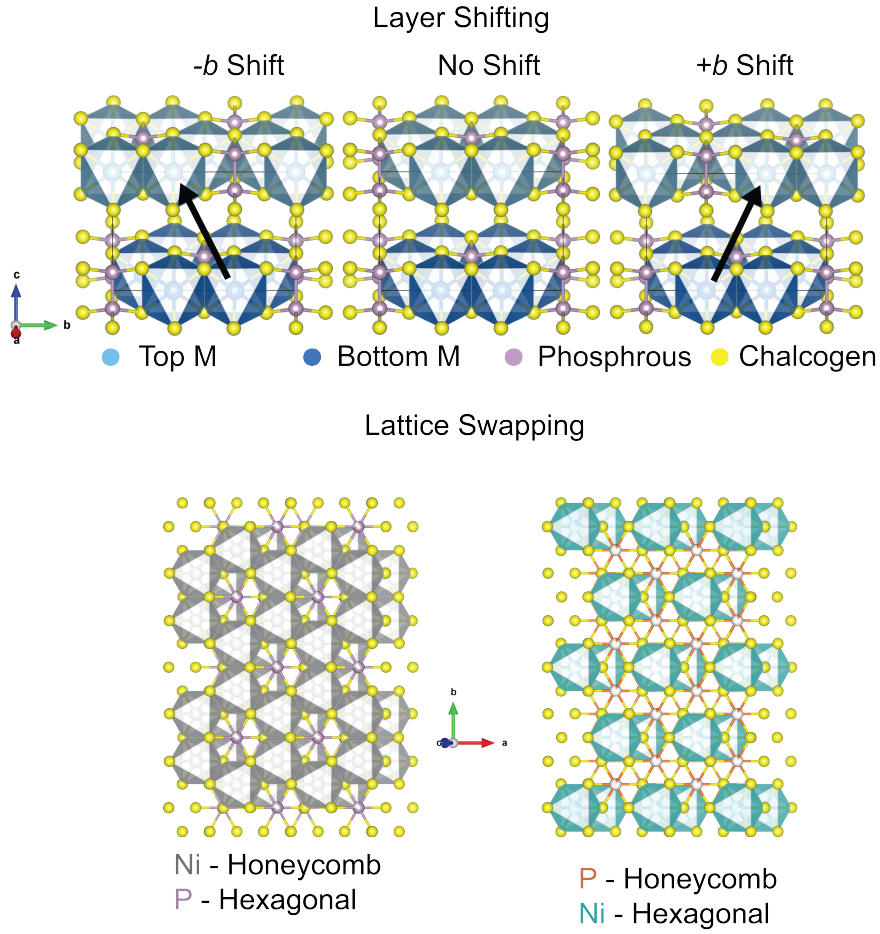



Figure 4.3: The addition of extra Wyckoff positions in $NiPQ_3$ can be interpreted as two types structural distortions, layer shifting or lattice swapping.

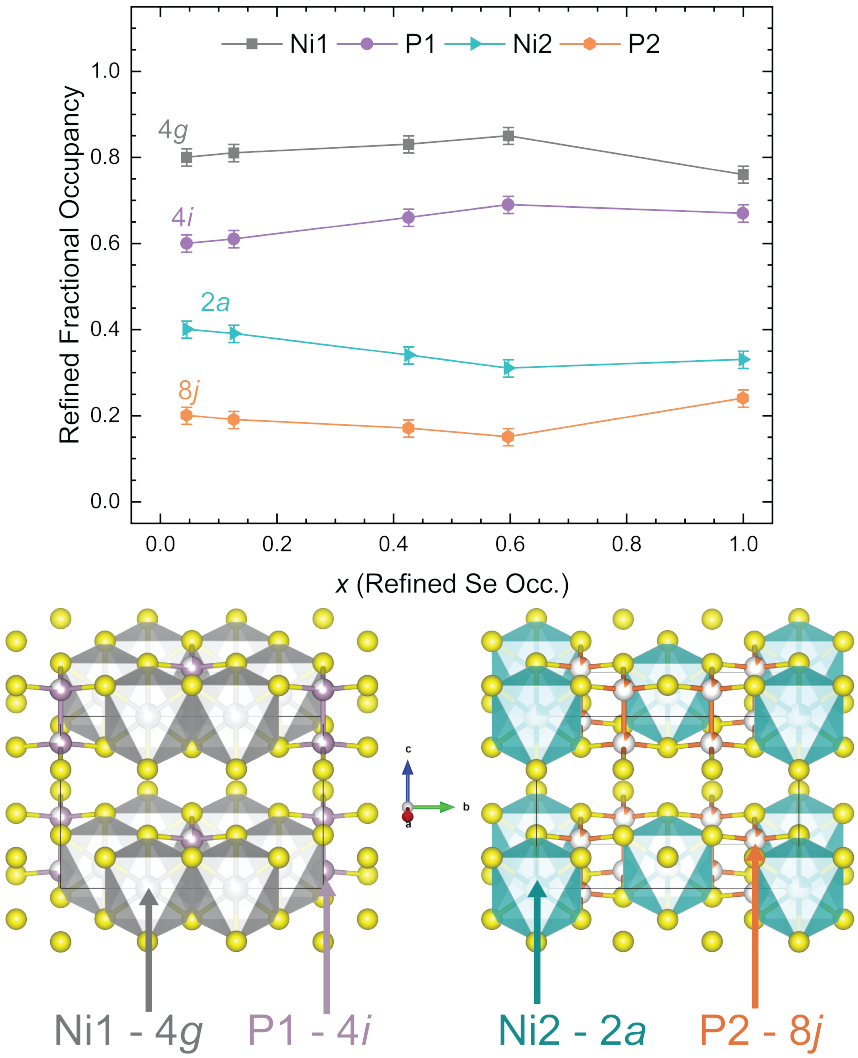



Figure 4.4: The fractional occupancies for these minority sites where found to be relatively constant regardless of the composition of $NiP(S_{1-x}Se_x)_3$.Top figure demonstrates a plot that describes the relationship of atomic site occupancy with respect to Se occupancy. Bottom figures demonstrates where each Wyckoff site is located in the $NiPQ_3$ crystal structure

the extra sites is not able to produce a calculated intensity pattern to match the observed intensities on certain high signal reflections. This poor fit is then reflected in residual parameters $R_{wp}$ and $R_f$. From these result we can deduce that these structural distortions have a measurable affect on the structure factor over certain reflections.

Interestingly, our single crystal neutron diffraction results imply that these structural defects can be minimized if the crystal thickness is reduced. **Figure 4.6 – 4.7** demonstrates how the thickness in a $NiP(S_{1-x}Se_x)_3$ crystal influences the amount of diffuse features observed. The selection of thin and triangular shaped crystal resulted in the removal of diffuse features. However, this effect comes at a cost because thinner crystals mean less sample mass, which results in less intense diffraction patterns.

A direct correlation was observed when comparing Se concentration to lattice parameters. This relationship is demonstrated by **Figure 4.8**. This expansion is most likely due

Table 4.1: Selected parameters from single crystal neutron diffraction of $NiP(S_{1-x}Se_x)_3$ where x = 0.29.

| | |
|---|---|
| Empirical formula | $Ni_2P_2S_{4.3}Se_{1.7}$ |
| Space group | $C2/m$ |
| Crystal system | Monoclinic |
| $a$(Å) | 5.914(4) |
| $b$(Å) | 10.249(6) |
| $c$(Å) | 6.690(3) |
| $\alpha$(°) | 90 |
| $\beta$(°) | 107.02(5) |
| $\gamma$(°) | 90 |
| Unit cell volume (Å$^3$) | 387.7(4) |
| Instrument | TOPAZ |
| Sample mass (mg) | 0.8 |
| Reflections collected | 450 |
| Goodness of fit | 2.4 |
| $F(000)$ | 113.2 |
| $R_f$ / $R_{f2}$ | 0.058 / 0.12 |
| Temperature (K) | 293 |

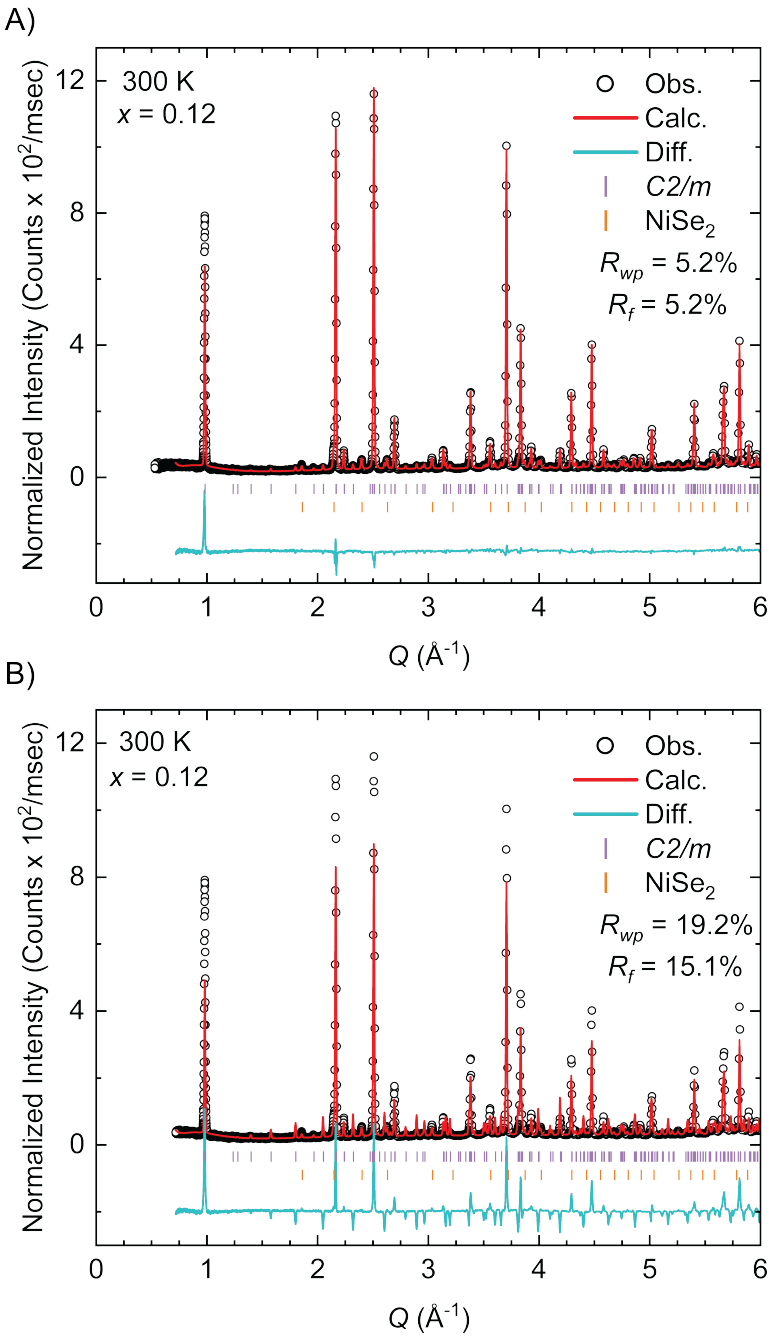



Figure 4.5: (A) Rietveld refinement on $x = 0.12$ sample with the inclusion of additional Wyckoff sites. (B) Without extra Wyckoff positions. Without the use of additional Wyckoff sites, residual parameters $R_{wp}$ and $R_f$ are over 15%, which is not suitable for publication.

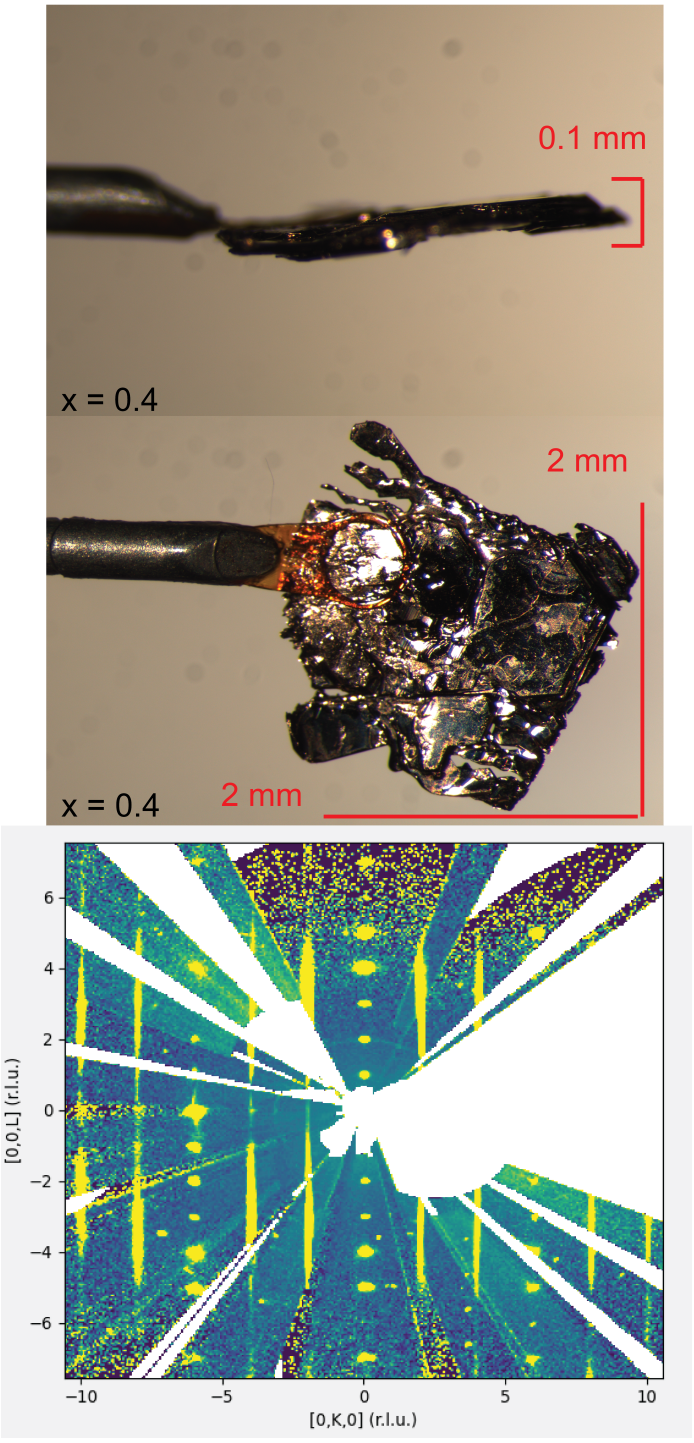



Figure 4.6: One of measured single crystals is significantly more thicker than the other crystal. The precession images demonstrate significant amounts of diffuse features for (02$kl$) reflections. We hypothesize that thicker crystals give rise to more structural disorder in $NiP(S_{1-x}Se_x)_3$.

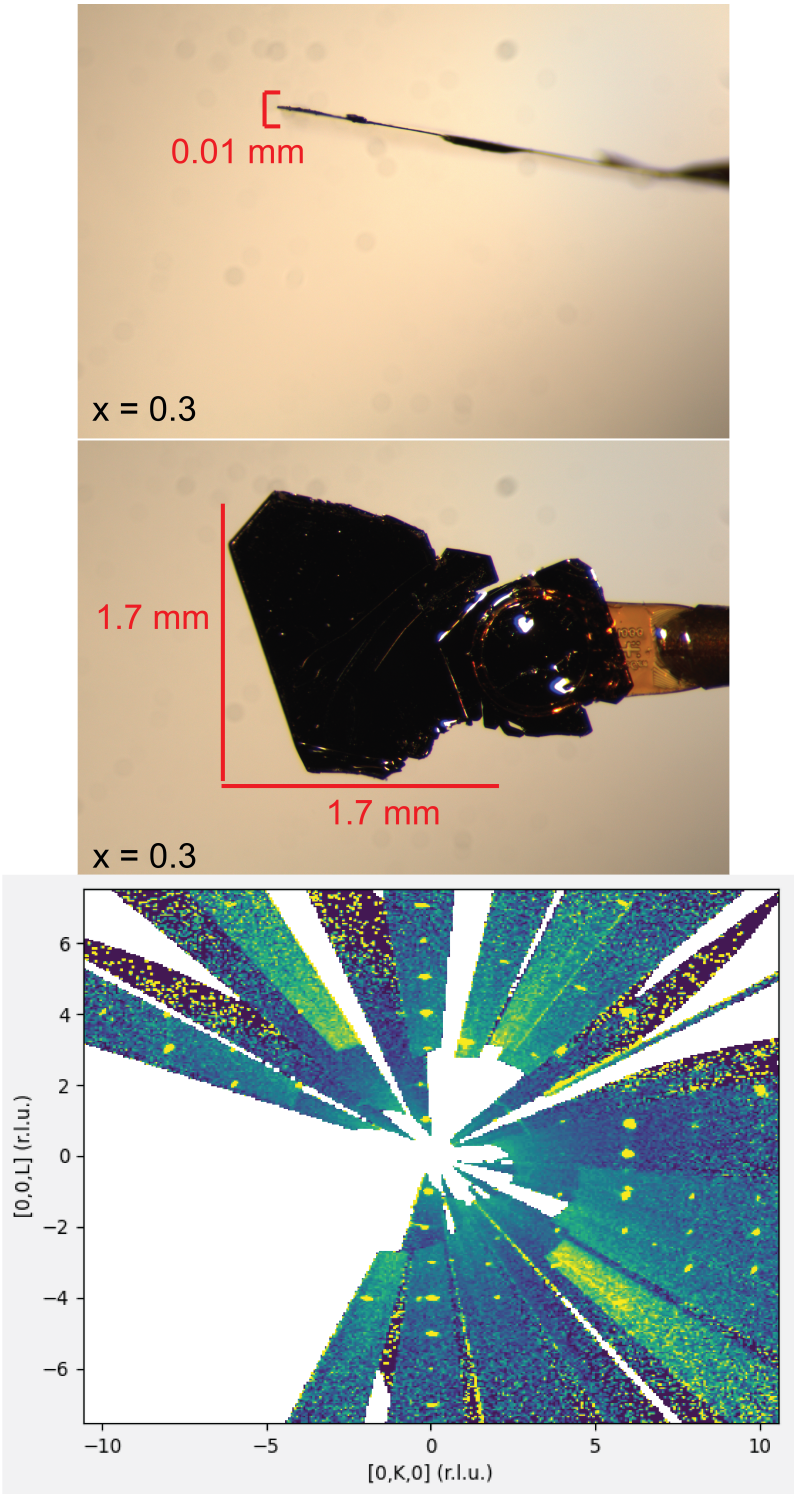



Figure 4.7: In contrast, a thinner crystal, on the order of 0.01 mm thickness, resulted in the removal of these diffuse features.

Table 4.2: Fractional atomic coordinates with Wyckoff site labels, equivalent isotropic displacement parameters($U_{eq}$) (Å$^2$), and occupancies of single crystal NiP($S_{1-x}Se_x$)$_3$ where x = 0.29.

| **Atom** | $x$ | $y$ | $z$ | $U_{eq}$ | **Occ.** |
|---|---|---|---|---|---|
| **Se1** (4*i*) | 0.2375(7) | 0.5 | 0.7457(7) | 0.025(2) | 0.28(2) |
| **S1** (4*i*) | 0.2375(7) | 0.5 | 0.7457(7) | 0.025(2) | 0.72(2) |
| **Se2** (8*j*) | 0.7550(5) | 0.3275(2) | 0.7474(4) | 0.026(2) | 0.29(1) |
| **S2** (8*j*) | 0.7550(5) | 0.3275(2) | 0.7474(4) | 0.026(2) | 0.71(1) |
| **Ni1** (4*h*) | 0.5 | 0.1669(1) | 0.5 | 0.018(1) | 1.0 |
| **P1** (4*i*) | 0.5549(6) | 0.5 | 0.6669(5) | 0.017(1) | 1.0 |

to the change in valence orbitals from sulfur's $3p$ to selenium's $4p$. Higher orbital energies occupy more space, and thus it follows that a larger atomic radius can lead to an uptick lattice parameter values.

Taking a look at the derived bond angles and bond distances from single crystal struc-

Table 4.3: Selected parameters from single crystal neutron diffraction of NiP($S_{1-x}Se_x$)$_3$ where x = 0.43.

| | |
|---|---|
| Empirical formula | $Ni_2P_{2.0}S_{3.4}Se_{2.6}$ |
| Space group | $C2/m$ |
| Crystal system | Monoclinic |
| $a$(Å) | 5.952(3) |
| $b$(Å) | 10.354(6) |
| $c$(Å) | 6.751(5) |
| $\alpha$(°) | 90 |
| $\beta$(°) | 106.98(1) |
| $\gamma$(°) | 90 |
| Unit cell volume (Å$^3$) | 397.9(4) |
| Instrument | TOPAZ |
| Sample mass (mg) | 2.4 |
| Reflections collected | 1757 |
| Goodness of fit | 2.6 |
| $F$(000) | 122.1 |
| $R_f$ / $R_{f2}$ | 0.047 / 0.11 |
| Temperature (K) | 293 |

Table 4.4: Fractional atomic coordinates with Wyckoff site labels, equivalent isotropic displacement parameters($U_{eq}$) (Å$^2$), and occupancies of single crystal NiP($S_{1-x}Se_x$)$_3$ where x = 0.43. The conventional unit cell was used.

| **Atom** | $x$ | $y$ | $z$ | $U_{eq}$ | **Occ.** |
|---|---|---|---|---|---|
| **Se1** (4*i*) | 0.7431(1) | 0 | 0.2471(1) | 0.0164(3) | 0.42(1) |
| **S1** (4*i*) | 0.7431(1) | 0 | 0.2471(1) | 0.0164(3) | 0.58(1) |
| **Se2** (8*j*) | 0.2519(1) | 0.1696(1) | 0.2472(1) | 0.0169(2) | 0.43(1) |
| **S2** (8*j*) | 0.2519(1) | 0.1696(1) | 0.2472(1) | 0.0169(2) | 0.57(1) |
| **Ni1** (4*g*) | 0 | 0.3332(1) | 0 | 0.0125(2) | 0.834(4) |
| **P2** (8*j*) | 0.0557(4) | 0.3334(4) | 0.1664(4) | 0.0027(1) | 0.166(4) |
| **P1** (4*i*) | 0.0565(2) | 0 | 0.1678(3) | 0.017(1) | 0.661(2) |
| **Ni2** (2*a*) | 0 | 0 | 0 | 0.018(1) | 0.339(2) |

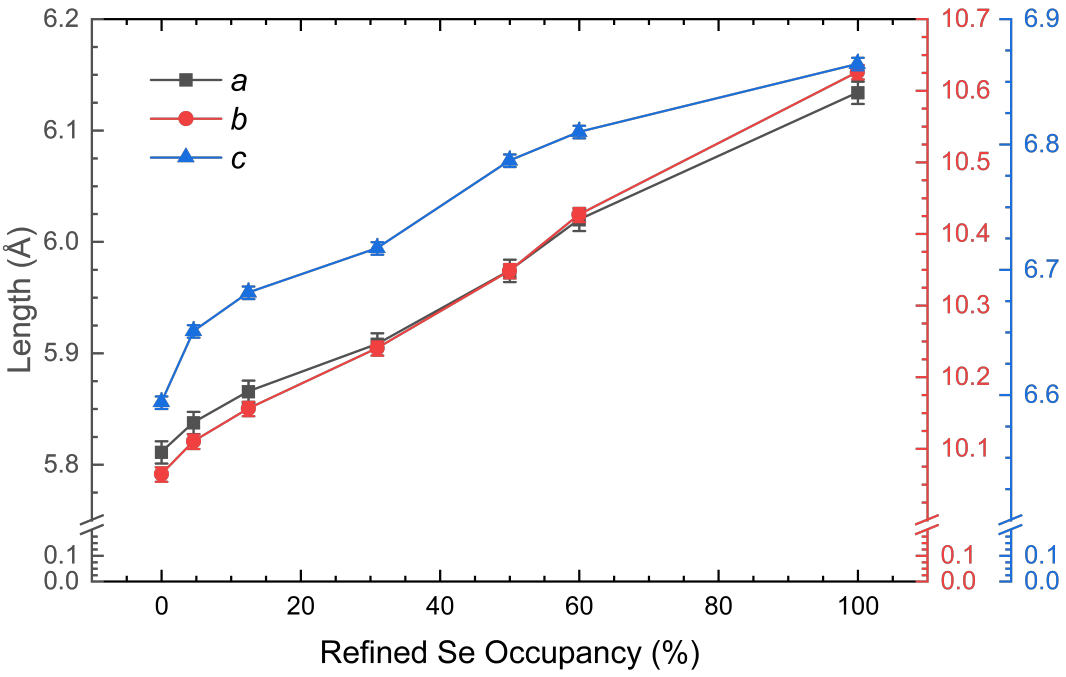



Figure 4.8: *abc* lattice parameters of $NiPQ_3$ compounds. For x = 0, parameters where derived from $NiPS_3$ CIF. For x = 4.6, 12.5, 60, 100, lattice parameters where derived from Rietveld refinement on PXRD data. For x = 31, 50, values were collected from solving the integrated intensities from SCXRD data. Se values are calculated values based on structural solutions.

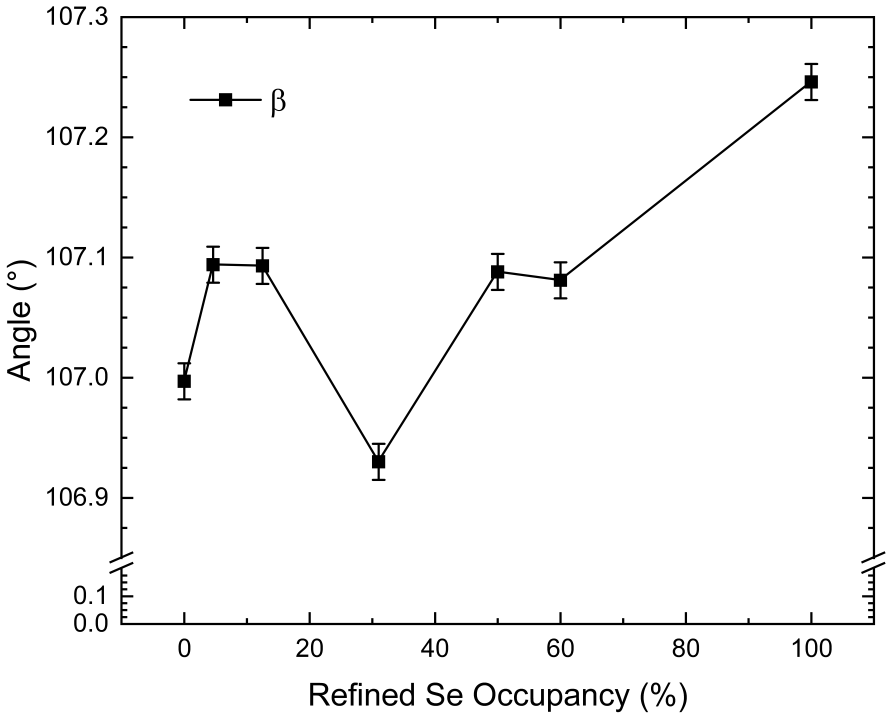



Figure 4.9: $\beta$ lattice parameter of $NiPQ_3$ compounds. Unlike the other bulk parameters this value does not change relatively much upon the introduction of additional selenium.

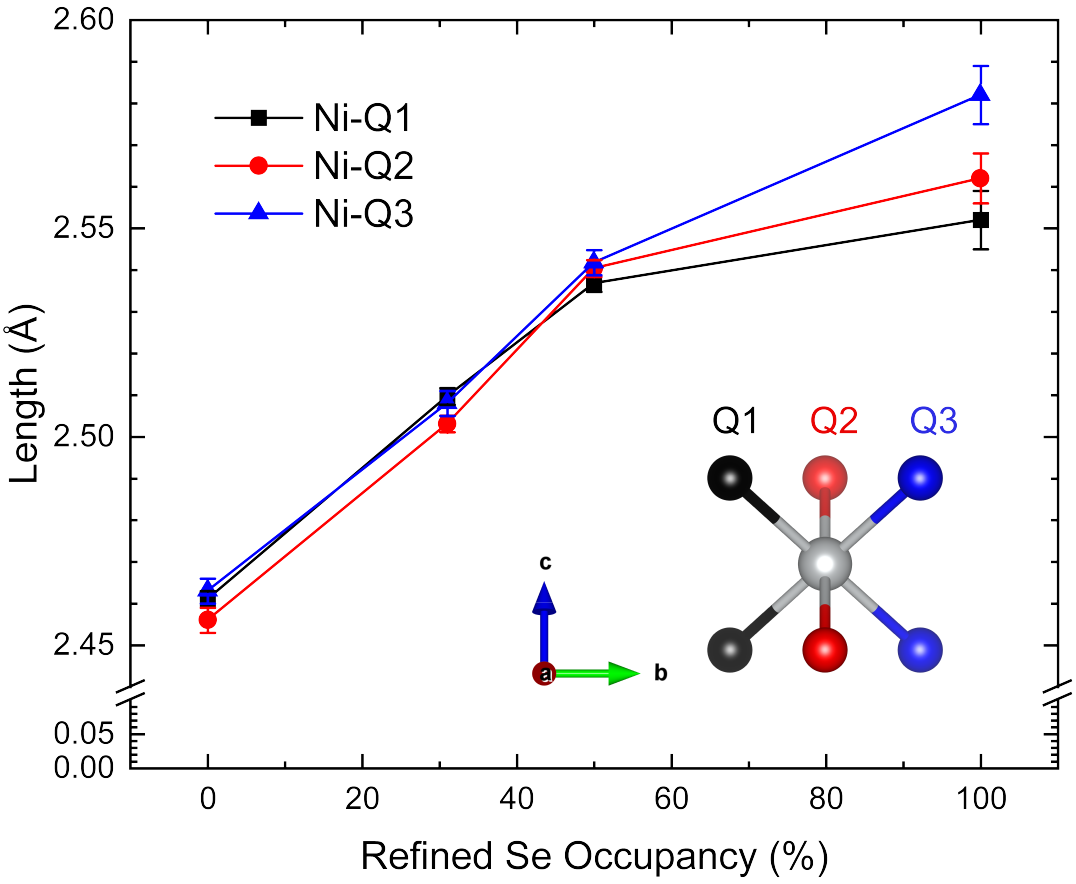



Figure 4.10: Bond lengths of chalcogen atoms with nickel. For x = 0, parameters where derived from $NiPS_3$ CIF. For x = 31, 50, parameter were measure from SCXRD while for x = 100 it was neutron powder diffraction.

tural solutions and powder Rietveld refinements, the relationship between selenium concentration and bond lengths was measured. The experimental results suggest that there is a general expansion in the length of bonds. Starting with the bonds between nickel and chalcogen atoms, we find that Ni is coordinated to six chalcogen atoms that form an octahedral. All Ni–Q bonds have a similar bond length until $NiPSe_3$ is formed. At this composition the Ni–Se bond lengths between begin to diverge from one another. The results are summarized in **Figure 4.10**.

Here **Figure 4.10** demonstrates that three discrete types of bond lengths can be observed

in $NiPSe_3$. From the perspective of the *a*-axis coming towards the viewer, the Ni-Q1 bond represents the chalcogen atoms bonded to the left of the Ni atom. Likewise Ni-Q2 represents the bond formed between the center chalcogen atoms and nickel. Lastly, Q3 is classified as the chalcogen atoms to the right of nickel.

It should be noted that chalcogen atoms Q1 and Q3 share the same Wyckoff position $8j$ while Q2 is $4i$. Theoretically, this configuration means that atomic position changes are coupled between Q1 and Q3. In contrast, because Q2 occupies a different Wyckoff position, allowed by crystal symmetry to potentially have divergent bond parameters from Q1 and Q3 atoms.

Coincidentally, in the same range of compositions listed in **Figure 4.10**, the atomic coordinates for Ni atoms on the *b*-axis shift from 0.33335 at x = 0% to 0.33300 at x = 100%. This shift in atomic position results in the nickel atoms shifting left relative to the axis provided by **4.10**. Thus, the Ni–Q bond length differences could be the result of Ni atomic position changes rather than chalcogen atomic position changes.

In terms of bond angles, the angles of the various Q-Ni-Q bonds suggest that a distorted octahedral shape forms between the Ni and chalcogen atoms. **Table 4.5** lists the angles of various arrangements that can occur among chalcogen and Ni atoms as a function of Se percent composition. According to experimental data, the angles formed by the chalcogen and Ni atoms are range bound by about one degree despite the introduction of Se. This result implies that selenium is insufficient to cause a dramatic change in bond geometry. Rather, there is some other variable that constrains the bond angles to a fixed range of values.

As for the $[P_2Q_6]^{4-}$ units, P–P and P–Q bond lengths where observed to increase with respect to Se composition (**Figure 4.11**). The creation of mixed anion phases did not cause two distinct P–Q bond lengths to form. Instead, all P–Q bond lengths are uniform. **Table 4.6** lists the bond angles of various arrangements among phosphorous and chalcogen atoms.

Bond angles were found to be constant within a range of about 1-2 degrees despite the appearance of Se. Overall, no dramatic change in geometry was observed $[P_2Q_6]^{4-}$ units.

Se substitution may have influenced Ni–Ni bond lengths. According to our experimental results, two discrete Ni–Ni bonds were observed. As demonstrated in **Figure 4.12**, the distances between neighboring Ni atoms are equivalent in $NiPS_3$. However, as Se concentration increases in $NiP(S_{1-x}Se_x)_3$ the distance between the Ni atoms becomes more visible with the separation reaching up to 0.02 Å in $NiPSe_3$.

Table 4.5: Bond angles of $NiP(S_{1-x}Se_x)_3$ for various arrangements between chalcogen atoms and nickel atoms. The labeling system follows **Figure 4.10** with the ' mark indicating the bottom chalcogen atom. Units for angles are in degrees while **X** is in percent.

| **Bond** | $x$ **= 0** | $x$ **= 31** | $x$ **= 50** | $x$ **= 100** |
|---|---|---|---|---|
| **Q1–Ni–Q2** | 85.23(8) | 84.33(6) | 84.53(5) | 85.7(2) |
| **Q1–Ni–Q3** | 85.06(6) | 84.28(6) | 84.50(5) | 85.3(1) |
| **Q2–Ni–Q3** | 85.1(1) | 84.30(6) | 84.48(6) | 85.4(3) |
| **Q1–Ni–Q3'** | 178.71(6) | 177.71(3) | 178.40(4) | 177.1(3) |
| **Q1–Ni–Q2'** | 93.94(8) | 94.21(6) | 94.50(5) | 92.6(2) |
| **Q1–Ni–Q1'** | 95.73(7) | 97.31(7) | 99.65(6) | 96.7(4) |
| **Q3–Ni–Q3'** | 94.17(9) | 94.17(7) | 94.38(6) | 92.8(4) |
| **Q2–Ni–Q2'** | 178.76(6) | 177.80(3) | 178.54(6) | 177.4(4) |
| **Q3–Ni–Q2'** | 95.75(9) | 97.21(6) | 96.51(6) | 92.4(3) |

Table 4.6: Bond angles of various arrangements between chalcogen atoms and phosphorus atoms in $NiP(S_{1-x}Se_x)_3$. Labeling system follows figure **Figure 4.11**. Units for angles are in degrees while **X** is in percent.

| **Bond** | $x$ **= 0** | $x$ **= 31** | $x$ **= 50** | $x$ **= 100** |
|---|---|---|---|---|
| **Q1–P–Q3** | 85.23(8) | 84.33(6) | 84.53(5) | 85.7(2) |
| **Q1–P–Q2** | 85.06(6) | 84.28(6) | 84.50(5) | 85.3(1) |
| **Q3–P–Q2** | 85.06(6) | 84.28(6) | 84.50(5) | 85.3(1) |
| **Q1–P–P** | 85.1(1) | 84.30(6) | 84.48(6) | 85.4(3) |
| **Q3–P–P** | 85.1(1) | 84.30(6) | 84.48(6) | 85.4(3) |
| **Q2–P–P** | 178.71(6) | 177.71(3) | 178.40(4) | 177.1(3) |

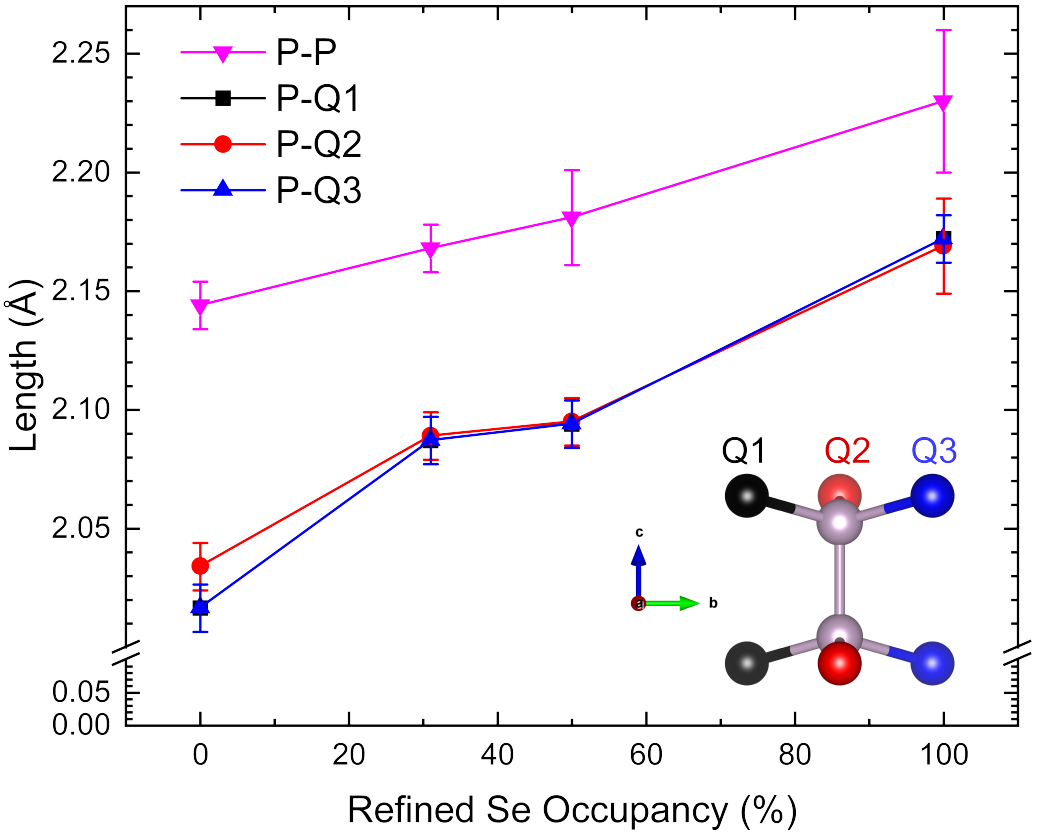



Figure 4.11: Bond lengths of chalcogen atoms with phosphorus and the P-P dimer in $NiP(S_{1-x}Se_x)_3$. The labeling used to differentiate the chalcogen atoms are not related to **Figure 4.10** and should be look at in isolation.

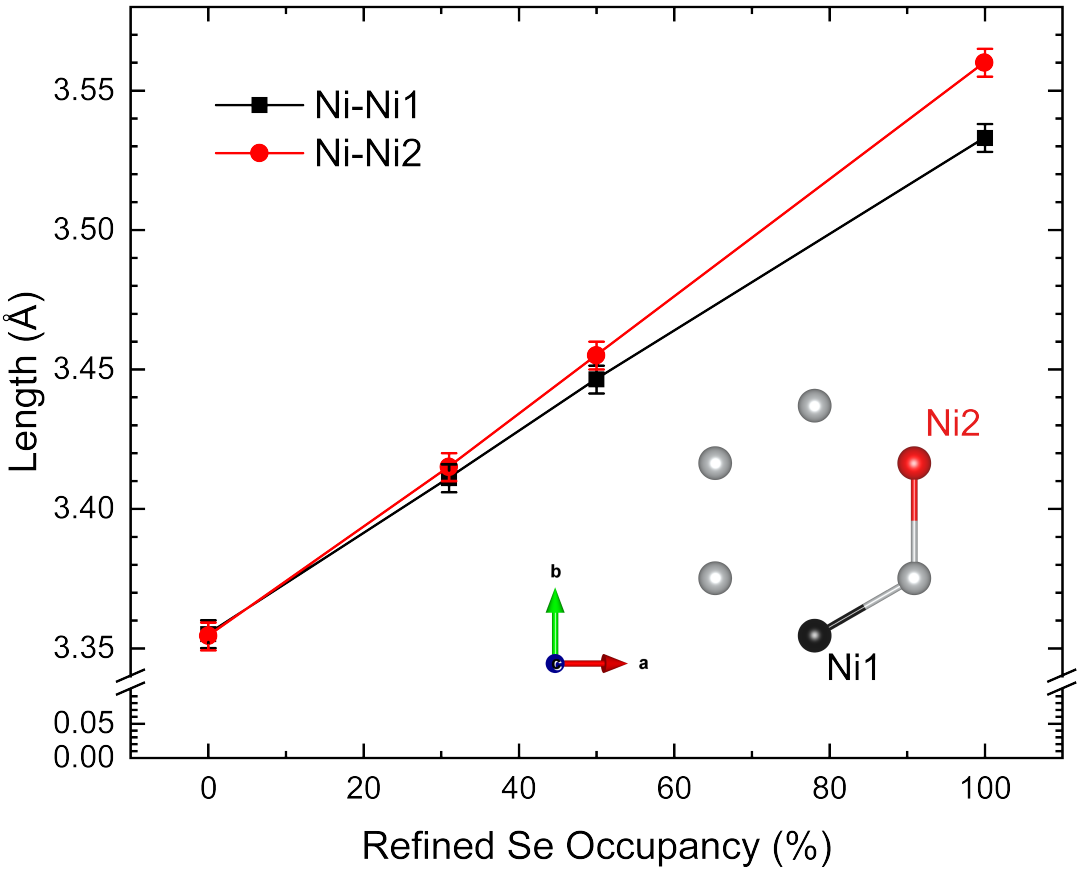



Figure 4.12: Bond lengths of between different neighboring nickel atoms in $NiP(S_{1-x}Se_x)_3$. The length between the Ni atoms begins to differ as more Se is introduced to the system.

### 4.3.2 Bulk Magnetic Property Measurements

According to magnetic susceptibility results, mixed anion in $NiP(S_{1-x}Se_x)_3$ compounds are observed to be antiferromagnetic compounds. In fact, powder magnetic susceptibility of several compositions can be seen in **Figure 4.13**, along with 1st derivative plots, (**Figure 4.14 - 4.15**), of $NiPS_{1.5}Se_{1.5}$ and $NiPSe_3$. The decrease in susceptibility is a sign that a portion of the magnetic moments are aligned against the direction of the applied field which is indicative of antiferromagnetic behavior.[106–108]

Another feature of note is the relatively constant susceptibility values before the onset of magnetic ordering. If $NiP(S_{1-x}Se_x)_3$ was in a paramagnetic state then there should be a general increase in susceptibility as temperature decreases.[172] The lack of observation of that phenomena implies that the flat curve shape from 200 K to 300 K is some transition state between the paramagnetic and antiferromagnetic state. The key implication from **Figure 4.13** is that susceptibility measurements for $NiP(S_{1-x}Se_x)_3$ must be done at higher temperatures in order to observe the paramagnetic state, which will allow for a proper Curie-Weiss analysis.

Below 50 K susceptibility begins to rise once again. This rise in susceptibility is due to $NiSe_2$. $NiSe_2$ is a paramagnetic material and has an observed susceptibility of $2 \times 10^{-4}$ emu/mol. This value is within an order of magnitude of the observed susceptibility for $NiP(S_{1-x}Se_x)_3$ and could be the origin for this rise in magnetic susceptibility at low temperatures.[179–181]

In order to find the Neél temperature, the local maximum of the first derivative between magnetic susceptibility and temperature was found. Given that antiferromagnetic materials exhibit gradual or second order transitions, an estimate for the transition temperature can be established by finding the local maximum in the slope. This point represents that the rate of change in susceptibility is decreasing symbolizing that magnetic moments are transitioning

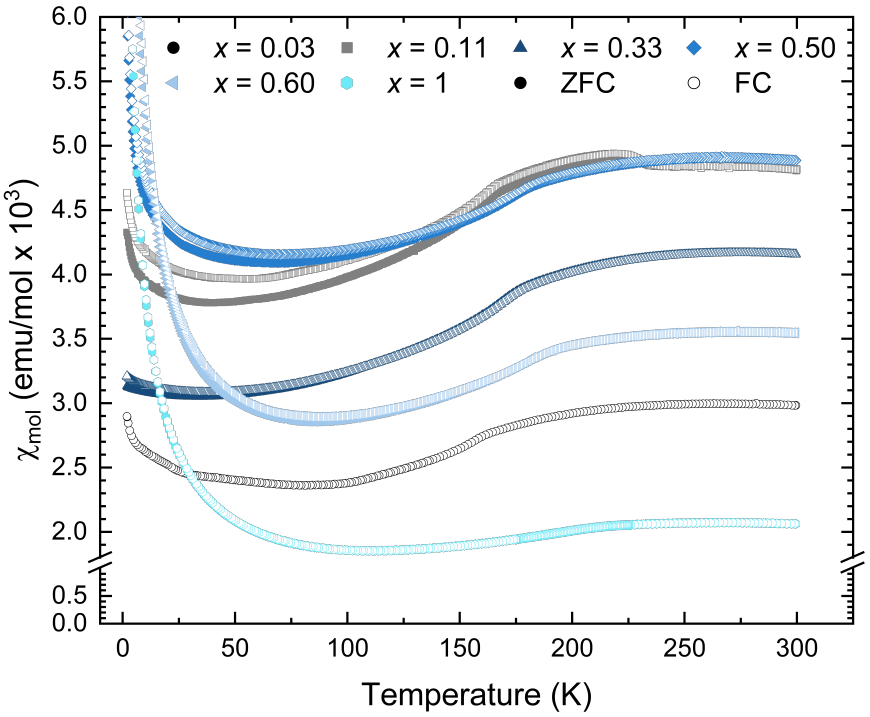



Figure 4.13: Powder magnetic susceptibility of $NiP(S_{1-x}Se_x)_3$

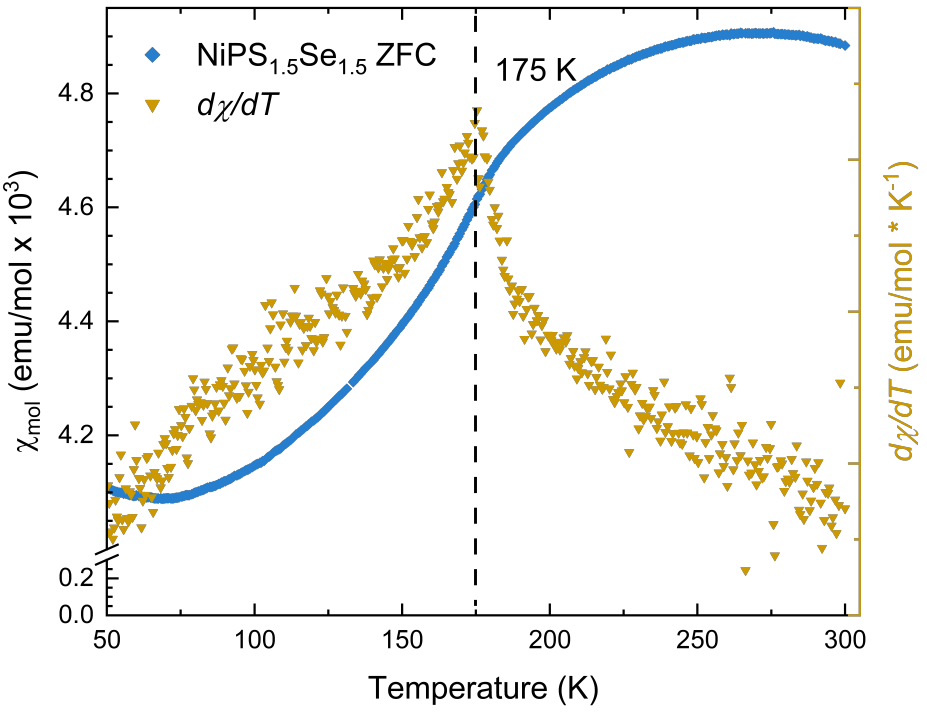



Figure 4.14: 1st derivative of powder magnetic susceptibility of $NiPS_{1.5}Se_{1.5}$

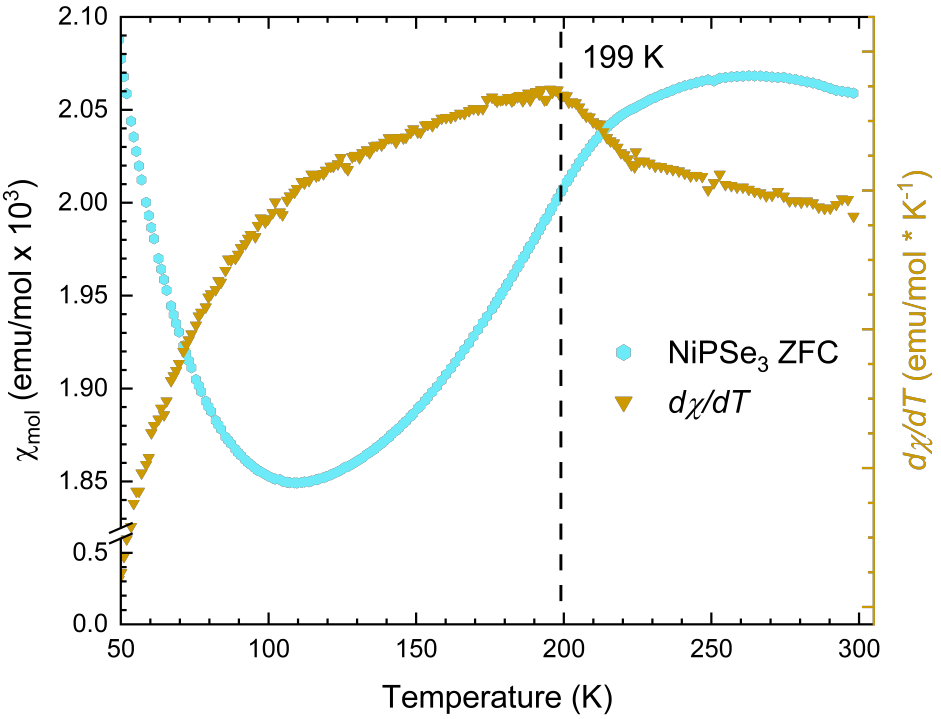



Figure 4.15: 1st derivative of Powder magnetic susceptibility of $NiPSe_3$

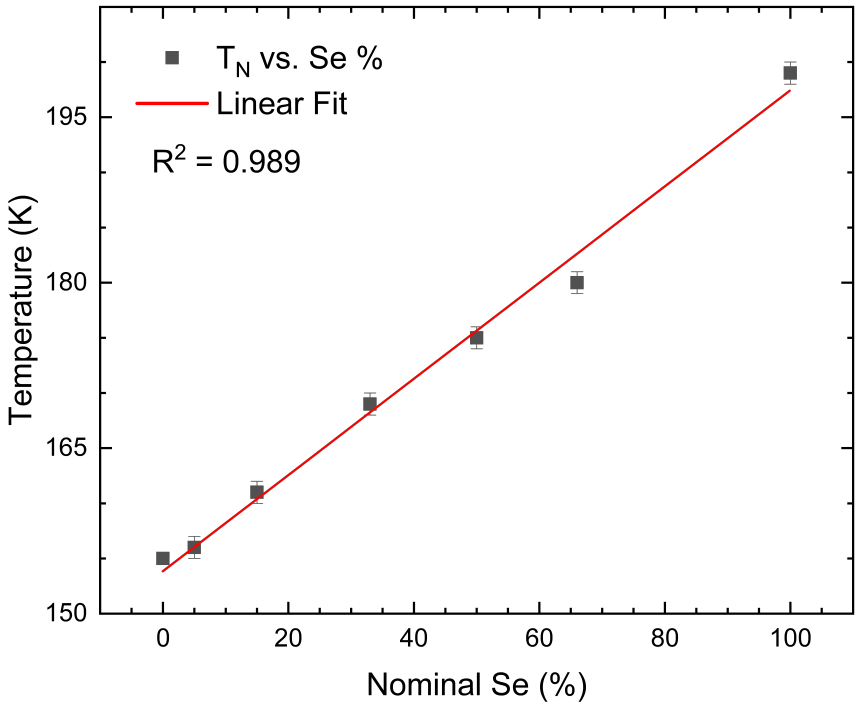



Figure 4.16: Using the 1st derivative approach, the $T_N$ was estimated for $NiP(S_{1-x}Se_x)_3$. A general increase in $T_N$ is observed when more Se is introduced.

to an antiferromagnetic state from the paramagnetic state. . A plot of calculated Neél temperature from this method versus nominal Se concentration results in a near perfect linear correlation (**Figure 4.16**). This result implies that there is direct correlation between the amount of Se in $NiP(S_{1-x}Se_x)_3$ an Neél temperature.

### 4.3.3 Magnetic Structure Analysis of Se-Subsituted $NiPS_3$

To determine the magnetic structure of $NiP(S_{1-x}Se_x)_3$, powder neutron diffraction was performed on four compositions (X = 0.04, 0.12, 0.60, 1) at 300 K and 10 K. **Figures 4.17 to 4.20** demonstrates the Rietveld refinement for these four compositions at 300 and 10

K. The key difference between the 300 K and 10 K data is the appearance of the (010) reflection, which appears before the (001) reflection near 0.5 $Å^{-1}$. The observation of a new reflection implies that $NiP(S_{1-x}Se_x)_3$ is an antiferromagnetic material. Interestingly, this (010) reflection would mean that the magnetic space group has lower symmetry than the crystallographic space group $C2/m$ due to the (010) reflection being systemically absent in $C2/m$ space group. Furthermore, from this (010) reflection we can also derive the propagation vector $\vec{k}$ = [010]. This result means that the magnetic unit cell has the same lattice parameters as the nuclear unit cell.

**Figure 4.21** displays the neutron diffraction results at this higher Å range. As one can see no magnetic peaks are observed up to 20.5 Å. This result provides additional evidence that $\vec{k}$ = [010]

Considering the symmetry breaking reflection it was decided to model the magnetic structure using the $P1$ magnetic space group. An additional constraint was added to the structural refinement by setting the magnetic moment of nickel minority sites to zero. Although all Ni atoms are magnetically active, due to the lack of a well-defined model that accounts for the structural disorders in $NiP(S_{1-x}Se_x)_3$, only Ni atoms in the $4g$ site had moments added to them. A Rietveld refinement that only includes the $4g$ Ni atoms should provide a sufficient approximation of the $NiP(S_{1-x}Se_x)_3$ magnetic structure because over 80% of all nickel atoms form a honeycomb lattice with no structural disorders according to **Figure 4.4**

**Table 4.7** lists the values of the magnetic moment extracted from the Rietveld refinement. The magnetic moments in $NiP(S_{1-x}Se_x)_3$ were observed to be near 1.5 $\mu_B$ in the $a$-direction and range between 0.8 to 1.3 $\mu_b$ in the $c$-axis. The total magnetic moment was calculated to be near 1.6 $\mu_B$ for all compositions.

The magnetic moment's preference for the $c$-axis direction can be partially explained by the lack of additional magnetic peaks with strong intensities to rival the (010) reflection.

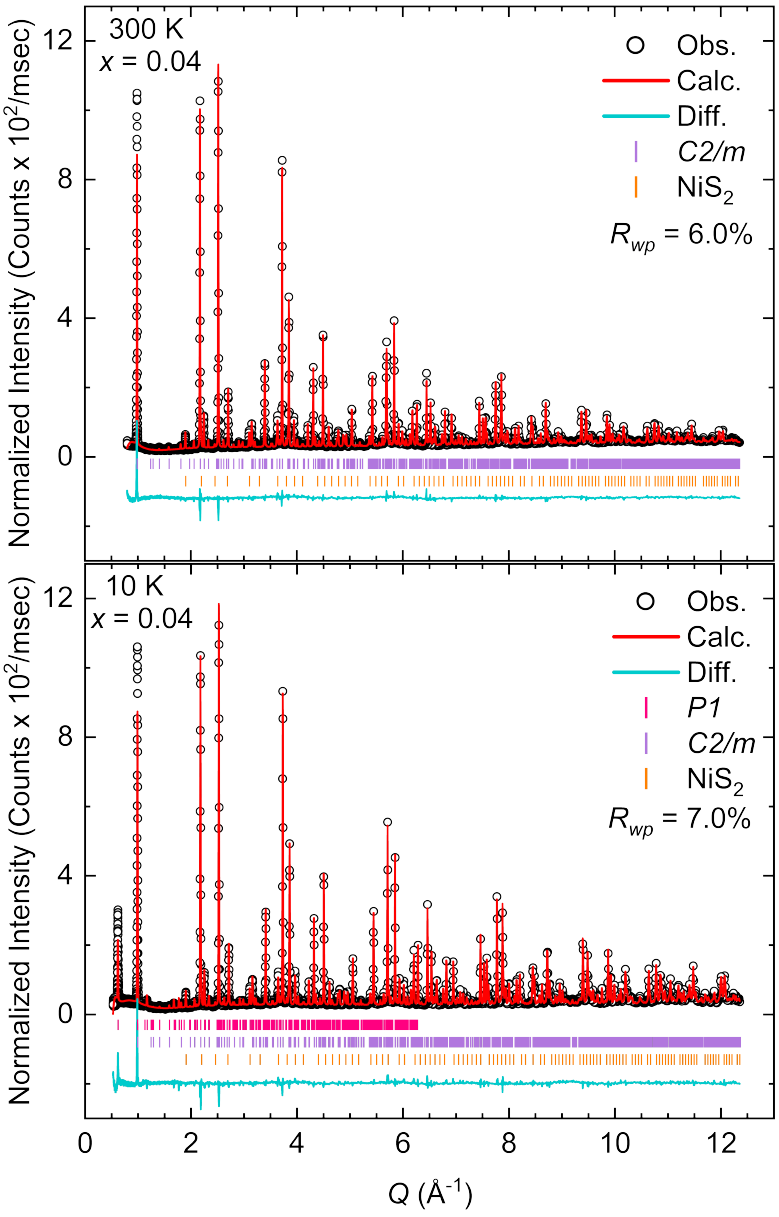



Figure 4.17: (Top) Rietveld refinement of NPD data of $NiP(S_{1-x}Se_x)_3$ where $x = 0.04$ at 300 K. (Bottom) 10 K

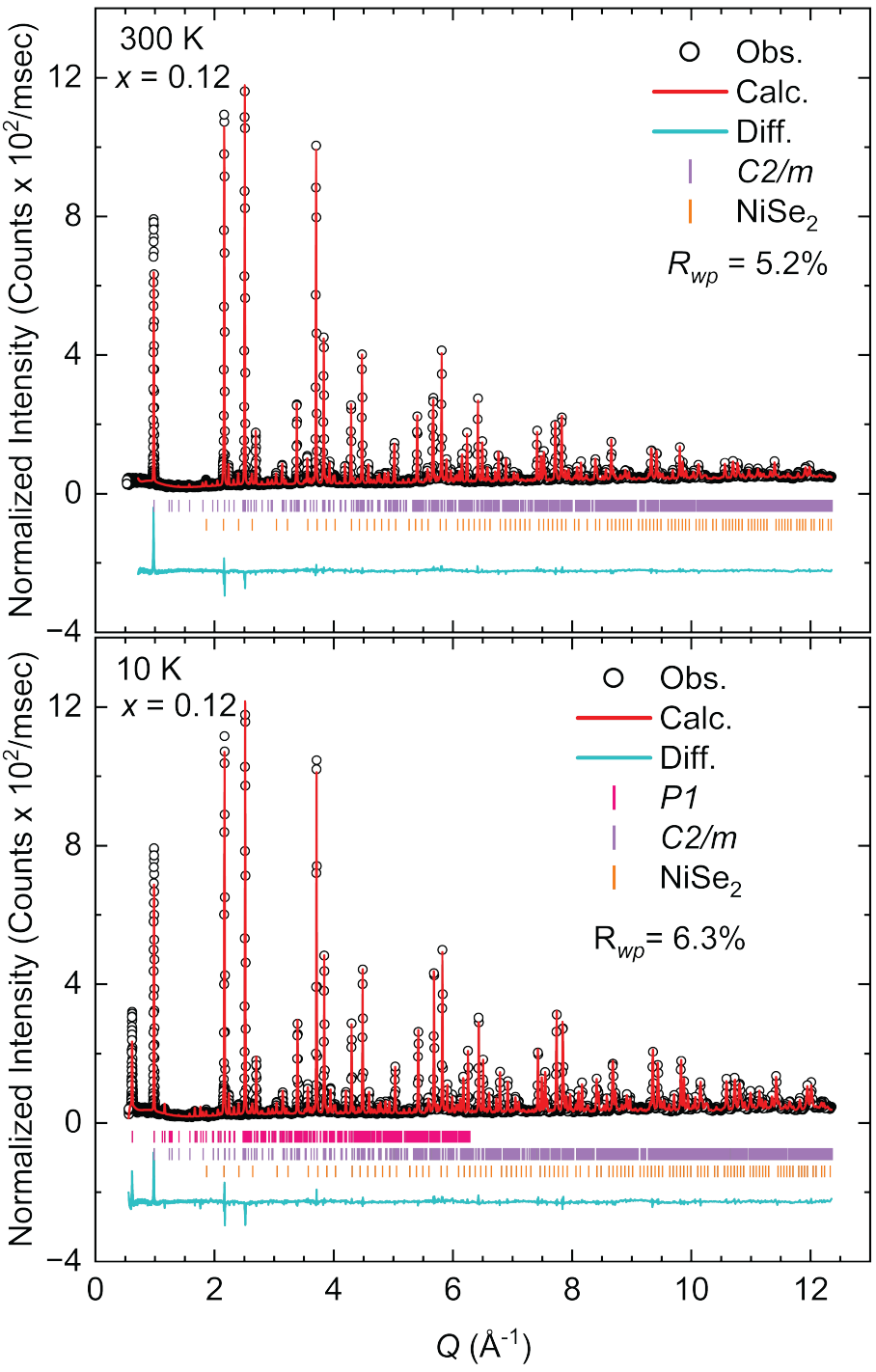



Figure 4.18: (Top) Rietveld refinement of NPD data of $NiP(S_{1-x}Se_x)_3$ where $x = 0.12$ at 300 K. (Bottom) 10 K

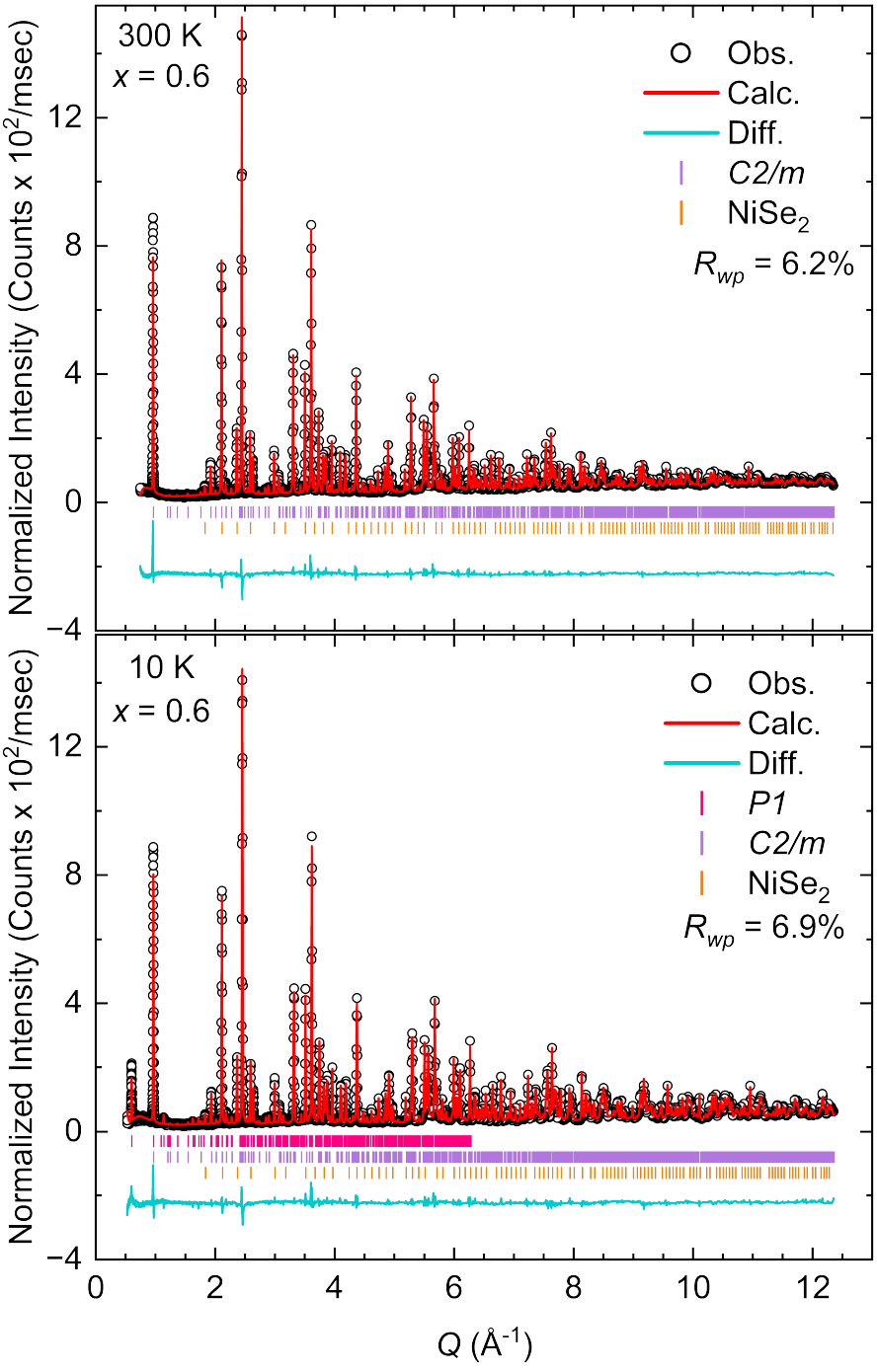



Figure 4.19: (Top) Rietveld refinement of NPD data of $NiP(S_{1-x}Se_x)_3$ where $x = 0.60$ at 300 K. (Bottom) 10 K

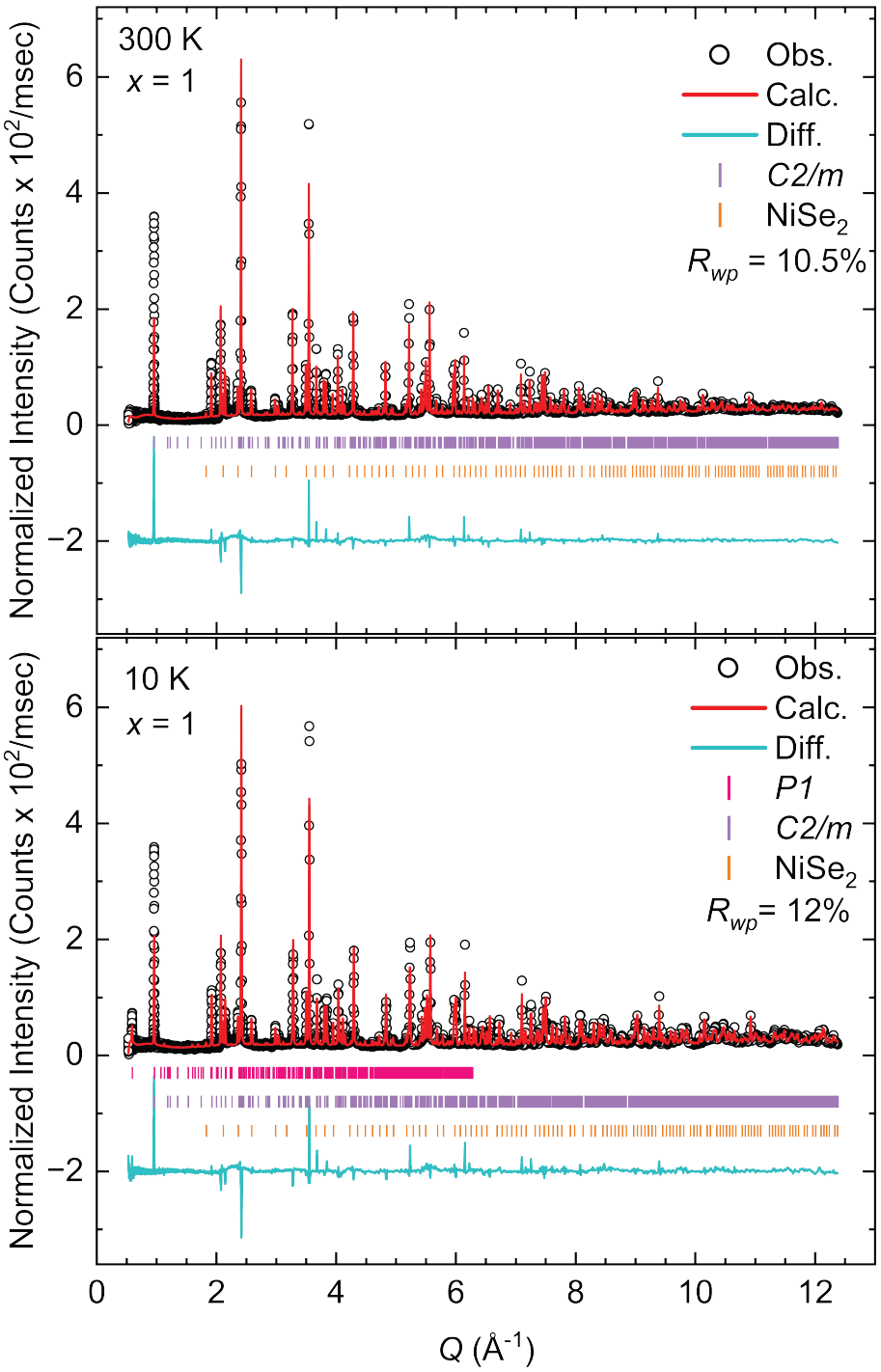



Figure 4.20: (Top) Rietveld refinement of NPD data of $NiP(S_{1-x}Se_x)_3$ where $x = 1$ at 300 K. (Bottom) 10 K

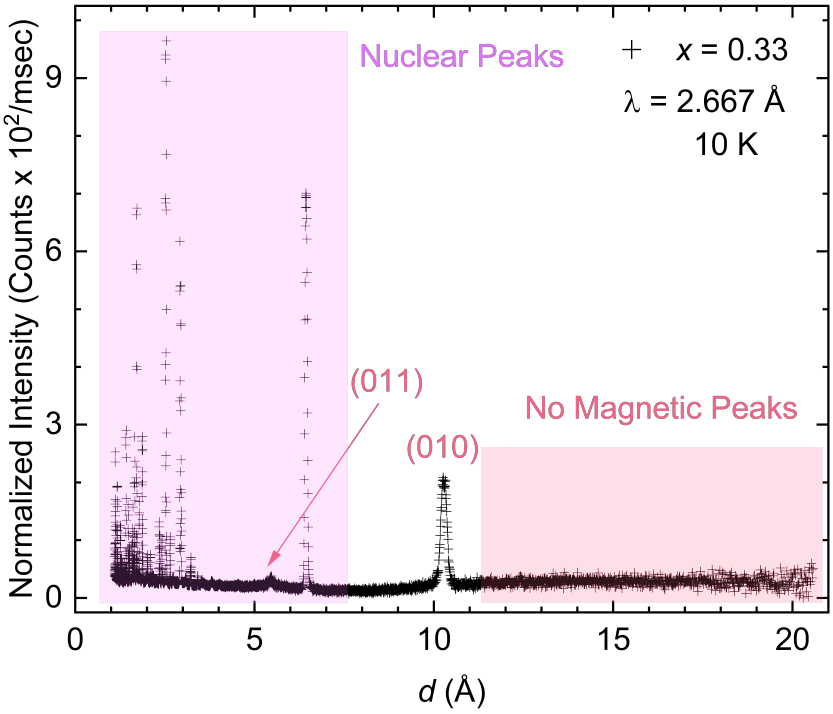



Figure 4.21: Neutron Powder diffraction of $NiP(S_{1-x}Se_x)_3$ where x = 0.33 at 10 K. No Magnetic peaks were observed beyond (010) reflection.

Since the (010) reflection is parallel to the *ac*-plane, it implies that the magnetic moments are oriented partially to the *a* and *c*-axis. Without the input from additional magnetic reflections, any moment direction along the *ac* plane will add intensity towards the (010) reflection.

It is possible that the combination of polycrystalline samples, structural deformities due to grinding and internal layer shifting all work together in bring a factor of randomness that prevents the observation of higher Q magnetic reflections, which only leaves (010) or reflections on the order of the unit cell to appear. Thus, to counteract the problems with the measurement of polycrystalline samples, neutron diffraction experiments were performed on single crystals.

Single-crystal neutron diffraction was performed at the TOPAZ instrument utilizing two different compositions of $NiP(S_{1-x}Se_x)_3$: X = 0.29 and X = 0.43. The nominal target composition for both of these compounds were X = 0.33 for the former and X = 0.5 for the latter. The experimental composition was derived from room temperature neutron diffraction data. This difference between nominal and experimental compositions indicates that there is some amount of selenium that is inhibited from incorporating in $NiP(S_{1-x}Se_x)_3$ during the CVT crystal growth process.

**Figure 4.23** and **4.24** display the (0KL) precession images derived from the TOPAZ instrument for the X = 0.29 and X = 0.43 samples at 300 K and 100 K. The most notable

Table 4.7: Magnetic Moments of $NiP(S_{1-x}Se_x)_3$ from neutron powder diffraction. $M_y$ was constrained to zero due to the excessive error values from the Rietveld refinement.

| **Se %** | $\mathbf{M}_x$ | $\mathbf{M}_y$ | $\mathbf{M}_z$ | $\mathbf{M}_{tot}$ |
|---|---|---|---|---|
| ***x* = 0.04** | 1.5(1) | 0 | 0.9(1) | 1.6(1) |
| ***x* = 0.12** | 1.6(1) | 0 | 0.9(1) | 1.6(1) |
| ***x* = 0.6** | 1.6(1) | 0 | 1.0(1) | 1.6(1) |
| ***x* = 1** | 1.4(3) | 0 | 1.4(4) | 1.5(7) |

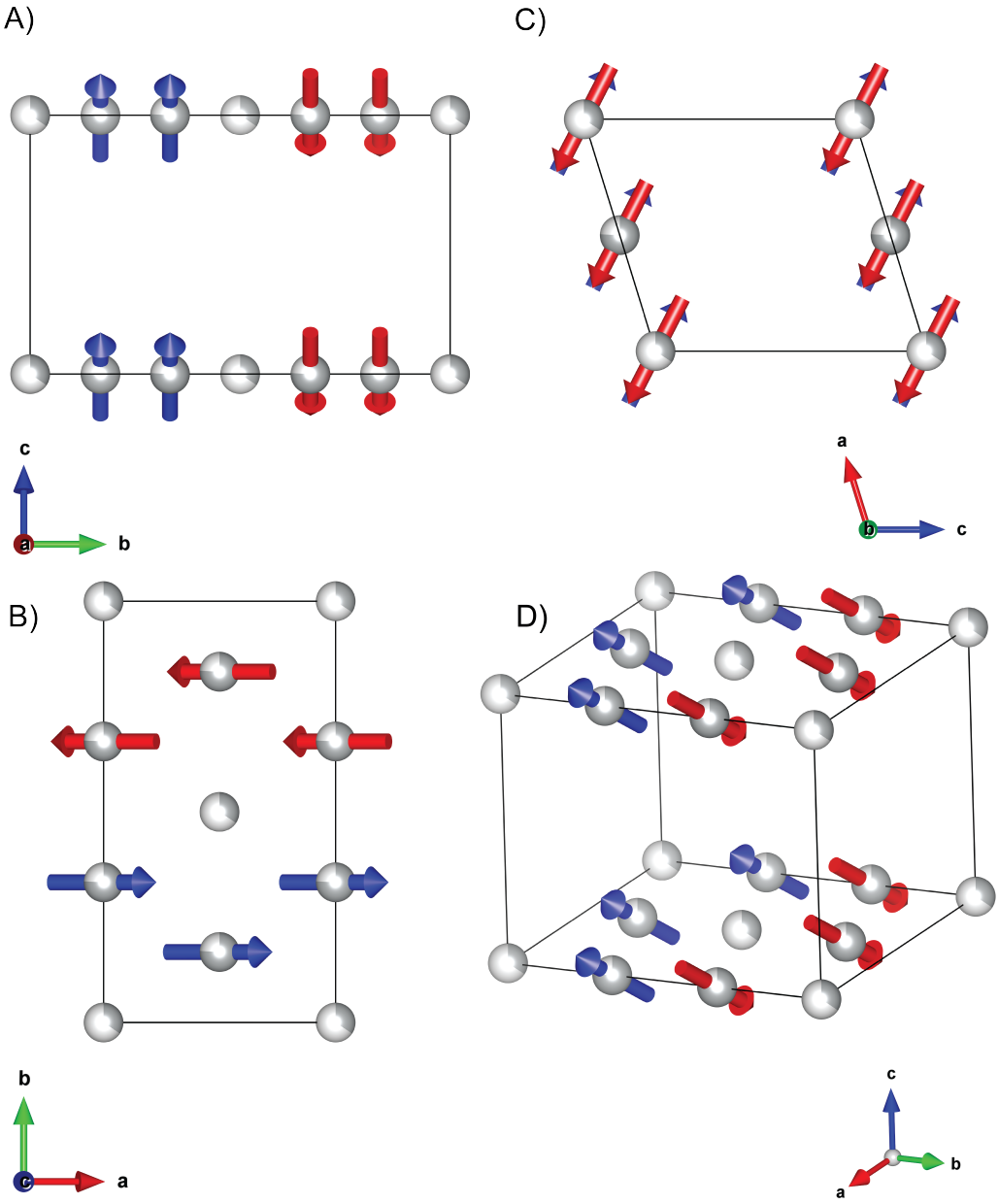



Figure 4.22: Proposed Magnetic unit cell from Rietveld refinement on NPD data for $NiP(S_{1-x}Se_x)_3$ from different viewing perspectives. A) *a*-axis. B) *c*-axis. C) *b*-axis. D) [111] zone axis.

difference between the two samples is the higher signal intensity and prevalence of vertical streaks along the $L$-direction demonstrated by the x = 0.43 sample. In contrast, the X = 0.29 sample has much less intense peaks, but no vertical streaks. Additionally, a high background can be observed for the X = 0.29 sample. This background comes from the growth of ice crystals on the sample, which means that during the measurement the instrument was exposed to water.

Nevertheless, the contrast in data quality can be attributed to sample mass and thickness with regards to reflection intensity and vertical streaks. The X = 0.43 sample weighed 3.4 mg and has a thickness near 0.15 mm. The X = 0.29 sample has a mass near 0.8 mg and a thickness of 0.01 mm. Additionally, due to time constraints, the total measurement time for the X = 0.29 sample was about half compared to the X = 0.43 sample.

Comparing the 300 K and 100 K measurements, we observe the appearance of new magnetic reflections near $(01L)$ and $(05L)$ indicating that $NiP(S_{1-x}Se_x)_3$ has antiferromagnetic ordering. The (010) reflection was also observed, which is indicative of a magnetic propagation vector of $\vec{k}$ =[010] for $NiP(S_{1-x}Se_x)_3$ is [010]. Thus, both NPD and SCND results both agree on the magnetic propagation vector.

Some small amount of streaking can be observed in the magnetic reflections for the X = 0.43 sample, however, the intensities are generally distinguishable from each other compared to their nuclear reflection counterparts. This difference in streaking intensity implies that the same structural deformities that affect the nuclear structure are not as influential to the magnetic structure.

For the $x$ = 0.29 sample, the intensities are much smaller. Yet, no extensive streaks can be found. However, due to the high background, caused from the scattering of ice crystals, the relatively low signal to noise ratio from the magnetic reflections will increase the error in the final structure solution.

Assuming that the origin of the vertical streaking comes from the crystal and not some

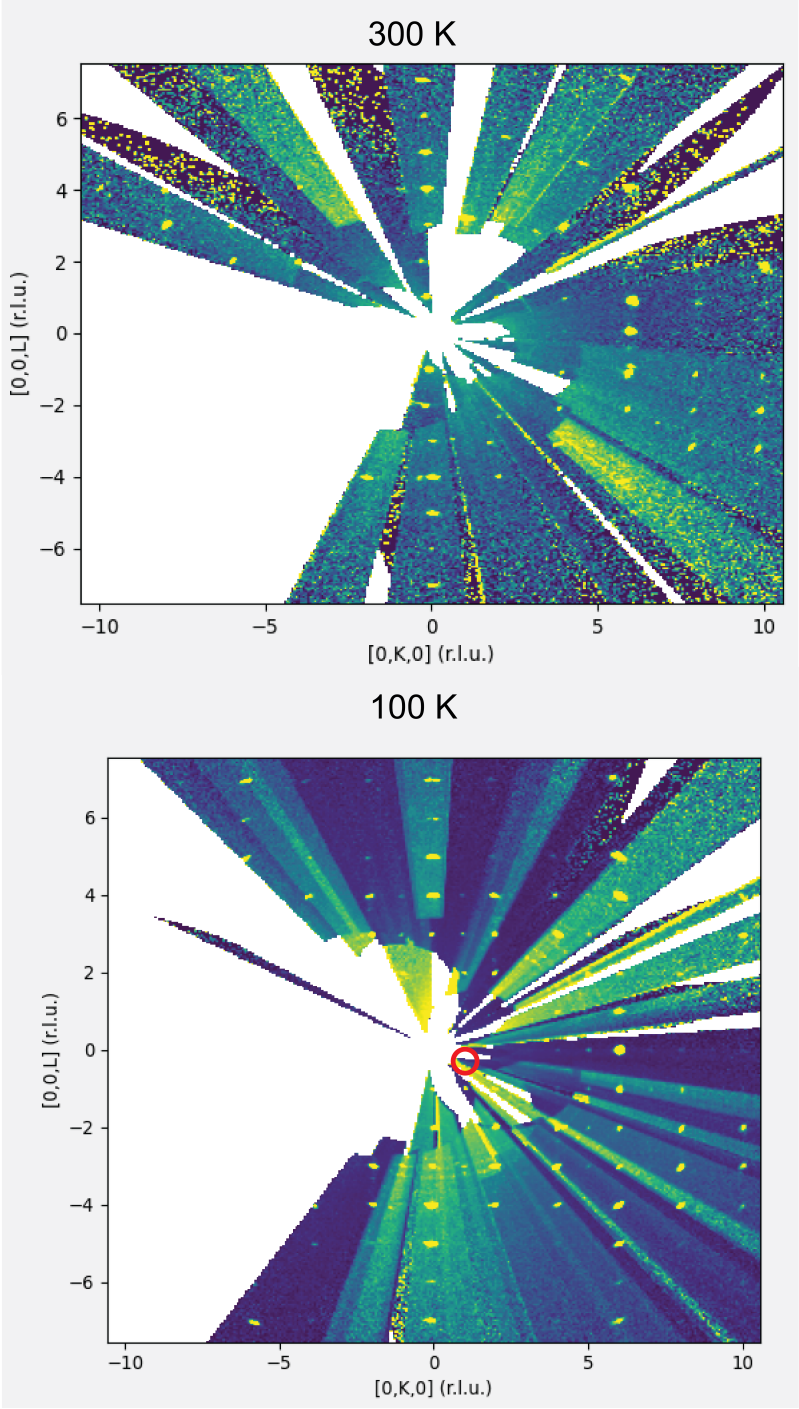



Figure 4.23: Single-crystal neutron diffraction (0KL) precession image of $NiP(S_{1-x}Se_x)_3$ where $x$ = 0.29. (Top) Measured at 300 K. (Bottom) Measured at 100 K. Lower temperature scan was measured for longer and at additional frames. $(0\bar{1}0)$ is highlighted by the red circle.

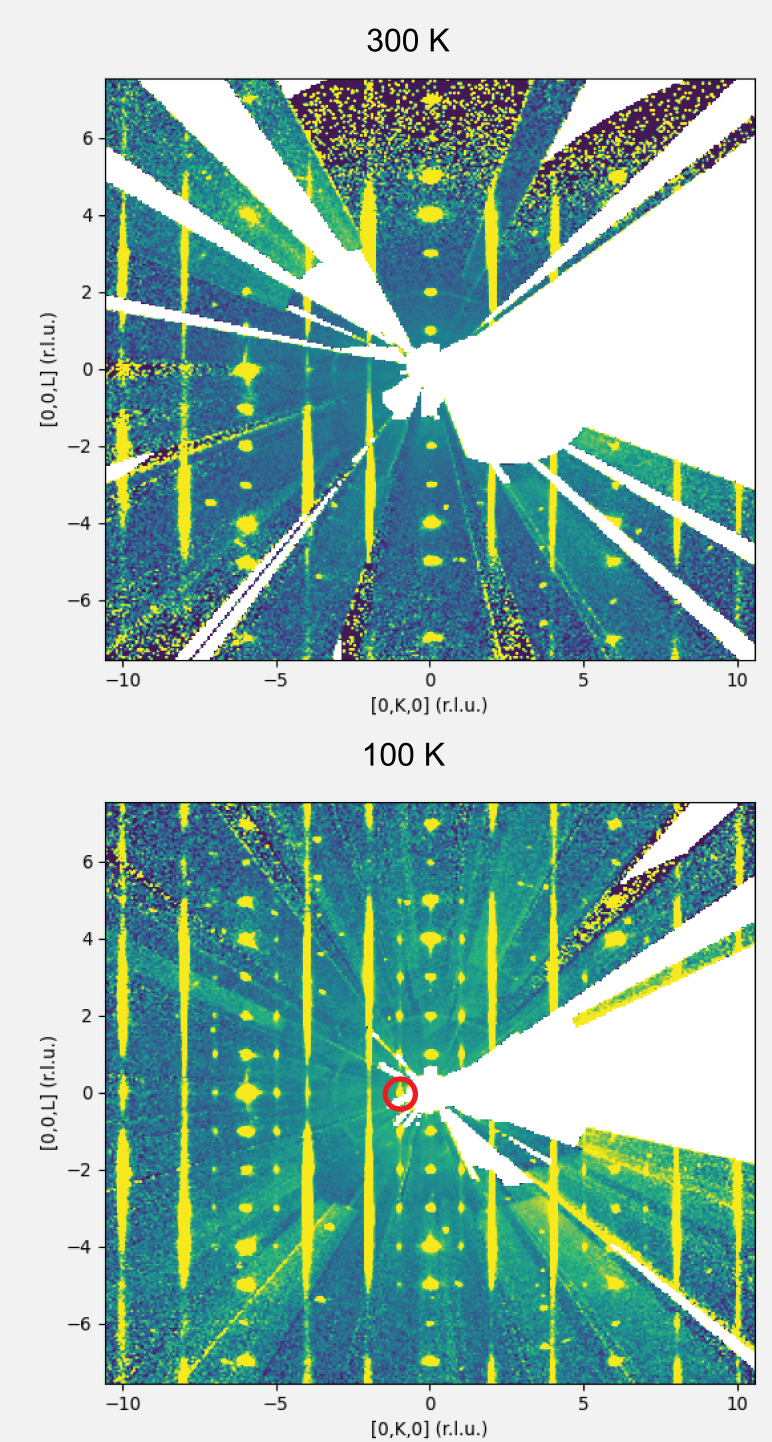



Figure 4.24: Single-crystal neutron diffraction (0KL) precession image of $NiP(S_{1-x}Se_x)_3$ where $x$ = 0.43. (Top) Measured at 300 K. (Bottom) Measured at 100 K. Lower temperature scan was measured for longer and at additional frames. (010) is highlighted by the red circle

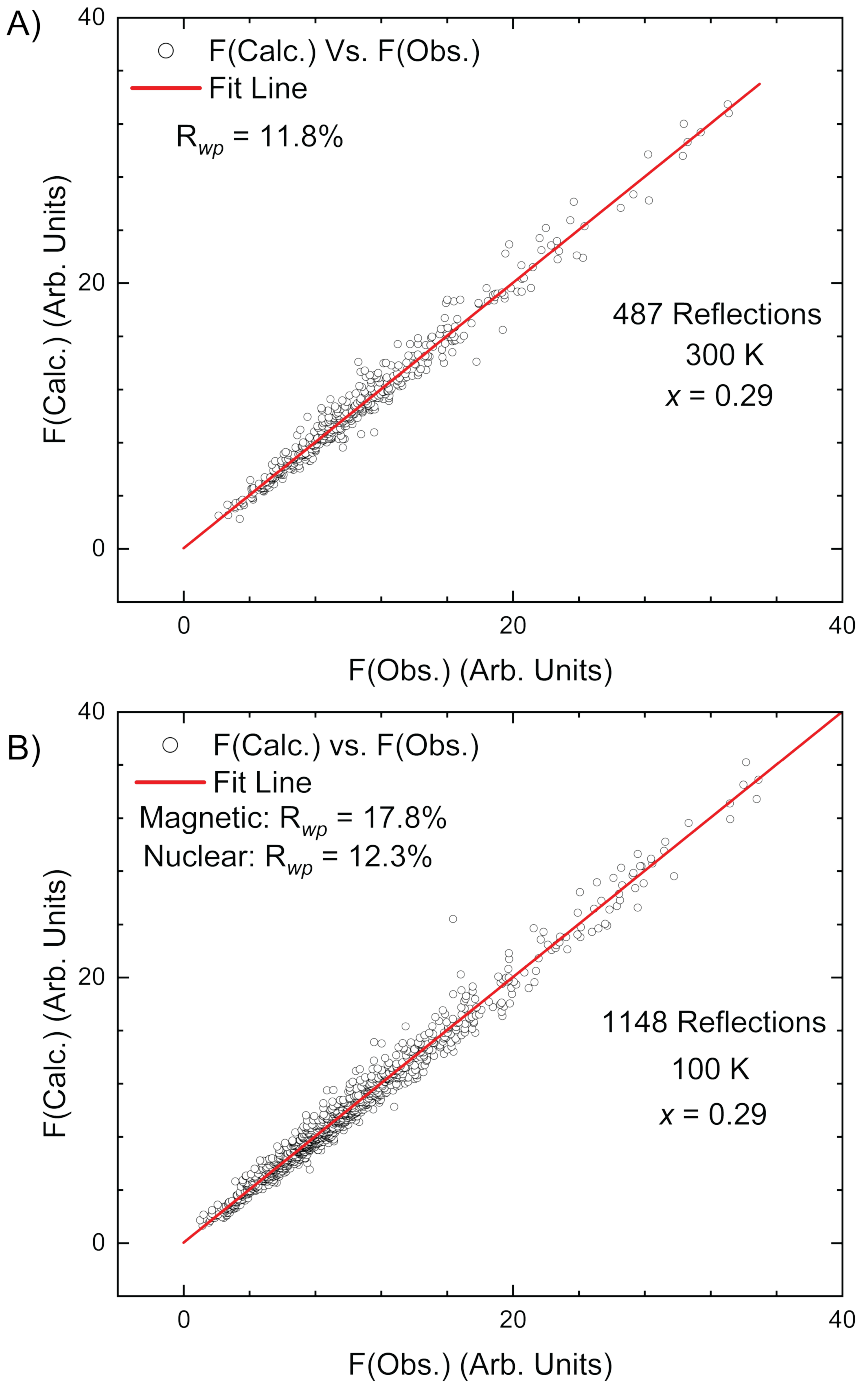



Figure 4.25: Calculated intensities versus. observed intensities plot for $NiP(S_{1-x}Se_x)_3$ where $x$ = 0.29. A) Represents data collected at 300 K. B) 100 K.

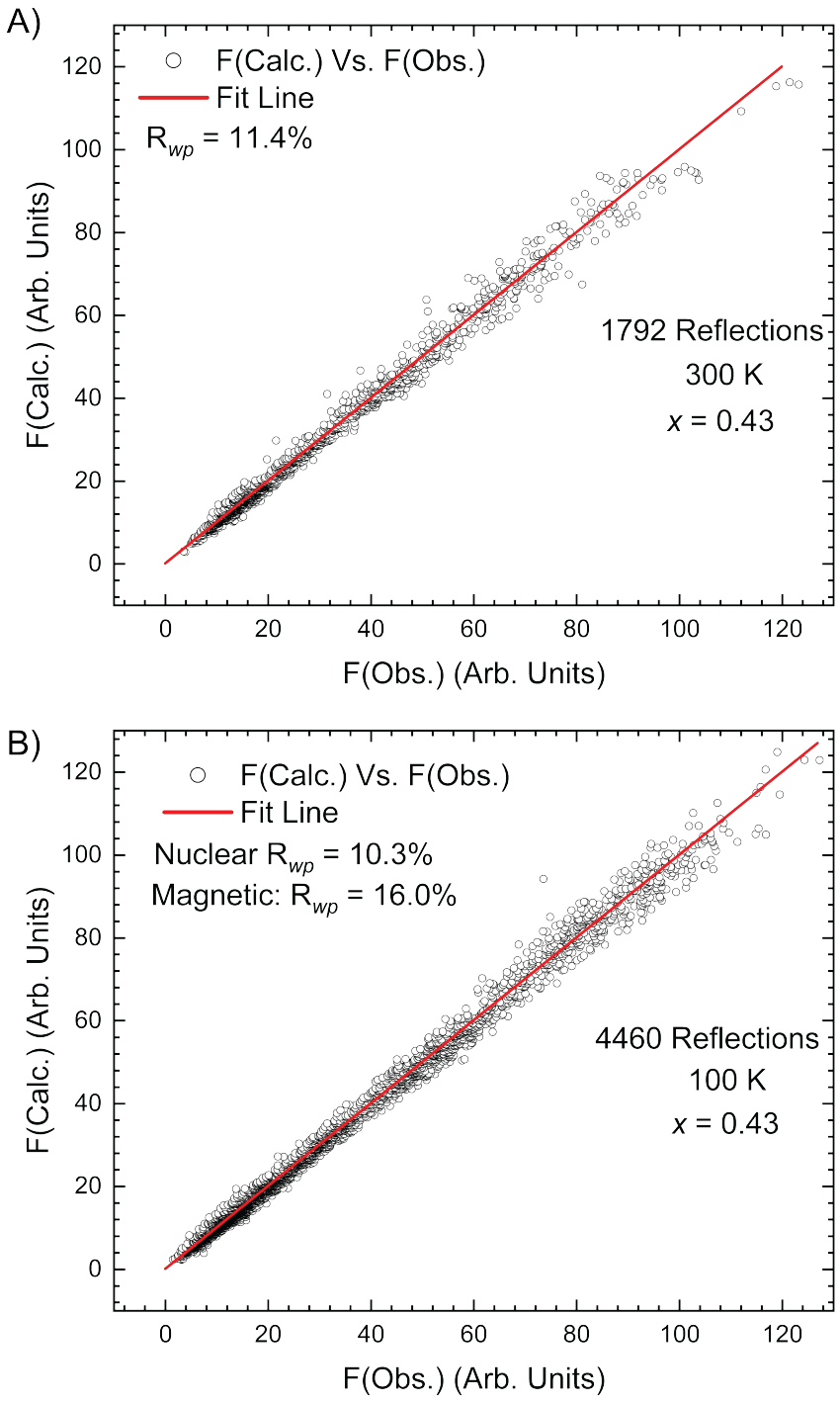



Figure 4.26: Calculated intensities versus observed intensities plot for $NiP(S_{1-x}Se_x)_3$ where $x$ = 0.43. A) Represents data collected at 300 K. B) 100 K.

residual impurity, these streaks can be thought as structural deformations of stacked layers that are all shifted from each other in the *ab*-plane. In the diffraction of single crystals, a reflection is the result of a repeating array of atoms that are spaced apart by a certain distance. For example, the (010) reflection indicates that there is a plane of atoms that are spaced apart by a length of one *b*-axis that constructively interfere with the incoming radiation. This interaction is what gives rise to the observation of the (010) reflection. Each reflection represents specific areas within a crystal unit cell that are separated by a particular distance that fulfills the conditions for Bragg diffraction. Thus, if a set of reflections, such as (02*L*), are all covered by vertical streaks, than it could suggest that there are regions within the unit cell that are polycrystalline which results in vertical streaking in a similar manner to how a powder diffraction pattern forms diffraction rings.

How the d-spacing would vary in this system is unclear, because certain reflection sets, such as (06*L*), exhibit no streaks, yet (02*L*), (04*L*), (08*L*), and (010*L*) do have streaks. Furthermore, the streaks do not appear to affect reflections oriented in the axes, such as (0*K*0) and (00*L*), meaning that these artifacts are tied to local structure and not on the scale of the unit cell. If these deformities were at the size of the unit cell, then the streaking would be seen at (00*l*) and (0*k*0). One potential explanation is that the sample could consists of many single crystals that are stacked and co-aligned to each other. Each co-aligned crystal would have nearly identical lattice parameters, but the placement of all of the atoms just sightly distorted for each crystal such that each crystals produces a (0*kl*) with different d-spacing. More plates means more (0*kl*) reflections with varying d-spacing values which would result in the vertical streak patterns observed in the precession images. Considering that the streaks occur in several reflections with varying *l*-values but no streaks were observed for (*hk*0) reflections, this phenomenon must include atoms within the *ab*-plane.

The structural solutions generated neutron diffraction data produced a relatively good fit. **Figure 4.25 – 4.26** displays the calculated vs. observed intensities plot for both sample

at 300 and 100 K. The residual parameters for both the nuclear and magnetic structure were under 15% and 20%. If these values are compared to previous neutron diffraction experiments done by Wildes *et.al*, then this work's residuals are lower. Lower residuals imply that the results displayed here are comparable if not higher in accuracy compared to previous works.

Despite the lower residuals, an argument can be made on why the structure solution for the X = 0.29 sample is the accurate model. The X = 0.29 sample has no observable vertical streaks which enable us to observe reflections that were previously masked by the structural deformities. In fact, because of the lack of these streaks, the structure solution for $NiP(S_{0.73}Se_{0.27})_3$) does not require the use of additional Wyckoff sites for the nickel and phosphorus atoms. Thus, this thin crystal gives us idea of how the crystal structure appears without significant structural distortions.

Nevertheless, the structure solutions for both samples point towards the magnetic unit cell exhibiting a lower symmetry than its nuclear unit cell because neutron diffraction results for both samples exhibit a reflection at (010). This reflection is systemically absent in $C2/m$ space group. Thus, the magnetic structure breaks the symmetry of the parent nuclear structure to a lower space group such as P1. Each moment in a Ni atom has three neighbors. Two of the neighboring moments are ferromagnetic and 1 is antiferromagnetic.

There are other orientation that can theoretically exist. These orientations are called stripy, zigzag, and Neél and can be seen in **Figure 4.27**. However, after trying all the orientations, the zigzag, or 2 FM and 1 AFM neighbor orientation, exhibited the best fit. The other orientations had issues of concern. For example, when trying to use the stripy arrangement the magnetic moments were much larger than anticipated with the total moment approaching 2.5(1) and 1.74(3) $\mu_B$ for the X = 0.29 and X = 0.43 samples. These values are with $M_y$ constrained to zero. Without this constraint, the measurement error exceeds the value of the $M_{total}$ for the X = 0.29 sample and about half for the X = 0.43 sample. A value

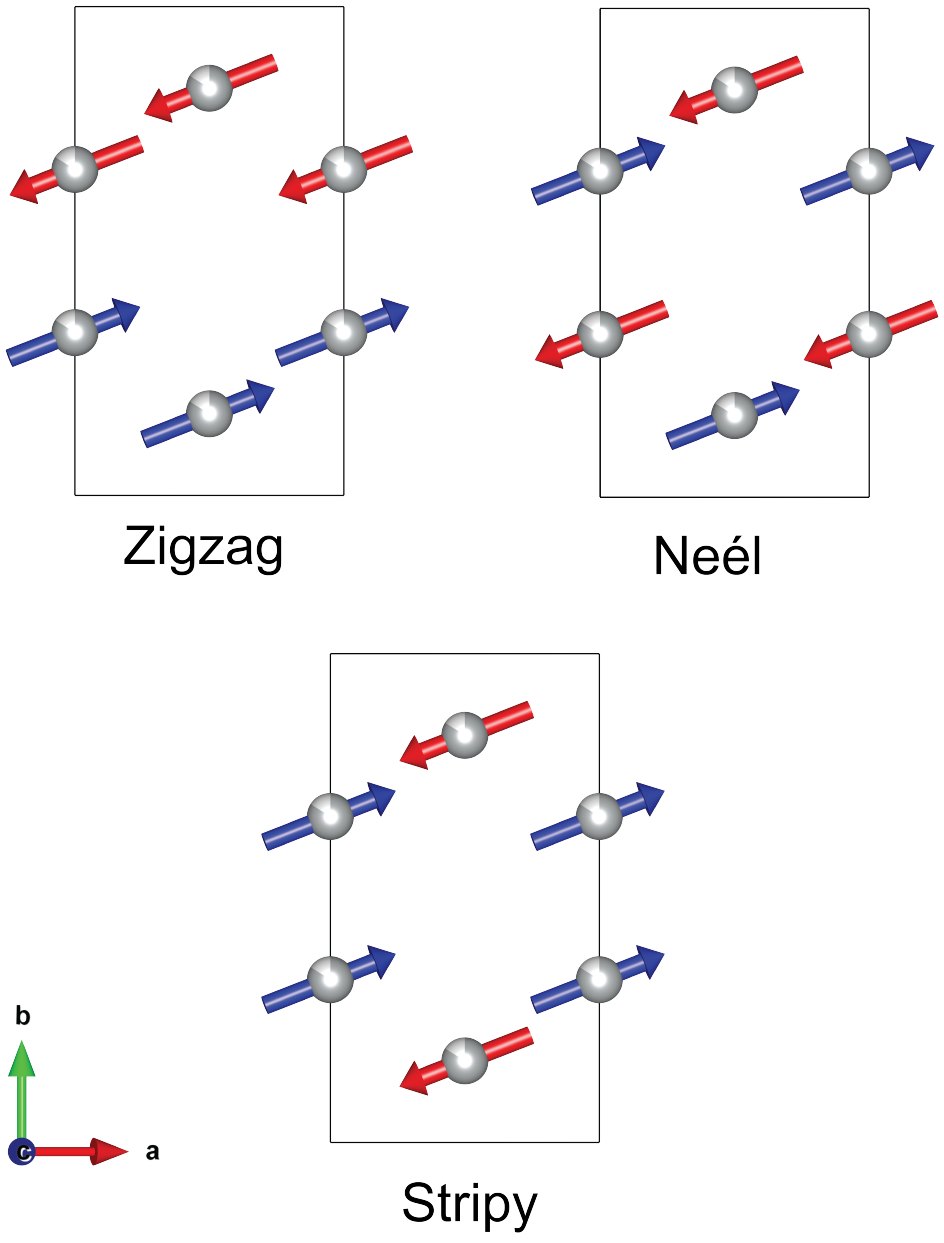



Figure 4.27: There are three ways the magnetic moments can orient themselves in the layered lattice. Of the three types the zigzag arrangement fits fits the observed diffraction pattern the best.

of 2.5(1)$\mu_B$ is also higher than the 2.0 $\mu_B$ expected spin-only total magnetic moment for a $Ni^{2+}$ ion. Generally, for a localized systems with 3*d* transition metals, spin-orbit coupling is typically not observed.

Likewise, there are some difficulties in using the Neél model to simulate the magnetic structure in $NiPQ_3$. For instance, the error in the measurement surpasses the measured value if the magnetic moments are free to roam in any direction so long as the Neél orientation is preserved. Additionally, if the moment contribution from one direction is restricted to zero, then the structure solution suggests that the moment size is near 0.8(1) $\mu_B$ for the X = 0.43 sample and 1.2(2)$\mu_B$ for the X = 0.29 sample. This value is much smaller than the spin-only magnetic moment of 2 $\mu_B$ and the measured value of 1.5 $\mu_B$ from this work's neutron powder diffraction data.

By comparing the results to previous NPD data and considering the stability of the refinements the $NiP(S_{1-x}Se_x)_3$ magnetic structure is best modeled under the zigzag arrangement because its weighted residuals are reasonably acceptable and this orientation agrees with the results from previous neutron powder diffraction data. The $R_{wp}$ for the zigzag model was calculated to be 17.8% and 16% for the X = 0.29 and X = 0.43 samples which is comparable to previous measurement done in literature residual.[160] Furthermore, zigzag model was found to be reproducible in the neutron powder diffraction data.

Comparing powder and single-crystal neutron diffraction data makes it clear on how selenium affects the magnetic behavior in $NiPQ_3$ compounds. Starting with the size of the moments, results for SCND demonstrate that the magnetic moment decreases as the amount of Se in $NiP(S_{1-x}Se_x)_3$ increased. The total moment size for $NiP(S_{1-x}Se_x)_3$ where X = 0.29 was measured at 1.42(2) $\mu_B$, while for X = 0.43 it was 1.1 (1)$\mu_B$. This result is contrary to the trend observed from NPD which was that the moments were observed to be 1.5(1) $\mu_B$ regardless of the amount of Se introduced to $NiP(S_{1-x}Se_x)_3$. Magnetic moment strength is corrolated to magnetic scattering. Thus, at first galance it would appear that that

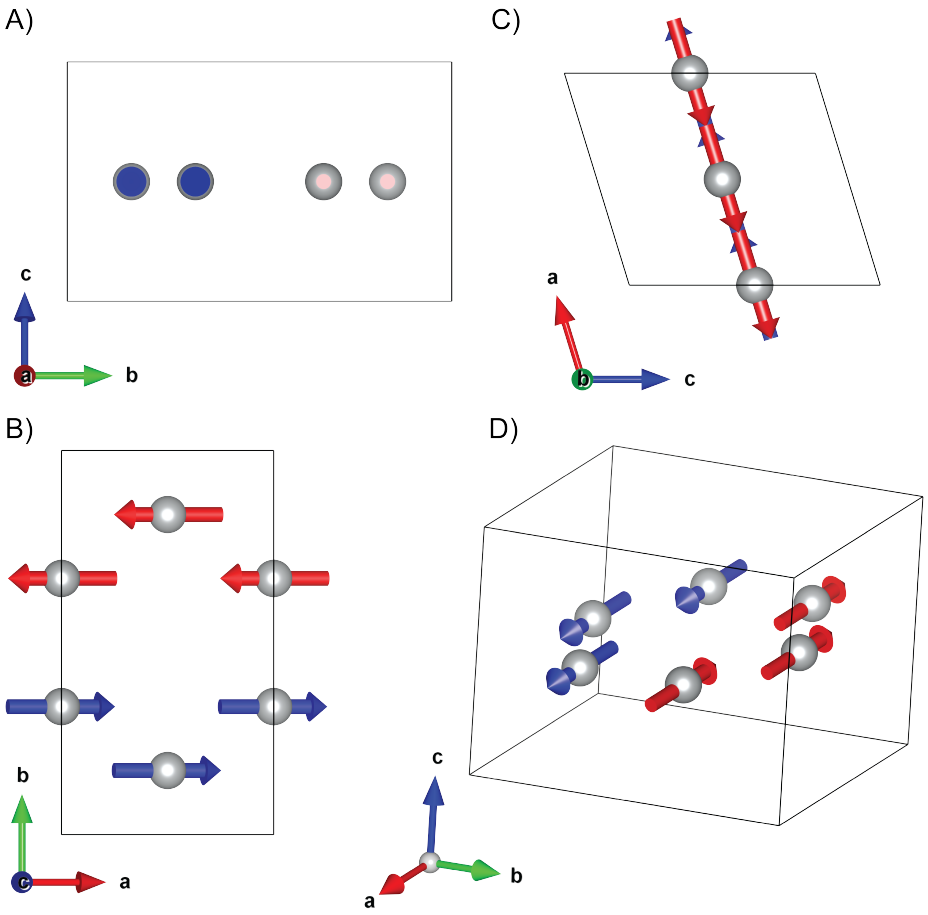



Figure 4.28: Proposed Magnetic Unit cell for $NiP(S_{1-x}Se_x)_3$ where x = 0.29. A) Displays *a*-axis. B) *c*-axis. C) *b*-axis. D) [111] zone axis.

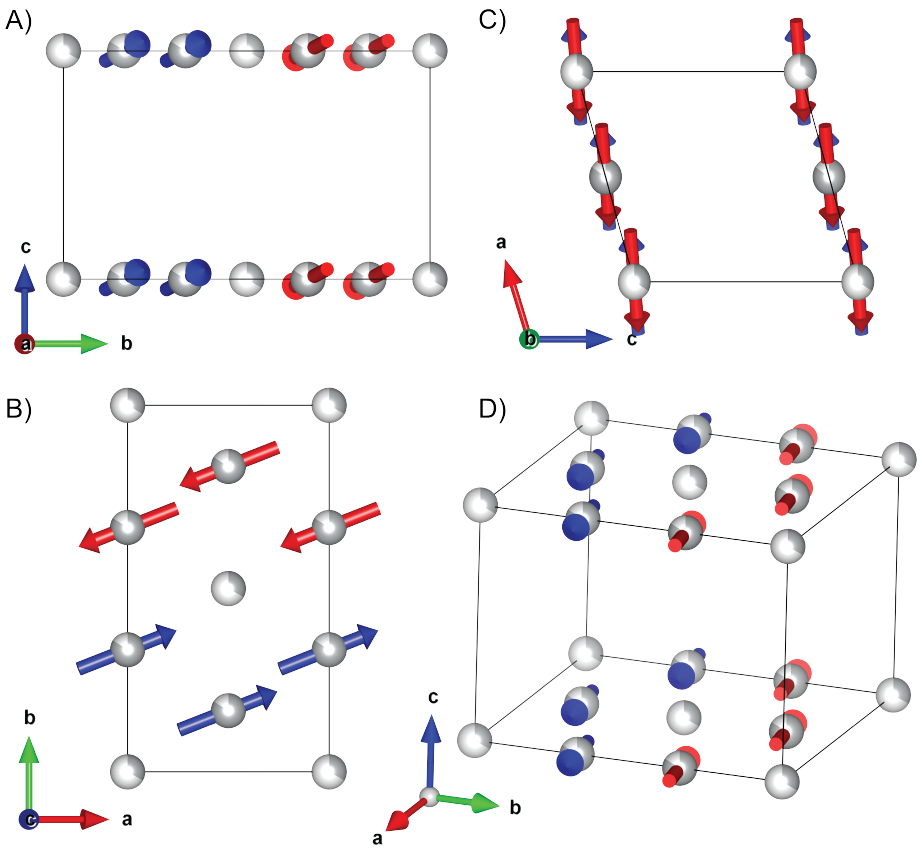



Figure 4.29: Proposed Magnetic Unit cell for $NiP(S_{1-x}Se_x)_3$ where x = 0.43. A) Displays *a*-axis. B) *c*-axis. C) *b*-axis. D) [111] zone axis.

the powder and the single crystal would scatter different from one another which is physically impossible. Instead, the divergence likely originates with the magnetic model. By only limiting the contribution to only 4*g* Ni atoms, the model is missing the scattering contribution the 2*a* Ni sites which may be the reason behind the different result $M_{tot}$ between NPD and SCND results.

Looking at the directional sub-components of the magnetic moment reveals a minor relationship between selenium amount and the orientation of the moment. The X = 0.29 sample demonstrated that moments primary point towards the *a*-axis. The *b* and *c*-axis contribution while measurable, also includes an error that is greater than observed value. For the x = 0.43 sample these values were found to be 1.02(2) $\mu_B$, 0.39(6) $\mu_B$, and 0.17 $\mu_B$ for the *a*, *b*, and *c*-axis. In contrast, data from neutron powder diffraction suggest that the moments have a sizable component in *c*-direction due to (010) magnetic reflection. In this case of mixed results, it is prudent to favor the SCND results over NPD results because the NPD data lacks the observation of multiple magnetic reflections, which helps evaluate the direction of the magnetic moment. Thus, according to the SCND results the addition of Se

Table 4.8: Magnetic moments of $NiP(S_{1-x}Se_x)_3$ from single crystal neutron diffraction. For X = 0.29 $M_y$ and $M_z$ were constrained to zero due to the excessive uncertainties in the structure solution. Units for the magnetic moment are in $\mu_B$

| ***x* =** | Model | $\mathbf{M}_x$ | $\mathbf{M}_y$ | $\mathbf{M}_z$ | $\mathbf{M}_T$ | $R_{wp}$% |
|---|---|---|---|---|---|---|
| **0.29** | Zigzag | 1.46(2) | 0 | 0 | 1.46(2) | 17.8 |
| **0.29** | Zigzag | 1.54(6) | 0.1(5) | 0.1(1) | 1.5(5) | 19.2 |
| **0.29** | Neél | – | – | – | – | * |
| **0.29** | Stripy | 2.6(1) | 0(3) | 0.1(2) | 3(3) | 18.1 |
| **0.29** | Stripy | 2.6(1) | 0 | 0.1(2) | 2.5(2) | 17.9 |
| **0.43** | Zigzag | 1.01(2) | 0.38(6) | 0.21(4) | 1.04(7) | 16.0 |
| **0.43** | Zigzag | 1.03(2) | 0 | 0.11(4) | 1.01(4) | 15.3 |
| **0.43** | Neél | 0.8(1) | 0.2(3) | 0.4(2) | 0.8(3) | 12.2 |
| **0.43** | Stripy | 1.79(1) | 0(1) | 0.15(5) | 1.8(8) | 14.9 |
| **0.43** | Stripy | 1.78(2) | 0 | 0.15(2) | 1.74(3) | 14.4 |

has little influence towards changing the direction of the magnetic moments since the the the moment direction is heavily biased towards the *a*-axis desite the addition of more Se.

## 4.4 Conclusion

The impact of varying selenium content in $NiP(S_{1-x}Se_x)_3$ onmagnetic properties was assessed. Neutron diffraction demonstrated that for multiple compositions, $NiP(S_{1-x}Se_x)_3$ are antiferromagnetic with a propagation vector of $\vec{k}$ = [010]. The magnetic space group for $NiP(S_{1-x}Se_x)_3$ compounds is P1. The magnetic moments where found to exhibit the zigzag orientation. Upon replacing S with Se, the Neél temperature increases from 155 K for 0% Se to nearly 200 K at 100% Se. The moment was found to decrease from 1.46(2) $\mu_B$ at 29% Se to 1.1(1) $\mu_B$ at 43% Se. The moment direction did not change significantly upon the introduction of addition Se.

Previous literature on $NiPS_3$ have reported a streaking phenomena in single crystal diffraction patterns that make it difficult to solve its magnetic and nuclear structure structure. If a thinner crystal is grown, then one could potentially minimize the amount of streaking observed. If the streaking features are removed, then usage of additional Wyckoff sites for nickel and phosphorus site are no longer needed.

# Chapter 5: Magnetic Structure Analysis of Mixed Anion $FeP(S_{1-x}Se_x)_3$

## 5.1 Introduction

Investigation of Fe chalcophosphate materials began as early as the 70's.[45,46,185] At that time, it was discovered that the crystal structures of $FePS_3$ and $FePSe_3$ were two-dimensional crystal lattices. Each of these lattice layers can be described by two general components, the honeycomb lattice formed by the Fe atoms and the $[P_2Q_6]^{4-}$ ethane-like units that are positioned in the center of the honeycomb formed. Depending on how these layers were stacked determines the space-group symmetry. For example, $FePS_3$ has a space-group symmetry of $C2/m$ with a monoclinic unit cell. The 2D lattice layers, from the perspective of one of the in-plane axes, appear to be directly stacked on top of each other. However, a glance at the other in-plane axis reveals that every stacked layer is shifted from its neighbors. This shift corresponds to the angle that defines the monoclinic unit cell (**Figure 5.1**). In contrast, $FePSe_3$ crystallizes with $R\bar{3}$ symmetry. In this space group each layer performs a translation operation equivalent to two-thirds in the *a*-axis and a third in the *b*-axis with respect to the previous layer. As a result, three translations are required for the unit cell to repeat itself.

After the discovery of 2D vdW magnetic material $Cr_2Ge_2Te_6$,[186] Fe chalcophosphates were quickly considered as a candidate material for 2D magnetism.[98,187] The seminal paper from Lee *et al.* was the first experimental observation of 2D magnetism in $FePS_3$. In their experiment they found that the Ising-type anti-ferromagnetism exhibited in the bulk

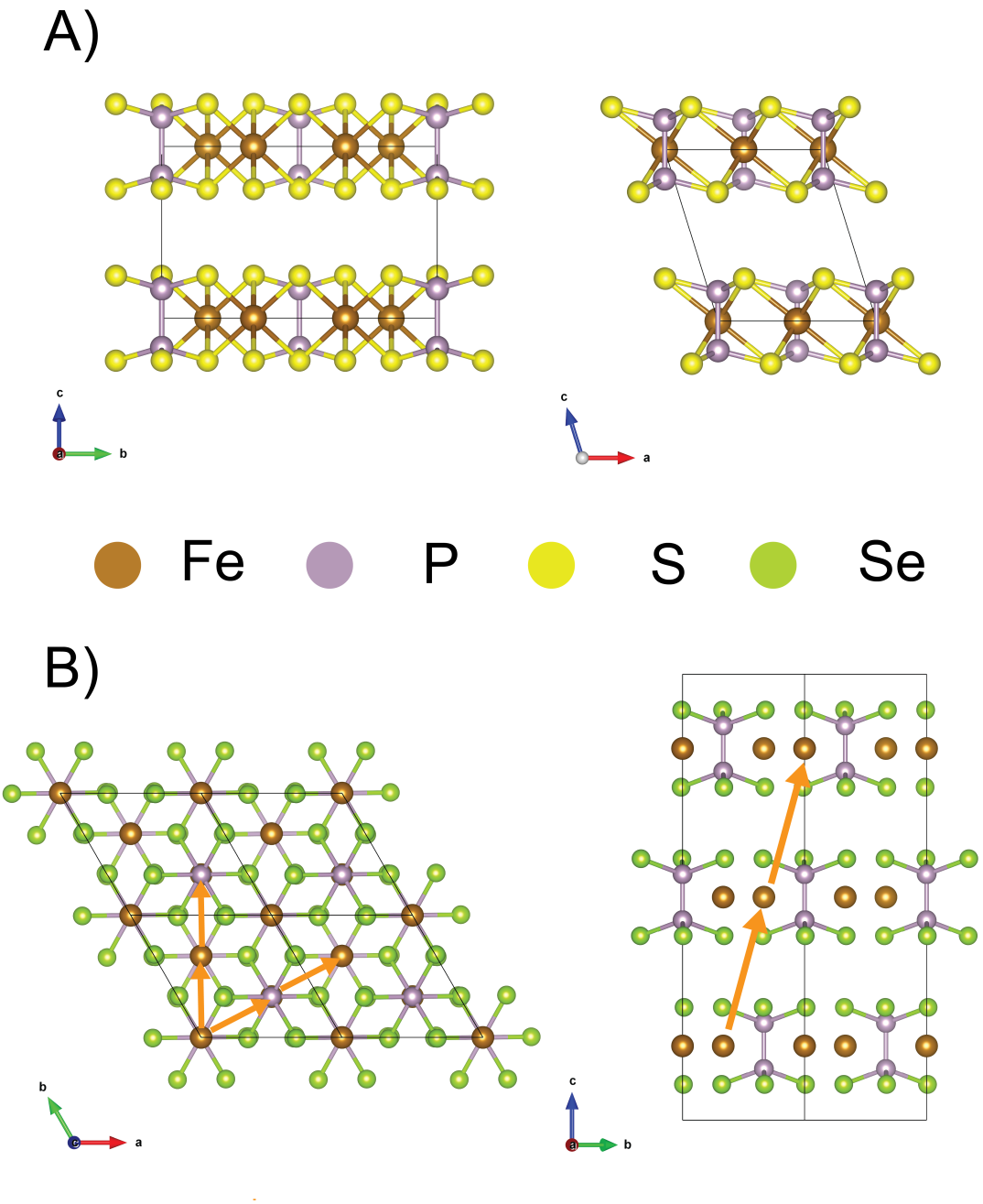



Figure 5.1: (A) Unit cell of $FePS_3$ along the *a* and *b*-axes. (B) Unit cell of $FePSe_3$. The orange arrow indicates that the stacking sequence is related to a translation in the *a* and *b* directions.

structure is preserved down to the monolayer limit. Furthermore, they found that the Neél temperature exhibits a weak dependence on the thickness of the sample because the ordering temperature did not dramatically decrease at the monolayer level compared to the bulk sample ($T_N$ = 125 $\pm$ 5 K). Thus, with the combination of a relatively high magnetic ordering temperature at the monolayer limit, and the ability to host a plethora of elementary excitations,[102,188,189] Fe chalcophosphates are candidate materials for spintronic devices with applications in computation and memory.[83]

Extensive research has been performed on the magnetic properties of $FePS_3$ and $FePSe_3$. In magnetic susceptibility, researchers have observed these compounds as Ising-type antiferromagnets with a Neél temperature near 125 $\pm$ 5 K.[190,191] Neutron diffraction experiments reveal that $FePS_3$ has a magnetic propagation vector of $\overrightarrow{k} = [01\frac{1}{2}]$ with the moments aligned perpendicular to the *ab*-plane (**Figure 5.2**). Each iron atom has two neighbors whose spins are co-aligned to each other while the third and final neighbor's spin is anti-aligned.[163,171,192]A total magnetic moment of 4.9 $\mu_B$ is observed for $FePS_3$. As for $FePSe_3$ the magnetic unit cell was found to be twice the size in the *a* and *c* leading to a propagation vector of $\overrightarrow{k} = [\frac{1}{2}0\frac{1}{2}]$ (**Figure 5.3**). Once again the moments are found to be mostly aligned to the *c*-axis and also have a total magnetic moment of 4.9 $\mu_B$.[70]

Recent work from Coak *et al.* sheds new light on a potential way to manipulate the magnetic structure through mechanical stress.[193] They reported that by applying a force above 20 kBar to $FePS_3$, the magnetic reflections that result in the $\overrightarrow{k} = [01\frac{1}{2}]$ propagation vector are suppressed while new reflections appear. These new reflections can be indexed with propagation vector of $\overrightarrow{k} = [010]$.

Taking inspiration from that work, we hypothesized that the creation of a mixed anion $FeP(S_{1-x}Se_x)_3$ would introduce a form of chemical pressure. Because of the different atomic sizes between S and Se, we estimate that the presence of larger atoms would distort the crystal structure via bond lengths. Using neutron powder diffraction, we found that

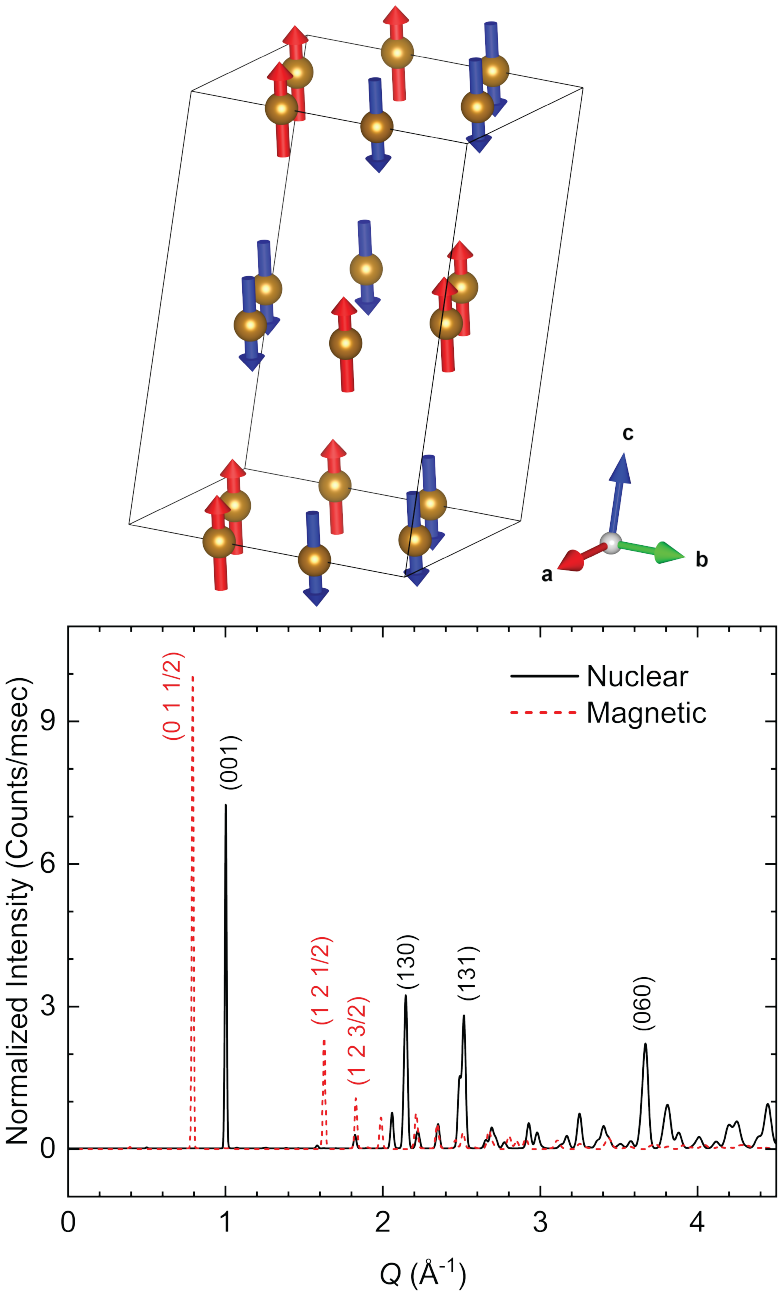



Figure 5.2: (Top) Magnetic structure of $FePS_3$ from the literature. This magnetic cell has propagation vector $\vec{k} = [01\frac{1}{2}]$. (Bottom) Simulated diffraction patterns of the magnetic (red dashes) and nuclear (black) structures of $FePS_3$ with select reflections labeled.

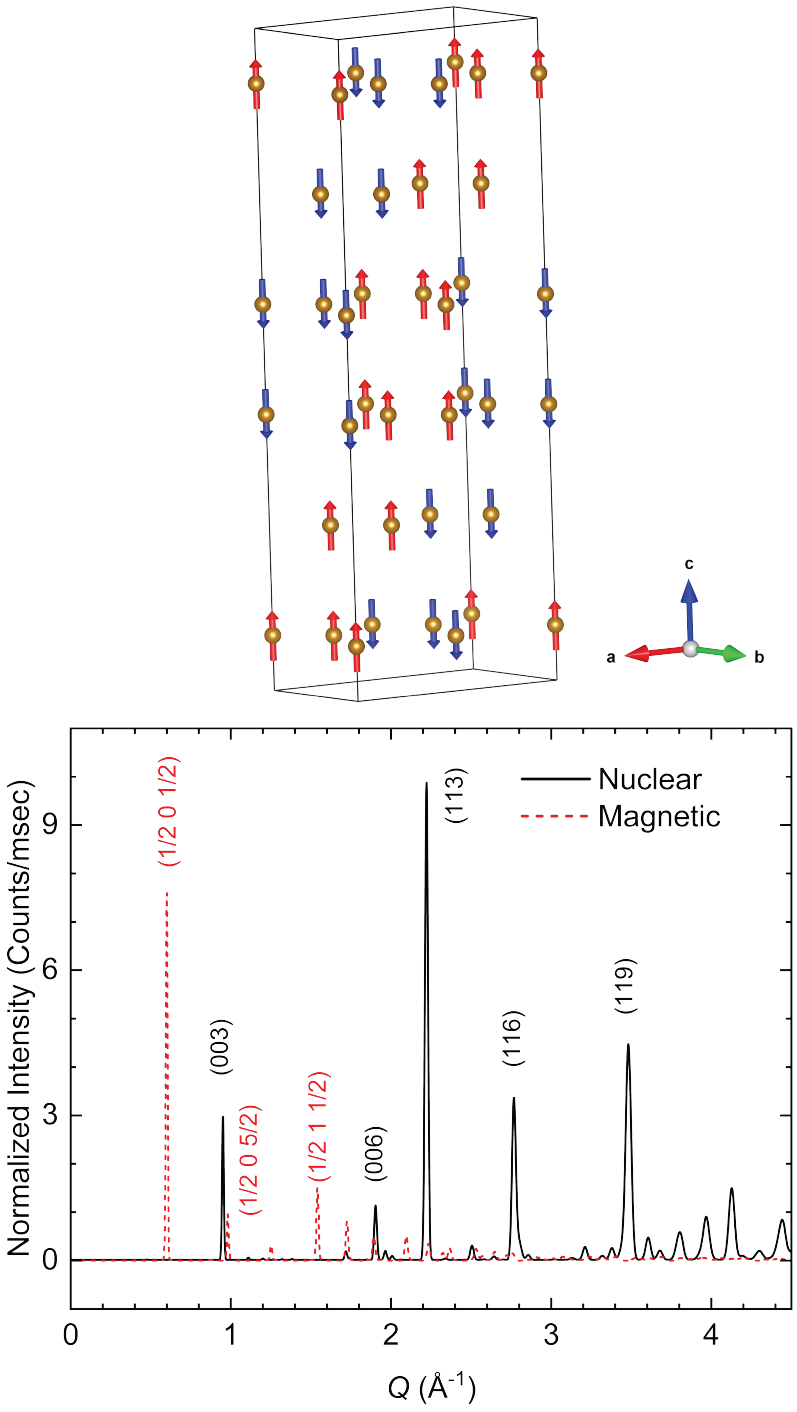



Figure 5.3: (Top) Magnetic structure of $FePSe_3$ from the literature. This magnetic cell has propagation vector $\vec{k} = [\frac{1}{2}0\frac{1}{2}]$. (Bottom) Simulated diffraction patterns of the magnetic (red dashes) and nuclear (black) structures of $FePSe_3$ with select reflections labeled.

substitution of Se in $FePS_3$ resulted in the observation of two magnetic propagation vectors ($\overrightarrow{k}$ = [01$\frac{1}{2}$] and $\overrightarrow{k}$ = [010]). Similarly, introducing sulfur into $FePSe_3$ also resulted in two propagation vectors appearing in the NPD data ($\overrightarrow{k}$ = [$\frac{1}{2}$0$\frac{1}{2}$] and $\overrightarrow{k}$ = [0$\frac{1}{2}$0]. Thus, through a combination of structural distortions, indirect exchange, and chemical pressure the magnetic structures of $FePS_3$ and $FePSe_3$ can be changed.

## 5.2 Experimental Methods

### 5.2.1 Synthesis

**Powder synthesis of $FeP(S_{1-x}Se_x)_3$:** $FeP(S_{1-x}Se_x)_3$ was synthesized using a direct combination of elemental iron (Sigma-Aldrich, 99.7%), phosphorus (Alfa-Aesar, 98.9%), sulfur (ACROS Organics, 99.5%), and selenium (Sigma-Aldrich, 99.5%). The elements were mixed and ground in an agate mortar and pestle inside an argon-filled glove box. The reagents were mixed in a stoichiometric ratio according to the nominal composition desired. For example, if the $FePS_2Se$ is targeted then the the ratio among Fe:P:S:Se is 1:1:2:1. The powder mixture was then placed in a quartz-glass ampule (Advalue Technologies) and sealed under a vacuum of $7.5 \times 10^{-3}$ Torr. The ampule was then heated in a box furnace with the following procedure: The furnace was heated to 440 $^\circ$ under a 2°C/min ramp and held at that temperature for a couple hours to prevent the rupture of the ampule from sulfur's vapor pressure. The furnace was then heated to 650°C with a 4°C/min ramp, and remained at this temperature for 4 days.

### 5.2.2 Neutron Diffraction

**Neutron powder diffraction:** Time-of-flight unpolarized neutron powder diffraction (NPD) was performed at Oak Ridge National Lab's Spallation Neutron Source on the POWGEN instrument. For these experiments each sample weighed about 5 grams. An 8-mm long vanadium can was used to hold each sample. The frame-2 instrument setting, which has a d-spacing coverage between 0.5-12.5 Å, was selected. To achieve good statistics, an exposure time of approximately 2 hrs was used. Each sample was measured at 300 K and 2 K.

### 5.2.3 Structural Refinement

**Refinement procedure:** Refinement program of choice in this case was GSAS-II. Constraints included assigning the S and Se atoms the same atomic positions and the same thermal parameters. Fe and P both have majority and minority sites with the majority sites actually representing the crystal structure while the minority sites partially represents the prevalence of layer shifting in the *ab*-plane. In the refinement, the majority Fe sites and minority P sites were constrained such that the sum of the occupancies was unity. The same constraints were applied in the case for majority P and minority Fe sites. Furthermore, all Fe sites share the same thermal parameters, and all P sites have the same thermal parameters. For the Rietveld refinement at 2 K magnetic moments were only calculated for the Fe majority sites. To determine magnetic space groups, the k-SUBGROUPMAG function from the Bilbao crystal server was used.[194,195]

### 5.2.4 Magnetic Susceptibility

Powder magnetic susceptibility measurements were performed with a Quantum Design MPMS®3. For both field-cool and zero field-cool measurements, the range of operation was between 2 K to 300 K with a scan rate of 2K / min under an applied field of 100 Oe.

## 5.3 Results and Discussion

### 5.3.1 Structural Characterization from Neutron Powder Diffraction

The NPD results reveal that the transition between the $FePS_3$ $C2/m$ monoclinic space group and the $FePSe_3$ $R\bar{3}$ trigonal space group occurs when $x$ nears 0.50 for $FeP(S_{1-x}Se_x)_3$ type structures. **Figure 5.4** shows the diffraction data collected at 300 K. Peaks indexed in red reference the $C2/m$ space group, and peaks indexed in blue correspond to the $R\bar{3}$ space group.

Two observations in this data set indicate the presence of a phase transition. The first sign is a shift in the intensities of peaks observed. Certain reflections reference the same observed peaks. For example, the reflection observed at 1 $Å^{-1}$ in **Figure 5.4** is indexed as (001) for $C2/m$ or (003) for $R\bar{3}$ symmetry. According to the data it can clearly be seen that this peak at 1 $Å^{-1}$ decreases as more Se substitutes S in the crystal structure. The second observation is the complete disappearance of some reflections. When a crystal structure transitions to a different enough symmetry, then a new set of reflection conditions will apply which allows the disappearance or emergence of Bragg reflections. Example of this phenomena can be found in the 2-3 $Å^{-1}$ region of **Figure 5.4**. Here, the (130) and (131) reflections disappear once $FeP(S_{1-x}Se_x)_3$ becomes Se-rich. Meanwhile, the (113) and (116) reflections emerge signifying a transition from $C2/m$ to $R\bar{3}$.

This phase transition may not be sharp but gradual. Signatures of both monoclinic and

trigonal space groups can be found in the diffraction pattern when $x = 0.5$. The widths of the peaks observed in the powder pattern indicate that there is a wide distribution of unit cells with structures between the two space groups.

For the majority of the samples, our Rietveld refinement suggest that no impurities form in our samples. The only composition that displayed signs of impurity formation is in the $x = 0.5$ sample. In that diffraction pattern there were a few peaks that could not be indexed due to the broadness of some reflections which masked other reflections. Ultimately, the impurities were not identified but common binaries such as, $FeS_2$, $FeSe_2$, FeSe, and FeS were not found in the diffraction pattern.

Before the magnetic structure of $FeP(S_{1-x}Se_x)_3$ can be determined, a good structural model for the nuclear structure must be found. Accordingly, a Rietveld refinement was performed on the collected NPD data at 300 K, which is a temperature well above the magnetic ordering temperature of 120 K.

The first structure solution utilized was from the literature,[70,171] and it produced a Rietveld refinement with mixed results, depending on whether the FePQ samples where S or Se-rich. If the sample was Se-rich then the structure solution record in the literature was sufficient to model the experimental diffraction patterns. However, if the $FeP(S_{1-x}Se_x)_3$ sample was S-rich then the refined structure solution consistently produced a simulated powder pattern with lower intensity for certain low Q reflections, such as (001).

To account for this problem, the same solution used for $NiP(S_{1-x}Se_x)_3$ compounds was applied to Fe chalcophosphates. This solution involved adding two additional Wyckoff positions to the structure model. One site placed a second Fe site in the $2a$ Wyckoff position which is a special position that restricts the Fe atom to the corner of the unit cell and the center of the face of the unit cell parallel to the *ab*-plane (**Figure 5.5**). The second site placed another P-P dimer in the $8j$ Wyckoff position, which coincidentally is in the same location as the Fe atoms that form the honeycomb lattice.

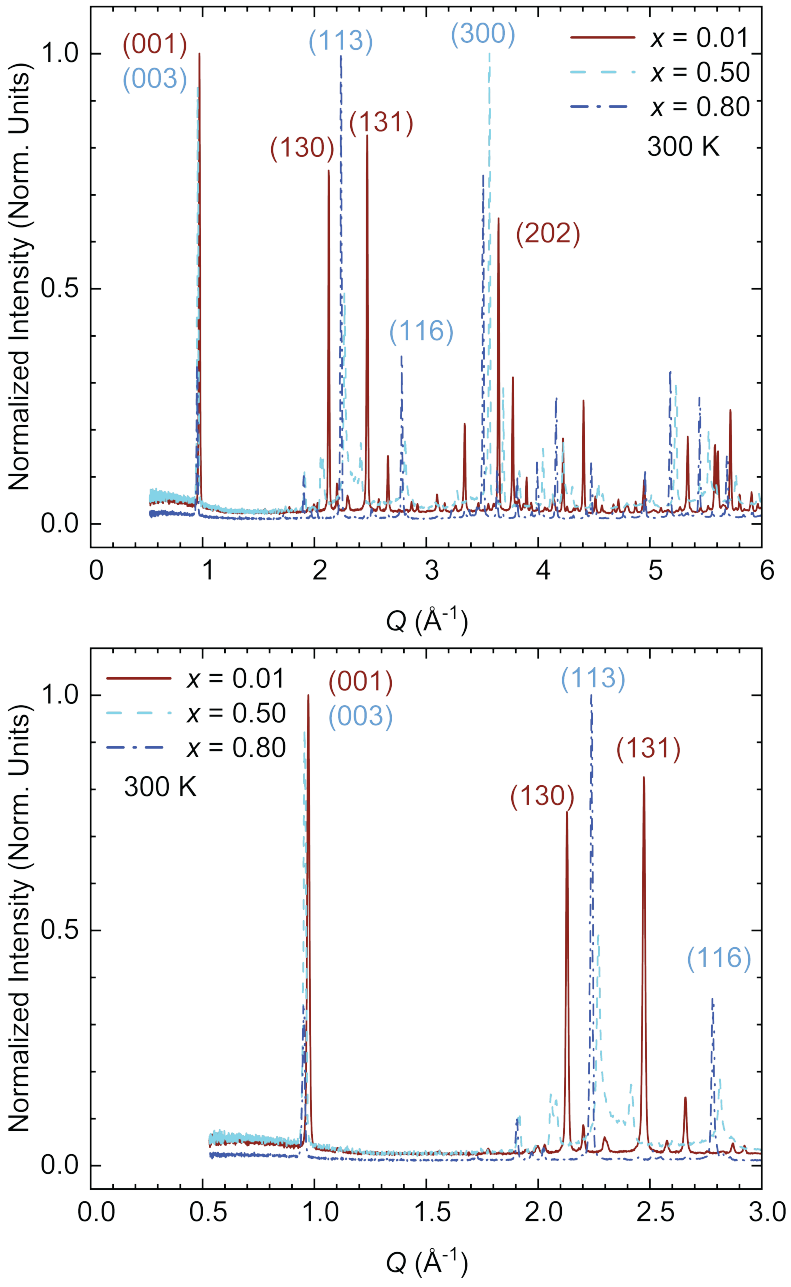



Figure 5.4: NPD of $FeP(S_{1-x}Se_x)_3$ for various values of $x$. Labels in red refer to the *C2/m* space group and those in blue to the $R\bar{3}$ space group.

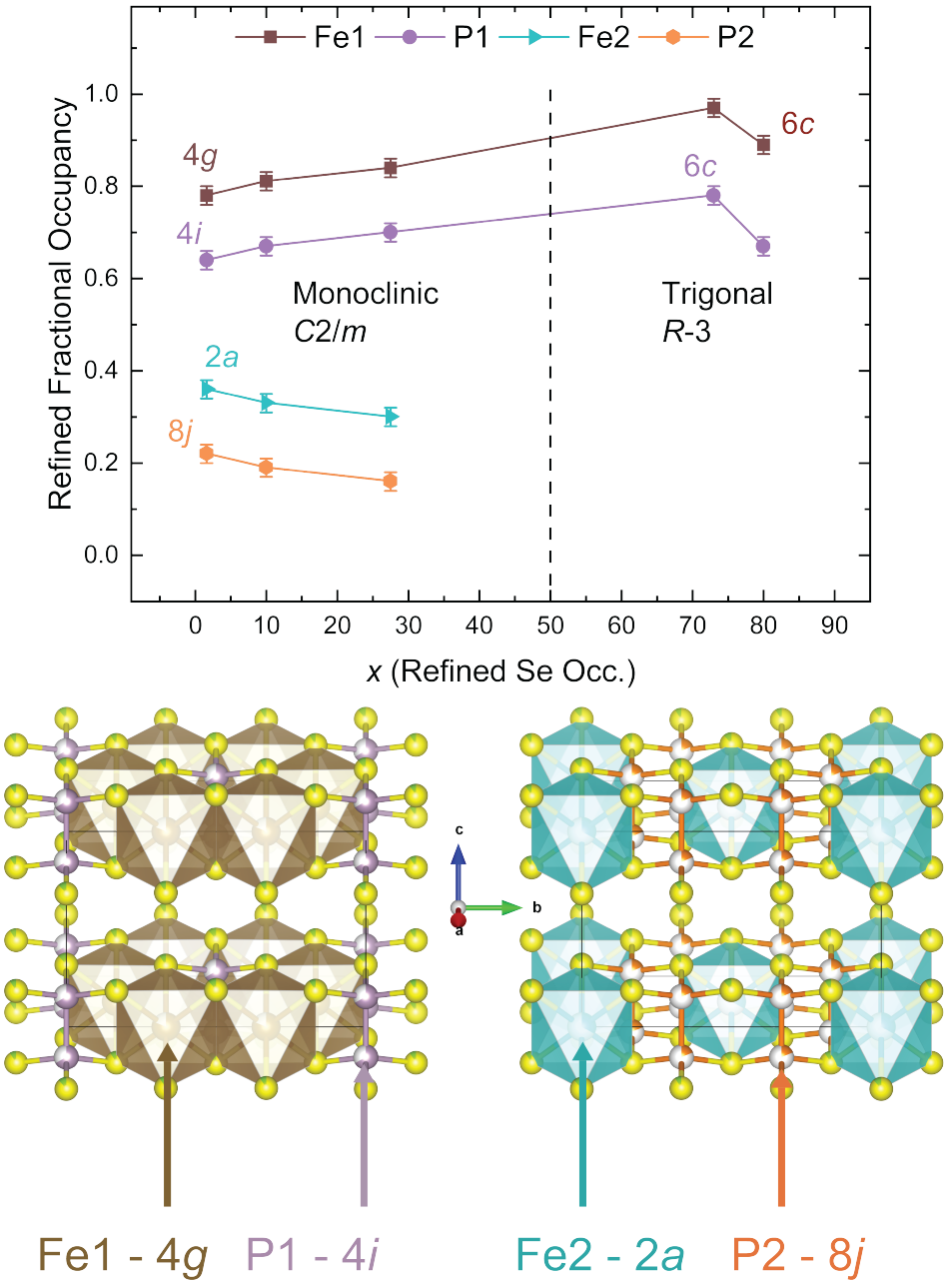



Figure 5.5: (Top) Refined fractional occupancy for Fe and P sites. (Bottom) Visual representation of where the Fe and P Wyckoff sites are located in the $FeP(S_{1-x}Se_x)_3$ crystal structure. The $x = 0.50$ data was omitted to the poor refinement statistics.

**Figure 5.6** compares a Rietveld refinement performed without the additional Wyckoff sites with one that does include these extra sites. By comparing the difference curves between these two figures, we found that the crystal structure with the extra sites fits the diffraction data more than the other model. The residual parameters, $R_{wp}$ and $R_f$ were also found to be lower in the extra-site model. A combination of lower residual parameters indicate that a structure solution's calculated diffraction pattern fits the observed diffraction pattern with respect to reflection intensity, peak widths, and background.[196]

In short, the introduction of selenium to $FePS_3$ results in a structural distortion by splitting the occupancies of the Fe and P atoms that gives the appearance of Fe and P atoms swapping positions. Once enough Se replaces S, the crystal structure transitions from monoclinic $C2/m$ to trigonal $R\overline{3}$.

The change in occupancies in relation to the percent of Se atoms, suggests that a significant amount of Fe and P atoms can be found in these new positions. **Figure 5.5** demonstrates that the $2a$ and $8j$ Wyckoff are observed to have a fractional occupancy near $\frac{1}{3}$ for the former and about $\frac{1}{5}$ for the latter site. Taking account of the multiplicity of the sites we calculated that about 16% of all Fe atoms and 40% of all P atoms occupy the $2a$ and $8j$ site, respectively. A small correlation was seen between an increase in Se presence and a decrease in the occupancy of these extra sites.

In the Se-rich side of the curve, for the $R\overline{3}$ space group the partial occupancies for the Fe and P atoms continue to be observed. Curiously when the Fe and P occupancies are fixed to 1, the residual parameters are worse meaning that this result implies that some type of structural distortion occurs in the trigonal structural phase. It is not known whether the cause of these vacancies is of the same kind observed in the S-rich sample. We conclude, that these the distortions have a weaker effect on the trigonal crystal structure than the monoclinic one because a relatively good fit can still be acquired without modeling the these distortions.

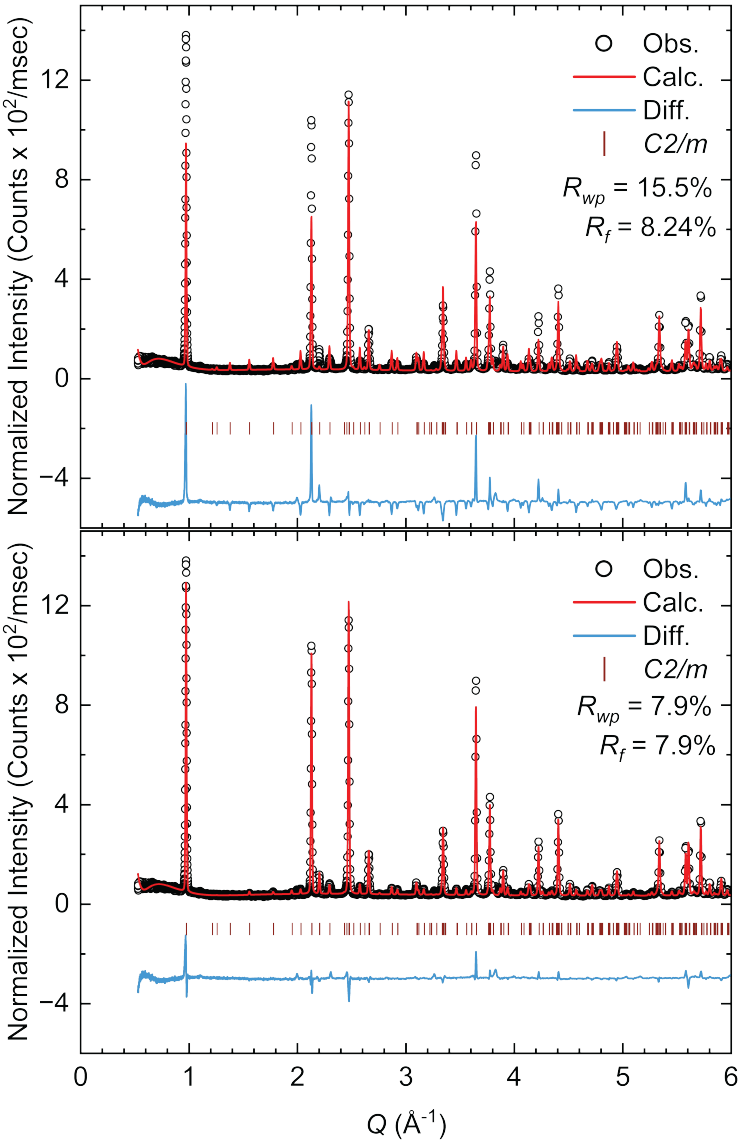



Figure 5.6: (Top) Rietveld refinement on NPD data collected at 300 K for $FeP(S_{1-x}Se_x)_3$ when $x$ = 0.01 without extra Wyckoff sites. (Bottom) With extra sites.

The lattice parameters indicate that there is a general expansion of the volume of the unit cell as Se concentration increases. This trend is apparent in **Table 5.1**. This expansion of the unit cell is mostly likely driven by Se-substitution. Due to its 4p orbitals, Se has a larger atomic radius than S. The bond distances have to increase to accommodate this repulsive force. Bond distances for Fe–Fe, Fe–Q, P–P, and P–Q are reported in **Table 5.2-5.5** and indicate that the bond distances increase as the Se content increases.

Finally, for x = 0.5 both the monoclinic and trigonal crystal structure were found to co-exist, leading to some form of phase separation in the diffraction pattern. At this composition the peak width is at its maximum, indicating that there is significantly more structural distortion for this sample than the others. Because of these diffuse features, the occupancies for the monoclinic and trigonal phases in this sample could not be calculated accurately. Even the calculated bond distances had some unrealistic values. For example, the P–P bond length, according to the refined structure model for the monoclinic phase, contracts is from to 2.22 Å from 1.72 Å. The $R_{wp}$ and the monoclinic phase's $R_f$ values are near 18% and 13.8%, respectively. These values are higher than all the other reported residual statistics, indicating that the structure solutions used to model other compositions of $FeP(S1-xSe_x)_3$ are inadequate to model the $x = 0.5$ sample.

Table 5.1: Lattice parameters of $FeP(S_{1-x}Se_x)_3$ for various compositions.

| **Se%** | **Space group** | **Lattice parameters (Å)** | **Angle (°)** | **Volume (Å$^3$)** |
|---|---|---|---|---|
| ***x* = 0.01** | $C2/m$ | $a$ = 5.96(1), $b$ = 10.33(1), $c$ = 6.74(1) | 107.1(1) | 396.2(1) |
| ***x* = 0.10** | $C2/m$ | $a$ = 5.99(1), $b$ = 10.38(1), $c$ = 6.77(1) | 107.0(1) | 402.5(1) |
| ***x* = 0.28** | $C2/m$ | $a$ = 6.04(1), $b$ = 10.47(1), $c$ = 6.83(1) | 107.0(1) | 413.3(1) |
| ***x* = 0.50** | $C2/m$ | $a$ = 6.10(1), $b$ = 10.57(1), $c$ = 6.86(1) | 106.9(1) | 423.6(1) |
| ***x* = 0.50** | $R\bar{3}$ | $a$ = 6.099(1), $c$ = 19.616(2) | Trigonal | 631.9(1) |
| ***x* = 0.73** | $R\bar{3}$ | $a$ = 6.155(1), $c$ = 19.698(1) | Trigonal | 646.2(1) |
| ***x* = 0.80** | $R\bar{3}$ | $a$ = 6.198(1), $c$ = 19.745(1) | Trigonal | 657.0(1) |

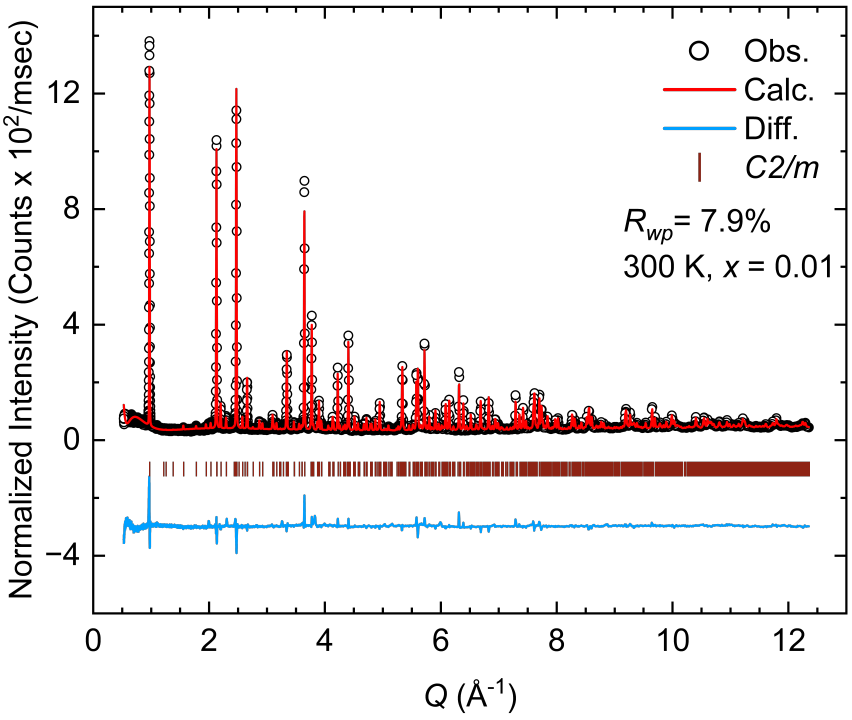



Figure 5.7: Rietveld refinement of neutron powder diffraction data of $FeP(S_{1-x}Se_x)_3$ with $x = 0.01$ at 300 K. $R_{wp} = 7.9\%$. $R_f = 7.9\%$.

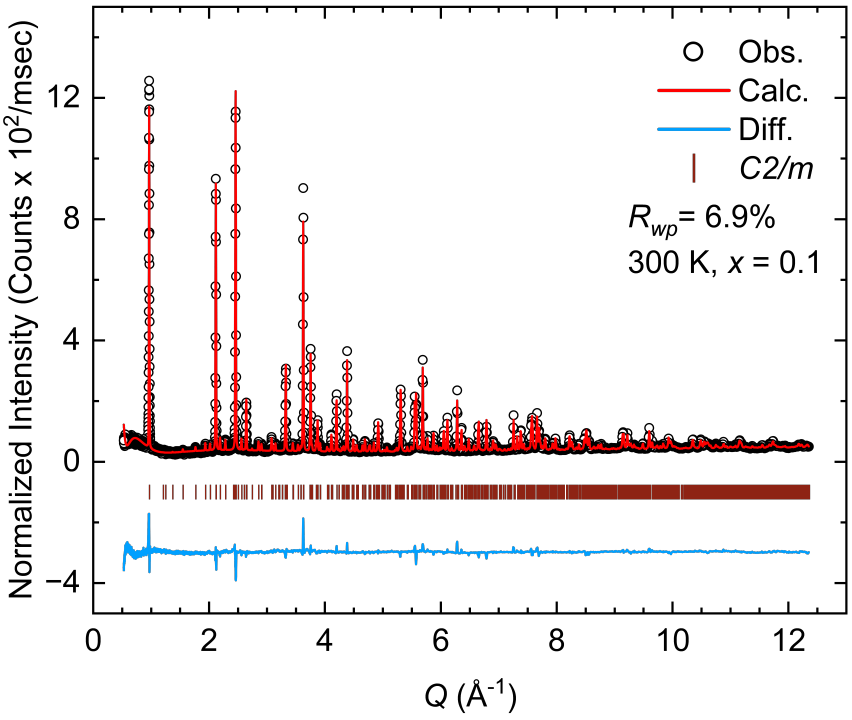



Figure 5.8: Rietveld refinement of neutron powder diffraction data of $FeP(S_{1-x}Se_x)_3$ where x = 0.10 at 300 K. $R_{wp}$ = 6.9%. $R_f$ = 8.5%.

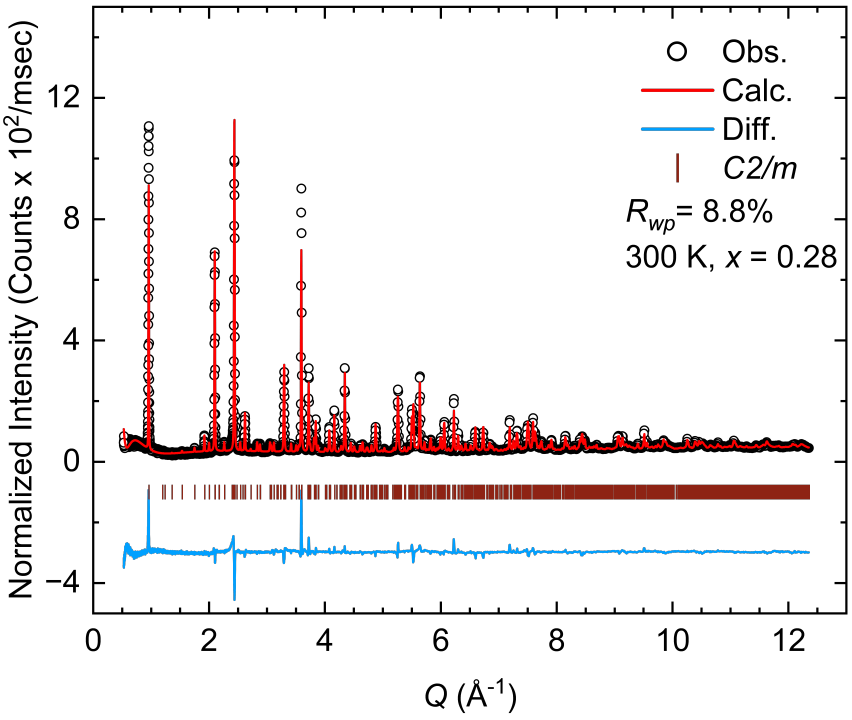



Figure 5.9: Rietveld refinement of neutron powder diffraction data of $FeP(S_{1-x}Se_x)_3$ with $x = 0.28$ at 300 K. $R_{wp} = 8.8\%$. $R_f = 7.0\%$.

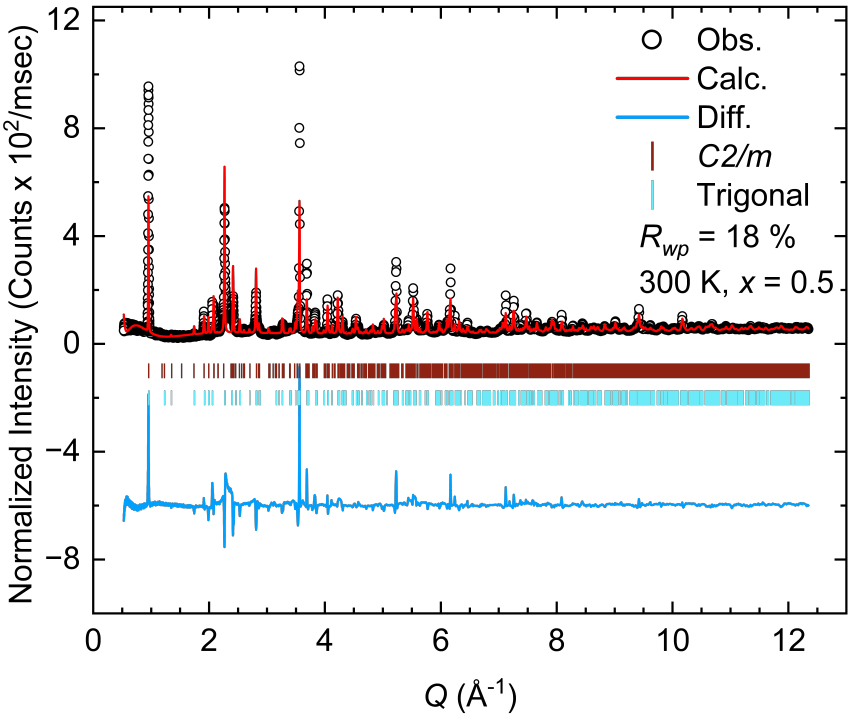



Figure 5.10: Rietveld refinement of neutron powder diffraction data of $FeP(S_{1-x}Se_x)_3$ with x = 0.50 at 300 K. $R_{wp}$ = 17.99%. Monoclinic $R_f$ = 13.8%. Trigonal $R_f$ = 9.9%

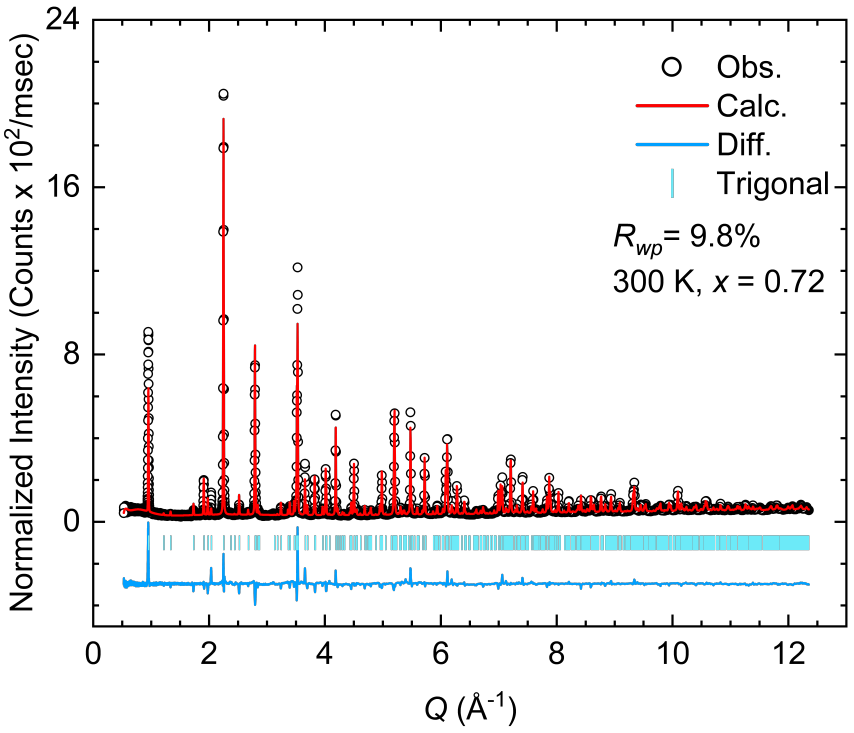



Figure 5.11: Rietveld refinement of neutron powder diffraction data of $FeP(S_{1-x}Se_x)_3$ where x = 0.73 at 300 K. $R_{wp}$ = 9.8%. $R_f$ = 7.9%.

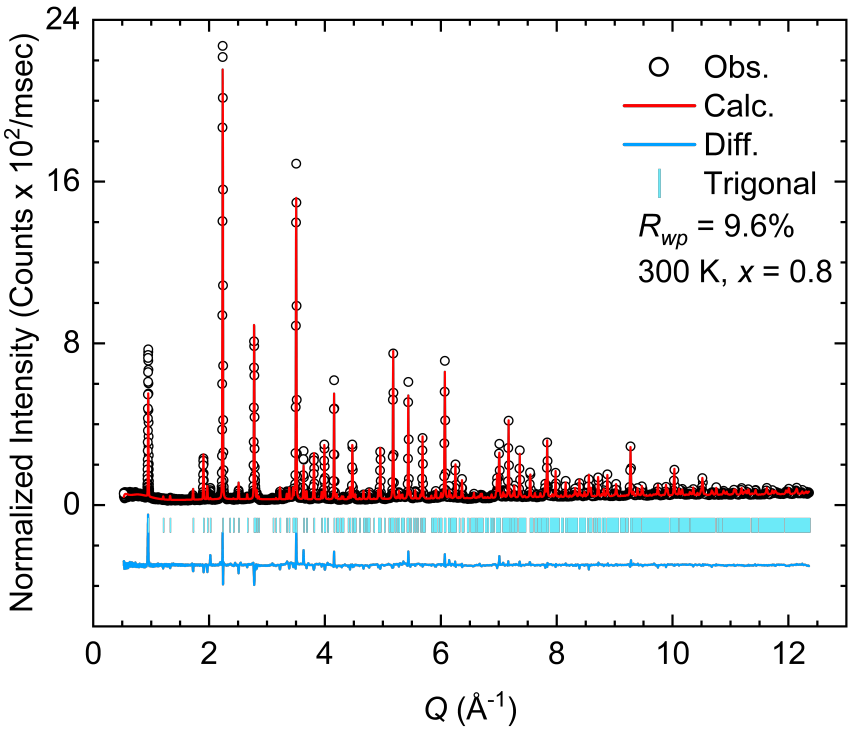



Figure 5.12: Rietveld refinement of neutron powder diffraction data of $FeP(S_{1-x}Se_x)_3$ where x = 0.80 at 300 K. $R_{wp}$ = 9.6%. $R_f$ = 7.9%.

Table 5.2: Average bond distances of between Fe and chalcogen atoms in $FeP(S_{1-x}Se_x)_3$).

| Composition | Space group | Bond type | Bond length (Å) |
|---|---|---|---|
| $x = 0.01$ | $C2/m$ | **Fe–Q** | 2.54(1) |
| $x = 0.10$ | $C2/m$ | **Fe–Q** | 2.56(1) |
| $x = 0.28$ | $C2/m$ | **Fe–Q** | 2.59(1)) |
| $x = 0.50$ | $C2/m$ | **Fe–Q** | 2.54(13) |
| $x = 0.50$ | $R\bar{3}$ | **Fe–S** | 2.89(6) |
| $x = 0.50$ | $R\bar{3}$ | **Fe–Se** | 2.58(2) |
| $x = 0.73$ | $R\bar{3}$ | **Fe–S** | 2.73(1) |
| $x = 0.73$ | $R\bar{3}$ | **Fe–Se** | 2.61(1) |
| $x = 0.80$ | $R\bar{3}$ | **Fe–S** | 2.76(1) |
| $x = 0.80$ | $R\bar{3}$ | **Fe–Se** | 2.62(1) |

Table 5.3: Average Fe-Fe bond distances in $FeP(S_{1-x}Se_x)_3$).

| Composition | Space group | Bond length (Å) |
|---|---|---|
| $x = 0.01$ | $C2/m$ | 3.44(1) |
| $x = 0.10$ | $C2/m$ | 3.46(1) |
| $x = 0.28$ | $C2/m$ | 3.49(1)) |
| $x = 0.50$ | $C2/m$ | 3.54(6) |
| $x = 0.50$ | $R\bar{3}$ | 3.52(1) |
| $x = 0.73$ | $R\bar{3}$ | 3.55(1) |
| $x = 0.80$ | $R\bar{3}$ | 3.57(1) |

Table 5.4: Average P-P bond distances in $FeP(S_{1-x}Se_x)_3$).

| Composition | Space group | Bond length (Å) |
|---|---|---|
| $x = 0.01$ | $C2/m$ | 2.13(1) |
| $x = 0.10$ | $C2/m$ | 2.19(1) |
| $x = 0.28$ | $C2/m$ | 2.22(1)) |
| $x = 0.50$ | $C2/m$ | 1.72(4) |
| $x = 0.50$ | $R\bar{3}$ | 2.46(3) |
| $x = 0.73$ | $R\bar{3}$ | 2.16(1) |
| $x = 0.80$ | $R\bar{3}$ | 2.15(1) |

### 5.3.2 Magnetic Structural Determination of Iron Chalcophosphates

Preliminary magnetic susceptibility measurements performed on $FeP(S_{1-x}Se_x)_3$ demonstrated that the creation of mixed anion $FeP(S_{1-x}Se_x)_3$ solid solutions yields small changes in the Neél temperature and in the shape of the magnetic susceptibility curve. As shown in **Figure 5.13**, $T_{max}$, that is the temperature where susceptibility reaches its maximum value, generally falls within a range between 110 K and 120 K. This observation indicates that despite changing the identity of the chalcogen atom, there is no substantial shift in the magnetic ordering temperature for $FeP(S_{1-x}Se_x)_3$ compounds. One notable aspect of this **Figure 5.13** is that some of the samples ($x$ = 0.01, 0.1, 0.28, 0.8) have some form of splitting between their zero-field and field cool curves characteristic of ferromagnetic behavior. However, this splitting can be attributed to some residual iron or iron oxide. Fe and Fe oxide are ferromagnetic above room temperature and due to the since sensitivity of the SQUID instrument these ferromagnetic impurities can be detected. Although magnetic susceptibility measurements demonstrate the lack of any significant changes to the magnetic order in mixed anion $FeP(S_{1-x}Se_x)_3$ compounds, results from neutron diffraction

Table 5.5: Average bond distances between P and chalcogen atoms in $FeP(S_{1-x}Se_x)_3$).

| **Composition** | **Space group** | **Bond type** | **Bond length (Å)** |
|---|---|---|---|
| $x$ **= 0.01** | $C2/m$ | **P–Q** | 2.06(1) |
| $x$ **= 0.10** | $C2/m$ | **P–Q** | 2.07(1) |
| $x$ **= 0.28** | $C2/m$ | **P–Q** | 2.09(1) |
| $x$ **= 0.50** | $C2/m$ | **P–Q** | 2.16(4) |
| $x$ **= 0.50** | $R\bar{3}$ | **P–S** | 2.22(7) |
| $x$ **= 0.50** | $R\bar{3}$ | **P–Se** | 2.09(2) |
| $x$ **= 0.73** | $R\bar{3}$ | **P–S** | 2.18(1) |
| $x$ **= 0.73** | $R\bar{3}$ | **P–Se** | 2.14(1) |
| $x$ **= 0.80** | $R\bar{3}$ | **P–S** | 2.30(1) |
| $x$ **= 0.80** | $R\bar{3}$ | **P–Se** | 2.15(1) |

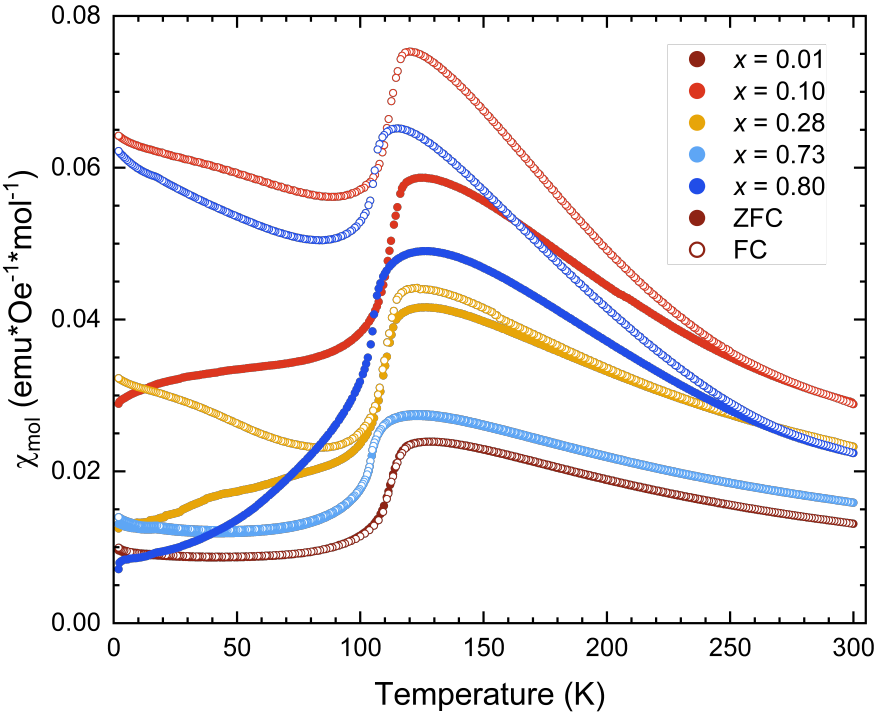



Figure 5.13: Magnetic susceptibility of $FeP(S_{1-x}Se_x)_3$ where H = 100 Oe. ZFC/FC splitting is most likely from some residual Fe, which is ferromagnetic below 1043 K. Additionally, it is also possible that higher susceptibility may also originate from Fe impurity.

reveals that Se does change the magnetic structure.

Contrary to the expectation set by the powder susceptibility data, NPD data reveal that in mixed anion $FeP(S_{1-x}Se_x)_3$ compounds, the combination of both S and Se introduces new magnetic peaks. As **Figure 5.14** demonstrates, for monoclinic $FeP(S_{1-x}Se_x)_3$, labeled in red, both the (010) and the $(01\frac{1}{2})$ reflections appear in the diffraction pattern. Furthermore, there is no single propagation vector that can index both reflections as one phase. Therefore, two propagation vectors, $\vec{k} = [01\frac{1}{2}]$ and $\vec{k} = [010]$ are needed to index all magnetic reflections. This additional propagation vector implies that there are two magnetic antiferromagnetic phases in S-rich $FeP(S_{1-x}Se_x)_3$.

These propagation vectors also describe the relationship of the magnetic unit cell to its nuclear unit cell. Propagation vector $\vec{k} = [01\frac{1}{2}]$ states that the magnetic unit cell loses the centering operation in the *b*-direction and has a *c*-lattice parameter twice as big as the nuclear unit cell. In contrast, propagation vector $\vec{k} = [010]$ implies that the other magnetic unit cell has the same lattice parameters as the parent unit cell but the centering operation in the *b*-direction is lost (**Figure 5.15**). If we compare this data with the result of Coak *et al.* our data set appears to have both low and high pressure AFM phases[193] simultaneously.

For trigonal $FeP(S_{1-x}Se_x)_3$, labeled in blue, two magnetic peaks also appear, $(\frac{1}{2}\ 0\ \frac{1}{2})$ and $(0\frac{1}{2}0)$. Coincidentally, these reflections cannot be described by a single propagation vector as well. These reflections require a propagation vector $\vec{k} = [\frac{1}{2}0\frac{1}{2}]$ for the former and a $\vec{k} = [0\frac{1}{2}0]$ for the latter. This result also implies that there are two antiferromagnetic phases in Se-rich $FeP(S_{1-x}Se_x)_3$. The magnetic unit cell described by propagation vector $\vec{k} = [0\frac{1}{2}0]$ signifies that the magnetic unit cell has twice the length in the *a* and *c* lattice parameters compared to the nuclear unit cell while the *b* lattice parameter remains the same as the parent unit cell. For the other magnetic unit cell it has a *b*-parameter that is twice as large compared to the parent unit cell, while the *a* and *c* parameters are the same (**Figure 5.16**).

Because of the phase separation in the $x = 0.5$ sample, the magnetic reflections from both the trigonal and monoclinic phases appear at together resulting in four magnetic phases appearing in the diffraction pattern for the $x = 0.5$ sample.

Additionally, due to the complexity of the magnetic unit cells, all magnetic unit cells were modeled using a $P1$ space group which is the lowest possible symmetry. While some unit cells may have higher symmetries, in order to test all possible spin configurations such as the zigzag, strippy, and Neél (**Figure 4.27**) spin configurations a $P1$ magnetic unit cell is necessary to accomplish this task.

Another observation of note is that there are significant diffuse features between the two magnetic reflections for the S-rich $FeP(S_{1-x}Se_x)_3$ compounds. We know that these features

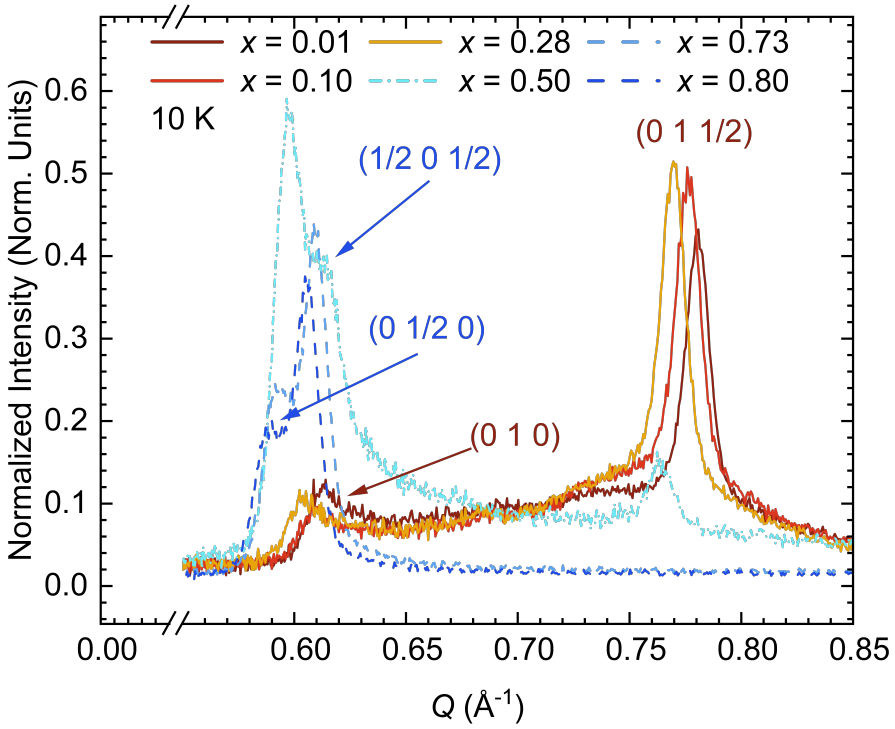



Figure 5.14: NPD of $FePS_{3-x}Se_x$ measured at 10 K. Intensities are normalized with respect to the reflection with the highest intensity.

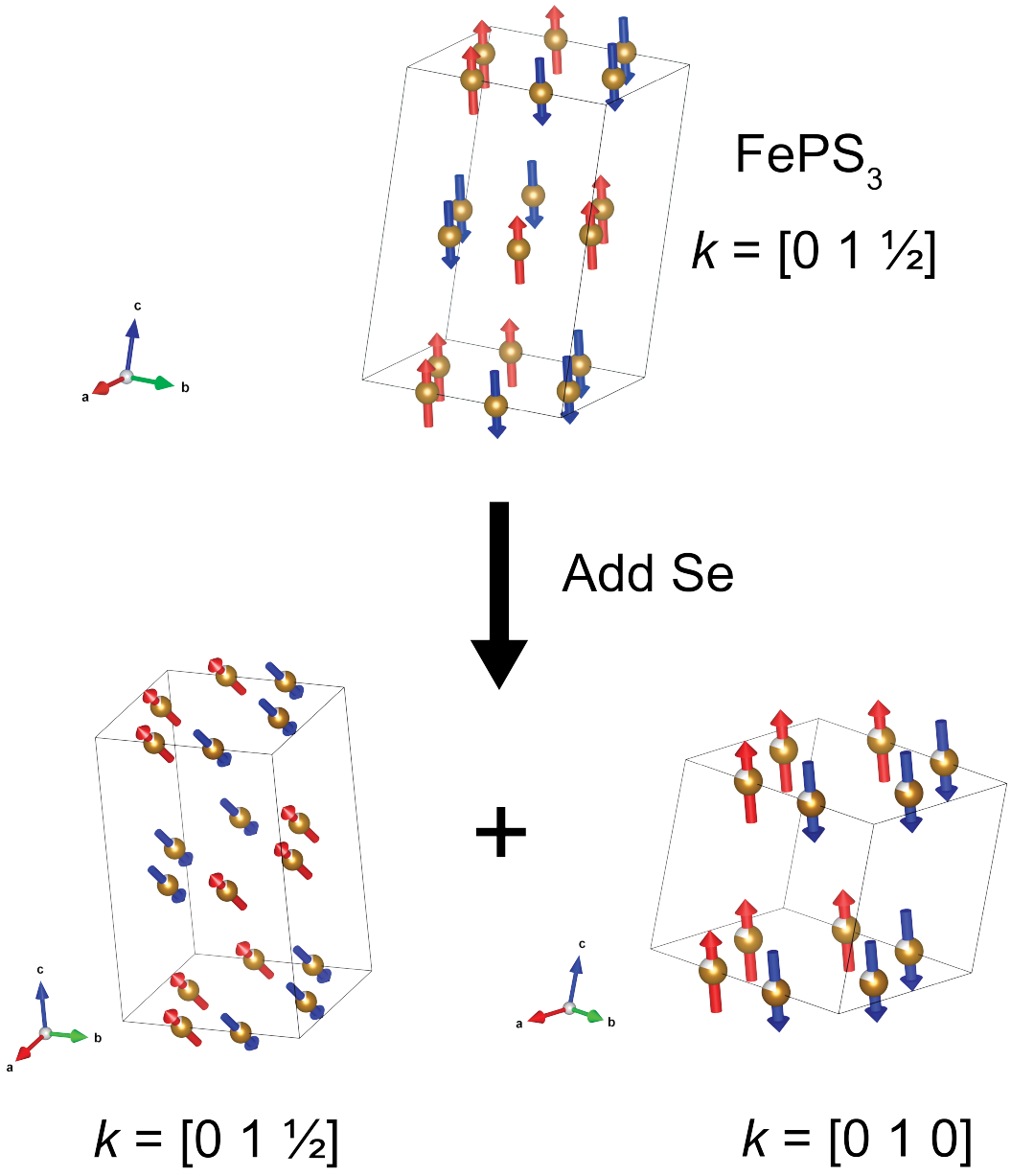



Figure 5.15: Partial substitution of sulfur with selenium in $FePS_3$ results in two observable magnetic phases in the diffraction pattern. For both phase the generally direction of the moments is normal to the *ab*-plane.

are exclusive to the magnetic structure, as these features were not observed in the measurements at 300 K. These features can reduce the strength of the magnetic moments. **Table 5.6** shows the calculated values for the total magnetic moment for the S-rich $FeP(S_{1-x}Se_x)_3$ compounds. According to our Rietveld refinement, the moments tend to be near 3.9 $\mu_B$ and 2 $\mu_B$ for the two magnetic phases found in monoclinic $FeP(S_{1-x}Se_x)_3$. Theoretically, a $3d$ transition metal with a $d^6$ high-spin octahedral coordination is expected to have a spin-only total magnetic moment of 4 $\mu_b$. Only one of the magnetic phases is near that value while the other is much lower. However, compared to literature both the moments from both phases are lower than the reported magnetic moment of 4.5 $\mu_B$ for $FePS_3$.[197]

The direction of the moments for these two magnetic phases are also different than what is reported in the literature. **Figure 5.15** shows that $FePS_3$ has its moments aligned to the $c$-axis. In contrast, in S-rich $FeP(S_{1-x}Se_x)_3$ that same magnetic phase now has a different direction for its moments. These moments now are partially in the $a$ and $c$ axes. As for the other magnetic phase it has its moments aligned to the $c$-axis. Lastly, the arrangement of the spins for both magnetic phase follow the zigzag configuration. This configuration means that each magnetic moment has 2 FM and 1 AFM neighbor.

For Se-rich $FeP(S_{1-x}Se_x)_3$, the magnetic phase with a propagation vector $\vec{k} = [\frac{1}{2}0\frac{1}{2}]$ has its total magnetic moments calculated to a value neat 4.7 $\mu_B$. The other phase has a total magnetic moment calculated near 3 $\mu_B$ (**Table 5.6**). The former value is similar to the value reported for $FePSe_3$, which is 4.9 $\mu_B$.[70] If

**Figure 5.16** displays the direction of the moments for both phases and compares them to the magnetic structure of $FePSe_3$. $FePSe_3$ has a propagation vector of $\vec{k} = [\frac{1}{2}0\frac{1}{2}]$ and its moments align with the stacking direction. Upon the introduction of S, that same phase has the direction of the moments shift 90° towards a direction normal to the layer stacking direction. The spins are arranged according to the zigzag configuration which is 2 FM neighbors and 1 AFM neighbor. The magnetic phase with propagation vector $\vec{k} = [0\frac{1}{2}0]$ has

its magnetic moments align with the layer stacking direction. However, the spin arrangement changes according to an ABBA pattern. Layer A has the stripy arrangement, which is 2 AFM and 1 FM neighbors while layer B exhibits the zigzag arrangement, which is 2 FM and 1 AFM neighbors.

Moving on to the quality of the fits. There is a general trend of the refinements done on lower temperature data outputting worse residual statistics than the ones from room temperature data. However, in this case it is important to distinguish between $R_{wp}$ and $R_f$. The former compares the raw intensities between observed and calculated patterns. Thus, it is a good indicator at how well the background is modeled and is a preliminary indicator of how well the intensities fit between the experimental and calculated patterns. $R_f$ describes the difference between the structure factors of the observed and calculated patterns. By comparing $F_{obs}$ with $F_{calc.}$ one gets a sense of how well the structure solution fits peak shape.

If we look at **Figure 5.18 - 5.23** we find a $R_{wp}$ values of upwards to 25%. Yet, the $R_f$ from the nuclear structure is under 7% and the $R_f$ from the various magnetic phases vary from 11% - 18%. This statistics reveal that the crystal structure solution used is able to fit many of the reflections in the observed diffraction pattern. However, the high $R_{wp}$ comes from a few select reflections whose intensities are drastically different than the calculated model. For example, the large diffuse features when $x$ ¡ 0.5 would contribute to a higher $R_{wp}$. For Se-rich phases there is a large difference in intensity in reflections near 1.9 $Å^{-1}$ and 2.2 $^{-1}$ that increases $R_{wp}$. Yet, most of the reflections fit well with the proposed crystal structure, which exhibits $R_f$ values near 6% while the magnetic structures display a $R_f$ values near 13%.

Because the structural distortions found in mixed anion $FeP(S1-xSe_x)_3$ are similar to those found in NiPQ compounds, the residual parameters should be compared to NiPS3. In fact, the magnetic structure with propagation vector $\vec{k}$ = [010] is identical to magnetic

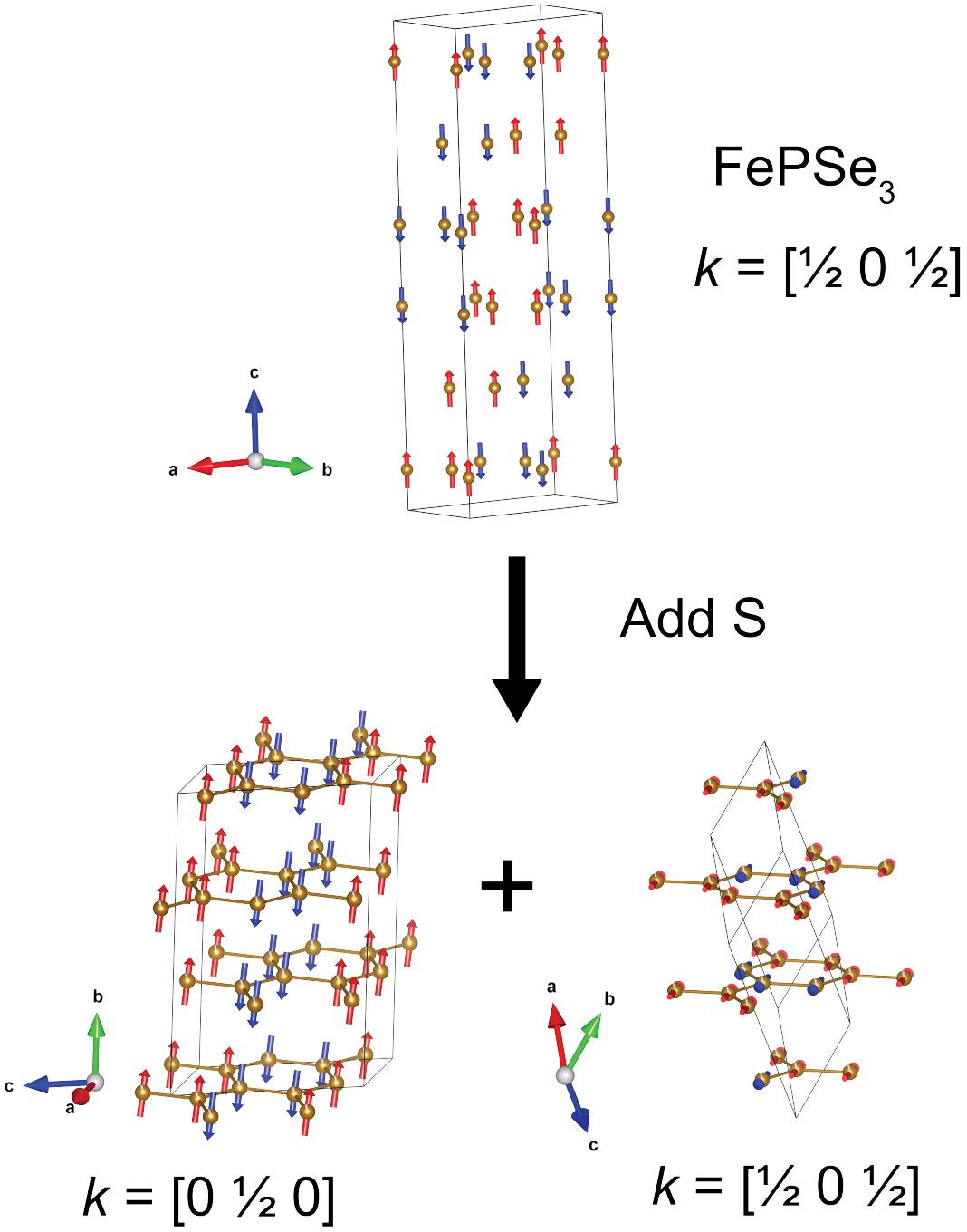



Figure 5.16: Partial substitution of selenium with sulfur in $FePSe_3$ results in two observable magnetic phases in the diffraction pattern. One phase has the moments in plane while the other phase has its moments aligned normal to the *ab*-plane.

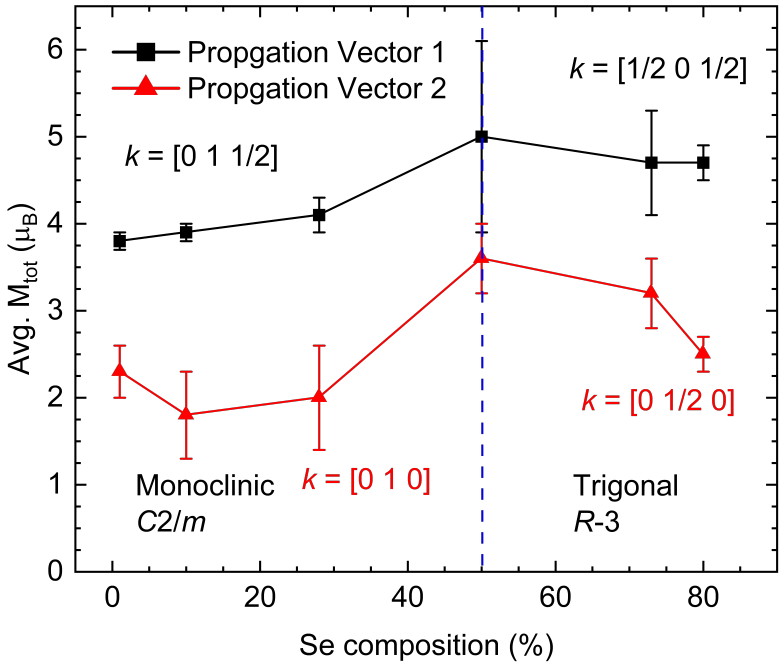



Figure 5.17: Magnitude of the total moment plotted as a function of Se-substitution. Propagation vector 1 represents $\vec{k}$ = [01$\frac{1}{2}$] and $\vec{k}$ = [$\frac{1}{2}$ 0 $\frac{1}{2}$] for the monoclinic and trigonal phases. Propagation vector 2 represents $\vec{k}$ = [010] and $\vec{k}$ = [0$\frac{1}{2}$0]. At $x = 0.5$ moment values were averaged.

structure observed in $NiPS_3$ However, $FeP(S_{1-x}Se_x)_3$ is different from $NiPS_3$ in that there are more diffuse features between the magnetic reflections. These diffuse features will worsen the residual parameters. According to literature, a reasonable fit for $NiPS_3$ would be a $R_{f2} = 23.8\%$. The $R_{f2}$ for our refinements range from 25% to 45%. Considering the diffuse features, we find that the quality of the fits to be adequate since they are of similar quality to the standard established in literature.

It is unclear why multiple magnetic phases appear in $FeP(S_{1-x}Se_x)_3$. Although there is a difference of about 2 $\mu_b$ between the magnetic phases, this result does not mean that the spin configuration for $Fe^{2+}$ switches between a high-spin state to a low-spin state (**Figure 5.24**. If this was the case, then we should see more distortions within the bond lengths, such that the crystal field energy changes to form low-spin $Fe^{2+}$. Additionally, because both low and high-spin states must exist together to give rise to the two magnetic phases, both coordination environments must be observed in the diffraction pattern. Considering the quality of fits for Rietveld refinements on room-temperature NPD data, the justification for the simultaneous existence of both the high and low-spin states lacks experimental evidence.

Additionally, it is possible for the total magnetic moments to be underrepresented. For monoclinic $FeP(S_{1-x}Se_x)_3$ the strength of the moments are lost due to diffuse features. For the trigonal phase, the Rietveld refinement is constrained due to the lack of other magnetic reflections for the $\vec{k} = [0\frac{1}{2}0]$ magnetic unit cell. If we ignore the fit optimization and try to estimate the total magnetic moment required to fully match the intensity of the $(0\frac{1}{2}0)$ reflection, the moments would need a value near 3.8 $\mu_B$. This value is close to the theoretical spin-only total magnetic moment for an $S = 2$ system. This phenomenon is similar to the one observed in $NiP(S_{1-x}Se_x)_3$. For those compounds, the calculated intensity was smaller than the observed intensity for the (010) magnetic reflection due to lack of additional magnetic reflections that should appear based on the magnetic structure model used.

Rather, the likely reason for the appearance of these new magnetic phases stems from the introduction of structural disorder through mixed anion substitution. Whether $FeP(S_{1-x}Se_x)_3$ is a monoclinic or trigonal crystal, we observe vacancies in the Fe and P sites. These vacancies have a direct relationship to structural disorder. For the monoclinic phase, the magnetic reflections already exhibit diffuse features, as demonstrated by the literature,[193] with the introduction of these structural disorders, through the presence of both S and Se, these features are magnified. Compared to the literature, our S-rich $FeP(S_{1-x}Se_x)_3$ samples display clear magnetic reflections from two magnetic phases along with diffuse features. Whereas, the $FePS_3$ NPD literature data reports diffuse features and the observation of well defined magnetic reflections for only one magnetic phase.[70,163,193]

Table 5.6: Rietveld Refinement results on 10 K NPD data for $FeP(S_{1-x}Se_x)_3$) for select compositions.

| **x = Se%** | **k** | $\mathbf{M}_T$ **($\mu_B$)** | $R_f$(%) | $R_{wp}$) **(%)** |
|---|---|---|---|---|
| **x = 0.01** | **[01$\frac{1}{2}$]** | **3.8(1)** | 13.8 | 12.6 |
| **x = 0.01** | **[010]** | **2.3(3)** | 17.5 | 12.6 |
| **x = 0.10** | **[01$\frac{1}{2}$]** | **3.9(1)** | 12 | 14.3 |
| **x = 0.10** | **[010]** | **1.8(5)** | 14.8 | 14.3 |
| **x = 0.28** | **[01$\frac{1}{2}$]** | **4.1(2)** | 11.8 | 14 |
| **x = 0.28** | **[010]** | **2.0(6)** | 12.8 | 14 |
| **x = 0.50** | **[01$\frac{1}{2}$]** | **5.1(7)** | 15.4 | 22.6 |
| **x = 0.50** | **[010]** | **4.1(4)** | 15.4 | 22.6 |
| **x = 0.50** | **[$\frac{1}{2}$0$\frac{1}{2}$]** | **4.9(9)** | 16.2 | 22.6 |
| **x = 0.50** | **[0$\frac{1}{2}$0]** | **3.2(2)** | 19.1 | 22.6 |
| **x = 0.73** | **[$\frac{1}{2}$0$\frac{1}{2}$]** | **4.7(6)** | 10.1 | 21.1 |
| **x = 0.73** | **[0$\frac{1}{2}$0]** | **3.2(4)** | 13.2 | 21.1 |
| **x = 0.80** | **[$\frac{1}{2}$0$\frac{1}{2}$]** | **4.7(6)** | 10.8 | 25.2 |
| **x = 0.80** | **[0$\frac{1}{2}$0]** | **2.5(2)** | 12.8 | 25.2 |

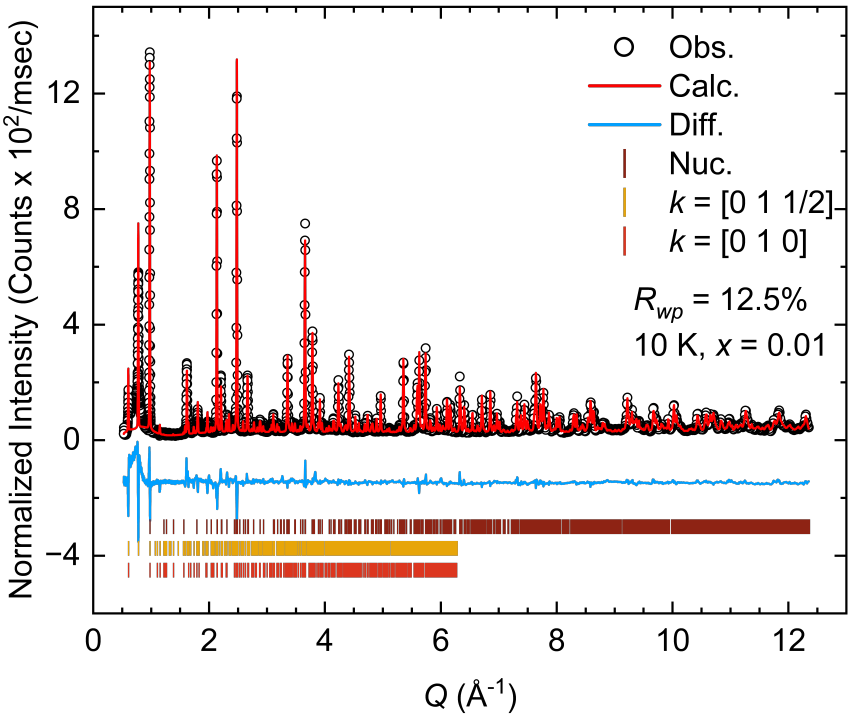



Figure 5.18: Rietveld refinement of neutron powder diffraction data of $FeP(S1-xSe_x)_3$ with $x$ = 0.01 at 10 K. The nuclear structure $R_f$ = 5.4%.

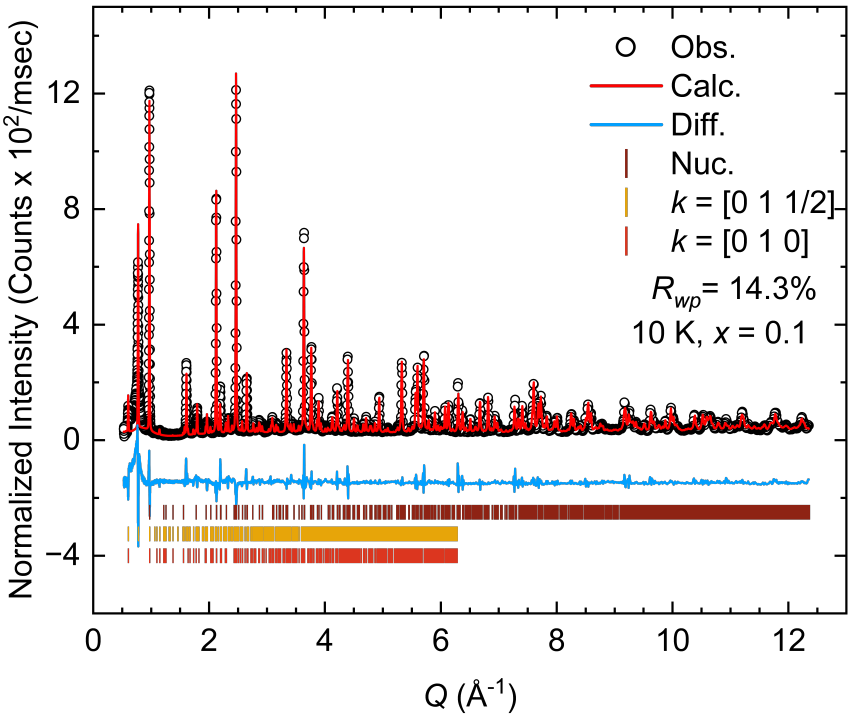



Figure 5.19: Rietveld refinement of neutron powder diffraction data of $FeP(S1-xSe_x)_3$ with $x$ = 0.10 at 10 K. Nuclear structure $R_f$ = 5.2%.

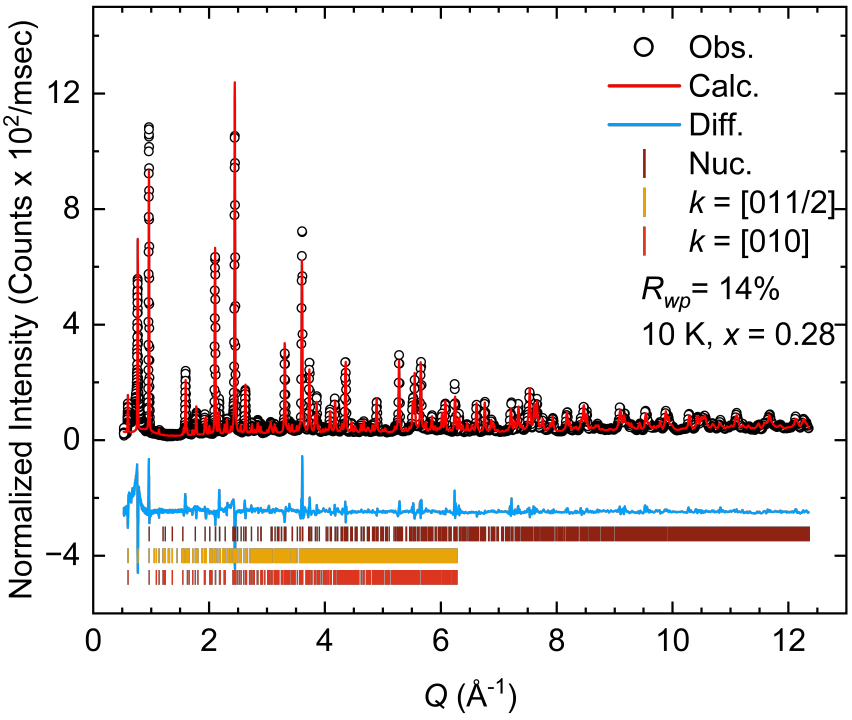



Figure 5.20: Rietveld refinement of neutron powder diffraction data of $FeP(S1-xSe_x)_3$ with $x = 0.28$ at 10 K. The nuclear structure $R_f = 4.7\%$.

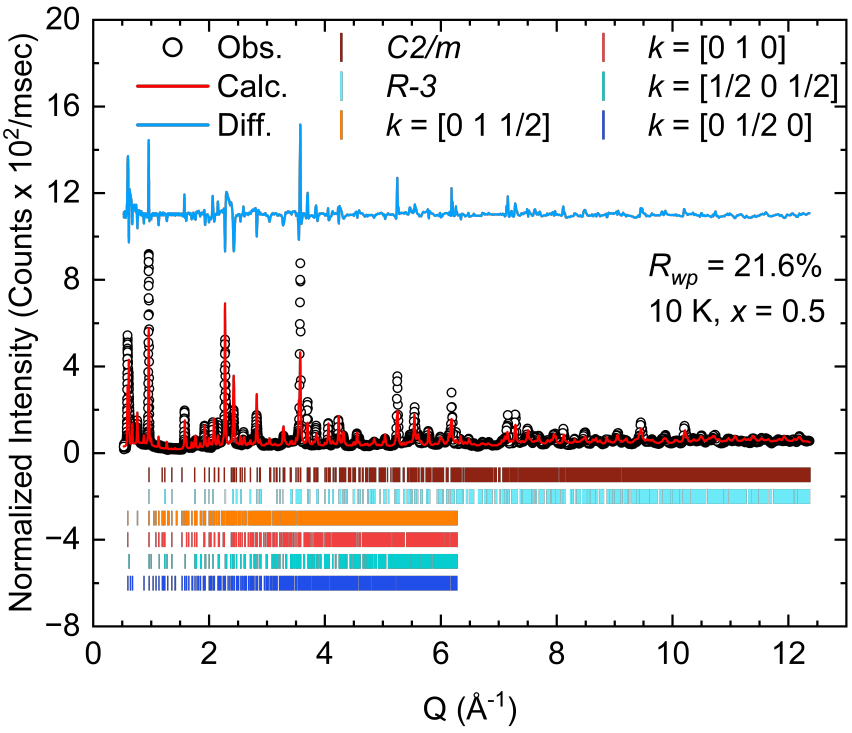



Figure 5.21: Rietveld refinement of neutron powder diffraction data of $FeP(S1-xSe_x)_3$ with $x$ = 0.50 at 10 K. Monoclinic $R_f$ = 11.9%. Trigonal $R_f$ = 15.4%

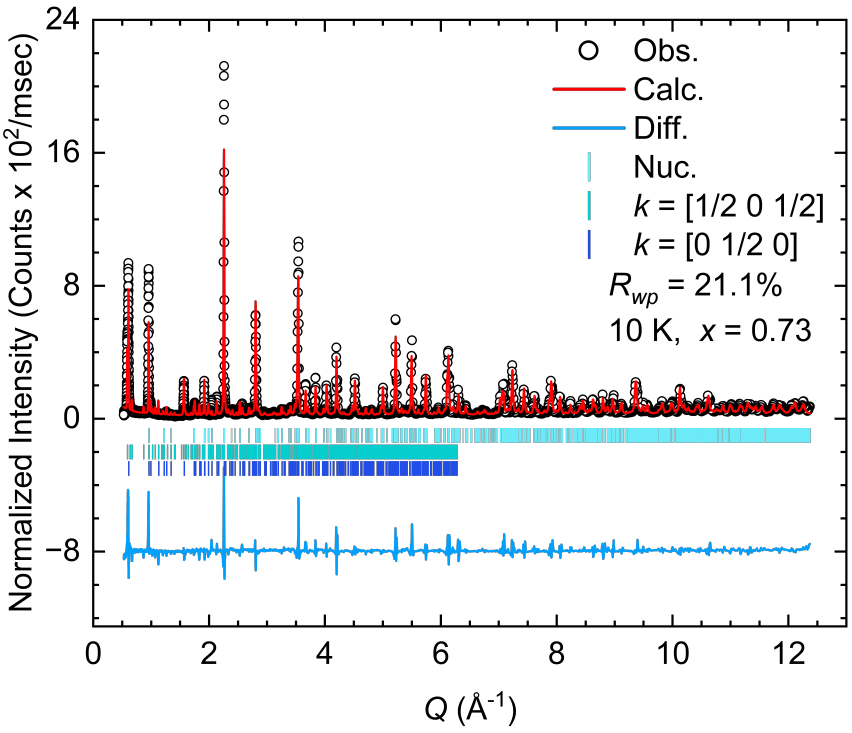



Figure 5.22: Rietveld refinement of neutron powder diffraction data of $FeP(S1-xSe_x)_3$ with $x$ = 0.73 at 10 K. The nuclear structure $R_f$ = 6.4%.

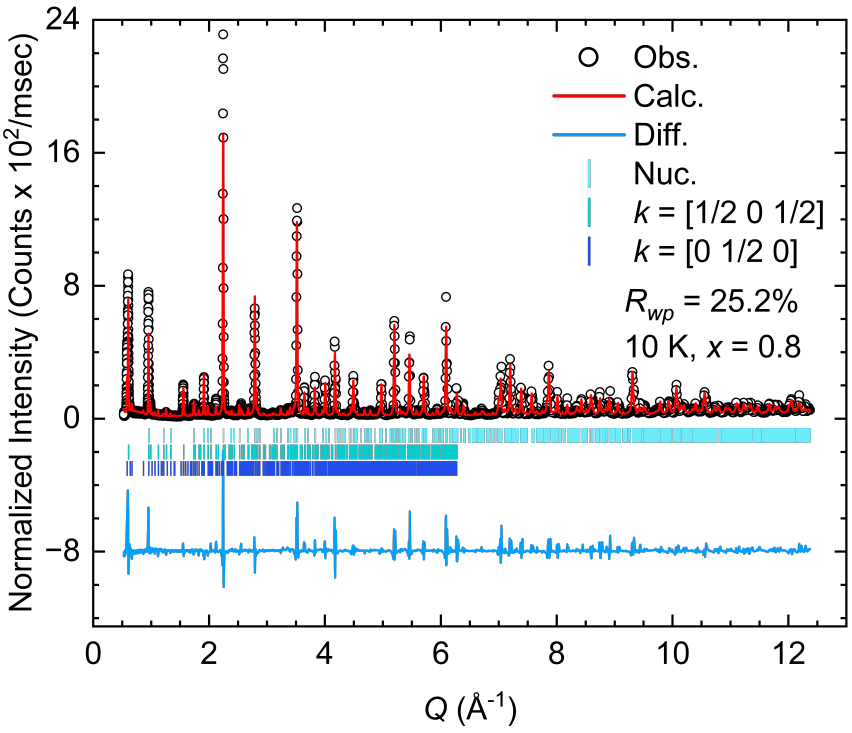



Figure 5.23: Rietveld refinement of neutron powder diffraction data of $FeP(S1-xSe_x)_3$ with $x$ = 0.80 at 10 K. The nuclear structure $R_f$ = 5.4%.

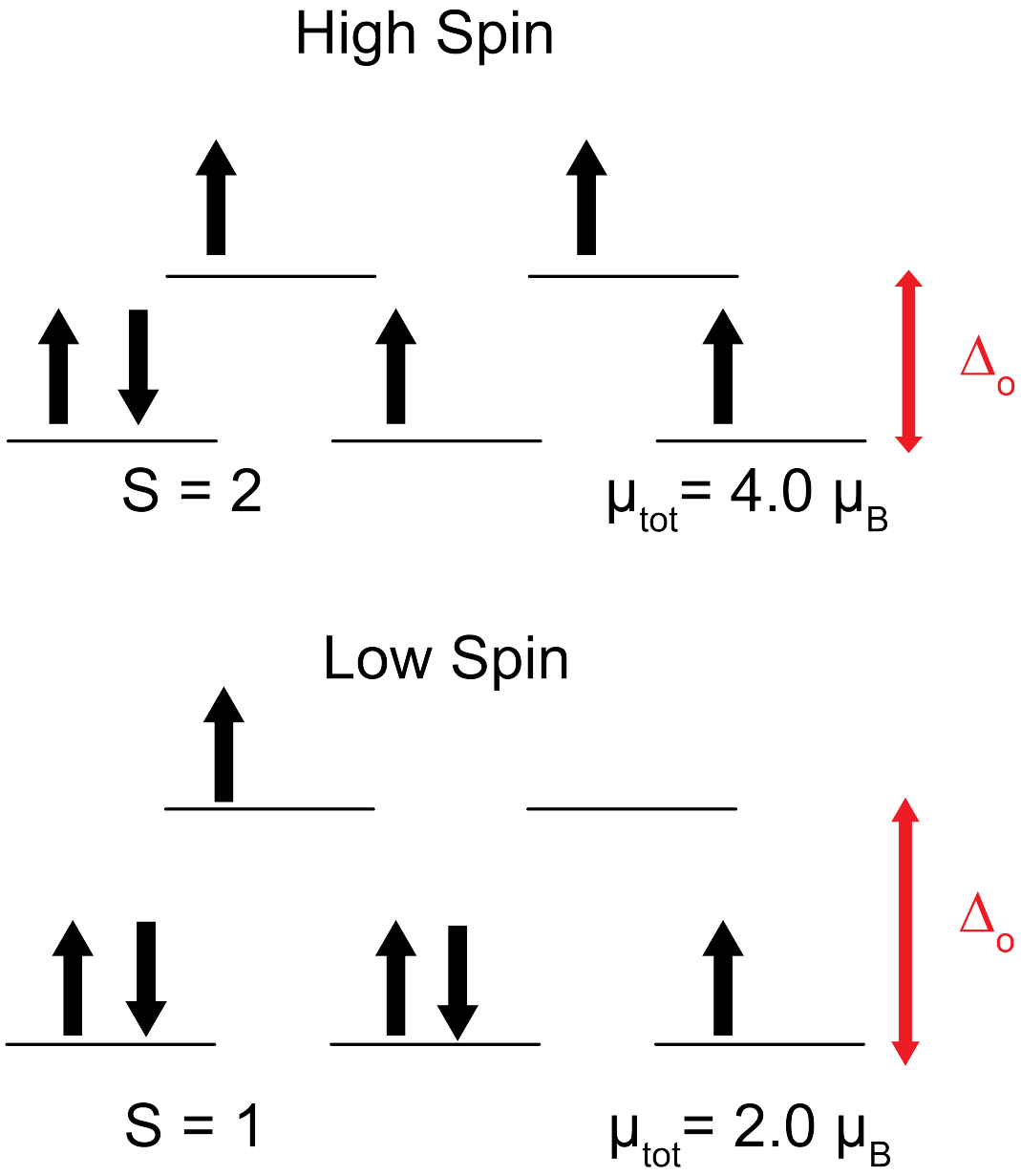



Figure 5.24: $Fe^{2+}$ with a high-spin configuration results in S = 2. A lower spin configuration will lead to S = 1. The total moment extracted from our diffraction results imply that k = $[\frac{1}{2}\ 0\ \frac{1}{2}]$ has S = 2 while the k = $[0\frac{1}{2}0]$ has S = 1 configuration.

## 5.4 Conclusions

In this chapter, the magnetic structure of novel mixed anion $FeP(S_{1-x}Se_x)_3$ was determined using NPD. Although preliminary magnetic susceptibility results indicate that these systems do not vary greatly from their $FePS_3$ and $FePSe_3$ counterparts, neutron diffraction revealed that new magnetic phases appear in $FeP(S_{1-x}Se_x)_3$ compounds. When $x < 0.5$, two magnetic phases with propagation vectors $\vec{k} = [01\frac{1}{2}]$ and $\vec{k} = [010]$ appear. When $x > 0.5$ two magnetic phases are also observed. One phase has $\vec{k} = [\frac{1}{2}0\frac{1}{2}]$ while the other has $\vec{k} = [0\frac{1}{2}0]$. This result was unexpected considering that both $FePS_3$ and $FePSe_3$ only have one magnetic phase. Curiously, the $\vec{k} = [010]$ and $\vec{k} = [0\frac{1}{2}0]$ magnetic phases are seen to have a magnetic moment that is consistently $S = 1$ lower than their counterparts. We claim that this difference in the magnetic moments between the two phases is the result of structural disorder introduced by mixed anion substitution and not a simultaneous existence of both a high and low-spin $Fe^{2+}$ electron configuration.

Future work includes single crystal susceptibility, high pressure studies and synthesizing new vdW materials. Due to the observation of in-plane moment direction from the NPD, one experiment to verify this result is perform single crystal magnetic susceptibility on $FeP(S_{1-x}Se_x)_3$ samples. Additionally, high quality susceptibility data can determine critical exponet values which describe the type of magnetic interactions the compound exhibits. Perhaps the creation of mixed anion $FeP(S_{1-x}Se_x)_3$ results in change in the magnetic i nteractions form an Ising type to Hesienburg or change the interaction to be more 3D like instead of 2D-like. Another future experiment is to perform high pressure NPD on $FeP(S_{1-x}Se_x)_3$. Considering that the magnetic structure of $FePS_3$ evolves as a function of pressure, high pressure studies on $FeP(S_{1-x}Se_x)_3$ could potentially result in more dramatic changes to the magnetic structure in Fe chalcophosphate materials. Perhaps the pressures will magnify or reduce the structural disorder in $FeP(S_{1-x}Se_x)_3$.

Lastly, further investigations into the nature of the magnetic interactions in $FeP(S_{1-x}Se_x)_3$ can be studied if another metal is introduced to the system, such as Mn, Co, and Ni. Each of these transition metals have different *d* electron counts and will exchange differently compared to Fe–Fe exchange in interactions. Additionally, perhaps mixed anion substitution can introduce the layer/lattice swapping disorder in other chalcophosphates such as $MnPS_3$.

# Chapter 6: Conclusions and Future Work

Neutron diffraction is a valuable technique for determining the magnetic structure of 2D materials. In this thesis, three novel vdW compounds that exhibit 2D magnetism were studied using neutron diffraction. Neutron diffraction revealed new insights about the magnetic behavior in each of the studied compounds that other prominent techniques, such as magnetic susceptibility cannot provide.

For $Fe_3GaTe_2$, prior to this work the literature reported that the crystal structure of this compound is analogous to that of $Fe_3GeTe_2$, that this compound exhibits ferromagnetism above room temperature based on susceptibility measurements and X-ray powder diffraction. The combination of both single-crystal and powder neutron diffraction techniques revealed that $Fe_3GaTe_2$ does not have an identical structure to $Fe_3GeTe_2$ due to an Fe interstitial site that sits between the vdW gaps. This site is magnetically active and its moments are anti-parallel to the moments from the other Fe sites. The importance of performing proper structural analysis and cross-referencing conclusions through a diversity of techniques cannot be overstated. The existence of these interstitial sites affects where the newly substituted atoms should go, and changes the way that FGaT should be modeled in theoretical calculations. In fact, preliminary NPD experiments on $Fe_{3-x}Co_xGaTe_2$ demonstrate that magnetic order can be manipulated to an extent (**Figure 6.1** - **6.2**)

Neutron-diffraction experiments on mixed anion $NiP(S_{1-x}Se_x)_3$ revealed that the magnetic structure has a propagation vector of $\vec{k}$ = [010]. The moments are organized in a zigzag configuration. However, single-crystal and powder neutron diffraction give differ-

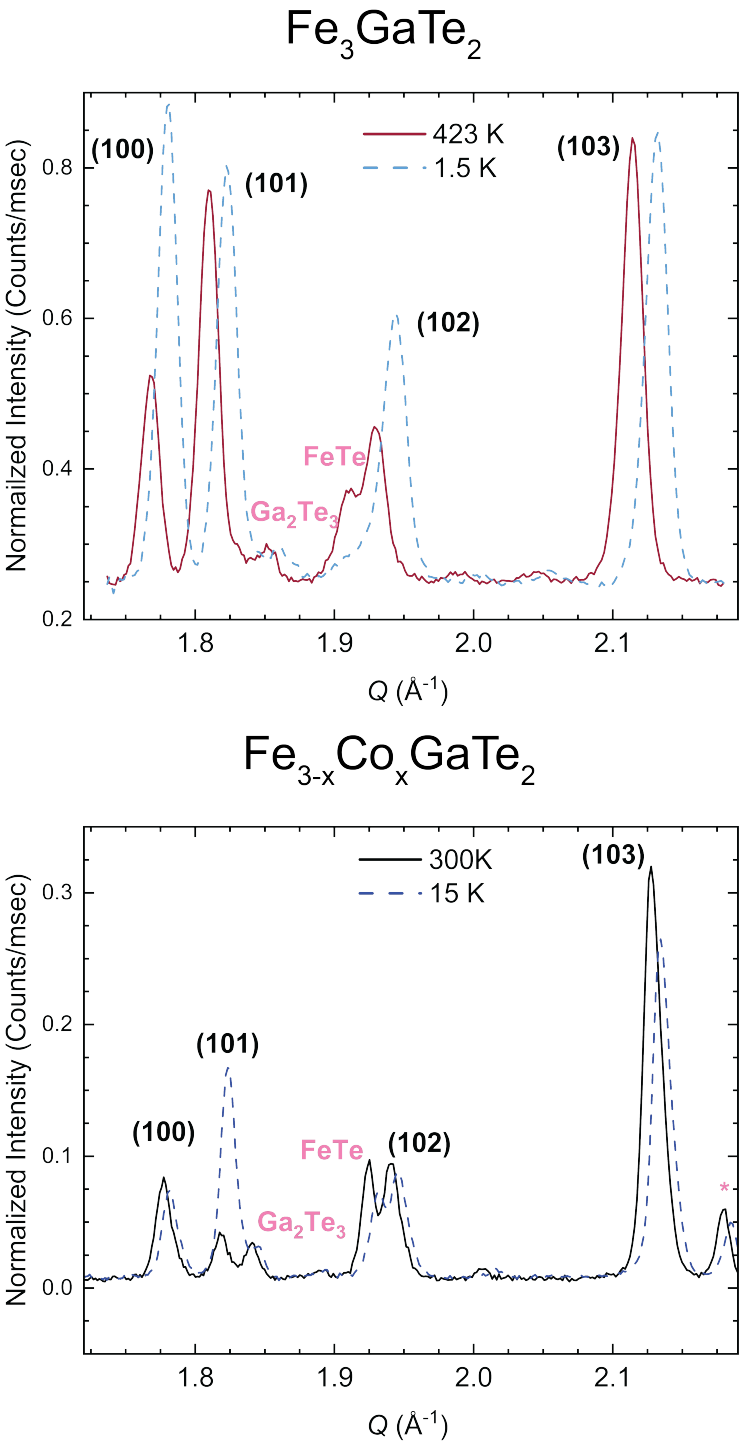



Figure 6.1: (Top) NPD of $Fe_3GaTe_2$. Magnetic reflections can be seen by comparing the intensities of the reflections at different temperature. For FGT the magnetic reflections are (100) and (102). (Bottom) NPD of $Fe_{3-x}Co_xGaTe_2$. Magnetic reflections shift to (101).(*) Represents an unknown impurity.

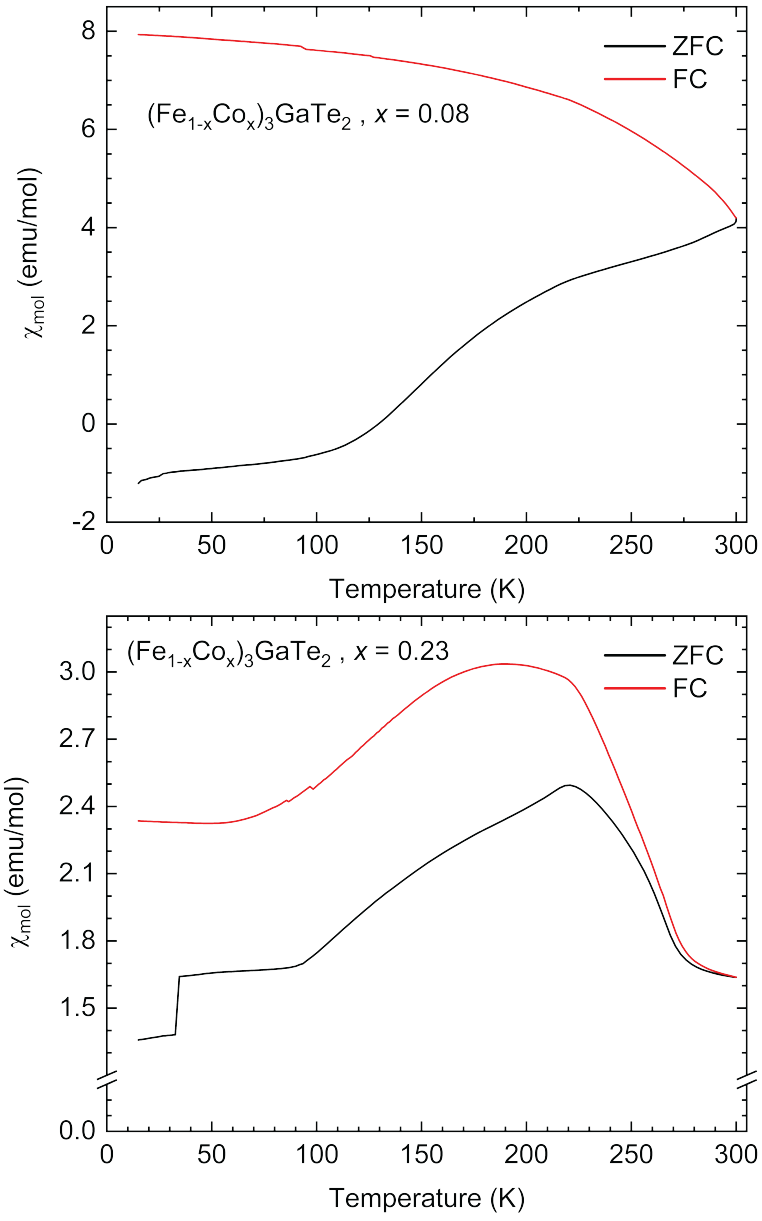



Figure 6.2: (Top) Powder magnetic susceptibility on $Fe_{3-x}Co_xGaTe_2$ sample where $x = 0.08$ (Bottom) $x = 0.23$. Compositions are nominal. Addition of Co reduces magnetic ordering temperature.

ent pictures of the magnitudes and directions of the moments. Results from the powder data suggest that the magnetic moments in $NiP(S_{1-x}Se_x)_3$ on average have a magnitude near $1.5\mu_B$ and are aligned about 20° from the *ab*-plane. In contrast, single crystal diffraction data indicates that the strength of the moments is near 1.5 $\mu_B$ at $x = 0.23$ and drops near 1 $\mu_B$ when $x = 0.43$. For both samples, the moments are primarily aligned to the *a*-axis and are not as aligned to the *c*-axis compared to the moments from NPD. These differences indicate that sample preparation is key when measuring $NiP(S_{1-x}Se_x)_3$ crystals. For instance, NPD patterns show that only two magnetic peaks that can be identified. Single-crystal diffraction on the other hand, exhibits several magnetic reflections. These additional reflections help to discern the direction of the magnetic moments.

Now that the magnetic magnetic structure for $NiP(S_{1-x}Se_x)_3$ is solved there are other potential avenues that can be used to engineer this compound. Li and $NH_3$ are two great intercalation candidates for this purpose. Lithium is typically used to electron dope magnetic metals to change the magnetic order. Intercalation with ammonia will fill the vdW gap and increase the unit cell size. Thus, the ammonia molecule could potentially affect the stacking order of the $NiP(S_{1-x}Se_x)_3$ monolayers. Ammonia may even inhibit the shifting of the layers in $NiP(S_{1-x}Se_x)_3$.

Lastly, the magnetic structure of mixed-anion $FeP(S_{1-x}Se_x)_3$ was determined, using NPD. It was revealed that by introducing Se to $FePS_3$ the magnetic structure is represented by two propagation vectors, $\vec{k} = [01\frac{1}{2}]$ and $\vec{k} = [010]$. If S is doped into $FePSe_3$ then the magnetic structure is also represented by two propagation vectors $\vec{k} = [\frac{1}{2}0\frac{1}{2}]$ and $\vec{k} = [0\frac{1}{2}0]$. To the best of our knowledge, this double propagation vector has not been observed in any of the other transition metal chalcophosphates. We hypothesized that the introduction of the structural distortion through mixed anion substitution is the underlying origin of this double-phase magnetic structure.

# Bibliography


[1] Yao, C.; Ma, Y. *iScience* **2021**, *24*, 102541.

[2] Chen, X.; Jiang, S.; Chen, Y.; Zou, Z.; Shen, B.; Lei, Y.; Zhang, D.; Zhang, M.; Gou, H. *Applied Energy* **2022**, *310*, 118602.

[3] ichi Shimoyama, J.; Motoki, T. *IEEJ Transactions on Electrical and Electronic Engineering* **2024**, *19*, 292–304.

[4] Stewart, G. R. *Reviews of Modern Physics* **2011**, *83*, 1589.

[5] Bussmann-Holder, A.; Keller, H. *Zeitschrift fur Naturforschung - Section B Journal of Chemical Sciences* **2019**, *75*, 3–14.

[6] Flores-Livas, J. A.; Boeri, L.; Sanna, A.; Profeta, G.; Arita, R.; Eremets, M. *Physics Reports* **2020**, *856*, 1–78.

[7] Kezilebieke, S.; Huda, M. N.; Vaňo, V.; Aapro, M.; Ganguli, S. C.; Silveira, O. J.; Głodzik, S.; Foster, A. S.; Ojanen, T.; Liljeroth, P. *Nature* **2020**, *588*, 424–428.

[8] Chappert, C.; Fert, A.; Dau, F. N. V. *Nature Materials* **2007**, *6*, 813–823.

[9] Hirohata, A.; Yamada, K.; Nakatani, Y.; Prejbeanu, L.; Diény, B.; Pirro, P.; Hillebrands, B. *Journal of Magnetism and Magnetic Materials* **2020**, *509*, 166711.

[10] Bhatti, S.; Sbiaa, R.; Hirohata, A.; Ohno, H.; Fukami, S.; Piramanayagam, S. N. *Materials Today* **2017**, *20*, 530–548.

[11] Gibertini, M.; Koperski, M.; Morpurgo, A. F.; Novoselov, K. S. *Nature Nanotechnology 2019 14:5* **2019**, *14*, 408–419.

[12] Dietl, T.; Ohno, H. *Reviews of Modern Physics* **2014**, *86*, 187.

[13] Zhang, L.; Dong, J.; Ding, F. *Chemical Reviews* **2021**, *121*, 6321–6372.

[14] Wang, F.; Shifa, T. A.; Yu, P.; He, P.; Liu, Y.; Wang, F.; Wang, Z.; Zhan, X.; Lou, X.; Xia, F.; He, J. *Advanced Functional Materials* **2018**, *28*, 1802151.

[15] Geim, A. K.; Grigorieva, I. V. *Nature 2013 499:7459* **2013**, *499*, 419–425.

[16] Duong, D. L.; Yun, S. J.; Lee, Y. H. *ACS Nano* **2017**, *11*, 11803–11830.

[17] May, A. F.; Yan, J.; McGuire, M. A. *Journal of Applied Physics* **2020**, *128*, 51101.

[18] Ci, P.; Chen, Y.; Kang, J.; Suzuki, R.; Choe, H. S.; Suh, J.; Ko, C.; Park, T.; Shen, K.; Iwasa, Y.; Tongay, S.; Ager, J. W.; Wang, L. W.; Wu, J. *Nano Letters* **2017**, *17*, 4982–4988.

[19] Fang, Z.; Li, X.; Shi, W.; Li, Z.; Guo, Y.; Chen, Q.; Peng, L.; Wei, X. *Journal of Physical Chemistry C* **2020**, *124*, 23419–23425.

[20] Rokni, H.; Lu, W. *Nature Communications 2020 11:1* **2020**, *11*, 5607–.

[21] Tang, K.; Qi, W.; Wei, Y.; Ru, G.; Liu, W. *Research* **2022**, *2022*.

[22] Liu, J.; Shen, T.; Ren, J. C.; Li, S.; Liu, W. *Applied Surface Science* **2023**, *608*, 155163.

[23] Liu, G. *Scientific Reports 2025 15:1* **2025**, *15*, 613–.

[24] Zhang, Q.; Mei, L.; Cao, X.; Tang, Y.; Zeng, Z. *Journal of Materials Chemistry A* **2020**, *8*, 15417–15444.

[25] Gong, C.; Zhang, X. *Science* **2019**, *363*.

[26] Liang, S.-J.; Cheng, B.; Cui, X.; Miao, F.; Liang, S.-J.; Cheng, B.; Miao, F.; Cui, X. Y. *Advanced Materials* **2020**, *32*, 1903800.

[27] Yu, X.; Zhao, G.; Gong, S.; Liu, C.; Wu, C.; Lyu, P.; Maurin, G.; Zhang, N. *ACS Applied Materials & Interfaces* **2020**, *12*, 24777–24785.

[28] Prabhu, P.; Jose, V.; Lee, J. M. *Matter* **2020**, *2*, 526–553.

[29] Novoselov, K. S.; Mishchenko, A.; Carvalho, A.; Neto, A. H. C. 2D materials and van der Waals heterostructures. 2016.

[30] Ribeiro-Palau, R.; Zhang, C.; Watanabe, K.; Taniguchi, T.; Hone, J.; Dean, C. R. *Science* **2018**, Look at SI for Device Fabrication.

[31] Jin, C.; Regan, E. C.; Yan, A.; Utama, M. I. B.; Wang, D.; Zhao, S.; Qin, Y.; Yang, S.; Zheng, Z.; Shi, S.; Watanabe, K.; Taniguchi, T.; Tongay, S.; Zettl, A.; Wang, F. *Nature* **2019**,

[32] Tran, K. et al. *Nature* **2019**,

[33] Luong, D. H.; Phan, T. L.; Ghimire, G.; Duong, D. L.; Lee, Y. H. *APL Materials* **2019**, *7*.

[34] Li, J. et al. *Nature* **2020**,

[35] Hidding, J.; Guimarães, M. H. D. *Frontiers in Materials* **2020**, *Volume 7 - 2020*.

[36] Kim, J. E.; Vu, V. T.; Vu, T. T. H.; Phan, T. L.; Kim, Y. R.; Kang, W. T.; Kim, K.; Lee, Y. H.; Yu, W. J. *Applied Sciences (Switzerland)* **2020**, *10*, 1–11.

[37] Zhang, Z.; Wang, Y.; Watanabe, K.; Taniguchi, T.; Ueno, K.; Tutuc, E.; LeRoy, B. J. *Nature Physics* **2020**, Read Later.

[38] Liu, Y.; Shao, Q. *ACS Nano* **2020**, *14*, 9389–9407.

[39] Manzeli, S.; Ovchinnikov, D.; Pasquier, D.; Yazyev, O. V.; Kis, A. *Nature Reviews Materials* **2017**,

[40] Al-Hilli, A.; Evans, B. *Journal of Crystal Growth* **1972**, *15*, 93–101.

[41] Agarwal, M. K.; Patel, P. D.; Joshi, R. M. *Journal of Materials Science Letters* **1986**, *5*, 66–68.

[42] Schäfer, H.; Grofe, T.; Trenkel, M. *Journal of Solid State Chemistry* **1973**, *8*, 14–28, Uses Iodide as vapor transport.

[43] Brec, R.; Schleich, D. M.; Ouvrard, G.; Louisy, A.; Rouxel, J. *Inorganic Chemistry* **1979**, *18*, 1814–1818.

[44] Brec, R. *Solid State Ionics* **1986**, *22*, 3–30.

[45] Klingen, W.; Eulenberger, G.; Hahn, H. *Zeitschrift für anorganische und allgemeine Chemie* **1973**, *401*, 97–112.

[46] Taylor, B.; Steger, J.; Wold, A.; Kostiner, E. *Inorganic Chemistry* **1974**, *13*, 2719–2721.

[47] Ouvrard, G.; Brec, R.; Rouxel, J. *Materials Research Bulletin* **1985**, *20*, 1181–1189.

[48] Nitsche, R.; Wild, P. *Materials Research Bulletin* **1970**, *5*, 419–423.

[49] Clement, R. *Journal of the Chemical Society, Chemical Communications* **1980**, 647–648.

[50] Piacentini, M.; Khumalo, F. S.; Olson, C. G.; Anderegg, J. W.; Lynch, D. W. *Chemical Physics* **1982**, *65*, 289–304.

[51] Grasso, V.; Santangelo, S.; Piacentini, M. *Solid State Ionics* **1986**, *20*, 9–15.

[52] Grasso, V.; Neri, F.; Silipigni, L.; Piacentini, M. *Il Nuovo Cimento D* **1991**, *13*, 633–645.

[53] Ohno, Y. *Solid State Communications* **1988**, *67*, 1089–1092.

[54] Joy, P. A.; Vasudevan, S. *Physical Review B* **1992**, *46*, 5134–5141.

[55] McCarthy, T. J.; Kanatzidis, M. G. *Inorganic Chemistry* **1995**, *34*.

[56] Manríquez, V.; Galdámez, A.; Villanueva, A.; Aranda, P.; Galván, J. C.; Ruiz-Hitzky, E. *Materials Research Bulletin* **1999**, *34*, 673–683.

[57] Regan, E. C.; Wang, D.; Paik, E. Y.; Zeng, Y.; Zhang, L.; Zhu, J.; MacDonald, A. H.; Deng, H.; Wang, F. *Nature Reviews Materials* **2022**, *7*, 778–795.

[58] Mueller, T.; Malic, E. *npj 2D Materials and Applications* **2018**, *2*, 1–12.

[59] Shi, J.; Wang, D.; Jiang, N.; Xin, Z.; Zheng, H.; Shen, C.; Zhang, X.; Liu, X. *ACS Nano* **2025**, *19*, 29977–29987.

[60] Bai, Y.; Li, Y.; Liu, S.; Guo, Y.; Pack, J.; Wang, J.; Dean, C. R.; Hone, J.; Zhu, X. *Nano Letters* **2023**, *23*, 11621–11629.

[61] Du, L. *Nature Reviews Physics* **2024**, *6*, 157–159.

[62] Jin, C.; Ma, E. Y.; Karni, O.; Regan, E. C.; Wang, F.; Heinz, T. F. *Nature Nanotechnology* **2018**, *13*, 994–1003.

[63] Abraham, J. J. et al. *Advanced Functional Materials* **2025**, e11057.

[64] Xing, W.; Qiu, L.; Wang, X.; Yao, Y.; Ma, Y.; Cai, R.; Jia, S.; Xie, X. C.; Han, W. *Physical Review X* **2019**, *9*, 011026.

[65] Bae, Y. J. et al. *Nature* **2022**, *609*, 282–286.

[66] Wu, Y. et al. *Nature Communications* **2020**, *11*, 1–6.

[67] Park, T. E. et al. *Physical Review B* **2021**, *103*, 104410.

[68] Liu, C.; Zhang, S.; Hao, H.; Algaidi, H.; Ma, Y.; Zhang, X. X. *Advanced Materials* **2024**, *36*, 2311022.

[69] Wang, N.; Tang, H.; Shi, M.; Zhang, H.; Zhuo, W.; Liu, D.; Meng, F.; Ma, L.; Ying, J.; Zou, L.; Sun, Z.; Chen, X. *Journal of the American Chemical Society* **2019**, *141*, 17166–17173.

[70] Wiedenmann, A.; Rossat-Mignod, J.; Louisy, A.; Brec, R.; Rouxel, J. *Solid State Communications* **1981**, *40*, 1067–1072.

[71] Carteaux, V.; Brunet, D.; Ouvrard, G.; Andre, G. *Journal of Physics: Condensed Matter* **1995**, *7*, 69–87.

[72] Yang, D.; Yao, W.; Chen, Q.; Peng, K.; Jiang, P.; Lu, X.; Uher, C.; Yang, T.; Wang, G.; Zhou, X. *Chemistry of Materials* **2016**, *28*, 1611–1615.

[73] Shen, X.; Lin, X.; Peng, Y.; Zhang, Y.; Long, F.; Han, Q.; Wang, Y.; Han, L. *Nano-Micro Letters* **2024**, *16*, 1–37.

[74] Chen, Q.; Wei, Y.; Zhai, P. B.; Gong, Y. J. *Rare Metals* **2024**, *43*, 6125–6143.

[75] Yan, Y.; Zeng, Z.; Huang, M.; Chen, P. *Materials Today Advances* **2020**, *6*, 100059.

[76] Xiao, W. Z.; Xu, L.; Rong, Q. Y.; Dai, X. Y.; Cheng, C. P.; Wang, L. L. *Applied Surface Science* **2020**, *504*, 144425.

[77] Yang, R.; Fan, Y.; Zhang, Y.; Mei, L.; Zhu, R.; Qin, J.; Hu, J.; Chen, Z.; Ng, Y. H.; Voiry, D.; Li, S.; Lu, Q.; Wang, Q.; Yu, J. C.; Zeng, Z. *Angewandte Chemie International Edition* **2023**, *62*, e202218016.

[78] Zhang, C.; Ren, K.; Wang, S.; Luo, Y.; Tang, W.; Sun, M. *Journal of Physics D: Applied Physics* **2023**, *56*, 483001.

[79] Huang, B.; Clark, G.; Klein, D. R.; MacNeill, D.; Navarro-Moratalla, E.; Seyler, K. L.; Wilson, N.; McGuire, M. A.; Cobden, D. H.; Xiao, D.; Yao, W.; Jarillo-Herrero, P.; Xu, X. *Nature Nanotechnology* **2018**, *13*, 544–548.

[80] Sierra, J. F.; Fabian, J.; Kawakami, R. K.; Roche, S.; Valenzuela, S. O. *Nature Nanotechnology* **2021**, *16*, 856–868.

[81] Kajale, S. N.; Hanna, J.; Jang, K.; Sarkar, D. *Nano Research* **2024**, *17*, 743–762.

[82] Kajale, S. N.; Nguyen, T.; Chao, C. A.; Bono, D. C.; Boonkird, A.; Li, M.; Sarkar, D. *Nature Communications 2024 15:1* **2024**, *15*, 1–8.

[83] Chen, H.; Liu, L.; Zhou, X.; Meng, Z.; Wang, X.; Duan, Z.; Zhao, G.; Yan, H.; Qin, P.; Liu, Z. *Advanced Materials* **2024**, *36*, 2310379.

[84] Pecharsky, V. K.; Zavalij, P. Y. *Fundamentals of powder diffraction and structural characterization of materials*, 2nd ed.; Springer: New York, 2009.

[85] Kisi, E. H.; Howard, C. J. *Applications of Neutron Powder Diffraction*; Oxford University Press, 2008.

[86] Chatterji, T. *Neutron Scattering from Magnetic Materials*; Elsevier, 2006.

[87] Cullity, B. D.; Stock, S. R. *Elements of X-ray Diffraction*, 3rd ed.; Prentice Hall: Upper Saddle River, NJ, 2001.

[88] of Crystallography, I. U. In *International Tables for Crystallography, Volume A: Space-Group Symmetry*, 5th ed.; Hahn, T., Ed.; International Tables for Crystallography; Kluwer Academic Publishers: Dordrecht, Boston, London, 2002.

[89] Rodríguez-Carvajal, J. *Physica B: Condensed Matter* **1993**, *192*, 55–69.

[90] Shull, C. G.; Smart, J. S. *Physical Review* **1949**, *76*, 1256.

[91] Profumo, S.; Odintsov, S. D.; Ratcliff, W. *Symmetry 2022, Vol. 14, Page 1215* **2022**, *14*, 1215.

[92] Kaneko, K.; Frontzek, M. D.; Matsuda, M.; Nakao, A.; Munakata, K.; Ohhara, T.; Kakihana, M.; Haga, Y.; Hedo, M.; Nakama, T.; Ōnuki, Y. *Journal of the Physical Society of Japan* **2019**, *88*, 013702.

[93] Takagi, R. et al. *Nature Communications* **2022**, *13*, 1–7.

[94] Mandujano, H. C.; Tafere, M. S.; Muniraju, N. K. C.; Creason, T. D.; McWhorter, T. M.; Gofryk, K.; Heitmann, T. W.; Zhang, Q.; Saparov, B.; Nair, H. S. *Dalton Transactions* **2023**, *52*, 5652–5662.

[95] Wang, M.; Lei, B.; Zhu, K.; Deng, Y.; Tian, M.; Xiang, Z.; Wu, T.; Chen, X. *npj 2D Materials and Applications* **2024**, *8*, 1–7.

[96] Wang, M.; Zhu, K.; Lei, B.; Deng, Y.; Hu, T.; Song, D.; Du, H.; Tian, M.; Xiang, Z.; Wu, T.; Chen, X. *Nano Letters* **2024**, *24*, 4141–4149.

[97] Kim, K.; Lim, S. Y.; Lee, J. U.; Lee, S.; Kim, T. Y.; Park, K.; Jeon, G. S.; Park, C. H.; Park, J. G.; Cheong, H. *Nature Communications* **2019**, *10*, 1–9.

[98] Lee, J. U.; Lee, S.; Ryoo, J. H.; Kang, S.; Kim, T. Y.; Kim, P.; Park, C. H.; Park, J. G.; Cheong, H. *Nano Letters* **2016**, *16*, 7433–7438.

[99] Li, Z. et al. *Nature Communications* **2024**, *15*, 1–11.

[100] Luo, J. et al. *Nano Letters* **2023**, *23*, 2023–2030.

[101] Scheie, A.; Park, P.; Villanova, J. W.; Granroth, G. E.; Sarkis, C. L.; Zhang, H.; Stone, M. B.; Park, J. G.; Okamoto, S.; Berlijn, T.; Tennant, D. A. *Physical Review B* **2023**, *108*, 104402.

[102] Ghosh, A.; Palit, M.; Maity, S.; Dwij, V.; Rana, S.; Datta, S. *Physical Review B* **2021**, *103*, 064431.

[103] Mardelé, F. L.; Mohelsky, I.; Jana, D.; Pawbake, A.; Dzian, J.; Lee, W. L.; Raju, K.; Sankar, R.; Faugeras, C.; Potemski, M.; Zhitomirsky, M. E.; Orlita, M. *Physical Review B* **2024**, *110*, 174414.

[104] Mardelé, F. L.; Mendili, A. E.; Zhitomirsky, M. E.; Mohelsky, I.; Jana, D.; Plutnarova, I.; Sofer, Z.; Faugeras, C.; Potemski, M.; Orlita, M. *Physical Review B* **2024**, *109*, 134410.

[105] Lopez, M.; Yan, P.; Zavalij, P. Y.; Javadi, A.; da Silva, I.; Wang, Z.; Ren, S.; Bennett, J. W.; Rodriguez, E. E. *J. Mater. Chem. C* **2025**, *13*, 15354–15361.

[106] Blundell, S. *Magnetism in Condensed Matter*; Oxford University Press, 2001.

[107] Coey, J. M. *Magnetism and Magnetic Materials* **2010**, *9780521816144*, 1–617.

[108] Spaldin, N. A. *Magnetic Materials: Fundamentals and Applications* **2010**, *9780521886697*, 1–274.

[109] Mi, M.; Xiao, H.; Yu, L.; Zhang, Y.; Wang, Y.; Cao, Q.; Wang, Y. *Materials Today Nano* **2023**, *24*, 100408.

[110] Ryu, J.; Kajale, S. N.; Sarkar, D. *MRS Communications* **2024**, *14*, 1113–1126.

[111] Baltz, V.; Manchon, A.; Tsoi, M.; Moriyama, T.; Ono, T.; Tserkovnyak, Y. *Reviews of Modern Physics* **2018**, *90*, 015005, Read later for Spintronics Info.

[112] Pan, Z. C.; Li, D.; Ye, X. G.; Chen, Z.; Chen, Z. H.; Wang, A. Q.; Tian, M.; Yao, G.; Liu, K.; Liao, Z. M. *Science Bulletin* **2023**, *68*, 2743–2749.

[113] Zhang, G.; Yu, J.; Wu, H.; Yang, L.; Jin, W.; Zhang, W.; Chang, H. *Applied Physics Letters* **2023**, *123*, 101901.

[114] Zhang, Y.; Li, X.; Sheng, J.; Yu, S.; Zhang, J.; Su, Y. *Applied Physics Letters* **2023**, *123*, 192402.

[115] Jin, W.; Zhang, G.; Wu, H.; Yang, L.; Zhang, W.; Chang, H. *ACS Applied Materials and Interfaces* **2023**, *15*, 36519–36526.

[116] Jin, W.; Zhang, G.; Wu, H.; Yang, L.; Zhang, W.; Chang, H. *Nanoscale* **2023**, *15*, 5371–5378.

[117] Bera, S.; Pradhan, S. K.; Khan, M. S.; Pal, R.; Pal, B.; Kalimuddin, S.; Bera, A.; Das, B.; Pal, A. N.; Mondal, M. *Journal of Magnetism and Magnetic Materials* **2023**, *565*, 170257.

[118] Zhao, Y.; Guo, Y.; Zhou, S.; Zhao, J. *Physical Review Materials* **2022**, *6*, 044005.

[119] Mayoh, D. A.; Wood, G. D.; Holt, S. J.; Beckett, G.; Dekker, E. J.; Lees, M. R.; Balakrishnan, G. *Crystal Growth and Design* **2021**, *21*, 6786–6792.

[120] Jang, S. W.; Yoon, H.; Jeong, M. Y.; Ryee, S.; Kim, H. S.; Han, M. J. *Nanoscale* **2020**, *12*, 13501–13506.

[121] Stahl, J.; Shlaen, E.; Johrendt, D. *Zeitschrift für anorganische und allgemeine Chemie* **2018**, *644*, 1923–1929.

[122] May, A. F.; Calder, S.; Cantoni, C.; Cao, H.; McGuire, M. A. *Physical Review B* **2016**, *93*, 014411.

[123] May, A. F.; Ovchinnikov, D.; Zheng, Q.; Hermann, R.; Calder, S.; Huang, B.; Fei, Z.; Liu, Y.; Xu, X.; McGuire, M. A. *ACS Nano* **2019**, *13*, 4436–4442.

[124] Zhang, G.; Guo, F.; Wu, H.; Wen, X.; Yang, L.; Jin, W.; Zhang, W.; Chang, H. *Nature Communications 2022 13:1* **2022**, *13*, 1–8.

[125] Zhang, L.; He, M.; Wang, X.; Zhang, H.; Han, K.; Liu, Y.; Zhang, L.; Cheng, Y.; Pan, J.; Qu, Z.; Wang, Z. *Journal of Physics D: Applied Physics* **2025**, *58*, 105005.

[126] Hu, G. et al. *Advanced Materials* **2024**, *36*, 2403154.

[127] Wu, H.; Yang, L.; Zhang, G.; Jin, W.; Xiao, B.; Yu, J.; Annas, A.; Zhang, W.; Wang, K.; Chang, H. *Small Methods* **2025**, 2401117.

[128] Jin, W. et al. *Advanced Functional Materials* **2024**, *34*, 2402091.

[129] Deng, Y.; Zhu, K.; Wang, M.; Hu, T.; Wang, Y.; Lei, B.; Chen, X. *Nanoscale* **2024**, *16*, 15793–15800.

[130] Deng, Y.; Wang, M.; Xiang, Z.; Zhu, K.; Hu, T.; Lu, L.; Wang, Y.; Ma, Y.; Lei, B.; Chen, X. *Nano Letters* **2024**, *24*, 9302–9310.

[131] Saha, R.; Meyerheim, H. L.; Göbel, B.; Mertig, I.; Parkin, S. S. P. *npj Spintronics 2024 2:1* **2024**, *2*, 1–7.

[132] Mi, S.; Guo, J.; Hu, G.; Wang, G.; Li, S.; Gong, Z.; Jin, S.; Xu, R.; Pang, F.; Ji, W.; Yu, W.; Wang, X.; Wang, X.; Yang, H.; Cheng, Z. *Nano Letters* **2024**,

[133] Shi, H. et al. *Nano Letters* **2024**, *22*, 39.

[134] Ruiz, A. M.; Esteras, D. L.; López-Alcalá, D.; Baldoví, J. J. *Nano Letters* **2024**,

[135] Deiseroth, H.-J.; Aleksandrov, K.; Reiner, C.; Kienle, L.; Kremer, R. K. *European Journal of Inorganic Chemistry* **2006**, *2006*, 1561–1567.

[136] Giannozzi, P. et al. *Journal of Physics: Condensed Matter* **2009**, *21*, 395502.

[137] Hohenberg, P.; Kohn, W. *Physical Review* **1964**, *136*, B864.

[138] Kohn, W.; Sham, L. J. *Physical Review* **1965**, *140*, A1133.

[139] Kohn, W.; Sham, L. J. *Physical Review* **1965**, *137*, A1697.

[140] Monkhorst, H. J.; Pack, J. D. *Physical Review B* **1976**, *13*, 5188.

[141] Algaidi, H.; Zhang, C.; Ma, Y.; Liu, C.; Chen, A.; Zheng, D.; Zhang, X. *APL Materials* **2024**, *12*, 11124.

[142] Zaliznyak, I. A.; Xu, Z. J.; Wen, J. S.; Tranquada, J. M.; Gu, G. D.; Solovyov, V.; Glazkov, V. N.; Zheludev, A. I.; Garlea, V. O.; Stone, M. B. *Physical Review B* **2012**, *85*, 085105.

[143] Stock, C.; Rodriguez, E. E.; Bourges, P.; Ewings, R. A.; Cao, H.; Chi, S.; Rodriguez-Rivera, J. A.; Green, M. A. *Physical Review B* **2017**, *95*, 144407.

[144] Demirdiş, S.; Su, Y.; Nemkowski, K.; Wang, R.; Huang, Z. X.; Cao, L. X. *Physica B: Condensed Matter* **2015**, *474*, 53–56.

[145] Rodriguez, E. E.; Stock, C.; Zajdel, P.; Krycka, K. L.; Majkrzak, C. F.; Zavalij, P.; Green, M. A. *Physical Review B* **2011**, *84*, 064403.

[146] Stoner, E. C. *Proceedings of the Royal Society of London. A. Mathematical and Physical Sciences* **1938**, *165*, 372–414.

[147] Wohlfarth, E. P. *Rev. Mod. Phys.* **1953**, *25*, 211–219.

[148] Tomarchio, L.; Polewczyk, V.; Mosesso, L.; Marty, A.; Macis, S.; Jamet, M.; Bonell, F.; Lupi, S. *npj 2D Materials and Applications* **2024**, *8*, 1–8.

[149] Guo, S.; He, Y.; Lv, X.; Jiang, M.; Wei, Y.; Deng, Y.; Pan, X.; Lan, S.; Wang, D.; Liu, A.; Guo, C.; Wang, L. *2D Materials* **2024**, *11*, 035008.

[150] Kang, S. et al. *Nature* **2020**, *583*, 785–789.

[151] Kim, C.; Jeong, J.; Park, P.; Masuda, T.; Asai, S.; Itoh, S.; Kim, H. S.; Wildes, A.; Park, J. G. *Physical Review B* **2020**, *102*, 184429.

[152] Wang, X.; Cao, J.; Lu, Z.; Cohen, A.; Kitadai, H.; Li, T.; Tan, Q.; Wilson, M.; Lui, C. H.; Smirnov, D.; Sharifzadeh, S.; Ling, X. *Nature Materials 2021 20:7* **2021**, *20*, 964–970.

[153] Jungwirth, T.; Marti, X.; Wadley, P.; Wunderlich, J. *Nature Nanotechnology* **2016**, *11*, 231–241, Read later for Spintronics Info.

[154] Li, H.; Ruan, S.; Zeng, Y.-J. *Advanced Materials* **2019**, *31*, 1900065.

[155] Toyoda, S.; Kruppe, J.; Yamakawa, K.; Analytis, J.; Orenstein, J. *Physical Review B* **2024**, *109*, 064408.

[156] Liao, J.; Huang, Z.; Shangguan, Y.; Zhang, B.; Cheng, S.; Xu, H.; Kajimoto, R.; Kamazawa, K.; Bao, S.; Wen, J. *Physical Review B* **2024**, *109*, 224411.

[157] Liu, C. et al. *Advanced Materials* **2023**, *35*, 2300247.

[158] Muhammad, Z.; Szpakowski, J.; Abbas, G.; Zu, L.; Islam, R.; Wang, Y.; Wali, F.; Karmakar, A.; Molas, M. R.; Zhang, Y.; Zhu, L.; Zhao, W.; Zhang, H. *2D Materials* **2023**, *10*, 025001.

[159] Pazek, S.; Efimenko, A.; Félix, R.; Roslova, M.; Querebillo, C. J.; Gorbunov, M. V.; Ovchinnikov, A.; Koitzsch, A.; Escudero, C.; Shemerliuk, Y.; Aswartham, S.; Büchner, B.; Omar, A.; Mikhailova, D. *Journal of Materials Chemistry A* **2024**, *12*, 3523–3541.

[160] Wildes, A. R.; Simonet, V.; Ressouche, E.; McIntyre, G. J.; Avdeev, M.; Suard, E.; Kimber, S. A.; Lançon, D.; Pepe, G.; Moubaraki, B.; Hicks, T. J. *Physical Review B - Condensed Matter and Materials Physics* **2015**, *92*, 224408.

[161] Zheng, Y.; Jiang, X. X.; Xue, X. X.; Dai, J.; Feng, Y. *Physical Review B* **2019**, *100*, 174102.

[162] Yan, X.; Chen, X.; Qin, J. *Materials Research Bulletin* **2011**, *46*, 235–238.

[163] Rule, K. C.; McIntyre, G. J.; Kennedy, S. J.; Hicks, T. J. *Physical Review B* **2007**, *76*, 134402.

[164] Selter, S.; Shemerliuk, Y.; Sturza, M. I.; Wolter, A. U.; Büchner, B.; Aswartham, S. *Physical Review Materials* **2021**, *5*, 073401.

[165] Budniak, A. K.; Zelewski, S. J.; Birowska, M.; Woźniak, T.; Bendikov, T.; Kauffmann, Y.; Amouyal, Y.; Kudrawiec, R.; Lifshitz, E. *Advanced Optical Materials* **2022**, *10*, 2102489.

[166] Kozlenko, D. P.; Lis, O. N.; Dang, N. T.; Coak, M.; Park, J. G.; Lukin, E. V.; Kichanov, S. E.; Golosova, N. O.; Zel, I. Y.; Savenko, B. N. *Physical Review Materials* **2024**, *8*, 024402.

[167] Matsuoka, T.; Kim, H. S.; Samanta, S.; Musfeldt, J. L.; Mandrus, D. G. *Frontiers in Materials* **2024**, *11*, 1362744.

[168] Graham, J. N.; Coak, M. J.; Son, S.; Suard, E.; Park, J. G.; Clark, L.; Wildes, A. R. *Physical Review Materials* **2020**, *4*, 084401.

[169] Basnet, R.; Ford, D.; Tenbarge, K.; Lochala, J.; Hu, J. *Journal of Physics: Condensed Matter* **2022**, *34*, 434002.

[170] Calder, S.; Haglund, A. V.; Kolesnikov, A. I.; Mandrus, D. *Physical Review B* **2021**, *103*, 024414.

[171] Kurosawa, K.; Saito, S.; Yamaguch, Y. *Journal of the Physical Society of Japan* **1983**, *52*, 3919–3926.

[172] Mugiraneza, S.; Hallas, A. M. *Communications Physics* **2022**, *5*, 1–12.

[173] Flem, G. L.; Brec, R.; Ouvard, G.; Louisy, A.; Segransan, P. *Journal of Physics and Chemistry of Solids* **1982**, *43*, 455–461.

[174] Chandrasekharan, N.; Vasudevan, S. *Journal of Physics: Condensed Matter* **1994**, *6*, 4569.

[175] Lançon, D.; Ewings, R. A.; Guidi, T.; Formisano, F.; Wildes, A. R. *PHYSICAL REVIEW B* **2018**, *98*, 134414.

[176] Mi, M.; Zheng, X.; Wang, S.; Zhou, Y.; Yu, L.; Xiao, H.; Song, H.; Shen, B.; Li, F.; Bai, L.; Chen, Y.; Wang, S.; Liu, X.; Wang, Y. *Advanced Functional Materials* **2022**, *32*, 2112750.

[177] Basnet, R.; Kotur, K. M.; Rybak, M.; Stephenson, C.; Bishop, S.; Autieri, C.; Birowska, M.; Hu, J. *Physical Review Research* **2022**, *4*, 023256.

[178] Shemerliuk, Y.; Zhou, Y.; Yang, Z.; Cao, G.; Wolter, A. U. B.; Büchner, B.; Aswartham, S. *Electronic Materials 2021, Vol. 2, Pages 284-298* **2021**, *2*, 284–298.

[179] Inoue, N.; Yasuoka, H.; Ogawa, S. *Journal of the Physical Society of Japan* **1980**, *48*, 850–856.

[180] Adachi, K.; Sato, K.; Takeda, M.; Lett, A. P.; Freiser, M. J.; Berg, F. H. *Journal of Applied Physics* **1968**, *39*, 900–900.

[181] Furuseth, S.; Kjekshus, A.; Andresen, A. F.; Nordal, V.; Lindberg, A. A.; Craig, J. C. *Acta Chemica Scandinavica* **1969**, *23*, 2325–2334.

[182] Goodenough, J. B.; Loeb, A. L. *Phys. Rev.* **1955**, *98*, 391–408.

[183] Kanamori, J. *Journal of Physics and Chemistry of Solids* **1959**, *10*, 87–98.

[184] Goossens, D. J.; James, D.; Dong, J.; Whitfield, R. E.; Norén, L.; Withers, R. L. *Journal of Physics Condensed Matter* **2011**, *23*, 065401.

[185] Hahn, H.; Klingen, W. *Die Naturwissenschaften* **1965**, *52*, 494.

[186] Gong, C.; Li, L.; Li, Z.; Ji, H.; Stern, A.; Xia, Y.; Cao, T.; Bao, W.; Wang, C.; Wang, Y.; Qiu, Z. Q.; Cava, R. J.; Louie, S. G.; Xia, J.; Zhang, X. *Nature 2017 546:7657* **2017**, *546*, 265–269.

[187] Wang, X.; Du, K.; Liu, Y. Y. F.; Hu, P.; Zhang, J.; Zhang, Q.; Owen, M. H. S.; Lu, X.; Gan, C. K.; Sengupta, P.; Kloc, C.; Xiong, Q. *2D Materials* **2016**, *3*, 031009.

[188] Sun, Y. J.; Lai, J. M.; Pang, S. M.; Liu, X. L.; Tan, P. H.; Zhang, J. *The Journal of Physical Chemistry Letters* **2022**, *13*, 1533–1539.

[189] Vaclavkova, D.; Palit, M.; Wyzula, J.; Ghosh, S.; Delhomme, A.; Maity, S.; Kapuscinski, P.; Ghosh, A.; Veis, M.; Grzeszczyk, M.; Faugeras, C.; Orlita, M.; Datta, S.; Potemski, M. *Physical Review B* **2021**, *104*, 134437.

[190] Joy, P. A.; Vasudevan, S. *Physical Review B* **1992**, *46*, 5425.

[191] Basnet, R. et al. *Advanced Electronic Materials* **2024**, *10*, 2300738.

[192] Lançon, D.; Walker, H. C.; Ressouche, E.; Ouladdiaf, B.; Rule, K. C.; Mcintyre, G. J.; Hicks, T. J.; Rønnow, H. M.; Wildes, A. R. *PHYSICAL REVIEW B* **2016**, *94*, 214407.

[193] Coak, M. J. et al. *Physical Review X* **2021**, *11*, 011024.

[194] Perez-Mato, J.; Gallego, S.; Tasci, E.; Elcoro, L.; de la Flor, G.; Aroyo, M. *Annual Review of Materials Research* **2015**, *45*, 217–248.

[195] Aroyo, M. I.; Kirov, A.; Capillas, C.; Perez-Mato, J. M.; Wondratschek, H. *Acta Crystallographica Section A* **2006**, *62*, 115–128.

[196] Toby, B. H. *Powder Diffraction* **2006**, *21*, 67–70.

[197] Wildes, A. R.; Rule, K. C.; Bewley, R. I.; Enderle, M.; Hicks, T. J. *Journal of Physics: Condensed Matter* **2012**, *24*, 416004.